# Development of an optical frequency standard

**Kovačić, Domagoj**

# Development of an optical frequency standard

**Kovačić, Domagoj**


University of Zagreb
Faculty of Science
Department of Physics

Nicolaus Copernicus
University in Toruń
Faculty of Physics, Astronomy
and Informatics

Domagoj Kovačić

# DEVELOPMENT OF AN OPTICAL FREQUENCY STANDARD

DOCTORAL DISSERTATION

Zagreb, 2023


University of Zagreb
Faculty of Science
Department of Physics

Nicolaus Copernicus
University in Toruń
Faculty of Physics, Astronomy
and Informatics

Domagoj Kovačić

# DEVELOPMENT OF AN OPTICAL FREQUENCY STANDARD

DOCTORAL DISSERTATION

Supervisors:
dr. sc. Ticijana Ban
prof. hab. Michał Zawada

Zagreb, 2023


Sveučilište u Zagrebu
Prirodoslovno-matematički
fakultet
Fizički odsjek

Sveučilište Nikola
Kopernik u Toruńu
Fakultet fizike, astronomije
i informatike

Domagoj Kovačić

# RAZVOJ OPTIČKOG FREKVENTNOG STANDARDA

DOKTORSKI RAD

Mentori:
dr. sc. Ticijana Ban
prof. hab. Michał Zawada

Zagreb, 2023

Za moje predivne roditelje Dragicu i Stjepana, najdivniju sestru
Ana-Mariju i najbolju baku na svijetu, baku Maricu.
Stara bako, nadam se da si ponosna na mene.

# Supervisor information

Dr. sc. Ticijana Ban was born in Pula, Croatia in 1972. She graduated from the Faculty of Science at the University of Zagreb in 1997 with a degree in Physics. She received her PhD in Physics in 2003 with the doctoral thesis titled: "Photoassociation and Photodissociation of Alkali Molecules" with dr. sc. Goran Pichler as her supervisor. Under the Fulbright research grant in 2010 she worked as a visiting scientist at JILA (Boulder, Colorado) in the group of Prof. Jun Ye. She is currently employed as a Permanent Senior Scientist at the Institute of Physics in Zagreb where she leads the Quantum technologies group, and is currently serving as a Deputy director. Her main scientific interests include experimental studies of the interaction of cold atoms inside high-finesse optical resonators with frequency comb excitation, and quantum memories based on electromagnetically-induced transparency in hot rubidium vapours.

Prof. hab. Michał Zawada is the Associate Professor in UMK, director of National Laboratory FAMO in Toruń (KL FAMO) and the PI of the ultra-cold matter experimental group. His group, i.a., designed and build the first Bose-Einstein condensate set-up, created the first ultracold molecules, and designed and build the first two Optical Lattice Clocks in Poland. His group reported the most accurate at that time, absolute measurement of the $^{1}\mathrm{S}_{0}$ - $^{3}\mathrm{P}_{0}$ clock transition in neutral $^{88}\mathrm{Sr}$ made over the 330 km-long stabilized fibre optic link. In parallel, his group develops and operates the dual species HgRb magneto-optical trap. Their research is also focused on the study of fine-structure constant variations, and on improving limits on the Higgs-portal coupling between dark scalars particles, topological defects and Standard Model matter. More recently, his group is developing next generation of optical atomic clocks, active standards based on a superradiance phenomena.

# Funding

During my three year stay at the Nicolaus Copernicus University in Toruń I have been the recipient of two separate scholarships for which I am immensely grateful. I (and work presented in this thesis) have been funded by the TEAM "A next-generation worldwide quantum sensor network with optical atomic clocks" (TEAM/2017-4/42/styp16) scholarship funded by Foundation for Polish Science (pl. Fundacja na rzecz Nauki Polskiej), co-financed by the European Union through the European Regional Development Fund. I have also been the recipient of the Opus 13 "Study of magic and magic-zero wavelength in optical lattice clocks with blue-detuned lattice" (UMO-2017/25/B/ST2/000429) scholarship funded by the National Science Centre (pl. Narodowe Centrum Nauki).

Additionally, parts of the experimental results presented in this thesis have also received funding from the EMPIR Programme co-financed by the Participating States and from the European Union's Horizon 2020 Research and Innovation Programme (EMPIR JRP-s15 ROCIT). The measurements were performed at the National Laboratory FAMO (KL FAMO) in Toruń, Poland, and were supported by a subsidy from the Polish Ministry of Science and Higher Education.






# Acknowledgements

No man is an island and apparently neither is his PhD thesis. There are many people without whom this thesis would never have seen the light of day and for whose help I am immensely grateful.

Firstly, thanks to my two amazing co-supervisors Ticijana Ban and Michał Zawada for being amazing supervisors, for their endless supply of determination, passion and patience. I would never have made it this far without your help and council. I am truly grateful for all that you've done for me and for shaping me into the person and physicist I am today.

To my Polish crew: To Marcin Bober for his warm welcome when I first arrived in Toruń and for sharing all manner of experimental tricks and know-how, and for the awesome music he plays in the car whenever we go to lunch. To Sławomir Bilicki, for letting me shadow him in the lab and patiently answering all sort of questions to which I should've probably already known the answer. To Piotr Morzyński, for his help with electronics and programming, so I still didn't have to learn what pointers in C are. To Marcin Witkowski, for just being plain awesome and letting me steal all those M3 s crews from his lab. I swear, only like half of them ended up falling through the holes in the optical table. To my Polish and Iranian dadashes, Adam Linek, Mateusz Narożnik and Omid Vartehparvar - to Adam Linek, and Mateusz Narożnik for letting me complain to them when stuff in the lab didn't work and for serving as mobile Google translate whenever I needed stuff made in the workshop. To Omid Vartehparvar for being a friend in my last year in Toruń and showing me that being a teacher isn't all that easy. I hope I thought you a few useful tricks in the lab and good luck with fermions. I believe in you, my dadash. To Piotr Masłowski, Monika Czajkowska and Marko Hum for their help with endless paperwork we had to fight through to make this thesis possible.

To my Croatian crew: Endless thanks to Neven Šantić, for teaching me how to crawl and walk when I first entered the QT lab and teaching me how to align an AOM. Oh, and I still want my polarimeter. To Danijel Buhin, for first bringing me into the QT lab and for all the days (and nights) we spent fighting... er, I mean, discussing our experimental results. To Damir Aumiler, for his amazing insights and for asking the crucial questions to whichever results Danijel and

I were presenting in the group meeting. To Vjekoslav Vulić for not making me feel like I'm a hundred years old and for all the L-profiles he had to 3D print. I swear, this 3rd version is the last one. To Ivana Puljić, for being fun as hell to watch while she talks with her equipment and for letting me defile her Spotify list with horrible, horrible music. Sorry, not sorry. To Mateo Kruljac for being a crazy ginger and always ready to help. Sorry about that desktop background, it was all Danijels' idea, I swear. To Marin Dujmić, for being a memelord with awesome puns. To Ana Cipriš, for being a true friend for the last seven years, from the time we wasted playing Battleship in 4th year solid state physics courses all the way up to now. Thank you for not abandoning me with all those mooses in Sweden, we both know I would never make it home without you.
Finally, thanks to my wonderful family - to my parents Dragica and Stjepan, my amazing sister Ana-Marija and best grandma in the world, grandma Marica. Thank you for all your help, love and support.

# Abstract

Obviously, this thesis on optical atomic clocks is not the first of its kind. Many excellent disertations on strontium optical atomic clocks and optical clocks in general are readily available [1, 2, 3, 4, 5, 6, 7]. I have used these thesses extensively while researching for and writing my own doctoral thesis. It is my hope that my own thesis will contribute in some small way to this vast sea of excellent doctoral works and aid future young researchers when they start their journey into the field of optical atomic clocks.

This thesis will primarily focus on the work I (and other members of in POZA group at Nicolaus Copernicus University) have done during my 3 year stay with the group of prof hab. Michał Zawada. In this thesis, I will do my best to clearly differentiate between my own work and work done by other members of the POZA team. As a dual PhD student, I've had the honor and the pleasure to be a member of two research groups. The first group is the Quantum technologies group (QT) lead by dr.sc. Ticijana Ban at Center for Advanced Laser Techniques (CALT) at the Institute of Physics in Zagreb, Croatia. The second group is the Polish optical atomic clock (POZA) group lead by prof. hab. Michał Zawada at Nicolaus Copernicus University in Toruń, Poland. When I first joined the POZA group, two bosonic optical clocks (which will be referred to as Sr 1 and Sr 2 in this thesis) were already fully operational. The construction of a third clock, which was to be based on effect of superradiance of strontium atoms in a blue magic wavelength lattice, was just beginning.

This thesis will be separated into six distinct chapters. Chapter 1 (which the reader is currently reading) covers the fundamentals of optical atomic clocks and introduces the terminology used in optical atomic clock physics such as accuracy, stability, fractional stability and so forth.

Chapter 2 provides the theoretical background of the steps required to achieve clock operation. It will introduce the basics of Doppler cooling and magneto-optical traps, as well as properties of the strontium atom and its isotopes. It will then focus on methods used in cooling of two different strontium isotopes - the bosonic $^{88}$Sr and fermionic $^{87}$Sr. It will then move on to introduction of optical lattices, their magic wavelengths and atomic polarizabilities of clock states of the strontium atom. It finally finishes with high-precision spectroscopy of the clock transition

in strontium and digital locking of the clock laser to the atomic line of the clock frequency.
Chapter 3 presents measurements of photoionization cross sections of atomic states used in optical clock cycle of $^{88}\mathrm{Sr}$. These photoionization cross sections where measured at the newly proposed blue magic wavelength. It will then present my own theoretical work on the study of feasibility of using blue magic wavelength optical lattice optical clocks. It will end by presenting my work of examining photoionization induced losses of atoms in blue magic wavelength optical lattice, the resulting constraints on blue magic wavelength lattice optical clocks and possible mitigation measures.
Chapter 4 presents experimental work done by myself and other members of POZA group on redesign and upgrading of Sr 1 optical clock to enable simultaneous (and intermittent) operation of both the bosonic and fermionic optical clock.
Chapter 5 presents results on my work on getting the fermionic optical clock in Sr 1 fully operational. It will examine the loading of the fermionic blue and red MOTs. Also, where feasible, it will make comparisons with its bosonic counterpart.
Chapter 6 will present the evaluation of systematic shifts (accuracy budget) for the bosonic optical clock in Sr 1 as part of our international March 2022 campaign.
Appendix A will show the work (in form of published articles) I've done (in collaboration with other members of the QT group) on cooling of $^{87}\mathrm{Rb}$ and $^{85}\mathrm{Rb}$ using a frequency comb, as well the examination of frequency-comb-induced radiation pressure force in dense atomic clouds.

Keywords: cold atoms, strontium optical atomic clock, blue magic wavelength, blue magic wavelength optical atomic clock, photoionization

# Wprowadzenie

Przedstawiana dysertacja oczywiście nie jest pierwszą tezą napisaną o optycznych zegarach atomowych. Wiele doskonałych rozpraw na temat optycznych zegarów strontowych i ogólnie optycznych zegarów atomowych jest łatwo dostępnych [1, 2, 3, 4, 5, 6, 7] . Szeroko korzystałem z tych tez podczas badań i pisania własnej pracy doktorskiej. Mam nadzieję, że moja własna praca przyczyni się w jakiś niewielki sposób do tego ogromnego morza doskonałych prac doktorskich i pomoże przyszłym młodym badaczom, gdy rozpoczną swoją podróż w dziedzinie optycznych zegarów atomowych. Teza ta skupi się przede wszystkim na pracy, którą ja (i inni członkowie grupy POZA na Uniwersytecie Mikołaja Kopernika w Toruniu) wykonaliśmy podczas mojego 3-letniego pobytu w grupie dr. hab. Michała Zawady. W tej pracy postaram się wyraźnie odróżnić pracę własną od pracy innych członków zespołu POZA. W czasie pracy nad podwójnym doktoratem miałem zaszczyt i przyjemność być członkiem dwóch grup badawczych. Pierwsza grupa to grupa technologii kwantowych (QT) kierowana przez dr. sc. Ticijanę Ban w Centrum Zaawansowanych Technik Laserowych (CALT) w Instytucie Fizyki w Zagrzebiu, Chorwacja. Druga grupa to grupa polskiego optycznego zegara atomowego (POZA) kierowana przez dr. hab. Michała Zawadę, prof. UMK, na Uniwersytecie Mikołaja Kopernika w Toruniu. Kiedy po raz pierwszy dołączyłem do grupy POZA, dwa bozonowe zegary optyczne (które w tej pracy będą określane jako Sr1 i Sr2) były już w pełni sprawne. Budowa trzeciego zegara, który miał bazować na efekcie nadpromienistości atomów strontu w sieci o niebieskiej magicznej długości fali, dopiero się zaczynała.

Ta teza została podzielona na sześć rozdziałów. Rozdział 1 (który czytelnik obecnie czyta) obejmuje opis podstaw optycznych zegarów atomowych i wprowadzenie terminologii stosowanej w fizyce zegarów atomowych, takiej jak dokładność, stabilność, stabilność względna i tak dalej. Rozdział 2 zawiera teoretyczne podstawy kroków wymaganych do skonstruowania optycznego zegara atomowego. W rozdziale przedstawione są podstawy chłodzenia dopplerowskiego i pułapki magnetooptycznej, a także właściwości atomu strontu i jego izotopów. Dalszy opis skupia się na metodach stosowanych w chłodzeniu dwóch różnych izotopów strontu - bozonowego $^{88}\mathrm{Sr}$ i fermionowego $^{87}\mathrm{Sr}$. Następnie wprowadzone są pojęcia sieci optycznej, magicznych dłu-

gości fal i polaryzowalności atomowej stanów zegarowych atomu strontu. Rozdział kończy się opisem precyzyjnej spektroskopii przejścia zegarowego w stroncie. Po zlokalizowaniu przejścia laser zegarowy jest cyfrowo stabilizowany do linii atomowej przejścia zegarowego.
Rozdział 3 przedstawia pomiary przekrojów fotojonizacyjnych stanów atomowych stosowanych w cyklu zegara optycznego $^{88}\mathrm{Sr}$. Przekroje te zostały zmierzone przy stosunkowo niedawno zaproponowanej niebieskiej magicznej długości fali. Następnie przedstawiona jest moja własna praca teoretyczna na temat możliwości wykorzystania optycznych zegarów atomowych z siecią optyczną o niebieskiej magicznej długości fali. Rozdział kończy się przedstawieniem mojej pracy badającej straty atomów wywołane fotojonizacją w sieci optycznej o niebieskiej magicznej długości fali, wynikające z tego ograniczenia optycznych zegarów atomowych i możliwe środki zaradcze.
Rozdział 4 przedstawia eksperymentalne prace wykonane przeze mnie i innych członków grupy POZA przy przeprojektowaniu i modernizacji zegara optycznego Sr 1 tak, aby umożliwić jednoczesne (i naprzemienne) działanie zarówno bozonowego, jak i fermionowego zegara optycznego.
Rozdział 5 przedstawia wyniki mojej pracy nad zapewnieniem pełnej sprawności fermionowego zegara optycznego w Sr 1. Zbadane zostały ładowanie fermionowych niebieskich i czerwonych pułapek magneto-optycznych. Ponadto tam, gdzie to możliwe, dokonano porównań do ich bozonowych odpowiedników.
Rozdział 6 przedstawi ocenę systematycznych przesunięć (budżet niepewności) częstości bozonowego zegara optycznego w Sr1 wykonanych w ramach międzynarodowej kampanii porównań częstotliwości w marcu 2022 r.
Załącznik A raportuje pracę (w formie opublikowanych artykułów), którą wykonałem (we współpracy z innym członkiem grupy QT) nad chłodzeniem $^{87}\mathrm{Rb}$ i $^{85}\mathrm{Rb}$ za pomocą grzebienia częstotliwości, a także badanie siły ciśnienia promieniowania indukowanego grzebieniem częstotliwości w gęstych chmurach atomowych.

Słowa kluczowe: zimne atomy, strontowy optyczny zegar atomowy, niebieska magiczna długość fali, fotojonizacja

# Prošireni sažetak

Ova teza o optičkim atomskim satovima nije prva te vrste. Mnoge izvrsne disertacije o stroncijevim optičkim atomskim satovima i optičkim satovima općenito su već dostupne [1, 2, 3, 4, 5, 6, 7]. Opsežno sam koristio ove teze dok sam istraživao i pisao svoj doktorski rad. Nadam se da će moja vlastita teza donekle pridonijeti ovom golemom moru izvrsnih doktorskih radova i pomoći budućim mladim istraživačima kada krenu na svoje putovanje u područje optičkih atomskih satova.

Ovaj diplomski rad prvenstveno će se fokusirati na rad koji sam ja (i drugi članovi POZA grupe na Sveučilištu Nikole Kopernika) obavili tijekom mog trogodišnjeg boravka u grupi prof.hab. Michała Zawade. U ovom diplomskom radu nastojat ću jasno razlikovati svoj doprinos od doprinosu ostalih članova POZA tima. Kao dvojni doktorand, imao sam čast i zadovoljstvo biti članom dviju istraživačkih grupa. Prva grupa je Grupa za kvantne tehnologije (QT) koju vodi dr.sc. Ticijana Ban u Centru za napredne laserske tehnike (CALT) na Institutu za fiziku u Zagrebu, Hrvatska. Druga grupa je Grupa za poljski optički atomski sat (POZA) koju vodi prof. hab. Michał Zawada na Sveučilištu Nikola Kopernik u Toruńu, Poljska. Kad sam se tek pridružio POZA grupi, dva bozonska optička sata (koji će se u ovom diplomskom radu nazivati Sr 1 i Sr 2) već su bila u potpunosti operativna. Izgradnja trećeg sata, koji se trebao temeljiti na učinku superradijativnosti atoma stroncija u optičkoj rešetci plave magične valne duljine, tek je počinjala.

Ova teza biti će podijeljena u šest zasebnih poglavlja. Poglavlje 1 (koje čitatelj upravo čita) pokriva osnove optičkih atomskih satova i uvodi terminologiju koja se koristi u fizici optičkih atomskih satova kao što su točnost, stabilnost, frakcionalna stabilnost i tako dalje.

Poglavlje 2 pružit će teorijsku pozadinu koraka potrebnih za postizanje rada optičkog atomskog sata. Upoznat će čitatelja s osnovama Dopplerovog hlađenja i magneto-optičkih zamki, kao i svojstvima atoma stroncija i njegovih izotopa. Zatim će se usredotočiti na metode koje se koriste u hlađenju dvaju različitih izotopa stroncija - bozonskog $^{88}\mathrm{Sr}$ i fermionskog $^{87}\mathrm{Sr}$. Zatim će se prijeći na uvod u optičke rešetke, njihove magične valne duljine i atomske polarizabilnosti satnog stanja atoma stroncija. Konačno završava visokopreciznom spektroskopijom satnog pri-

jelaza u stronciju koja se koristi za pronalaženje satnog prijelaza u optičkom atomskom satu. Nakon što je prijelaz lociran, digitalno zaključavamo naš satni laser na atomsku liniju satnog prijelaza.

Poglavlje 3 predstavit će mjerenja fotoionizacijskih poprečnih presjeka atomskih stanja koja se koriste u ciklusu optičkog sata za $^{88}\mathrm{Sr}$. Ovi presjeci izmjereni su na novopredloženoj plavoj magičnoj valnoj duljini. Zatim će predstaviti moj vlastiti teorijski rad na proučavanju izvedivosti korištenja optičkih rešetki sa plavom magičnom valnom duljinom u optičkim atomskim satovima. Završit ću predstavljanjem mog rada na ispitivanju gubitaka atoma u magneto-optičkoj stupici izazvanih fotoionizacijom atoma u optičkoj rešetki sa plavom magičnom valnom duljinom, rezultirajućih ograničenja optičkih satova sa optičkim rešetkama sa plavom magičnom valnom duljinom i mogućih mjera za ublažavanje navedenih gubitaka.

Poglavlje 4 predstavit će eksperimentalni rad koji sam obavio ja i drugi članovi grupe POZA na redizajnu i nadogradnji Sr 1 optičkog sata kako bi se omogućio istovremeni (i isprekidani) rad bozonskog i fermionskog optičkog sata.

Poglavlje 5 predstavit će preliminarne rezultate mog rada na postizanju operabilnosti fermionskog optičkog sata u Sr 1. Ispitat će se spremanje atoma u plavu i crvenu fermionsku magneto-optičku stupicu. Također, gdje je to moguće, napravit će se usporedbe sa bozonskom plavom i crvenom magneto-optičkom stupicom.

Poglavlje 6 predstavit će procjenu sistematskih pomaka (eng. systematic shifts) satnog prijelaza za bozonski optički sat u Sr 1 kao dio naše međunarodne kampanje iz ožujka 2022.

U poglavlju 7 dan je zaključni pregled rezultata ovog doktorskog rada, kao i perspektive za daljnja istraživanja.

Dodatak A će pokazati rad (u obliku objavljenih članaka) koji sam obavio (u suradnji s drugim članovima QT grupe) na hlađenju $^{87}\mathrm{Rb}$ i $^{85}\mathrm{Rb}$ korištenjem frekventnog češlja, kao i ispitivanje sile zračenja inducirane frekventnim češljem u gustim atomskim oblacima.

Ključne riječi: hladni atomi, stroncij, optički atomski sat, optička rešetka, plava magična valna duljina, fotoionizacija

# Contents


**1 Introduction** **1**
1.1 Importance of (optical atomic) clocks . . . 1

**2 Theoretical background of optical clock operation** **5**
2.1 Doppler cooling . . . 5
2.2 The strontium atom . . . 8
2.3 Cooling of strontium . . . 10
2.4 Cooling of bosonic $^{88}$Sr . . . 11
2.5 Cooling of fermionic $^{87}$Sr . . . 15
2.6 Optical lattices . . . 19
2.7 Lamb-Dicke regime of the optical lattice . . . 22
2.8 Atomic polarizability and magic wavelength . . . 25
2.9 High-precision spectroscopy of $^1\mathrm{S}_0 \rightarrow {}^3\mathrm{P}_0$ . . . 30

**3 Feasibility of blue magic wavelength optical lattice clocks** **35**
3.1 Confinement of atoms in blue-detuned optical lattice . . . 35
3.2 Photoionization of atoms in blue-detuned optical lattice . . . 45
3.2.1 Photoionization of $^1\mathrm{P}_1$ . . . 45
3.2.2 Photionization of $^3\mathrm{S}_1$ . . . 50

**4 Strontium optical clock experiment in KL FAMO** **54**
4.1 High-finesse optical cavities for 689 nm and 698 nm lasers . . . 54
4.2 Vacuum setup . . . 57
4.3 The Zeeman slower . . . 59
4.4 Blue MOT on $^1\mathrm{S}_0 \rightarrow {}^1\mathrm{P}_1$ transition . . . 61
4.5 Red MOT cooling on $^1\mathrm{S}_0 \rightarrow {}^3\mathrm{P}_1$ transition . . . 63
4.6 Red-detuned 813 nm dipole trap . . . 66
4.6.1 Optical cavity Pound-Drever-Hall frequency locking . . . 67
4.7 The clock transition spectroscopy . . . 69
4.7.1 Phase noise cancellation . . . 69

**5 Characterization of the fermionic optical clock** **72**
5.1 Fermionic blue MOT . . . 72
5.2 Fermionic red MOT . . . 74

**6 Evaluation of systematic shifts of bosonic optical clock (Sr 1)** **81**
6.1 Linear and quadratic Zeeman shift . . . . . 81
6.2 Lattice light shift . . . . . 83
6.3 Probe light shift . . . . . 84
6.4 Density shift . . . . . 86
6.5 Collisional effects . . . . . 87
6.6 Black body radiation . . . . . 87
6.7 Gravitational red shift . . . . . 89
6.8 Accuracy budget . . . . . 89

**7 Conclusion** **90**

**References** **131**

# List of Figures


1.1 Evolution of fractional systematic uncertainty of atomic clocks over the years . 2
1.2 Schematic of measurements of accuracy and stability with different accuracies and stabilities . . . . . 2

2.1 The basic principles of Doppler cooling and trapping of atoms . . . . . 7
2.2 Relevant energy levels for $^{88}$Sr with corresponding lifetimes $\tau$ and linewidths $\Gamma$. 12
2.3 Fermionic energy levels . . . . . 16
2.4 Fermionic MOT operation compared to MOT operation of alkali atomic species 18
2.5 A two-dimensional (2D) optical lattice potential created by two orthogonal sets of of counter-propagating beams . . . . . 22
2.6 Harmonic oscillator and possible transitions in the Lamb-Dicke regime . . . . . 24
2.7 Sideband spectroscopy of the clock transition and lifetime in lattice . . . . . 25
2.8 Dynamic polarizability of the clock transition states . . . . . 28
2.9 Magnetically induced spectroscopy of the forbbiden clock transition in bosonic optical clock . . . . . 31
2.10 Optical clock cycle in an optical clock . . . . . 32
2.11 Spectroscopy of the $^1$S$_0$ $-^3$ P$_0$ of bosonic strontium . . . . . 33

3.1 (left) Band structure for 3 lowest energy bands (n=0,1,2) for a blue-detuned optical lattice and bandwidth . . . . . 38
3.2 External lattice potential as seen by atoms in a vertical optical lattice . . . . . 39
3.3 Wannier-Stark (WS) states in position representation for different lattice depths for 390 nm (left) and 813 nm (right) magic wavelength lattices . . . . . 40
3.4 Wannier-Stark ladder of states for the ground and excited clock states . . . . . 41
3.5 Relative coupling strengths $|\frac{\Omega_{\Delta M}}{\Omega}|^2$ of the "carrier" $\Omega_0$ and the 4 "sidebands" $\Omega_{\pm1,\pm2}$ . . . . . 42
3.6 Calculated Wannier-Stark resonances for 5,10 and 20 $E_r$ lattice depths for blue-detuned and red-detuned optical lattices . . . . . 43
3.7 Schematic energy level diagram showing relevant optical transitions used in the basic cycle of a strontium optical lattice clock . . . . . 46
3.8 The timing sequence of the lasers used in the $^1$P$_1$ photoionization experiment . 47
3.9 Typical fluorescence of $^{88}$Sr atoms detected while loading into the blue MOT in the presence (left) and in the absence (right) of the photoionizing 389.889 nm light . . . . . 48

3.10 The photoionization cross section from the $^1P_1$ state as a function of the wavelength of the ionizing light . . . 49
3.11 The timing sequence of the lasers used in the $^3S_1$ photionization experiment . . 51
3.12 The total effective intensity $I_{eff}$ experienced by the atoms trapped in the motional ground state of a 3D blue-detuned magic wavelength optical lattice . . . 52

4.1 The high-finesse optical clock cavity setup for the 698 nm clock laser . . . 55
4.2 Installation of granite plates onto the anti-vibrational platform to reduce the overall load on the platform . . . 56
4.3 Schematic of the ultrahigh vacuum setup in KL FAMO. The setup consists of an oven, a Zeeman slower with mu-metal magnetic shielding and vacuum chamber 58
4.4 Magnetic field created by the Zeeman coils and simulated fields with and without the magnetic shielding . . . 59
4.5 Schematic design of the Zeeman slower . . . 60
4.6 Relevant atomic blue MOT frequencies for $^{88}$Sr and $^{87}$Sr and frequencies of blue MOT laser beams used for Zeeman slower and 3D MOT cooling . . . 61
4.7 Experimental setup for blue MOT in KL FAMO . . . 62
4.8 Relevant atomic red MOT frequencies for $^{88}$Sr and $^{87}$Sr and frequencies of red MOT laser beams used for 3D MOT bosonic (fermionic) trapping and fermionic stirring . . . 64
4.9 Experimental setup for red MOT in KL FAMO . . . 65
4.10 Optical setup for the 813 nm dipole trap . . . 67
4.11 Beat of 813 nm Ti-Sa laser with the frequency comb . . . 68
4.12 Relevant atomic clock frequencies for $^{88}$Sr and $^{87}$Sr and frequencies for bosonic and fermionic clock transitions . . . 69
4.13 Experimental setup for clock spectroscopy with phase noise cancellation . . . 70

5.1 Number of atoms as a function of loading time for fermionic and bosonic blue MOT . . . 73
5.2 Spectroscopy of $^1S_0 \rightarrow {}^3P_1$ transition for different total intensities of the trapping beam . . . 75
5.3 Spectroscopy over the $F = 9/2 \rightarrow F' = 9/2$ stirring transition with the trapping beam during SF red MOT being either turned off or turned on . . . 77
5.4 The decay in flourescence in the fermionic SF red MOT phase as a function of the duration of the SF red MOT phase was measured . . . 78

6.1 Depedence of the quadratic Zeeman shift of the clock transition as a function of magnetic field . . . 82
6.2 Dependence of the lattice light shift as a function of lattice light intensity . . . 84
6.3 Dependence of the probe light shift as a function of probe light intensity . . . 85
6.4 Dependence of density shift as a function of number of atoms in the optical lattice 86
6.5 The simulated temperature distribution of the vacuum systems and theirs surroundings . . . 88

# Chapter 1

# Introduction

## 1.1 Importance of (optical atomic) clocks

The ability to measure and keep time has played an essential role in the rise of modern civilisation. Since the first humans emerged from the savanas of Africa to form the nuclei of what would become the first human civilisations, timekeeping has been an important part of their lives. It allowed them to plan many social endeavours from trade, religious ceremonies to agriculture. With the introduction of duodecimal (12) and sexigesimal (60) timekeeping system by the ancient Summerians, the basis of how we measure hours and days has been set. These first attempts to measure time were done using astronomy by monitoring the motions of celestial objects. As one might expect, these methods weren't very precise and without a universal standard. Other units in the metric system such as length and weight had similar issues, with different kingdoms and empires using different metrics and units.

By the time of the French revolution, some strides were made to create blue an universal metric system, mostly focusing on the measurement of distance and weight. The first played a crucial role in design of naval maps and sea navigation, while measurement of weight had an important role in everyday trade and commerce.

By 1967, other units such as the Ampere, the Kelvin, the mole, the candela and the second were also defined, with the second "defined by taking the fixed numerical value of the caesium frequency, $\Delta\nu_{\mathrm{Cs}}$, the unperturbed ground-state hyperfine transition frequency of $^{133}\mathrm{Cs}$, to be 9192631770 when expressed in the unit Hz, which is equal to $\mathrm{s}^{-1}$". From this point on, measurement of time and frequency has become inextricably linked. What distinguishes time and frequency for other units is our ability to measure them with unprecedented stability and accuracy, far beyond of what we can do with other physical quantities. The first caesium clock developed in 1955 [9] had an accuracy at $10^{-10}$ level. It is no surprise that the statement of late

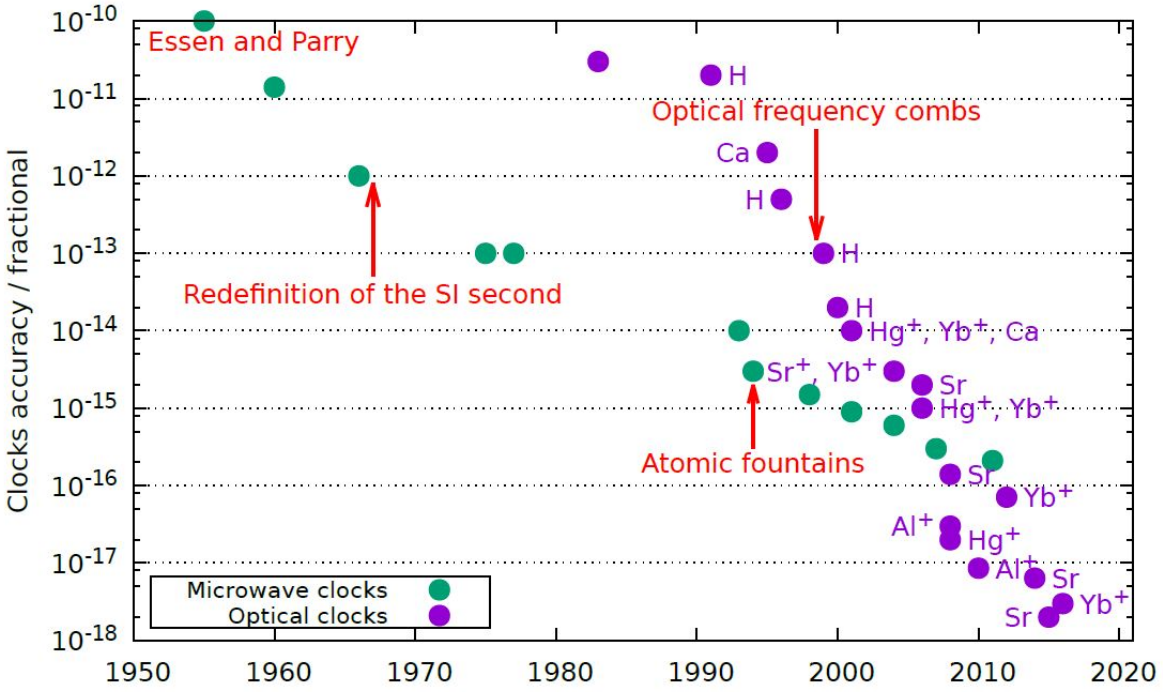


Figure 1.1: Evolution of fractional systematic uncertainty of atomic clocks over the years. The best strontium optical atomic clocks reach systematic uncertainty of 2 x $10^{-18}$ [8].

Nobel physics laurate Arthur Schawlow: "Never measure anything but frequency!" has become almost an axiom of the timekeeping community. After 50 years of development, state-of-the-art microwave atomic clocks have reached accuracy of $10^{-16}$ and 1.6 x $10^{-14}$ stability at 1 s, limited only by the quantum projection noise limit [10]. The evolution of fractional systematic uncertainty of atomic clocks over years is shown in Fig. 1.1. Clearly, to make the next step in development of frequency standards, a new type of frequency standard would be required. However, before we move into that, we should clarify the two terms we used to characterise our clocks - accuracy and stability. The schematic of accuracy and stability is shown in Fig. 1.2. Due to external perturbations (electric and magnetic fields, light fields, black body radiation

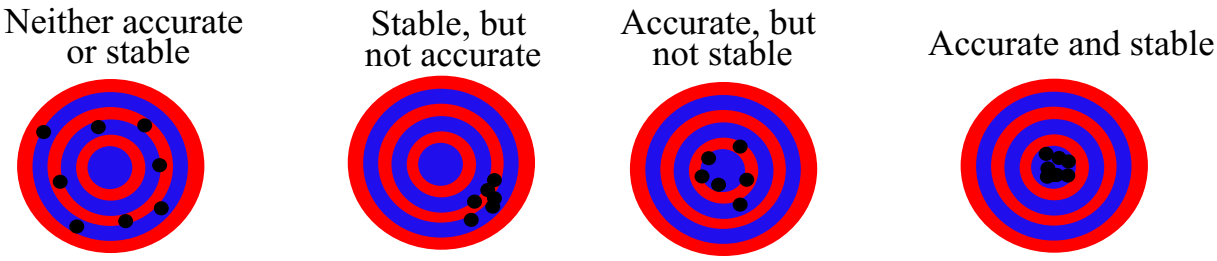


Figure 1.2: Schematic of measurements of accuracy and stability with different accuracies and stabilities.

etc), the experimentally measured clock transition frequency will be shifted from the true value of the unperturbed transition. Clock accuracy tells us how much our measured clock transition frequency is shifted from this true value and is usually expressed as either the shift in absolute value $\Delta\nu$ (in Hz) or fractional shift $\Delta\nu/\nu$ where $\nu$ is the absolute transition frequency of the clock transition. Clock stability is the statistical measurement which tells us how our clock transition frequency changes in time. In this thesis it will be expressed as fractional frequency stability, which is the ratio of stability and the absolute frequency of the clock transition. Frequency of the atomic clock transition $\omega$, when perturbed by environmental influences is given as [5]

$$\omega = \omega_0(1 + \epsilon + y(t)), \tag{1.1}$$

where $\omega_0$ is the frequency of the unperturbed transition, $\epsilon$ is the fractional frequency correction due to systematic effects and $y(t)$ is the fractional fluctuation of the frequency of the clock transition in time.

The evaluation of stability of the clock transition is represented using the Allan variance [11]

$$\sigma_y^2(\tau) = \langle \frac{1}{2}(\overline{y_{k+1}} - \overline{y_k})^2 \rangle, \tag{1.2}$$

where the $\overline{y_k}$ is the mean value of the fractional frequency deviation around $t_k$

$$\overline{y_k} = \frac{1}{\tau}\int_{t_k}^{t_k+\tau} y(t)dt = \frac{1}{\tau}\int_{t_k}^{t_k+\tau} \frac{\nu(t) - \nu_0}{\nu_0}dt, \tag{1.3}$$

where $\nu_0$ is the nominal frequency over some period $\tau$. The Allan deviation, given as the square root of the Allan variance, is equal to

$$\sigma_y(\tau) = \frac{\chi}{2\pi Q S/N}\frac{t_c}{\tau}, \tag{1.4}$$

where $Q = \frac{\nu}{\Delta\nu}$ is the line quality factor of the clock transition for clock linewidth $\Delta\nu$, $S/N$ is the signal-to-noise ratio achieved in measurement cycle time $t_c$, and $\chi$ is a constant of the order of unity which depends on the transition lineshape used in measurement [1]. Clearly, to improve stability of our clock we wish to push both $Q$ and $S/N$ in Eq. 1.4 to be as large as possible. However, to increase $S/N$ ratio, one would have to increase the number of atoms in the microwave clock. This would bring issues with atomic collisions which would affect clock accuracy.

An alternative option is increasing the quality factor by using an atomic transition with a higher frequency. Therein lies the motivation to move from microwave to optical atomic clocks. As-

suming all other parameters being equal, the change from microwave to optical transition increases clock stability by 4 orders of magnitude.

Optical atomic clocks can generally be separated into two groups - those which use ions and those which use neutral atoms. Ion clocks were first developed. Ions can be trapped in a Paul trap [12] for whose development Wolfgang Paul was awarded the Nobel Prize in 1989 "for his development of a method for using electrical currents and electromagnetic fields to capture charged atoms in a trap". The Paul-type traps use a quadrupole potential which varies in time, trapping the atom using Coulumb force. An ion can be stored in such a trap for days or even months. There are, however, disadvantages of using ions. Since ions strongly interact with other ions or particles, only a few ions can be trapped at a time. Many ion clocks, such as $Al^+$ [13, 14], $Ca^+$ [15, 16], $Yb^+$ [17, 18], $Sr^+$ [19, 20, 21], $In^+$ [22, 23, 24], $Hg^+$ [25], $Ra^+$ [26], $Ar^+$ [17] are in development. The best $Yb^+$ ion clocks can reach accuracy of $3 \text{ x } 10^{-18}$ [18]. In contrast to ion clocks, optical lattice clocks are based on cooling and trapping of neutral atoms in an optical lattice dipole potential. Since atoms are neutral particles, their interaction with each other and their environment is much weaker compared to ions. This enables trapping and interrogation of many atoms in a single trap. However, their neutral charge also makes trapping them more complicated due to their weaker interaction with electric fields. In development of optical lattice clocks, the greatest focus was placed on earth-alkaline and earth-like-alkaline atoms. These atoms have simple energy structure and narrow intercombination lines such as the $^1S_0 \rightarrow {}^3P_0$ double forbidden transition with sub-Hertz linewidth. Current limitations of the observed linewidth come from maximum interrogation time of clock transition of about 1 s due to limited coherence time of the clock laser. Optical lattice clocks can be operated using a number of earth-alkali atoms, like Sr [8, 27, 28, 29], Yb [30, 31, 32, 33] and Hg [34, 35, 36]. This thesis will focus on my work done on the strontium optical lattice clocks which we will discuss in much greater detail in the following chapters.

# Chapter 2

# Theoretical background of optical clock operation

This section provides the theoretical background of optical clock operation and the steps required to achieve clock operation. First I will discuss the theoretical background of Doppler cooling and magneto-optical trapping of atoms, the first step in all cold atoms experiments. After that I will discuss the atomic properties of strontium, our chosen atom for atomic clock operation. I will then finally cover each stage in an optical clock cycle, starting with the two-stage cooling, loading of atoms in the optical lattice and ending with the high-precision spectroscopy of the clock transition.

## 2.1 Doppler cooling

We begin our journey into the magical forests of optical atomic clocks in the same place as most cold atom experiments do - by building a magneto-optical trap (MOT) - a system consisting of spatially-varying magnetic fields and laser beams used to cool and trap atoms. The method used to cool atoms is (quite appropriately) called Doppler cooling and is depicted in Fig. 2.1 a). This technique has been first proposed by Hänsch and Schawlow in 1975 [37] with first experimental demonstration of both neutral atoms [38] and ions [39] in the following years.
We consider a simplified picture of a two-state atom moving in 1D with velocity $\vec{v_x}$ in x direction from left to right in an EM field created by two counter-propagating laser beams as shown in Fig. 2.1 a). In Fig. 2.1 a), the atom is depicted by a blue sphere with the two black circles around the sphere representing the two possible energy states of the atom. Photons from both beams have frequency $\omega_l$ which is smaller than the transition frequency $\omega_0$ of the atomic transition. We say the laser is red-detuned (with detuning given as $\delta = \omega_l - \omega_0$ (in Hz) where $\delta < 0$ for

red-detuned beams and where $\delta > 0$ for blue-detuned beams). Due to the Doppler shift $\vec{k_x} \cdot \vec{v_x}$, where $\vec{k_x}$ is the wavevector of the photons in x direction, the atom will see photons coming from the right as shifted up in frequency (blue-detuned) and therefore in resonance with the atomic transition, while photons coming from the left are out of resonance. This will cause the atom to preferentially absorb photons whose wavevector direction is opposite to the direction of atoms' velocity which will result in lowering of its velocity. After absorbing a photon, the atom will jump to its excited internal state and after a short period of time de-excite back to the ground state via spontaneous emission. In spontaneous emission photons are emitted in a random direction. Therefore, over many absorption-emission cycles, the spontaneous emission will not contribute to the change of atoms' velocity. This process of preferential absorption and spontaneous emission, referred to as Doppler cooling, will over many cycles reduce the velocity of the atom. The story about Doppler cooling can easily be extended from 1D to 3D by simply adding two additional sets of counter-propagating beams, creating 3 mutually orthogonal sets of counter-propagating beams in 3 directions (x,y,z), as shown in Fig. 2.1 c).
Let us consider how these cycles of absorption-emission would affect an ensemble of atoms in an idealized gas as this will be our starting point in an optical clock. The 3D velocity distribution of such an ensemble of atoms is given by the Maxwell-Boltzmann distribution for which the root mean square velocity is given as $\mathrm{v_{rms}} = \sqrt{\frac{3\mathrm{k_B T}}{\mathrm{m_a}}}$ where $\mathrm{T}$ is temperature of the gas, $\mathrm{m_a}$ is mass of individual atoms and $\mathrm{k_B}$ is the Boltzmann constant [40]. We can easily see that a reduction in $\mathrm{v_{rms}}$ velocity of the Maxwell-Boltzmann distribution will also result in cooling down of the atomic ansamble.

From the description of Doppler cooling, one may initially expect that the laser beams will continue to slow down the atom until it reaches zero velocity. In terms of temperature of an ansamble of atoms, this corresponds to cooling to absolute zero. That, however, is not the case. There is a lower limit to the temperature achievable with Doppler cooling. This temperature is called the Doppler temperature and is given as $\mathrm{T_{Doppler}} = \frac{\hbar\Gamma}{2\mathrm{k_B}}$ where $\Gamma = 2\pi\gamma$ where $\gamma$ is the natural linewidth (in Hz) of the atomic transition used for Doppler cooling and $\hbar$ is the reduced Planck constant. In other words, temperatures achievable by Doppler cooling are limited by the properties of the atom being cooled, i.e. the linewidth of the cooling transition. This limit appears due the spontaneous emission described is Fig. 2.1. In spontaneous emission photons are emitted in a random direction. The kicks in momentum the atom receives from the emission of photons result in random walk of the atom. The rate of these spontaneous emission kicks is given by the lifetime of the upper state of the atom. A shorter lifetime (i.e, a larger natural linewidth $\gamma$) will result in higher rate of spontaneous emission kicks. This increases the atoms' velocity, heating the atomic ansamble and giving a higher Doppler temperature. At equilibrium

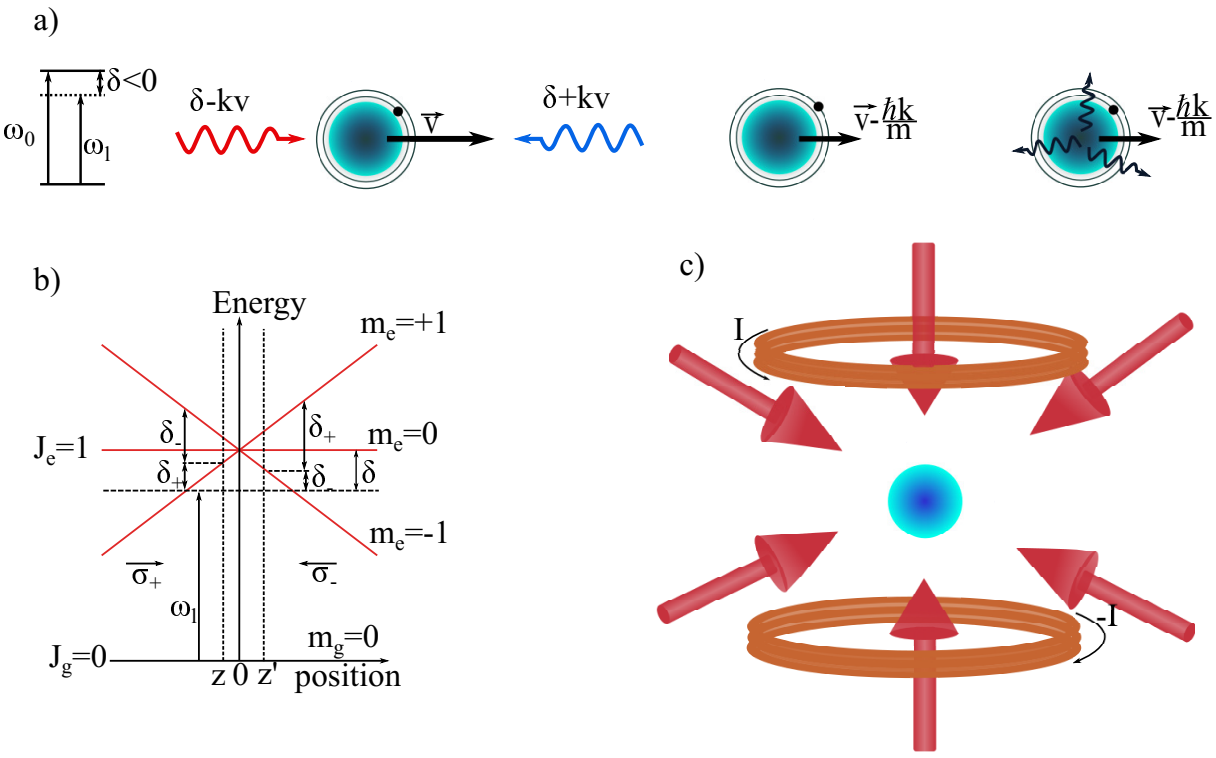


Figure 2.1: The basic principles of Doppler cooling and trapping of atoms. Top figure shows an atom with velocity $\vec{v}$ moving from left to right in an EM field created by two counterprogating laser beams. Both beams are detuned by $\delta = \omega_l - \omega_0 < 0$. However, due to the Doppler shift, the atom sees the photons coming from the right (left) as blue-detuned (red-detuned) and therefore in (out of) resonance with its atomic transition. This will make the atom preferentially absorb photons from the right which lowers its velocity. The Zeeman splitting of magnetic sublevels of the upper state of $J_g = 0 \rightarrow J_e = 1$ transition is shown in bottom right figure. For an atom at position z, a laser with frequency $\omega_l$ will be detuned by $\delta_+$ ($\delta_-$) from the $m_e = 1$ ($m_e = -1$) magnetic sublevels of the excited state $J_e = 1$. Since at position z we have $\delta_+ < \delta_-$, the atom will preferentially absorb photons from the $\sigma_+$ circularly-polarized beam, pushing it towards the center of the trap. Similarly, for atom at z' we have $\delta_- < \delta_+$, and the atom preferentially absorbs $\sigma_-$ circularly-polarized beam, again pushing the atom towards the center of the trap.

the heating and cooling rate are equal, and the temperature at this equilibrium is the Doppler temperature [40].

Temperatures below this limit are usually called sub-Doppler temperatures and can be achieved by using different sub-Doppler cooling techniques such as Sisyphus [41] or evaporative [42] cooling. This temperature is called recoil temperature and it is given as $T_{recoil} = \frac{\hbar^2 k^2}{m_a k_B}$. This limit arises from the fact that there is a minimum amount of momentum $\hbar k$ a single photon can impart on the atom to change its velocity.

So far we've spoken only about cooling of atoms. However, cooling down atoms alone isn't sufficient as atoms will eventually diffuse out of the area of overlap of the cooling beams and escape. To trap atoms we require a spatially-dependent, restoring force which will ensure atoms are pushed to the center of the trap and prevent them from escaping. This will also ensure high enough density of atoms for experimental purposes thus enabling sufficient signal-to-noise for experiments. The trapping is achieved by adding a linear magnetic field gradient to the optical part of the trap [43]. To explain trapping of atoms, we will assume the case with the simplest internal structure where the atom has total angular momentum $|\mathrm{J_g} = 0, \mathrm{m_g} = 0\rangle$ in the ground state and $|\mathrm{J_e} = 1, \mathrm{m_e} = 0, \pm 1\rangle$ in the excited state.
We now place our cooled atoms into magnetic field with a linear gradient by using a set of magnetic coils in anti-Helmholtz configuration, as depicted in Fig. 2.1 c). This magnetic field will split the magnetic sublevels $\mathrm{m_e} = -1, 0, +1$ of the excited state $\mathrm{J_e}$, as shown in Fig. 2.1 b). We now consider what will happen with an atom at some position z in the magneto-optical trap. The atom is in an EM field created by counter-propagating two laser beams with the same laser frequency $\omega_\mathrm{l}$ but different circular polarization $\sigma_+$ and $\sigma_-$. Due to the splitting, the laser will be detuned by different detunings $\delta_+$ ($\delta_-$) from the $\mathrm{m_e} = 1$ ($\mathrm{m_e} = -1$) magnetic sublevels. Since at position z $\delta_+$ is smaller in value than $\delta_-$, the atom will preferentially absorb photons from the $\sigma_+$ beam. This will push atoms to the center of the trap. Conversely, at position z', $\delta_- < \delta_+$ is valid. The atom will then prefer to absorb photons from the $\sigma_-$ beam and again be pushed towards the center of the trap. This effectively traps the atoms at the center of the trap and prevents them from escaping.

## 2.2 The strontium atom

In the previous section we covered the basics of cooling and trapping of atoms, but haven't said anything specific about the properties of the atom we wish to use in our optical clock experiment, strontium.
Strontium (Sr) is an earth-alkali chemical element with the atomic number Z=38. As an earth-alkali element, strontium has 2 electrons in its outer $[\mathrm{Kr}]5\mathrm{s}^2$ shell. Since the last two electrons of strontium are in the s-shell, strontium has angular momentum L=0 in the ground state. Additionally, as there are 2 electrons (both with s=1/2 spin) in the s-shell, the total spin can be either S=0 or S=1. This will give raise to either a singlet (S=0) or triplet (S=1) states. Due to LS coupling, total angular momentum J=L+S of the ground $^1\mathrm{S}_0$ singlet state will be J=0. The two lowest excited p-states will be either the singlet $^1\mathrm{P}_1$ state with J=1 or triplet $^3\mathrm{P}_\mathrm{J}$ with J=0,1,2.
Along with the electronic structure of strontium, we also need to consider its nuclear structure.

| Isotope | Abundance (%) | Nuclear spin (I) |
|---|---|---|
| $^{88}$Sr | 82.58 | 0 |
| $^{87}$Sr | 7 | $\frac{9}{2}$ |
| $^{86}$Sr | 9.86 | 0 |
| $^{84}$Sr | 0.56 | 0 |

Table 2.1: Abundances and nuclear spin for stable isotopes of strontium [44].

Strontium has 4 stable isotopes, listed in Table 2.1. The three bosonic isotopes $^{84}$Sr, $^{86}$Sr, $^{88}$Sr all have even number of protons and neutrons and therefore have nuclear spin I=0. In bosonic strontium optical clocks, the most commonly used isotope is $^{88}$Sr as it will give the best signal-to-noise ratio of the clock transition due to its high natural abundance.
The last isotope we'll consider is $^{87}$Sr. It is the only stable fermionic isotope of strontium, with nuclear spin of $\mathrm{I} = \frac{9}{2}$. Due to non-zero nuclear spin, $^{87}$Sr will have a hyperfine structure. The hyperfine structure in atoms arises from interaction between the nuclear magnetic dipole moment and magnetic field created from moving electrons in the electron cloud. To describe this structure we define a new quantum number - total angular momentum F=J+I with $\mathrm{m_F}$ being the projections of total angular momentum to the quantization axis. Each hyperfine energy level contains 2F+1 magnetic sublevels which are degenerate in energy in abscence of external magnetic fields. However, when an external magnetic field is applied, their degeneracy is broken and an energy shift of different sublevels is induced. The described effect is known as the Zeeman effect. If the energy shift induced by magnetic field is small compared to the hyperfine splittings, then F is a good quantum number and the interaction Hamiltonian is equal to [45]

$$H_Z = \mu_B g_F F_z B_z, \tag{2.1}$$

where $\mu_\mathrm{B}$ is the Bohr magneton, $\mathrm{F_z}$ is the projection of the hyperfine quantum number F in the direction of the quantization axis (in this case the z direction), $\mathrm{B_z}$ is the magnetic field in the z direction and $\mathrm{g_F}$ is the hyperfine Landé g-factor. The hyperfine Landé g-factors are named after Alfred Landé who first described them in 1921 [46]. The hyperfine Landé g-factor $\mathrm{g_F}$ is given as [47]:

$$g_F = g_J \frac{F(F+1) + J(J+1) - I(I+1)}{2F(F+1)} - \frac{\mu_N}{\mu_B} g_I \frac{F(F+1) + I(I+1) - J(J+1)}{2F(F+1)}, \tag{2.2}$$

where $g_J$ and $g_I$ are the fine and nuclear g-factors, respectively, and $\mu_\mathrm{N}$ is nuclear magneton. Since $\mu_\mathrm{N} << \mu_\mathrm{B}$, the second term in Eq. 2.2 can usually be ignored. However, in the case of $^{87}$Sr, this term will be of great importance as it will create additional challenges in cooling and

clock operation of fermionic strontium.

## 2.3 Cooling of strontium

Now that we have familiarized ourselves with the strontium atom, let us consider the relevant transitions used in cooling of strontium. The most common method involves cooling in two separate stages. First stage is done via the 32 MHz broad $5s^2\ {}^1S_0 \rightarrow 5s5p\ {}^1P_1$ singlet transition. The second stage is done via the much narrower 7.5 kHz $5s^2\ {}^1S_0 \rightarrow 5s5p\ {}^3P_1$ intercombination triplet transition. We will discuss both stages, for both $^{88}Sr$ and $^{87}Sr$, in more detail in following chapters. However, we should first explain the differences between narrow line and broad line cooling. Historically, most of the early laser cooling experiments, such as those done on sodium [38] or rubidium [48], were done on broad spectral lines. A spectral line of natural linewidth $\Gamma$ is considered broad if $\frac{\Gamma}{\omega_r} >> 1$ where $\omega_r/2\pi = \hbar k^2/2m_a$ is the recoil frequency.
For the strontium ${}^1S_0 \rightarrow {}^1P_1$ blue MOT transition with natural linewidth of $\Gamma = 2\pi \cdot 32$ MHz, this ratio is on the order of $\frac{\Gamma}{\omega_r} \approx 10^3$. For the much narrower ${}^1S_0 \rightarrow {}^3P_1$ red MOT transition with $\Gamma = 2\pi \cdot 7.5$ kHz, the ratio is only $\frac{\Gamma}{\omega_r} = 1.6$. Such large difference in $\frac{\Gamma}{\omega_r}$ for the two transitions has a significant consequence on cooling dynamics. To consider cooling dynamics, we first need to introduce saturation intensity $I_s$ and saturation parameter s.
Saturation intensity of a given transition with transition wavelength $\lambda$ and upper state lifetime $\tau$ is given as [40]

$$I_s = \frac{\pi h c}{3\lambda^3 \tau}, \tag{2.3}$$

and where $h$ is the Planck constant and $c$ is speed of light. From this, we define an on-resonance saturation parameter $s_0$ as the ratio of intensity of light $I$ and saturation intensity

$$s_0 = \frac{I}{I_s}, \tag{2.4}$$

Finally, saturation parameter s for some atomic transition with linewidth $\Gamma$ is given as

$$s = \frac{s_0}{1 + (2\Delta/\Gamma)^2}, \tag{2.5}$$

where the transition is being driven by laser light with intensity $I$ and detuned by $\Delta = 2\pi \cdot \delta$ from atomic resonance. Importance of saturation parameter can be explained by considering a population of atoms in a two-state system (ground and excited state). For $s << 1$, population will mostly be in the ground state. For $s >> 1$ the population will be equally distributed between ground and excited state. In other words, saturation parameter tells us how successfully

we are transferring atoms between ground and excited state [40]. Additionally, because of saturation, experimentally observed linewidth of a transition $\Gamma_{\mathrm{E}}/2\pi$ will actually be broader than natural linewidth $\Gamma/2\pi$

$$\Gamma_E = \Gamma\sqrt{1+s_0}, \tag{2.6}$$

Let us now return to narrow line cooling dynamics where we consider 3 different regimes as first discussed in [1, 49]. The 3 regimes are controlled by s and $\Delta$ [1]:

**Regime (I)** ($s >> 1, |\Delta| > \Gamma_{\mathrm{E}}$): Atoms are trapped in a box-like geometry. They experience (near) free-flight behaviour between "hard" walls of the potential. Viscous damping settles down the atoms to potential minimum of the MOT due to gravity.

**Regime (II)** ($s >> 1, |\Delta| < \Gamma_{\mathrm{E}}$): Atoms experience standard Doppler cooling described by damped harmonic oscillator. Radiation pressure force will have a dispersion-shaped feature.

**Regime (III)** ($s \approx 1$): Single photon interaction regime. Here recoil energy becomes important and a full quantum mechanical approach is required [49, 50].

In red MOT cooling of strontium considered in this thesis, only regime (I) and (II) are employed. Additionally, the small $\frac{\Gamma}{\omega_{\mathrm{r}}} = 1.6$ ratio of the narrow line transition will have a role to play for the red MOT cooling of fermionic $^{87}\mathrm{Sr}$, but more on that in latter sections.

In addition, the difference in the $\frac{\Gamma}{\omega_{\mathrm{r}}}$ ratio for $^1\mathrm{S}_0 \rightarrow^3 \mathrm{P}_1$ and $^1\mathrm{S}_0 \rightarrow^1 \mathrm{P}_1$ transitions will affect the maximum value of the radiation pressure force for the two transitions. Maximum value of the radiation pressure force can be expressed with $\mathrm{F} = \frac{\hbar \mathrm{k} \Gamma}{2}$ [40]. For a broad transition, such as $^1\mathrm{S}_0 \rightarrow^1 \mathrm{P}_1$, the maximum radiation pressure force is about $10^5$ times larger than gravitational force. This allows us to ignore gravity in conventional experiments with broad spectral lines. For the narrow $^1\mathrm{S}_0 \rightarrow^3 \mathrm{P}_1$ red MOT transition in strontium, radiation pressure force is only 16 times larger than gravity [1, 49]. For intercombination transitions of lighter earth-alkali (such as Ca and Mg), the cooling force is weak enough (i.e. the rate at which atoms repeat the cooling cycles is low enough) that the force of gravity dominates and makes magneto-optical trapping of atoms difficult or even impossible. This required development of alternative cooling schemes [51, 52]. This makes gravity a significant effect in narrow line cooling.

## 2.4 Cooling of bosonic $^{88}\mathrm{Sr}$

Let us now turn our attention to the cooling of specific isotopes of strontium. We'll begin with cooling methods for $^{88}\mathrm{Sr}$. The energy structure with all transitions relevant for bosonic clock operation, their lifetimes and linewidths is given in Fig. 2.2 and Table 2.2. Firstly, note that the clock transition of bosonic strontium is strictly forbidden and has natural linewidth equal to zero. Therefore, for purpose of comparison with the linewidths of other transitions in Fig. 2.2,

I've put the linewidth of the fermionic $^{87}$Sr as well. More details on both fermionic and bosonic clock transitions and their linewidth will be provided in the chapter on high-precision spectroscopy of the clock transition. As already stated, cooling of strontium is most commonly

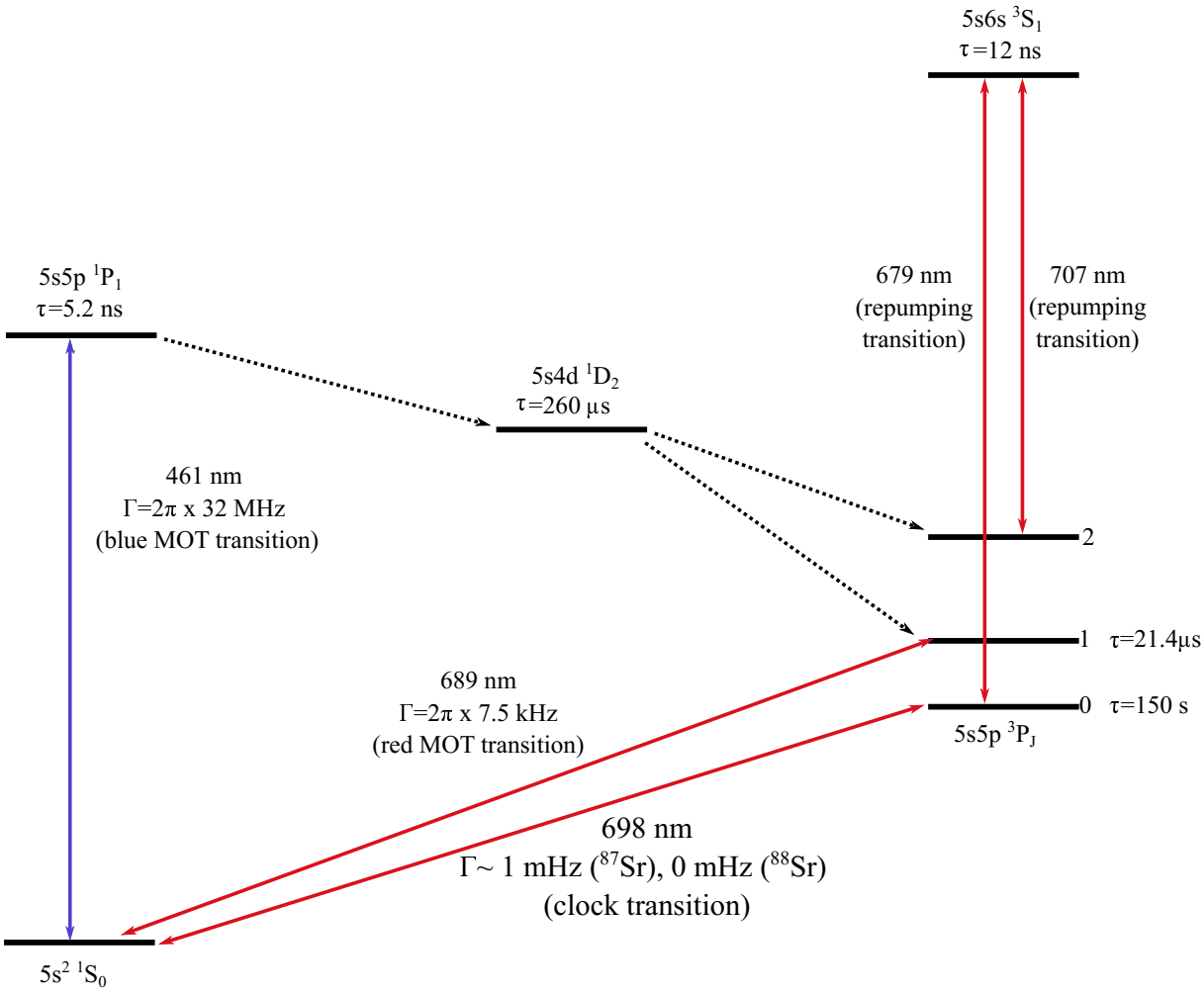


Figure 2.2: Relevant boson energy levels for $^{88}$Sr with corresponding lifetimes $\tau$ and linewidths $\Gamma$. The full colored arrows show transitions (blue MOT transition, red MOT transition, clock transition, repumping transitions) driven by different lasers in optical clock operation. The dashed black arrows show the transitions (decay channels) not driven by lasers in optical clock operation. Additionally, note that the bosonic clock transition is strictly forbidden due to $J = 0 \rightarrow J = 0$ selection rule and therefore has natural linewidth equal to zero. Instead, the linewidth of fermionic strontium is provided, for comparison purposes with other transitions.

done in two stages. Let us first discuss the first of two stages. The stage is usually referred to as blue MOT cooling and uses the broad $5s^2\ ^1S_0 \rightarrow 5s5p\ ^1P_1$ transition. The blue MOT $5s^2\ ^1S_0 \rightarrow 5s5p\ ^1P_1$ transition is well suited for cooling and trapping. It has a broad spectral line of 32 MHz. The short lifetime in the upper $^1P_1$ will lead to a large scattering rate. This

| Transition | Transition frequency (THz) | $\Gamma/2\pi$ | $I_{sat}$ |
|---|---|---|---|
| $5s^2\ {}^1S_0 \rightarrow 5s5p\ {}^1P_1$ | 650.5037 | 32 MHz | $42.7\ \mathrm{mW/cm^2}$ |
| $5s^2\ {}^1S_0 \rightarrow 5s5p\ {}^3P_1$ | 434.8291 | 7.5 kHz | $3\ \mu\mathrm{W/cm^2}$ |
| $5s^2\ {}^1S_0 \rightarrow 5s5p\ {}^3P_0$ | 429.2280 | $1(0)$ mHz $^{87}$Sr($^{88}$Sr) | |
| $5s5p\ {}^3P_0 \rightarrow 5s6p\ {}^3S_1$ | 441.3327 | 1.4 MHz | $0.7\ \mathrm{mW/cm^2}$ |
| $5s5p\ {}^3P_2 \rightarrow 5s6p\ {}^3S_1$ | 423.9135 | 0.56 MHz | $3.2\ \mathrm{mW/cm^2}$ |

Table 2.2: Transition frequencies, linewidths and saturation intensities for transitions relevant in cooling of strontium, taken from [4, 53, 54]. For the clock transition, linewidths for both the fermionic and bosonic clock transition are given. Note that the linewidth for the bosonic clock transition is zero as it is a double forbidden transition.

allows us to slow down atoms with initial velocities of few hundred m/s to just few m/s in about 1 second [28].

However, unlike in its alkali counterparts, the cooling transition isn't completely closed as atoms may decay to the $5s5p\ {}^3P_J$ triplet via the $5s6d\ {}^1D_2$ state. About 1 in 50000 atoms will decay via this channel. From $^1D_2$ state the atom can decay to either $^3P_1$ or $^3P_2$ state of the triplet.

The decay to $^3P_1$ isn't of great concern. Due to its short lifetime (compared to $^3P_2$) of just $\tau = 21.4\ \mu$s, the atom will quickly decay back into the ground state and return to the blue MOT cooling cycle. The decay to $^3P_2$ state is another matter entirely. The $^3P_2$ (and $^3P_0$) are both long-lived meta-stable states. Should the atom end up in any of those two states, it will get stuck there and effectively escape the cooling cycle. For this purpose most optical clocks use two repumping lasers at 679 nm and 707 nm which pump the atoms into the $5s6p\ {}^3S_1$ state. The selection rules allow the atom to decay from this short-lived state back to $^1S_0$ via the $^3P_1$ state. Generally, one could avoid the use of repumping lasers, but this leads to a drop in the number of cooled atoms by about an order of magnitude.

There are, however, a few experimental challenges in using the blue MOT transition. One of them is the wavelength of the blue MOT cooling transition and the other is the relatively high saturation intensity of $42.7\ \mathrm{mW/cm^2}$. Due to the transition being in the blue part of the spectrum, where achieving high laser powers can prove challenging, this previously required the use of Master Oscillator Power Amplifier (MOPA) systems which would inject light from a master laser into a tapered amplifier and produced high laser powers (usually above 1 W) at 922 nm which was then frequency-doubled to 461 nm via a doubling stage, usually in the form of a resonant cavity doubler. However, recent developments in laser diode technologies have brought to market both high-power blue laser diodes and injection-locked amplifier lasers without MOPA and doubling stages, making the experimental requirements for the blue MOT in strontium much less of a headache. A second experimental issue is a consequence of the

broad natural linewidth. Such a broad linewidth requires a high magnetic field gradient of about $\frac{\mathrm{dB}}{\mathrm{dz}} = 50\ \frac{\mathrm{G}}{\mathrm{cm}}$ which calls for high currents of about 100 A [6]. In addition, the broad transition also causes a relatively high Doppler limit temperature. For the 32 MHz linewidth, Doppler tempeture is about 1 mK. This temperature is insufficiently low for clock operation [55, 56]. In terms of population, a typical blue MOT will have about $10^7 - 10^9$ atoms [6, 49].

The use of the narrow ${}^1\mathrm{S}_0 \rightarrow {}^3\mathrm{P}_1$ transition to further lower the temperature of atoms in strontium MOT was first suggested by Hall et al. [57] and achieved experimentally by Katori et al. [58] and Vogel et al. [59]. Due to the narrow linewidth of just 7.5 kHz [58, 59, 60], Doppler temperature of atoms cooled via ${}^1\mathrm{S}_0 \rightarrow {}^3\mathrm{P}_1$ is about 1 $\mu$K. However, there is an experimental issue when swapping from blue to red MOT cooling. Due to the large difference in width of the their Doppler profiles (i.e. the large difference in Doppler temperatures), it is not possible to efficiently directly transfer atoms from the blue to the red MOT. In other words, the narrow linewidth will make the red MOT laser interact with only a narrow class of atom velocities in the blue MOT. This will lead to a large loss of atoms in the red MOT.

The solution proposed by Wallis and Ertmer [61] and implemented by Katori et al. [58] was to modulate the laser frequency of 689 nm laser and artificially broaden the laser spectrum. The modulation allowed matching of the Doppler profiles of red and blue MOTs. Such spectrally broadened red MOT laser ensures that the atoms interact with different frequency components and are continuously cooled. Therefore, red MOT cooling stage is usually divided into two substages - broadband (BB) and single frequency (SF) cooling stage.

In broadband stage, the laser frequency of the cooling laser is artificially broadened by frequency modulation. This increases the velocity capture range of red MOT and allows us to cool the atomic cloud to temperatures on the order of a few dozen $\mu\mathrm{K}$. This broadening of the laser frequency during the broadband phase bridges the gap between blue ($\mathrm{T}_{\mathrm{Doppler}} \approx 1\ \mathrm{mK}$) and SF ($\mathrm{T}_{\mathrm{Doppler}} \approx 1\ \mu\mathrm{K}$) red MOT phase. Additionally, during the broadband phase, the trapping magnetic field gradient is ramped up from 1 $\mathrm{G/cm}$ to 10 $\mathrm{G/cm}$ to compress and increase the density of the atomic cloud. In terms of detuning, during the broadband stage the laser is detuned by about 0.5-1 MHz. Due to the low saturation intensity of 7 $\mu\mathrm{W/cm}^2$, total laser power of a few mW of 689 nm light is sufficient to achieve regime (II) where standard Doppler cooling mechanism take place.

In the final step the modulation is turned off, moving the cooling to regime (I) with single frequency operation. In this regime, the atoms are cooled to their final temperature of around 1 $\mu\mathrm{K}$ and they can be loaded into an optical lattice.

## 2.5 Cooling of fermionic $^{87}$Sr

The discussion so far made no comparison between cooling of different isotopes of strontium, but it's clear from nuclear spins in Table. 2.1 this is something which we must address before continuing.

Out of the four stable isotopes of strontium, $^{87}$Sr sticks out as the only fermionic isotope with nuclear spin of $\frac{9}{2}$ which gives this isotope a rich hyperfine structure shown in Fig. 2.3. The hyperfine structure creates hyperfine isotopic shifts of different transitions of $^{87}$Sr when compared to the bosonic $^{88}$Sr. These isotope shifts, given as the difference in transition frequencies between different hyperfine transitions of $^{87}$Sr and the corresponding $^{88}$Sr transitions, are shown in Table. 2.3.

| Isotope shift | $^1S_0 \rightarrow {}^1P_1$ (MHz) | $^1S_0 \rightarrow {}^3P_1$ (kHz) | $^1S_0 \rightarrow {}^3P_0$ (kHz) |
|---|---|---|---|
| $^{87}$Sr − $^{88}$Sr | -46.5 | -62186.5 | -62171 |
| $^{87}$Sr(F = 7/2) − $^{88}$Sr | -9.7 | 1351933.1 | |
| $^{87}$Sr(F = 9/2) − $^{88}$Sr | -69 | 221676.6 | |
| $^{87}$Sr(F = 11/2) − $^{88}$Sr | -51.8 | -1241485.8 | |

Table 2.3: Isotopic frequency shifts of different hyperfine states of $^{87}$Sr from $^{88}$Sr for transitions relevant to optical clock operation, taken from [6, 4, 62]. The isotopic shifts are given as the difference in transition frequencies of hyperfine transitions of $^{87}$Sr and the corresponding transitions of $^{88}$Sr.

This structure created significant challenges in using $^{87}$Sr for clock operation. The difficulty arises from the large difference in Landé g-factors of the ground $^1S_0$ and excited $^3P_1$ hyperfine states and narrow linewidth of the $^1S_0 \rightarrow {}^3P_1$ transition [63]. Let us examine this issue a bit closer.

We begin again with blue MOT cooling. Blue MOT cooling of fermionic strontium uses the singlet $^1S_0, F = 9/2 \rightarrow^1 P_1, F' = 11/2$ transition. The $^{88}$Sr − $^{87}$Sr isotope shift is about 52 MHz [4]. This shift in transition frequency is easily implemented by changing the frequency of the blue MOT laser. Additionally, $^3P_2$ state now also has hyperfine structure, spanning from $F' = 5/2$ to $F' = 13/2$. An atom decaying from $^1P_1$ state via $^1D_2$ can therefore end up in any hyperfine state of $^3P_2$. To ensure proper operation of fermionic blue MOT, we again have to pump atoms which end up in $^3P_2$ into $^3S_1$. This can be done by simply scanning the frequency of 707 nm laser across all the hyperfine states. This will pump atoms from any hyperfine state of $^3P_2$ into $^3S_1$ [64]. The temperature of such a fermionic blue MOT will again reach the Doppler limit [63]. The reduction in atomic population compared to bosonic blue MOT will be about an order of magnitude. This reduction comes from the difference in natural abundances of the $^{87}$Sr and $^{88}$Sr.

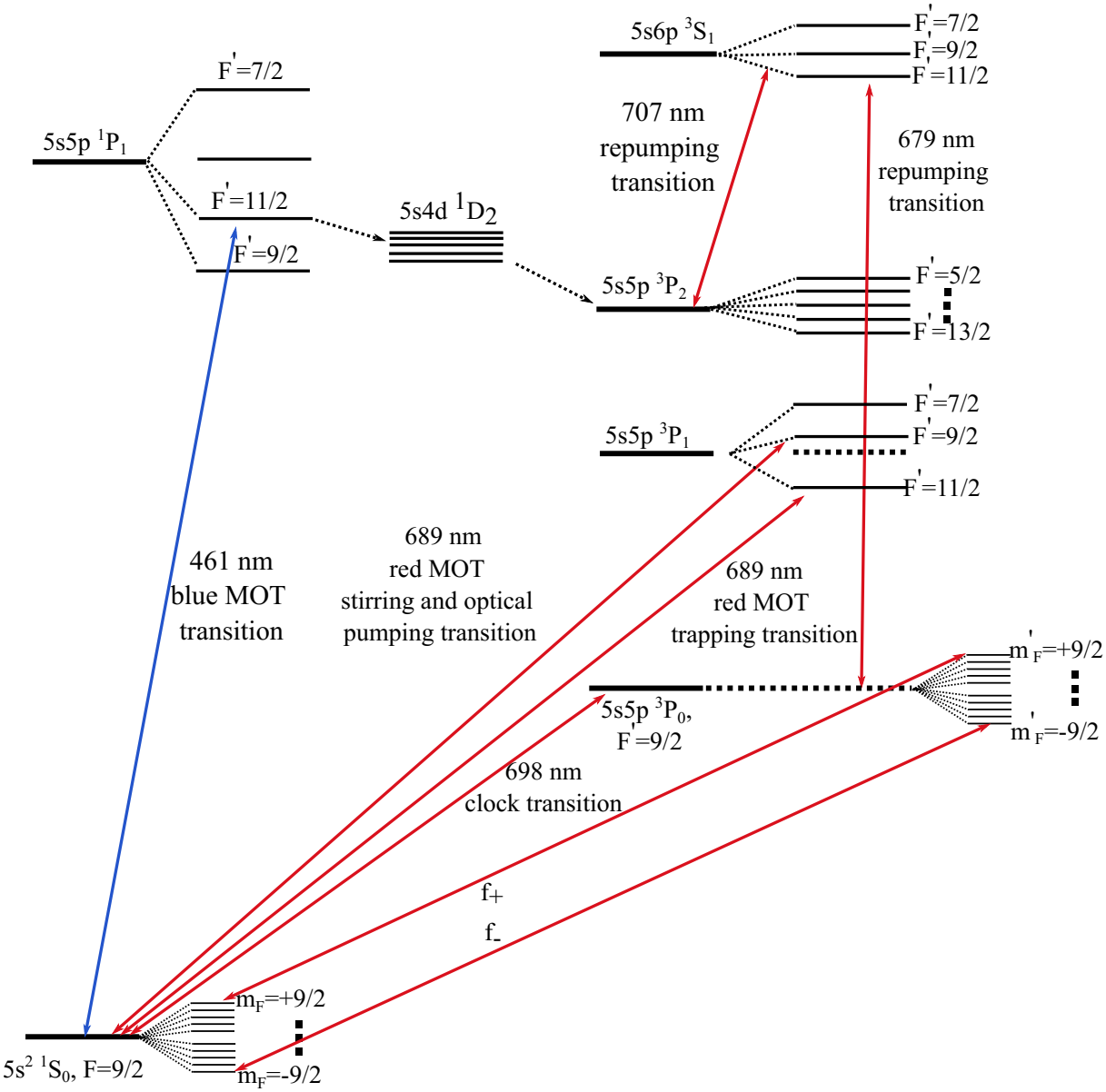


Figure 2.3: Fermionic energy levels. Due to nuclear spin of $I = 9/2$, $^{87}Sr$ has rich hyperfine structure. The colored arrows shows the transitions (blue MOT, red MOT stirring and optical pumping, red MOT trapping, clock and repumping) which are driven by different lasers in fermionic optical clock operation. The black dashed arrows show the decay channels which are not driven by lasers.

Once atoms are loaded into the blue MOT, it is time to transfer them to the red MOT. For fermions, red MOT cooling transition is the $^1S_0, F = 9/2 \rightarrow {}^3P_1, F' = 11/2$ transition. When this was first attempted by the Katori group, they found that the lifetime of fermionic red MOT was ten times shorter than its bosonic counterpart [63]. Let us examine what makes red MOT cooling of $^{87}Sr$ so much different than blue MOT or cooling of an alkali atomic species, all of

which have hyperfine structure too.

The answer is two-fold. Firstly, in traditional alkali atomic species, like rubidium and sodium, ground and excited atomic states have similar hyperfine Landé g-factors $g_F$ (for ground and excited states denoted as $g_g$ and $g_e$ in Fig 2.4 a), respectively). This means that in the presence of a magnetic field B the resonant frequency for a given polarization is nearly independent of ground state magnetic sublevel $m_F$. In this case, an atom in any ground state $m_F$, when placed in magnetic field B(x) with linear gradient, will feel a restoring force towards the center of trap. Behaviour described above is shown in Fig. 2.4 b) and corresponds to standard MOT operation described in previous chapter.

Strontium, however, belongs to the group of earth-alkali elements. From Eq. 2.2 it is clear that the hyperfine Landé g-factor $g_F$ of excited state $^3P_1, F = 11/2$ state will have contributions from both terms in Eq. 2.2 as F, J and I are all non-zero values. Since $\mu_N << \mu_B$, the biggest contribution to $g_F$ comes from the term related to $g_J$.

The situation is quite different for the ground $^1S_0, F = 9/2$ state. Since $J = 0$ and $F = I$, contribution from $g_J$ is zero. This means only the nuclear spin g-factor $g_n$ contributes to the total g-factor of the ground state. Therefore, hyperfine Landé g-factor of the excited state ($g_e$) is much larger than g-factor of the ground state ($g_g$). Due to such large difference in Landé factors, there exists a strong dependence of the transition frequency for different values of the magnetic field. Zeeman shifts for different magnetic sublevels of excited state for the fermionic cooling transition $F = 9/2 \rightarrow F = 11/2$ have been depicted in Fig. 2.4 d).

To make importance of Landé g-factors in MOT trapping clear, we'll consider a specific example of an atom in the ground magnetic sublevel $m_g = 9/2$. Due to selection rules, an atom after the apsorption of a photon can end up either in $m_e = 7/2$ (green line in Fig. 2.4 d)) or $m_e = 11/2$ (purple line) excited state. Due to small Landé factor of the ground state, the sign of the Zeeman shift of these two possible sublevels is the same (both positive for $z > 0$ and negative for $z < 0$), in stark contrast with the alkali case where they always have different signs. This means that an atom in some position $z < 0$ can absorb light beam with either $\sigma^+$ or $\sigma^-$ polarization, pushing it either towards or away from the center of the trap. Luckily, in this specific case, due to the large difference in Clebsch-Gordan coefficients (shown in Fig. 2.4 c)) the atom has a 55:1 chance of absorbing the photon with the "correct" $\sigma^+$ polarization and be pushed towards the trap center. However, from Fig. 2.4 c), we can see that this ratio becomes less and less favorable for smaller $m_g$ sublevels. An additional issue is the narrowness of the $^1S_0 \rightarrow {}^3P_1$ transition. The ratio of the $^1S_0 \rightarrow {}^3P_1$ linewidth to the recoil frequency is about $\frac{\Gamma}{\omega_r} = 1.6$. This means, if the atom absorbs only a few photons with the "wrong" polarization, it will be quickly pushed out of resonance and escape the cooling cycle.

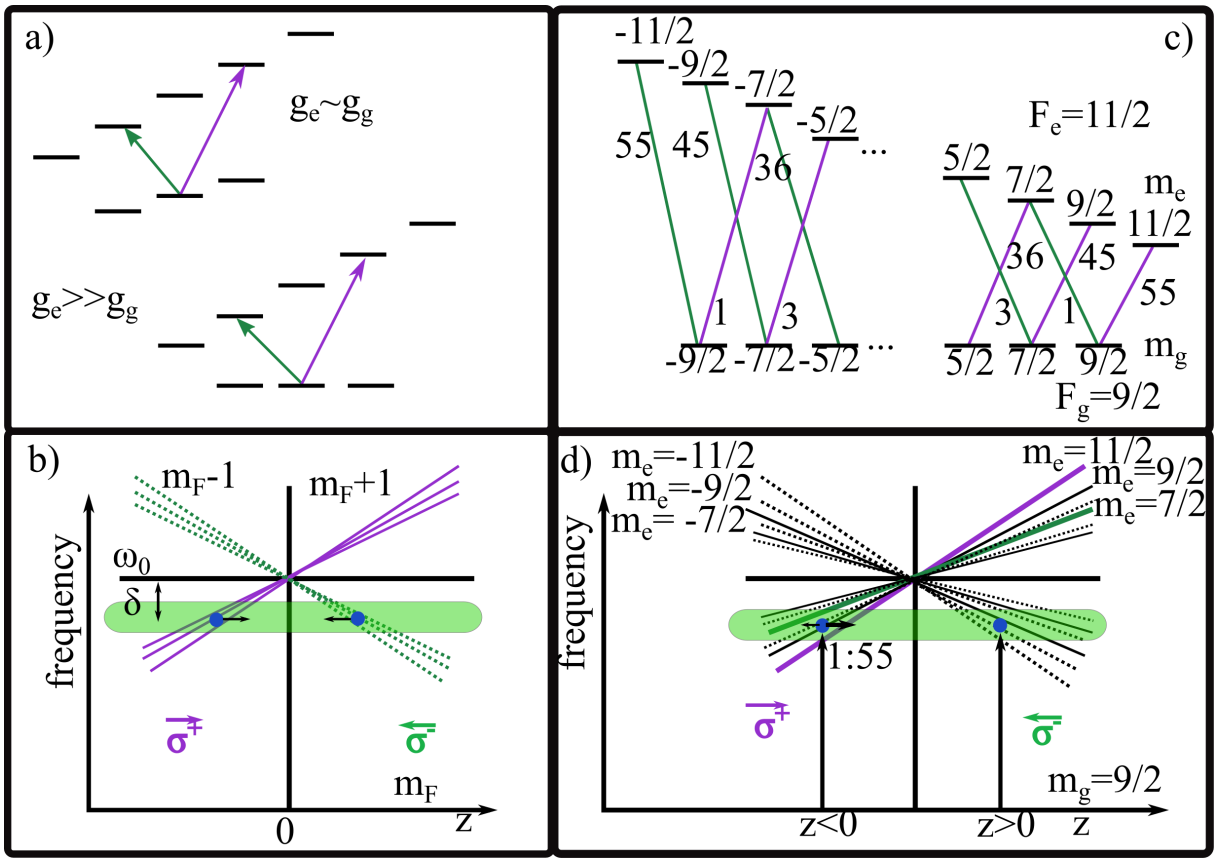


Figure 2.4: Fermionic MOT operation compared to MOT operation of alkali atomic species. Comparison of Landé g-factors for alkali ($g_e \approx g_g$) and earth-alkali ($g_e >> g_g$) elements is shown in top left figure. Position-dependent frequencies arising from magnetic field and transitions to higher (lower) magnetic sublevels $\Delta m_F = +1$ ($\Delta m_F = -1$) are shown with purple (green) lines. For alkali elements, splittings of magnetic sublevels are shown in bottom left figure. For any position z in the trap, detunings of magnetic sublevels $m_{F+1}$ and $m_{F-1}$ will always have opposite sign. This ensures an atom in state $m_F$ will preferentially absorb photons from just one beam, trapping atoms in the MOT.
The splittings for strontium have different structure where $m_F + 1$ and $m_F - 1$ states can have the same sign at some position z. An atom in the ground state $m_F = 9/2$ at position $z < 0$ can absorb photons from either beam, pushing it away or towards the trap. Owing to stronger Clebsch-Gordan coefficients (shown in top right figure), the atom has a 55:1 chance of absorbing the photons which will push him towards the center. Conversely, at $z > 0$, there are no states resonant with the laser beam for the $m_g = 9/2$ state and the atom will leave the trap and be lost. To resolve these issues, an additional "stirring" laser must be introduced into red MOT cooling scheme for fermionic strontium. This stirring laser will drive the $^1S_0, F = 9/2 \rightarrow {}^3P_1, F' = 9/2$ transition and perform a randomization of the magnetic sublevels of the ground state. So if an atom is in an "unconvenient" ground magnetic sublevel for the cooling transition to work properly, the stirring laser can cycle it so that in the next cycle it may have a more convenient ground sublevel for trapping to work.

The situation seems even more dire for an atom in some position $z > 0$. Here, there are no excited states which are resonant with the atom in the ground $m_g = 9/2$ state, so the atom will simply drift out of the MOT and be lost. All of these issues reduce the lifetime of the fermionic red MOT by an order on magnitude compared to its bosonic version. The solution to these issues, suggested by Katori group in 2002 [63], was to add an additional "stirring" laser to the red MOT cooling scheme, shown in Fig. 2.3. The stirring laser drives the $F = 9/2 \rightarrow F' = 9/2$ transition. This transition does not trap atoms (since $\Delta F = 0$), but it can both cool and, more importantly, optically pump atoms. In other words, the stirring laser performs a randomization of the magnetic sublevels of the ground state, so if an atom is in an "unconvenient" ground magnetic sublevel for the cooling transition to work properly, the stirring laser can cycle it so that in the next cycle it may have a more convenient ground sublevel for cooling to work.

## 2.6 Optical lattices

Once we have cooled down our atoms to the range of about 1 $\mu$K it is time to load them into an optical lattice before we can perform the high resolution spectroscopy of the clock transition. This section discussing optical lattices follows the approach laid out in Grimm et al. [65]. Dipole traps use far-resonant atom-light interaction to trap atoms in minima of laser light potential. Due to the light frequency being far-resonant with any relevant atomic transition, there is a low scattering rate of photons by the atoms.

The simplest model for dealing with atoms in dipole traps is the oscillator model where the atoms are treated as dipoles in a classical EM field. A laser light field is generally given as [5, 65]

$$E(r,t) = \hat{\epsilon}E(r)e^{-i\omega_l t} + c.c., \tag{2.7}$$

where $E(r)$ is the spatially dependent amplitude of light field polarized in direction $\hat{\epsilon}$ with frequency $\omega_l$. The light field induces a dipole moment with polarization given as

$$p(r,t) = \hat{\epsilon}p(r)e^{-i\omega_l t} + c.c. \tag{2.8}$$

The light field and induced polarization are connected through a simple equation

$$p = \alpha(\omega_l)E, \tag{2.9}$$

where $\alpha$ is the atomic polarizability. Atomic polarizability is a property of the atom. It provides information about the reply of the atom with an electric dipole moment to an electric field

imposed on the atom. Atomic polarizability generally depends on the internal structure of the atom. The interaction potential between the induced dipole moment and the electric field is given as

$$U_{dip} = -\frac{1}{2} < pE >= -\frac{1}{2e_0 c} Re(\alpha) I, \tag{2.10}$$

where field intensity is given by $I = 2e_0 c|\widetilde{E}|^2$ and $e_0$ is vacuum permitivity. The angular brackets denote the time average over the rapid oscillating terms. The real part of polarizability describes the dipole oscillations responsible for dispersive properties of the interaction. The imaginary part of polarizability, which describes absorbative properties of the interaction, in $<$ pE $>$ is averaged to zero.

The imaginary part of polarizability does however appear if one considers the power absorbed by an oscillator from the driving field, which is then re-emitted as dipole radiation

$$P_{abs} =< \dot{p}E >= 2\omega_l Im(\widetilde{p}\widetilde{E}^*) = \frac{\omega_l}{\epsilon_0 c} Im(\alpha) I. \tag{2.11}$$

As light is a stream of photons of energy $\hbar\omega_l$, the light-atom interaction can be interpreted as scattering of photons in cycles of absorption and spontaneous emmission. This allows us to define a scattering rate $\Gamma_{sc}$

$$\Gamma_{sc}(r) = \frac{1}{\hbar e_0 c} Im(\alpha) I(r). \tag{2.12}$$

Now, Eq. 2.10 and Eq. 2.12 are physically correct, but the real and imaginary polarizability makes them somewhat inconvenient to use. Luckily, it is possible to relate both the dipole potential and scattering rate to more "experimental" parameters such as detuning, linewidth and frequency of atomic transition, given as [65]

$$U_{dip}(r) = \frac{3\pi c^2}{2\omega_0^3} \frac{\Gamma}{\Delta} I(r), \tag{2.13}$$

$$\Gamma_{sc}(r) = \frac{3\pi c^2}{2\hbar\omega_0^3} (\frac{\Gamma}{\Delta})^2 I(r). \tag{2.14}$$

These two equations give all the basic properties of a dipole trap. They can be simply connected by the following equation

$$\hbar\Gamma_{sc} = \frac{\Gamma}{\Delta} U_{dip}. \tag{2.15}$$

Let us consider the implications of this equation. First, it points to the importance of the detuning.

For $\delta < 0$, i.e. when the frequency of the laser is red-detuned from the relevant atomic transi-

tion, the potential will be negative and attract atoms into the light field. The minima of potential will correspond to maxima of light intensity.
For $\delta > 0$, i.e. when the frequency of the laser is blue-detuned from the relevant atomic transition, dipole trap repels atoms out of the light field and minima of the potential is the minima of light intensity. We therefore generally have two types of dipole traps - red-detuned ($\delta < 0$) or blue-detuned ($\delta > 0$) traps. The optical potential is related to the intensity of light by Eqs. 2.10 and 2.13. Intensity of light from a single beam with Gaussian distribution is given as [65]

$$I(r,z) = \frac{2P}{\pi w_0^2} e^{\frac{-2r^2}{w_0^2}}, \tag{2.16}$$

where $P$ is power of the input light, $r$ is the radial coordinate of intensity of light and $w_0$ is the minimum beam waist. Generally, waist of the lattice is a function of z along the axial direction and is given as $w(z) = w_0\sqrt{1+(z/z_R)^2}$ where $z_R = \pi w_0^2/\lambda$ is the Rayleigh length. However, in Eq. 2.16 we assumed that the area which atoms take in the optical lattice (usually a few hundred microns) is much smaller than the Rayleigh length (usually a few centimeters). This removes the axial dependence of the lattice waist which simplifies the expression for lattice potential in Eq. 2.10 and 2.13. The 1D lattice potential, created by a retro-reflected Gaussian beam which forms a standing wave, is then given as [65]

$$U(r,z) = U_0 e^{\frac{-2r^2}{w_0^2}} sin^2(kz), \tag{2.17}$$

where $U_0$ is the depth of the optical lattice and $r$ denotes the radial coordinate of the lattice potential. Lattice depth $U_0$, most commonly measured in energies of recoil $\mathrm{E_r}$, is an important parameter of the optical lattice. It will tell us how well an atom is trapped within the optical lattice and whether the atom can tunnel between lattice sites. More discussion on strength of trapping of atoms in the lattice and effect of tunneling between sites on optical clock operation will be provided in a later chapter.
An example of the potential of a two-dimensional (2D) optical lattice is shown in Fig 2.5. Four counter-propagating beams form a 2D optical lattice potential. The red (blue) colored peaks show regions of high (low) lattice potential with atoms (depicted as small spheres) loaded into the minima of the lattice potential. Depending on detuning, atoms are either loaded into the maxima or minima of light intensity for red and blue-detuned optical lattices, respectively. It is important to mention that in 1D blue-detuned optical lattices there is no trapping of atoms in the radial direction. Confinement in all three orthogonal directions can be achieved, for instance, by a 3D optical lattice trap, made up of three independent 1D optical lattices [66].

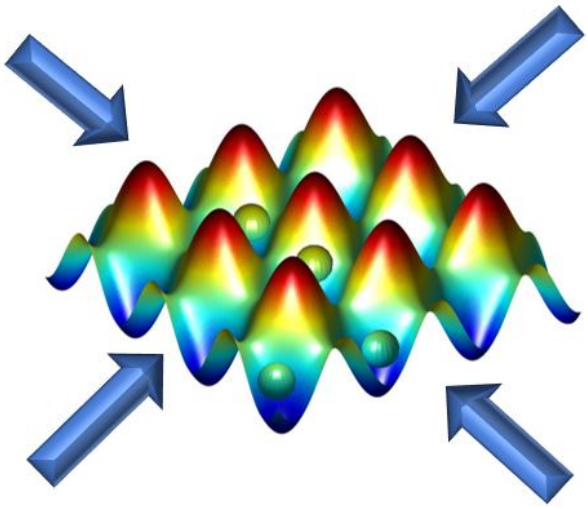

Figure 2.5: A two-dimensional (2D) optical lattice potential created by two orthogonal sets of of counter-propagating beams. The lattice has a "box-of-eggs"-type shape. Red peaks (blue dips) respresent regions of high (low) lattice potential. The atoms in an optical lattice are trapped in the minima of lattice potential.

## 2.7 Lamb-Dicke regime of the optical lattice

In the previous chapters, we have used the Doppler effect mostly to our benefit, employing it along with recoil momentum of atoms to cool down and trap atoms in the MOT. Sadly, it is time for us and photon recoil to go from friends to enemies. Our issue with photon recoil is the following - during the spectroscopy of the clock transition, photons transfer their recoil momentum to the atoms, perturbing the clock transition. This was first noted in paper by Dicke [67] where he suggests that a recoil-free regime of spectroscopy could be achieved by the photon transferring its momentum to the potential wall of the lattice instead of the atom.
From the quantum-mechanical point of view, total energy of the atom in a optical lattice potential can be separated into internal energy (energy of its electronic states) and external energy (atoms vibrational states from motion of its center of mass in the well of the optical potential). For the case considered by Dicke, the photon frequency $\nu$ of an atom trapped in a 1D square potential of width $a$ can be written as [67]

$$\nu = \nu_0 + h/(8m_a a^2)(n^2 - m^2), \tag{2.18}$$

with $n$ and $m$ being integer numbers, indicating the vibrational states and $\nu_0$ the frequency of the unperturbed transition. The atom oscillating in the potential interacts with the walls of the

well for an infinitesimal time, but there is a finite probability for the photon momentum to be transferred to the well walls instead of the atom, given as $P = \frac{sin^2(\pi a/\lambda)}{(\pi a/\lambda)^2}$. In other words, if the atom is confined to a region smaller than $a < \lambda/2$, the photon will not excite the vibrational states of the atom, but instead transfer its momentum the walls of the potential. This particular regime is called Lamb-Dicke regime[1].

To see if an atom in an optical lattice is in the Lamb-Dicke regime, a parameter called the Lambe-Dicke parameter is commonly defined. The Lamb-Dicke parameter is given as the square root of the ratio of the photon recoil frequency $\omega_\mathrm{r}$ and the vibrational frequency of the atom $\omega_\mathrm{z}$

$$\eta = \sqrt{\frac{\omega_r}{\omega_z}} = k_z z_0. \tag{2.19}$$

The recoil frequency, defined earlier in section 2.3., is the frequency of photons of the probe beam. The vibrational frequency $\omega_\mathrm{z}$ is the frequency of oscillations of the trapped atom in the axial direction of the optical lattice, i.e. the direction of propagation of the counter-propagating beams of the optical lattice. The vibrational frequency $\omega_\mathrm{z}$ is also referred to as axial Rabi frequency. We can now approximate the lattice potential with a simple harmonic oscillator. For the harmonic oscillator, the vibrational frequency is equal to $\frac{\omega_\mathrm{z}}{2\pi} = (\frac{2\mathrm{U}_0}{\mathrm{m_a z_r}})^{1/2}$ [65].

Alternatively, Dicke parameter can be defined as $\eta = \mathrm{k_z z_0}$ where $\mathrm{k_z}$ is the wavevector of the trapping field and $z_0 = \sqrt{\frac{\hbar}{2m\omega_z}}$ is the characteristic oscillator length (i.e. the width of the motional wave function of the atom).

Lamb-Dicke regime refers to the condition when $\eta^2 << 1$. To ensure this condition is satisfied, the vibrational frequency $\omega_\mathrm{z}$ must be much larger than the recoil frequency $\omega_\mathrm{r}$. This is achieved by ensuring our lattice has very high lattice depth $U_0$, usually few dozen or hundred of recoil energies. In that case, the atom is well trapped within the harmonic potential and the laser spectroscopy of the atom shows 3 distinct resonances: A central carrier at $\omega_0$ which changes *only* the atoms' internal electronic state and two (red and blue) sidebands seperated by $\pm\omega_\mathrm{z}$ from central carrier which excite the electronic state and add (remove) a quantum of motion [55, 68], as shown in Fig. 2.6.

The central carrier resonance corresponds to the $|^1\mathrm{S}_0, \mathrm{n} = 1\rangle \rightarrow |^3\mathrm{P}_0, \mathrm{m} = 1\rangle$ transition on left figure in Fig. 2.6. The strength of the carrier is equal to the frequency of Rabi transition $\Omega$ of the harmonic oscillator. The strength of the red (blue) sideband is reduced by the Dicke parameter $\eta$. Additionally, we can define the well-resolved sideband regime $\Gamma << \omega_\mathrm{z}$ where the central resonance is well seperated from the sidebands. In this regime we are able to estimate the axial

[1] More details on Lamb-Dicke can be found in original paper by Dicke [67] or e.g. [68].

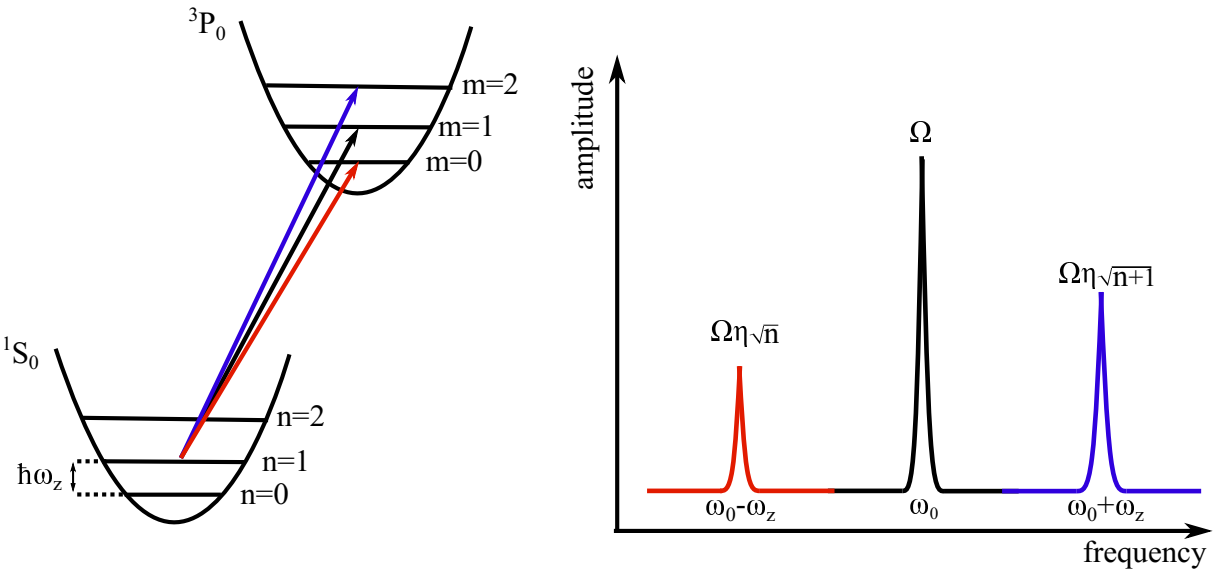


Figure 2.6: Possible transitions in the Lamb-Dicke regime. Scheme of the harmonic potential of the ground and excited states of the clock transition is shown on the left figure. An atom confined in a harmonic potential is in n=1 vibrational state of the ground $^1S_0$ state. For $|^1S_0, n = 1\rangle \rightarrow |\,^3P_0, m = 1\rangle$ transition, only the internal state of the atom will change. For the $|^1S_0, n = 1\rangle \rightarrow |\,^3P_0, m = 2\rangle$ and $|^1S_0, n = 1\rangle \rightarrow |\,^3P_0, m = 0\rangle$, the atom will change both its internal and vibrational state. The resonances corresponding to the three transitions are shown on the right figure. The spectrum features a central resonance at the atomic transition frequency $\omega_0$ and red (blue) sideband shifted by $-\omega_z$ $(+\omega_z)$ from the carrier. The strength of carrier and sidebands are characterised by the Rabi frequency of the atomic transition $\Omega$ and the Dicke parameter $\eta$. Figure adapted from [68].

temperature of the trap by measuring the peak ratio of the two sidebands [5]

$$T_z = \frac{\hbar\omega_z}{k_B \ln(\frac{A_{blue}}{A_{red}})}, \tag{2.20}$$

where $\frac{A_{blue}}{A_{red}}$ is the ratio of heights of blue and red sidebands.
The axial Rabi frequency also provides information about the lattice depth of the optical lattice $U_0$ from Eq. 2.17

$$U_0 = \frac{\hbar^2\omega_z^2}{4E_r}. \tag{2.21}$$

Along with oscillating in the axial direction, the atom can oscillate in the radial direction as well. The oscillation frequency in the radial direction is called the radial Rabi frequency and is given as

$$\omega_r = \frac{\lambda\omega_z}{\sqrt{2}\pi w_0}. \tag{2.22}$$

An example of sideband spectroscopy of the clock transition is shown in Fig. 2.7 (left). With

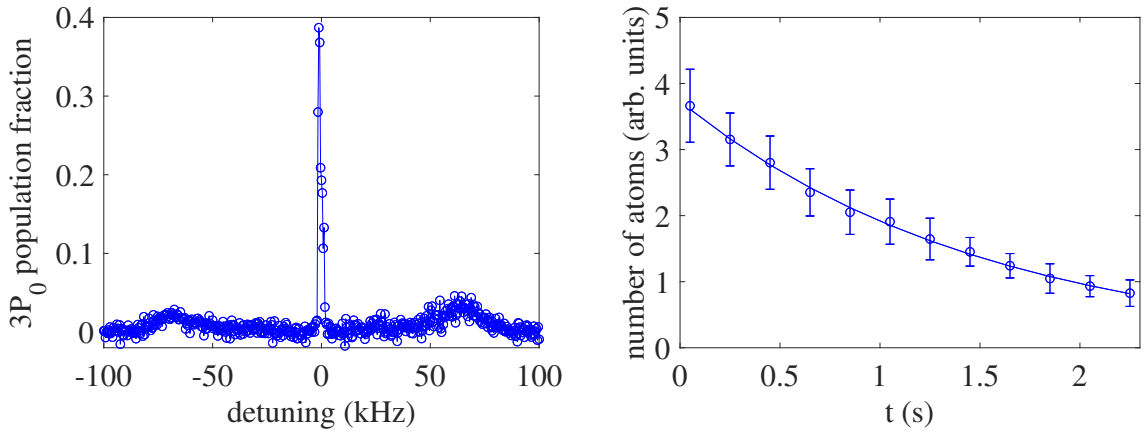


Figure 2.7: (left) Sideband spectroscopy of the clock transition for lattice depth of 85 $E_r$ giving an axial lattice temperature of about 15 $\mu$K. The central peak corresponds to the clock transition frequency. Blue points represent the population fraction in the excited clock state as a function of clock laser detuning from the clock resonance. The blue line was added for better visual clarity of the central resonance. (right) Lifetime of atoms in the trap. Blue points on the right figure represent the number of atoms in the trap as a function of time atoms spent in the trap. An exponentially decaying function, represented by sold blue line, was fitted to the data set. We find the lifetime of atoms in the lattice to be equal to 1.5(1) seconds.

axial frequency of $\omega_z = 64$ kHz corresponding to lattice depth of 85 $E_r$ it gives an axial lattice temperature of around 5 $\mu$K. Additionally, measurement of lifetime of atoms in the lattice is shown of Fig. 2.7 (right). The number of atoms (blue circles in Fig. 2.7 (right)) in the lattice as function of time the atoms have been loaded in the lattice was measured. An exponentially decaying function (blue line in Fig. 2.7 (right)) was fit to the dataset and the lifetime of atoms in the lattice was determined. In the measurement in Fig. 2.7 (right), the lifetime was found to be $\tau = 1.5(1)$ seconds.

## 2.8 Atomic polarizability and magic wavelength

In the previous chapter we introduced atomic polarizability as a parameter which relates the polarization of a dipole to an externally applied electric field. In other words, it provides information about the reply of an electric dipole to electric field. We, however, didn't go into any specifics of the role atomic polarizability plays in operation of an optical clock. So let us briefly speak more about it.

Theory of atomic polarizability is quite complex, so I'll provide a simplified overview of the

subject. A more in-depth discussion on the matter can be found elsewhere [69].

When an atom or molecule is in the presence of an external electric field, it will experience a shifting and splitting of its spectral lines. This is the well known Stark effect. Additionally, the Stark effect can be classified as AC or DC Stark effect, depending whether the electric field is from an EM wave, i.e. a laser source (AC Stark effect), or from a static distribution of charges (DC Stark effect). The shifting of the line caused by the AC Stark effect is referred to as AC Stark shift or light shift. The term light shift comes from the fact that the shift happens due to interaction between the atom and light. The shift in transition frequency $\Delta\omega$ of some atomic transition due to the AC Stark effect can be calculated by using perturbation theory [70]. The leading contribution arises in the second order of perturbation theory, and it is quadratic in the electric field and corresponds to the electric dipole term. The shift in frequency is given as [71]

$$\Delta\omega = -\frac{1}{4}\Delta\alpha(\omega_l)E^2 - \frac{1}{64}\Delta\gamma(\omega_l)E_0^4, \tag{2.23}$$

where $\Delta\alpha = \alpha_\mathrm{e} - \alpha_\mathrm{g}$ and $\Delta\gamma = \gamma_\mathrm{e} - \gamma_\mathrm{g}$ are the relative *dynamic* polarizabilities and *hyperpolarizabilities* between two atomic states, respectively. The term *dynamic* comes from the fact that the source of the Stark shift is an oscillating electric field [71]. *Hyperpolarizability* is the proportionality factor for the second term in Eq. 2.23, which is quartic in E. Hyperpolarizability generally includes higher order corrections to the AC Stark shift. The discussion above raises the question how the AC Stark shift affects our optical clock. Well, we wish for our $^1\mathrm{S}_0 \rightarrow {}^3\mathrm{P}_0$ clock transition frequency to be unperturbed when probed with the 698 nm clock laser. By loading atoms into a deep enough optical lattice we suppress the recoil shift (i.e. perturbations) which would be induced by the 698 nm probe beam in the absence of an optical lattice.

On the other hand, we don't want our lattice to induce an AC Stark on the clock transition. This issue of lattice-induced AC Stark shift was resolved by Katori et al. [80] where it was proposed that atoms be loaded into what was called a *magic wavelength* optical lattice. The main idea is the following: to ensure there is no AC Stark shift from the optical lattice, the relative dynamic polarizability $\Delta\alpha$ must be equal to zero. For that to hold, we must choose a specific, *magic wavelength* for our lattice. At this magic wavelength, the polarizability of the ground $^1\mathrm{S}_0$ and excited $^3\mathrm{P}_0$ are the same, i.e. $\alpha_\mathrm{g}(\omega_\mathrm{magic}) = \alpha_\mathrm{e}(\omega_\mathrm{magic})$ and the electric dipole term in Eq. 2.23 will cancel out. The frequency of the clock transition will then be unperturbed by the AC Stark shift and independent of the intensity of the trapping light (assuming higher order contributions are neglible).

To determine the magic wavelength, we have to calculate the polarizabilities of the ground and excited state of the clock transition ($\alpha_\mathrm{g}(\omega_\mathrm{l})$ and $\alpha_\mathrm{e}(\omega_\mathrm{l})$) and find their intersect points. For this

| | $5s^2\ ^1S_0$ | $5s5p\ ^3P_0$ | | |
|---|---|---|---|---|
| Upper state | $\omega_{ik}$ ($2\pi$ x THz) | $\omega_{ik}$ ($2\pi$ x THz) | $\xi$ | $A_{ik}$ ($x10^6 s^{-1}$) |
| $5s6s\ ^3S_1$ | - | 2.773 | 1.071 | 84.6 |
| $5s7s\ ^3S_1$ | - | 4.356 | 1.045 | 17.5 |
| $5s8s\ ^3S_1$ | - | 4.984 | 1.039 | 8.22 |
| $5s9s\ ^3S_1$ | - | 5.303 | 1.036 | 4.52 |
| $5s10s\ ^3S_1$ | - | 5.487 | 1.035 | 2.77 |
| $5p^2\ ^3P_1$ | - | 3.97 | 1.036 | 127 |
| $5s4d\ ^3D_1$ | - | 0.724 | 1.053 | 0.345 |
| $5s5d\ ^3D_1$ | - | 3.899 | 1.01 | 61 |
| $5s6d\ ^3D_1$ | - | 4.781 | 1.008 | 26.7 |
| $5s7d\ ^3D_1$ | - | 5.192 | 1.008 | 14.2 |
| $5s8d\ ^3D_1$ | - | 5.419 | 1.007 | 8.5 |
| $5s9d\ ^3D_1$ | - | 5.59 | 1.007 | 5.5 |
| $5s5p\ ^1P_1$ | 4.09 | - | - | 190.7 |
| $5s6p\ ^1P_1$ | 6.42 | - | - | 1.86 |
| $5s7p\ ^1P_1$ | 7.33 | - | - | 4.3 |
| $4d5p\ ^1P_1$ | 7.76 | - | - | 14.5 |
| $5s8p\ ^1P_1$ | 7.76 | - | - | 16.7 |
| $5s9p\ ^1P_1$ | 8.00 | - | - | 11.7 |
| $.5s10p\ ^1P_1$ | 8.17 | - | - | 7.6 |
| $5s11p\ ^1P_1$ | 8.28 | - | - | 4.88 |

Table 2.4: Transition parameters used to calculate the atomic polarizabilities of the Sr clock states. The transition radial frequencies from clock to upper states are given in $2\pi$ x THz and transition rates $A_{ik}$ are given in $10^6$ $s^{-1}$. Parameter $\xi$ are the correction factors needed for calculation of the excited clock state [76]. All values are taken from [1, 2, 7] and references provided therein.

I will use the procedure as laid out in [1]. More precise methods, which also calculate higher-order contributions to the AC Stark shift are available elsewhere [69, 72, 73, 74, 75].
The dynamic polarizability of an atomic state as a function of wavelength is given as [1]

$$\alpha(\omega_l) = 6\pi\epsilon_0 c^3 \sum_k \frac{A_{ik}}{\omega_{ik}^2(\omega_{ik}^2 - \omega_l^2)}, \tag{2.24}$$

where $A_{ik}$ are the transition rates between state *i* and excited states *k* while $\omega_{ik}$ are the transition frequencies between state *i* and excited states *k* . The transition rates $A_{ik}$ can be related to the lifetimes $\tau$ of atoms in the excited state as $\tau = \frac{1}{A_{ik}}$.
To calculate polarizabilities of ground $5s^2\ ^1S_0$ (excited $5s5p\ ^3P_0$) clock transition we use relevant transition frequencies and transition rates between ground (excited) state and other higher

states given in [1, 2, 7] and references therein. Additionally, literature most commonly reports the total transition rate $A_{ik}$ from a given excited state to the fine structure manifold below. Since the excited clock state is part of a triplet manifold, we'll also have to consider the branching ratios from some higher state (e.g $^3\mathrm{D}_1$) to each fine structure sublevel of the $^3\mathrm{P}_\mathrm{J}$ manifold. More details on the procedure is provided in [1]. I would like to point out that magic wavelengths for

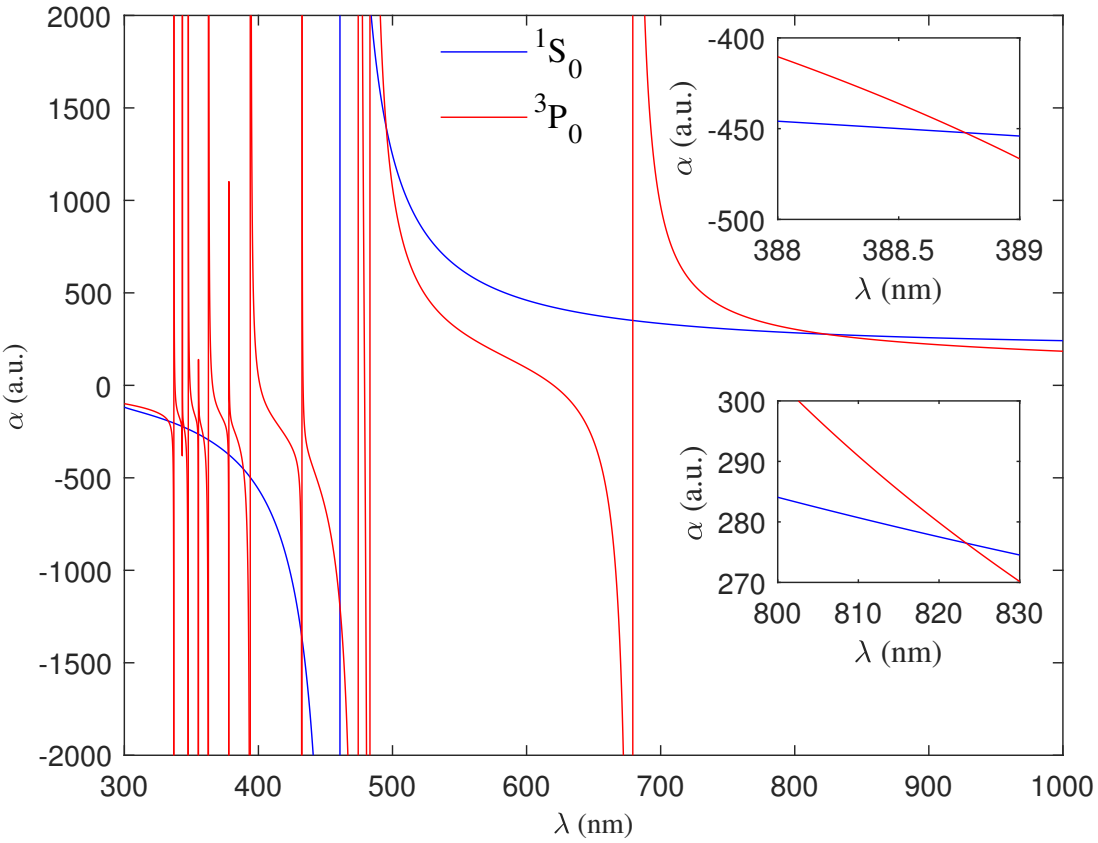


Figure 2.8: Dynamic polarizability $\alpha$ of the ground and excited clock states (in atomic units (a.u)) as a function of lattice wavelength $\lambda$. The insets show polarizabilities for the blue- and red- detuned optical lattices with wavelengths of 390 and 813 nm.

the blue- and red-detuned lattice are already well known and were found to be at $389.889\ \mathrm{nm}$ [77] and $813.428\ \mathrm{nm}$ [78, 79, 80], respectively. Note that in the papers referenced above, not only the dynamic polarizability but higher order hyperpolarizability effects are considered. In contrast, my own approach presented here is rather simplistic as it considers only the dynamic polarizability.

Let us now to calculate the magic wavelength for a blue- and red-detuned optical lattice.

The dynamic polarizabilities of the ground $^1\mathrm{S}_0$ and excited $^3\mathrm{P}_0$ clock states as function of wave-

length are given in Fig. 2.8 with polarizability given in atomic units (a.u.). The transition parameters in Eq. 2.24 used to calculate the polarizabilities of the two clock states are given in Table 2.4, taken from [1, 2, 7] and references provide therein. The top inset in Fig. 2.8 shows the polarizability of the ground and excited clock state in the region around 390 nm. Here my calculations taken from the upper inset in Fig. 2.8 give a magic wavelength of $\lambda_{\mathrm{b}}^{\mathrm{calc}} = 388.88\ \mathrm{nm}$ which is within $1\ \mathrm{nm}$ (0.3%) of the reported value of $\lambda_{\mathrm{b}}^{\mathrm{rep}} = 389.889\ \mathrm{nm}$ [77].

For the more commonly used red-detuned optical lattice (bottom inset in Fig. 2.8) however, I found a significantly larger disagreement. The previously reported value of red-detuned optical lattice is $\lambda_{\mathrm{r}}^{\mathrm{rep}} = 813.428\ \mathrm{nm}$, while my calculations give $\lambda_{\mathrm{r}}^{\mathrm{calc}} = 823.3\ \mathrm{nm}$. One possible reason of such large discrepancy comes from the fact that in our calculations of polarizability we have ignored the contribution of the continuum states ($\omega_{\mathrm{l}} \to 0$) to the scalar polarizability [2, 81] as well as the fact I ignore the contribution of hyperpolarizability to the polarizability of the clock states.

To examine this possibility, we can quickly calculate the values of $\alpha_{^1\mathrm{S}_0}^{\mathrm{calc}}(0)$ and $\alpha_{^3\mathrm{P}_0}^{\mathrm{calc}}(0)$. These values of polarizability are calculated for $\omega_{\mathrm{l}} \to 0$ in Eq. 2.24. The polarizabilities are equal to $\alpha_{^1\mathrm{S}_0}^{\mathrm{calc}}(0) = 190.99$ a.u. and $\alpha_{^3\mathrm{P}_0}^{\mathrm{calc}}(0) = 350.9$ a.u.. This is in good agreement with results from [2, 73, 69] which give the polarizabilities to be $\alpha_{^1\mathrm{S}_0}^{\mathrm{rep}}(0) = 197.2$ a.u. and $\alpha_{^3\mathrm{P}_0}^{\mathrm{rep}}(0) = 351$ a.u. for the ground and excited clock state, respectively. However, we must note the somewhat larger discrepancy for the $^1\mathrm{S}_0$ state which may account for the larger difference between our calculated $\lambda_{\mathrm{r}}$ and those reported. This is due to the fact that a red-detuned lattice has lower frequency and is therefore more sensitive to contributions of the continuum states.

Finally, let us now turn to the calculated values of polarizability at the two magic wavelengths. For the magic wavelength of blue-detuned lattice at $\lambda_{\mathrm{b}} = 388.88\ \mathrm{nm}$ the polarizabilities of the ground and excited clock state are $\alpha_{^1\mathrm{S}_0} = \alpha_{^3\mathrm{P}_0} = -459$ a.u. which matches well with previously reported $\alpha_{^1\mathrm{S}_0} = \alpha_{^3\mathrm{P}_0} = -455$ a.u. [82]. For the red-detuned lattice, the scalar polarizability at my calculated magic wavelength of $\lambda_{\mathrm{r}} = 823.3$ comes out as $\alpha_{^1\mathrm{S}_0} = \alpha_{^3\mathrm{P}_0} = 276.5$ a.u. Our calculated polarizability for the red-detuned lattice shows a larger deviation from polarizability of $\alpha_{^1\mathrm{S}_0} = \alpha_{^3\mathrm{P}_0} = 286.0$ a.u., as reported in literature [74]. For the magic wavelength of $\lambda\mathrm{r} = 813.428\ \mathrm{nm}$, we find the polarizabilities of the ground and excited clock state to be equal to $\alpha_{^1\mathrm{S}_0} = 279.6$ and $\alpha_{^3\mathrm{P}_0} = 286.9$. We again find a more significant discrepancy for the polarizability of $^1\mathrm{S}_0$ state from the one reported in literature.

This work may seem like an excercise in futility, but we will use some of these results in one of the following sections when dealing with Wannier-Stark states in the optical lattice and photoionization losses in a blue-detuned optical lattice. In any case, the AC Stark shift due to the presence of optical lattice is currently controlled to the level of $10^{-18}$ at magic wavelengths and

does not limit the operation of the optical clock.

## 2.9 High-precision spectroscopy of $^1\mathrm{S}_0 \rightarrow {}^3\mathrm{P}_0$

The interrogation of a narrow line clock transition and digital lock of the clock laser to the atomic line of the clock transition is the final frontier of any optical clock experiment. For strontium, the $^1\mathrm{S}_0 \rightarrow {}^3\mathrm{P}_0$ clock transition was for chosen of a variety of reasons. First, there exist convenient magic wavelengths of the optical lattice, making the transition quite resistant to perturbations due to Stark effect. Additionally, the transition is exceedingly narrow with a predicted natural linewidth of $\Gamma = 2\pi$ x 1 mHz for $^{87}\mathrm{Sr}$. For bosons, the clock transition is strictly forbidden and has natural linewidth equal to zero. This raises the question how is it then even possible to have an bosonic optical clock. I will first quickly explain the narrowness of the linewidth for fermions and then discuss bosons. The narrowness of the linewidth of $^{87}\mathrm{Sr}$ comes from its hyperfine structure. Due to the hyperfine structure, there is mixing of the $|^3\mathrm{P}_0\rangle$ state with other hyperfine states with the same hyperfine quantum number. Therefore, $|^3\mathrm{P}_0\rangle$ is not a pure LS state (state due to coupling of atoms' angular momentum L and spin S), but a mixture of different states with the same hyperfine quantum number F=9/2 [1]:

$$|^3P_0\rangle = |^3P_0^0\rangle + \widetilde{\alpha_0}|^3P_1\rangle + \widetilde{\beta_0}|^1P_1\rangle + \widetilde{\gamma_0}|^3P_2^0\rangle, \tag{2.25}$$

where $\widetilde{\alpha_0}, \widetilde{\beta_0}$ and $\widetilde{\gamma_0}$ are hyperfine interaction mixing coefficients and superscript 0 denotes the pure LS state. Both $|^3\mathrm{P}_1\rangle$ and $|^1\mathrm{P}_1\rangle$ can also be written as a superposition of pure LS coupling states with the same J=1:

$$\begin{aligned} |^3P_1\rangle &= \widetilde{\alpha}|^3P_1^0\rangle + \widetilde{\beta}|^1P_1^0\rangle, \\ |^1P_1\rangle &= -\widetilde{\beta}|^3P_1^0\rangle + \widetilde{\alpha}|^1P_1^0\rangle. \end{aligned} \tag{2.26}$$

Combining Eqs. 2.25 and 2.26 the upper clock state in $^{87}\mathrm{Sr}$ can be written as a superposition of pure states:

$$|^3P_0\rangle = |^3P_0^0\rangle + (\widetilde{\alpha}\widetilde{\alpha_0} - \widetilde{\beta}\widetilde{\beta_0})|^3P_1^0\rangle + (\widetilde{\alpha_0}\widetilde{\beta} + \widetilde{\beta_0}\widetilde{\alpha_0})|^1P_1^0\rangle + \widetilde{\gamma_0}|^3P_2^0\rangle. \tag{2.27}$$

This mixing of different states produces a non-zero linewidth of the clock transition. However, this is only valid for fermionic strontium whose hyperfine structure enables mixing of different states. For bosons, the clock transition is completely forbidden. To induce a coupling between the two clock states, first a coupling between $^3\mathrm{P}_0$ and $^3\mathrm{P}_1$ needs to be induced. To do that, a

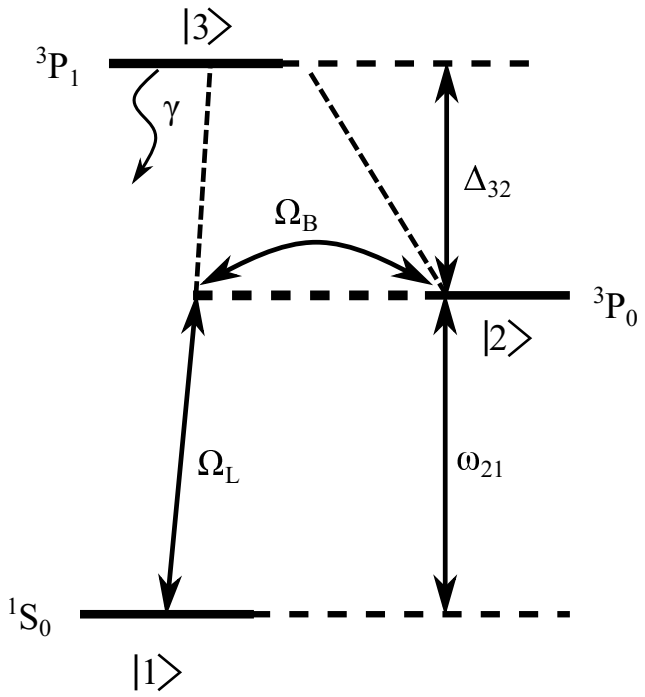


Figure 2.9: Magnetically induced spectroscopy of the forbbiden clock transition in bosonic optical clock. The use of a strong bias magnetic field induces a coupling between the $^3P_0$ and $^3P_1$ state. Because of it, the upper clock state is not longer a pure state but a mixture of the two states. Due to this mixing, the bosonic clock transition becomes weakly allowed, enabling the operation of a bosonic optical clock. $\Omega_B$ is the coupling matrix element between the two excited states due to the strong magnetic field, while $\Omega_L$ is the matrix coupling element induced by the electric field of the clock transition probe beam. The clock transition is given by $\omega_{21}$, the detuning between the upper two states of the triplet is given by $\Delta_{32}$ and decay rate from the $^3P_1$ state is given by $\gamma$. More details on magnetically induced spectroscopy are given in the main text and are available in Taichenachev et al. [83].

strong bias field B combined with quite high intensity in the clock transition probe beam needs to be employed. This method, called magnetically induced spectroscopy, was first proposed by Taichenachev et al. [83]. Then the upper clock state is given as [83, 84]

$$|^3P_0\rangle = |^3P_0^0\rangle + \frac{\Omega_B}{\Delta_{32}}|^3P_1^0\rangle, \tag{2.28}$$

where $\Omega_B = \frac{\langle ^3\mathrm{P}_0|\hat{\mu}\cdot\mathrm{B}|^3\mathrm{P}_1\rangle}{\hbar}$ is the coupling matrix element between the two states, $\hat{\mu}$ is the magnetic-dipole operator and $\Delta_{32}$ is the splitting between the two states. Due to the mixing in Eq. 2.28, the clock transition in bosonic strontium becomes weakly allowed, enabling the operation of a bosonic optical clock. The Rabi frequency for the clock transition is then equal to $\Omega_{12} = \frac{\Omega_L\Omega_B}{\Delta_{32}}$ where $\Omega_L = \frac{\langle\, ^3P_1|\hat{d}\cdot E|\, ^1S_0\rangle}{\hbar}$ is the matrix coupling element induced by the elec-

tric field of the clock transition probe beam. From there, the linewidth of the bosonic clock transition is given as [83]

$$\gamma_{12} \sim \gamma \frac{\Omega_L^2/4 + \Omega_B^2}{\Delta_{32}^2}. \tag{2.29}$$

This broadening effectively comes from the fraction of population transferred by the two fields to the $|3\rangle$ state, which decays with a rate $\gamma$. As this broadening is inversely proportional to the square of the large frequency splitting $\Delta_{32}$ between the two states, it is an extremely small quantity, usually on the order of microhertz [83]. Only by applying high magnetic field can the line be sufficiently broadened to be experimentally detectable. This method of enabling the

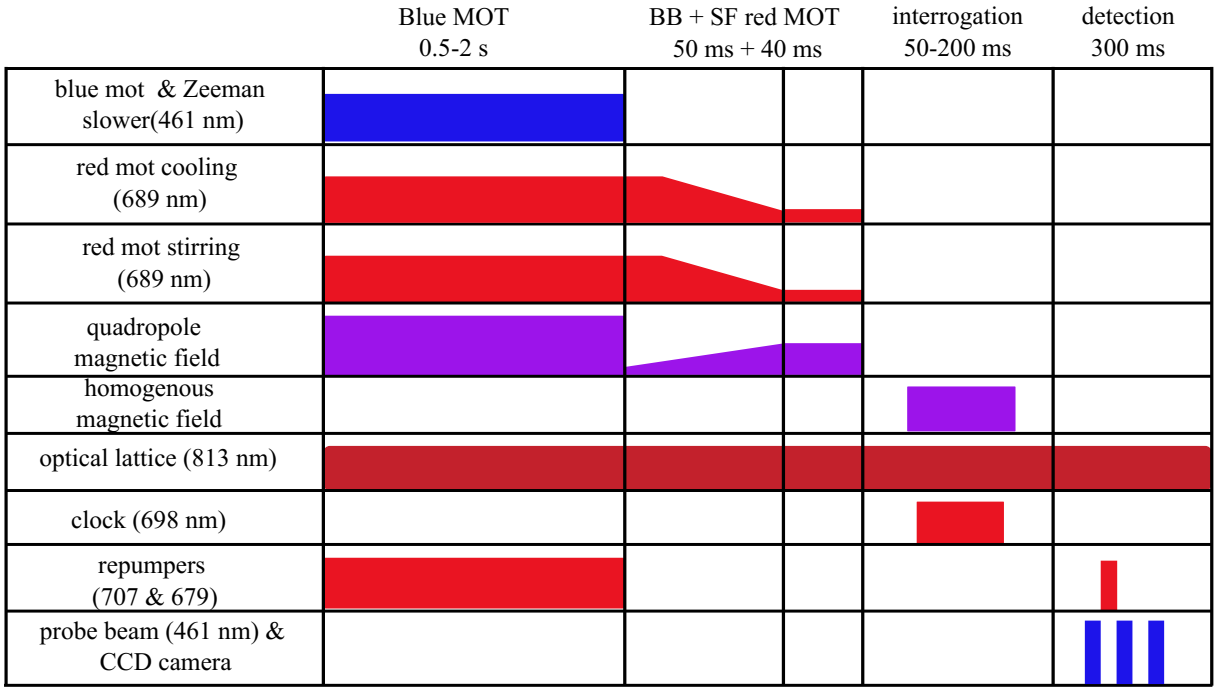


Figure 2.10: Optical clock cycle in an optical clock. Atoms are first cooled in the two stage cooling (blue and red MOT) and then loaded into the optical lattice. The clock transition is then interrogated by the clock beam. Finally, in the detection stage, the populations of atoms in the ground and excited state are measured. First, the atoms in the ground $^1S_0$ clock state are excited using a 461 nm probe beam and the flourescence of the decaying atoms is measured on a CCD camera. Then, atoms in excited $^3P_0$ clock state are repumped through $^3S_1$ to the ground state using the 707 nm and 679 nm lasers. The atoms are then excited using the 461 nm laser and the flourescence of the decaying atoms is again measured on the CCD camera.

clock transition doesn't come without a cost. The use of bias magnetic field and high intensity probe beam induces a large shift of the clock transition, affecting the accuracy of the optical clock. This will be discussed more in one of the following chapters when I'll present the accuracy budget of our optical clock measured during a recent campaign.

To perform a high-precision spectroscopy of the optical clock transition, we optically interrogate the clock transition on an ensamble of atoms loaded in the optical lattice. After the interrogation, a portion of the atomic population will be transferred to the upper $^3\mathrm{P}_0$ clock state, with the rest of the atoms remaining in the ground $^1\mathrm{S}_0$ state. To measure the populations in the two clock states we use the detection method shown in Fig. 2.10. By using a 461 nm flouresscence probe beam, atoms in the ground clock state are excited to the $^1\mathrm{P}_1$ state and then we measure on a CCD camera the flourescence produced by the emitting atoms as they relax back to the ground level. However, this is a destructive detection method as probing by flourescence beam will eject the atoms out of the optical lattice.

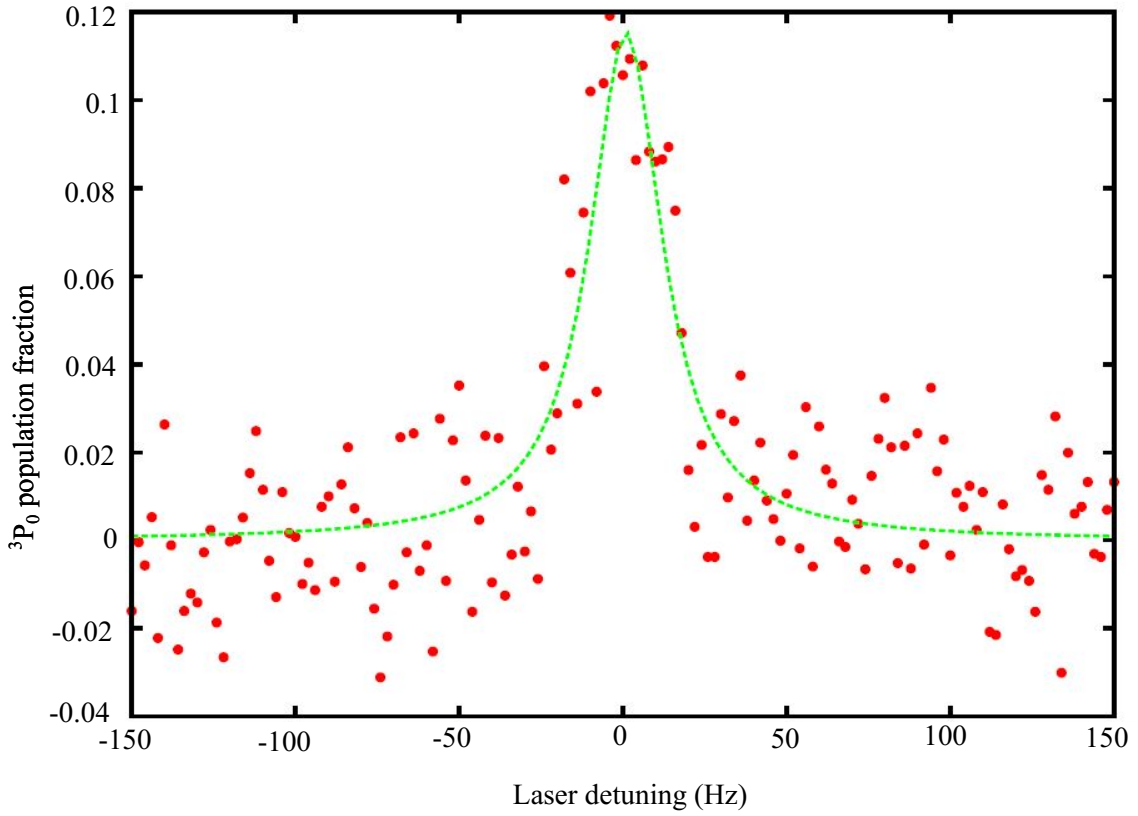


Figure 2.11: Spectroscopy of the $^1\mathrm{S}_0 - ^3\mathrm{P}_0$ of bosonic strontium. A Lorentz function is fitted to the measured data, giving a measured linewidth (FWHM) of 27(1) Hz. Taken from [28].

At that point, atoms in the excited clock state are transferred to the ground state by using the repumping beams at 707 and 679 nm. This method is called electronic shelving. The repumpers will transfer atoms firstly to $^3\mathrm{P}_1$ via $^3\mathrm{S}_1$, and then atoms will decay to the ground state. We then again measure the population of the transferred atoms by using the 461 nm probe beam and measuring the flourescence produced by the atoms. This probing will again blow atoms out of

the optical lattice. This means that after each detection stage is completed, atoms need to be loaded into the optical lattice again by using the procedure explained earlier in this chapter.
For the high-precision spectroscopy of the clock transition, we plot the fraction of the population in the excited clock state $\frac{P_e}{P_g+P_e}$ as a function of detuning of the clock transition interrogation beam where $P_g$ and $P_e$ are populations of atoms in the ground and excited clock state after interrogation of the clock transition. You should note, that what you see in each of the flourescence pictures taken is proportional to the populations, and the proportional coefficient shortens in a fraction.
An example of the high-precision spectroscopy of the clock transition for bosonic strontium is given in Fig. 2.11. A Lorentz function is fitted to the measured data, giving a FWHM linewidth of 27(1) Hz [28].
Now, in the low saturation limit, the amplitude of the sidebands from Fig. 2.7 is at least an order of magnitude smaller than the amplitude of the clock transition, limiting the linewidth of the transition to the Fourier limit. Therefore, the primary limit to the linewidth comes from the interrogation time of the clock transition, which is in turn limited by the coherence time of the laser. Current state-of-the-art lasers stabilised to high-finesse fused-silica Fabry-Perrot cavities operated at 124 K reach fractional uncertainty of $4\text{x}10^{-17}$. This fractional uncertainty translates into laser linewidths below $10\ \text{mHz}$ and laser coherence times of up to 55 seconds [85].
Finally, once the atomic line of the clock transition is located, the clock laser is digitally locked to the atomic resonance. This is done by measuring the population fraction to the left and right of the clock resonance (i.e. red- and blue-detuned from resonance). From the difference in population fractions a correction signal is generated. With a feedback loop, we then compensate for any drift of the clock laser frequency from the clock transition, digitally locking the clock laser to the clock transition.

# Chapter 3

# Feasibility of blue magic wavelength optical lattice clocks

This section will present our work on measurements of photionization cross sections of $^1\mathrm{P}_1$ and $^3\mathrm{S}_1$ states in $^{88}\mathrm{Sr}$ in blue magic wavelength optical lattice. It will also present my work on examination of feasibility of using blue magic wavelength optical lattices. Finally, it will show calculations of photionization induced losses of atoms in a blue magic wavelength optical lattice clock and possible ways to mitigate those losses. My work in particular will focus on calculations of Wannier and Wannier Stark states in blue magic wavelength lattice. I will examine two different cases - the Wannier states in a horizontal optical lattice and the Wannier-Stark states in a vertical optical lattice. Our goal in this section is to determine both the experimental requirements, possible issues and critical defects in using blue magic wavelength optical lattices in optical atomic clocks.

## 3.1 Confinement of atoms in blue-detuned optical lattice

As mentioned above, in a blue-detuned magic wavelength optical lattice, atoms are confined at the minima of light intensity as opposed to a red-detuned magic wavelength optical lattice where they are loaded into maxima of light intensity. However, the atoms cannot be trapped in a simple 1D blue-detuned magic wavelength lattice trap because they will escape along the radial directions. Confinement in all three orthogonal directions can be achieved, for instance, by a 3D optical lattice trap, made up of three independent 1D optical lattices [86]. Moreover, a 3D optical lattice will reduce the influence of interactions between atoms on the optical clock's accuracy. To examine the feasibility of using blue-detuned optical lattice in an optical clock, we must check the experimental requirements and possible impediments to its use in clock opera-

tion and compare it with the commonly-used red-detuned optical lattice. To do just that, we will use the approach presented in Lemonde et al. [87] when making comparisons between results for commonly used red-detuned latices and the blue-detuned optical lattices. We consider an atom emerged into the periodic potential of an optical lattice with the periodicity equal to half the wavelength of the lattice $\frac{\lambda}{2}$. We will study two seperate cases: case a) atom in a horizontally oriented lattice where there is no contribution of the gravity to the Hamiltonian and case b) where the lattice is vertically oriented and gravity contributes to the total Hamiltonian.
This is not to say that there is no gravity at all in case a). But we are interested in the motion of the atom in the axial direction of the lattice so we can examine the tunneling between different lattice sites, calculate atoms' energy levels and wavefunctions with the goal of learning about the real experimental requirements to ensure for the atom to be in the Lamb-Dicke regime. And for the horizontal lattice, all of this happens the x or y direction, while gravity is perpendicular to it (in z direction) and therefore it has no influence on the energy levels and wavefunctions of the atom.
This will be radically different once we consider case b) when gravity will play an integral role in explaining the tunelling effects in a vertical lattice. Clearly, a vertical case presents a more complicated case, and so we shall begin with the easier case - the horizontal optical lattice.

**Case a: The horizontal optical lattice**

We begin as any 3rd year undergraduate student would, by writing out the Hamiltonian of the atom in the horizontal lattice:

$$H(q) = \frac{\hbar q^2}{2m_a} + \frac{U_0}{2}(1 - cos(2k_l x)), \tag{3.1}$$

where $q$ is the atoms' quasimomentum and $k_l$ is wavevector of the optical lattice with periodicity of $\frac{\pi}{k_l}$. Lattice depth $U_0$ is usually given in units of recoil energy $E_r = \frac{(\hbar k_l)^2}{2m_a}$. It should be noted that we've elected to ignore the radial direction of the potential and have decided to focus only on the axial direction. At this point, we use the periodicity of the optical lattice and employ Bloch's theorem which simply states that the wavefunction of a particle in a periodic lattice must be of the form [89, 90]

$$\psi_{n,q}(x) = u_{n,q}(x)e^{iqx}, \tag{3.2}$$

where $u_{n,q}(x)$ and $\psi_{n,q}(x)$ are Bloch functions and Bloch waves, respectively. Both Bloch functions and Bloch waves are dependent on quasimomentum $q$ and energy band quantum number $n$ with Bloch functions being generally periodic with $\frac{\lambda}{2}$. In quasimomentum space, this corresponds to the periodicity of Brillouin zones and we can therefore limit the range of the

quasimomentum $q$ to the $1^{st}$ Brillouin zone $q \in [-k_l, k_l]$.
Due to periodicity of the lattice, Bloch waves are also periodic $\psi_{\mathrm{n,q}}(\mathrm{x}) = \psi_{\mathrm{n,q+Q_m}}(\mathrm{x})$ with $Q_m = 2mk_l, m \in Z$. This periodicity also allows us to write both the potential and and Bloch functions as a Fourier series

$$V(x) = \sum_m \widetilde{V}(m) e^{iQ_m x}, \tag{3.3}$$

$$u_{n,q}(x) = \sum_m \widetilde{u}_{n,q} e^{iQ_m x}. \tag{3.4}$$

By inserting Eq. 3.4 and Eq. 3.2 into Eq. 3.1, we get a tridiagonal N x N Hamiltonian matrix [89]

$$\begin{bmatrix} & & \dots & & \\ \dots & \frac{U_0}{2} & \frac{\hbar^2(q+Q_{m-1})^2}{2m_a} + \frac{U_0}{2} & \frac{U_0}{2} & 0 & \dots \\ \dots & 0 & \frac{U_0}{2} & \frac{\hbar^2(q+Q_m)^2}{2m_a} + \frac{U_0}{2} & \frac{U_0}{2} & \dots \\ \dots & 0 & 0 & \frac{U_0}{2} & \frac{\hbar^2(q+Q_{m+1})^2}{2m_a} + \frac{U_0}{2} & \dots \\ & & \dots & & & \end{bmatrix} \begin{bmatrix} \dots \\ \widetilde{u}_{n,q}(m-1) \\ \widetilde{u}_{n,q}(m) \\ \widetilde{u}_{n,q}(m+1) \\ \dots \end{bmatrix} = \epsilon_n(q) \begin{bmatrix} \dots \\ \widetilde{u}_{n,q}(m-1) \\ \widetilde{u}_{n,q}(m) \\ \widetilde{u}_{n,q}(m+1) \\ \dots \end{bmatrix}$$

where $\epsilon_{\mathrm{n}}(\mathrm{q})$ are the energy bands we wish to calculate. To do so, we first must truncate our matrix at some maximum index $\mathrm{m}$ and find the eigenenergies of the Hamiltonian. But before dive into it, let us also consider the Bloch wave functions with regards of physics of an atom in a lattice. It is well known that Bloch states describe delocalised quantum states which span through the entire potential. But we aim to describe an atom in the Lamb-Dicke regime of the lattice where the atom is effectively localised within a single lattice site. Clearly, the Bloch states will not do. What we can do is define a set of functions given as the discrete Fourier transformation of the Bloch wave functions with respect to the site locations, with each such defined function centered around a lattice site of the potential [89]. This will localise a state within a single lattice, just as one would expect for an atom in the Lamb-Dicke regime. Such states are called Wannier states and are given as

$$w_n(x - x_i) = \frac{1}{\sqrt{N}} \sum_{q \in BZ1} e^{-iqx_i} \psi_{n,q}(x), \tag{3.5}$$

where $\mathrm{x_i}$ are the site locations of the lattice potential.
In a horizontal lattice, atoms with the same vibrational quantum number $\mathrm{n}$ located in neighbouring lattice sites are degenerate in energy with the degeneracy simply coming from the symmetry of the optical lattice. This degeneration amplifies the tunelling between neighbouring wells, spatially spreading the atoms' position wavefunction across multiple lattice sites. The tunnelling between different sites creates a band structure in the energy spectrum of the atom in the lattice. This will shift and broaden the linewidth of clock transition once the atoms is probed by the clock laser [87]. The energy bands of Eq. 3.1 are

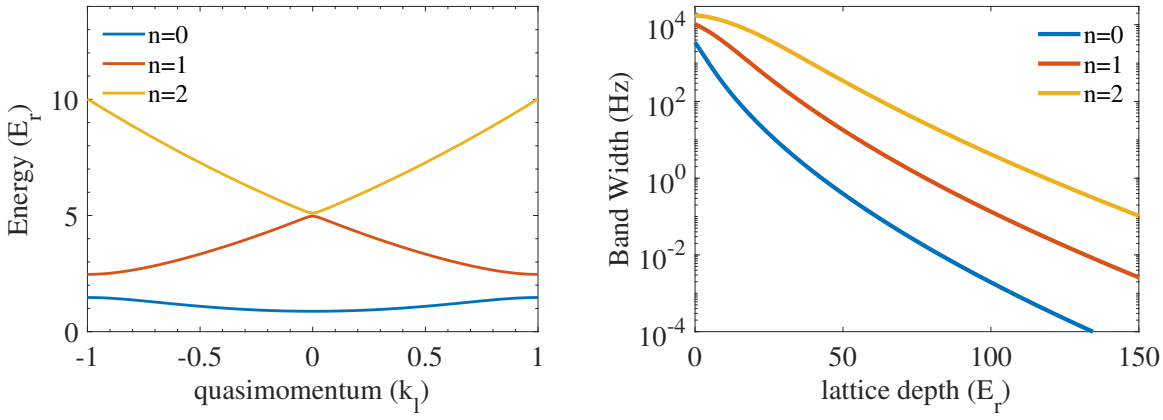


Figure 3.1: Band structure for 3 lowest energy bands (n=0,1,2) for a blue-detuned optical lattice with lattice depth of 2 $E_r$. Interaction of the atoms in the lattice with the clock laser allows them to jump between energy bands.
(right) Bandwidth, defined as $\frac{|E_{n,q=k_l} - E_{n,q=0}|}{\hbar}$, given as a function of lattice depth for the 3 lowest energy bands. To achieve clock stability of $10^{-18}$, band width should be $\approx 1$ mHz which requires lattice depths of $\approx$ 90 $E_r$ for the atoms in the ground band.

usually represented as shown in Fig. 3.1. The broadening of the clock transition due to the existence of the band structure is usually described with a bandwidth parameter $\frac{|E_{n,q=k_l} - E_{n,q=0}|}{\hbar}$ of a band. Dependence of the bandwidth on lattice depth for the 3 lowest energy bands is shown in Fig. 3.1 (right). To achieve clock stability of $10^{-18}$, bandwidth should be $\approx 1$ mHz which requires lattice depths of $\approx$ 90$E_r$ for the atoms in the ground band [87].

### Case b: The vertical optical lattice

We now turn our attention to the more complicated of the two cases where atoms are trapped in a vertical optical lattice. Due to the presence of gravity, the atom will now experience a tilted optical lattice, as shown in Fig. 3.2 and such a lattice no longer supports bound states. In principle an atom trapped within some lattice site will eventually tunnel out into continuum, but the lifetime of a quasi-bound state grows exponentially with lattice depth and even for shallow lattices depths of 5 $E_r$ the lifetime the state is on the order of $10^{10}$ s which is much longer than the duration of the experiment [87]. The external Hamiltonian of the atom in the vertical lattice is given as

$$H(q) = \frac{\hbar q^2}{2m_a} + \frac{U_0}{2}(1 - cos(2k_l z)) + m_a g z, \tag{3.6}$$

with gravity lifting the degeneracy between energy states in adjacent wells. The energy separation between adjacent states corresponds to the change in gravitational potential between adjacent states $\hbar\Delta_g = m_a g \frac{\lambda}{2}$. Since this Hamiltonian doesn't have bound states, the analysis from previous subsec-

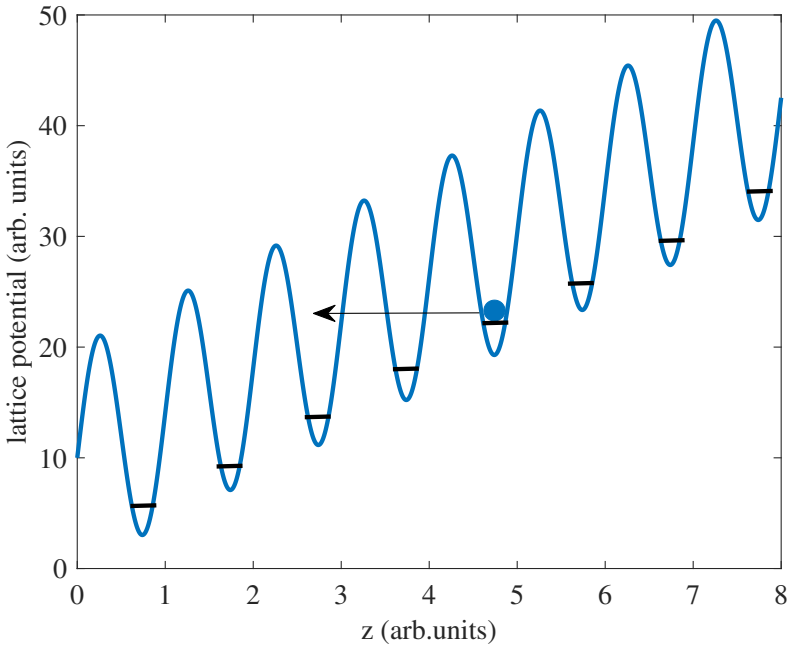


Figure 3.2: External lattice potential as seen by atoms in a vertical optical lattice. The linear contribution of gravity tilts the lattice and the lattice no longer supports bound states. An atom trapped in ground state (black horizontal line) of a lattice site would eventually tunnel into the continuum, but even for shallow lattices of 5 $E_r$ the lifetime of the quasibound state in $10^{10}$ s [87].

tion is no longer possible and so to examine the case of the vertical optical lattice we have calculate the eigenstates of the lattice. These eigenstates are called Wannier-Stark (WS) states $|W_m\rangle$ where $\mathrm{m}$ denotes the m-th well of the lattice. In the tight-binding approximation, WS states can be calculated as a superposition of Wannier states $\mathrm{w_m}$ where each Wannier state is weighed by the appropriate Bessel function [88]. The WS states in position representation centered around $\mathrm{m} = 0$ lattice for different lattice depths for a blue- and red-detuned optical lattice are shown in Fig. 3.3. In the calculation of WS states, we also assume that the atom can only tunnel to the nearest and second-nearest neighbouring lattice sites (located at $\mathrm{z} = -2, -1, 1, 2$ on x axis of Fig. 3.3). As seen in Fig. 3.3 (right), for the widely used 813 nm optical lattice, a Wannier-Stark state consists of a "central" peak and two smaller "revival" peaks, even for very shallow lattices of 5 $E_r$. For lattice depth of 10 $E_r$, the revival peaks are already a hundred times smaller than the main peak and the wavefunction is localised in a single lattice site and tunneling between neighbouring lattice sites is strongly suppressed.

By comparison, similar main-to-sidepeak ratios in a blue-detuned optical lattice require twice the lattice depth, i.e. 20 $E_r$ due to shorter distance between lattice sites due to smaller lattice wavelength and smaller degeneration of energy states in adjacent lattice sites.

Let us now add a probe laser (i.e. the $698$ nm clock laser) which will couple the internal ground $|g, W_m\rangle$ and excited $|e, W_{m'}\rangle$ state of the atom in the lattice. This coupling creates a structure called the Wannier-

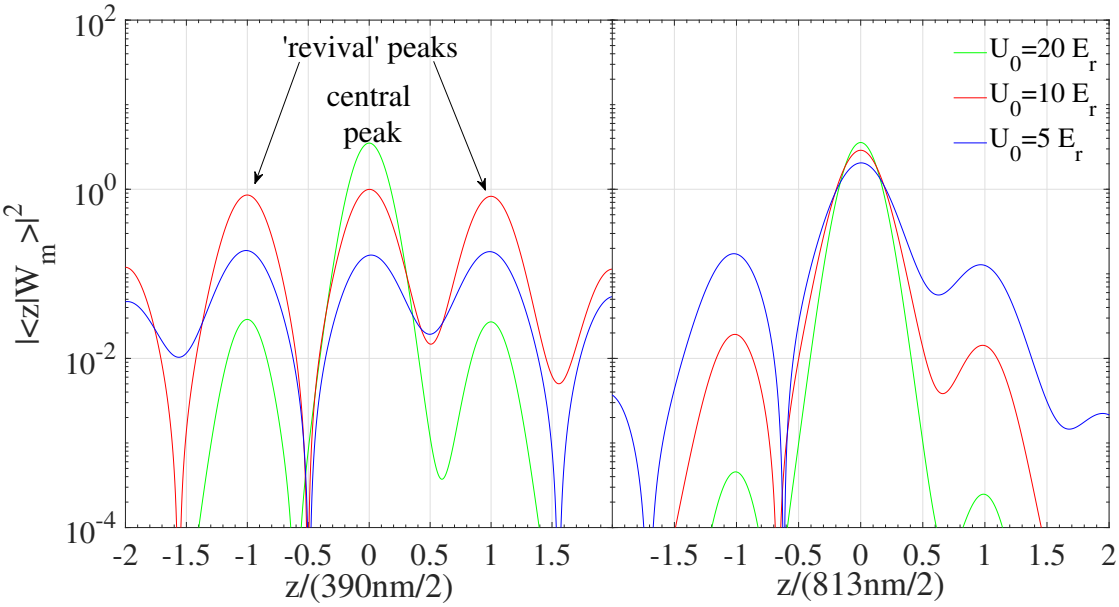


Figure 3.3: Wannier-Stark (WS) states in position representation for different lattice depths for 390 nm (left) and 813 nm (right) magic wavelength lattices. For 813 nm optical lattice with lattice depth of 10 $E_r$, the revival peaks will already be two orders of magnitude lower than the central peak, indicating strong localisation of the atom in a single lattice site and strong suppression of tunnelling between lattice sites. For the 390 nm optical lattice, similar revival-to-peak ratio requires lattice depth of 20 $E_r$, posing more stringent experimental requirements on blue magic wavelength lattice depth to ensure Lamb-Dicke regime.

Stark ladder of states and is shown in Fig. 3.4. The ladder is made up of a set of WS states with a single state in every lattice site. Due to the coupling between the internal ground and excited atomic state induced by the probe laser, and atom in the 'central' ground $|\mathrm{g}, \mathrm{W_m}\rangle$ WS state can couple either into the excited WS state in the same lattice site $|\mathrm{e}, \mathrm{W_m^{'}}\rangle$ or it can couple to one of the adjacent $|\mathrm{e}, \mathrm{W_{m'\pm1}}, \rangle$ or second-adjacent $|\mathrm{e}, \mathrm{W_{m'\pm2}}, \rangle$ states by tunnelling between lattice sites. Each of these couplings is described by different coupling strengths $\Omega_\mathrm{m}$. The internal ground and excited state are coupled by probe frequency $\omega_\mathrm{eg}$ and the splitting between energy levels of WS states in adjacent lattice sites is given by $\hbar\Delta_\mathrm{g}$. The coupling between the ground and excited WS states due to the probe laser results in a translation in momentum state by $\mathrm{e}^{\mathrm{ik_c\hat{z}}}$ where $\mathrm{k_c}$ is the wavevector of the probe laser. The couplings are given as

$$\Omega_{\Delta m} = \Omega\langle W_m|e^{ik_c\hat{z}}|W_{m'}\rangle, \tag{3.7}$$

with $\Omega$ being the Rabi frequency. In these calculations, we'll set the Rabi frequency at $\frac{\Omega}{2\pi} = 10$ Hz. The relative coupling strengths $|\frac{\Omega_{\Delta M}}{\Omega}|^2$ of the "carrier" $\Omega_0$ and the first 4 "sidebands" $\Omega_{\pm1,\pm2}$ as a function of lattice depth are shown in Fig. 3.5 for both the blue-detuned (left) and red-detuned (right) optical lattice. For the 813 nm lattice (Fig. 3.5 (right)), coupling strength of the "carrier" quickly rises to unity

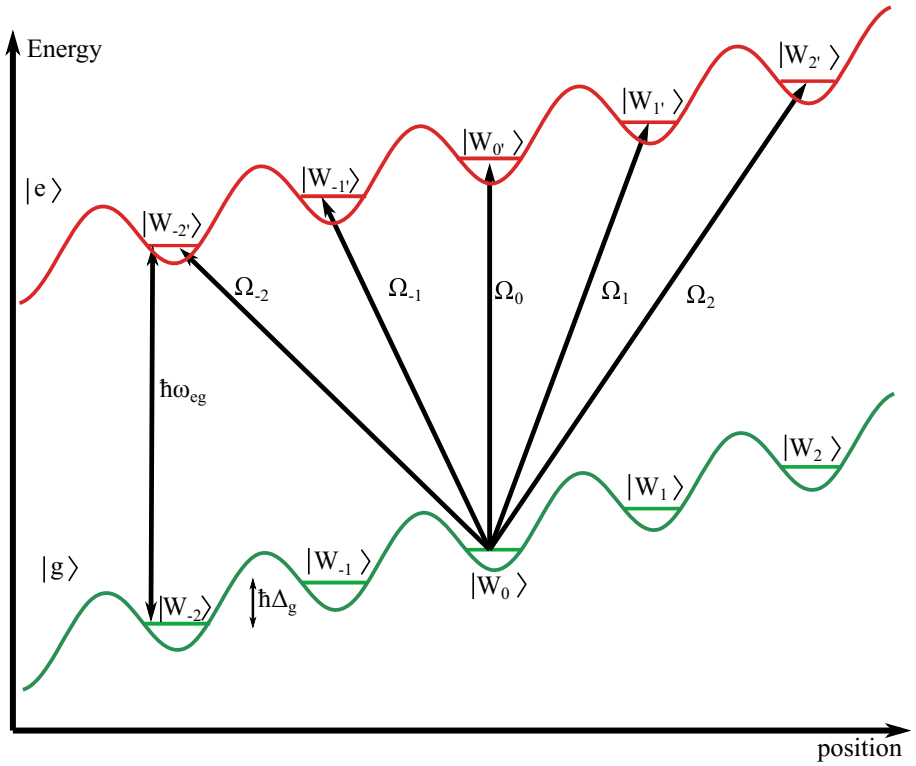


Figure 3.4: Wannier-Stark ladder of states for the ground and excited clock states. An atom is initially in the ground Wannier-Stark (WS) state $|\mathrm{W_m}\rangle$ for m=0 (i.e. $|\mathrm{W_0}\rangle$) in the optical lattice for the electronic clock ground state $|\mathrm{g}\rangle$. The atom is then excited into the excited clock state $|\mathrm{e}\rangle$ by the clock probe beam with frequency $\omega_{\mathrm{eg}}$, where $\omega_{\mathrm{eg}}$ is the transition frequency of the clock transition. The atom can then couple into different excited Wannier-Stark states $|\mathrm{W_{m'}}\rangle$ where $\mathrm{m'} = -2', -1', 0', 1', 2'$. Coupling into each excited WS state is characterized by different coupling strength $\Omega_{\mathrm{m}}$ (m=-2,-1,0,1,2). The splitting between adjacent WS states due to gravity is given as $\hbar\Delta_{\mathrm{g}}$.

and the atom oscillates with the Rabi frequency within the "central" lattice site with strong suppression of tunnelling to neighbouring lattice sites. For the 390 nm lattice (Fig. 3.5 (left)), we see strong Rabi oscillations for lattices shallower than 10 $E_r$ similar to those reported by Tackmann et al. [91]. Beyond that point, the "carrier" goes to unity while the sidebands quickly fall off. Let us compare the coupling strengths of the carrier and the sidebands for the two cases we've considered earlier - 10 $E_r$ deep red-detuned lattice and 20 $E_r$ deep blue-detuned lattice. For both cases we get similar relative coupling strengths to the nearest and second-nearest lattice sites, $|\frac{\Omega_{\pm1}}{\Omega}|^2$ and $|\frac{\Omega_{\pm2}}{\Omega}|^2$, respectively. The coupling to the nearest lattice site $|\frac{\Omega_{\pm1}}{\Omega}|^2$ is $10^{-2}$ smaller than the carrier, while the coupling to the second-nearest lattice site $|\frac{\Omega_{\pm2}}{\Omega}|^2$ is $10^{-4}$ times smaller than the carrier coupling strength. This again shows that to achieve similar levels of trapping and suppression of tunnelling, a blue-detuned optical lattice requires a lattice depth twice as deep compared to a red-detuned optical lattice.

To calculate the populations of the ground and excited WS states, we consider the evolution of the excited

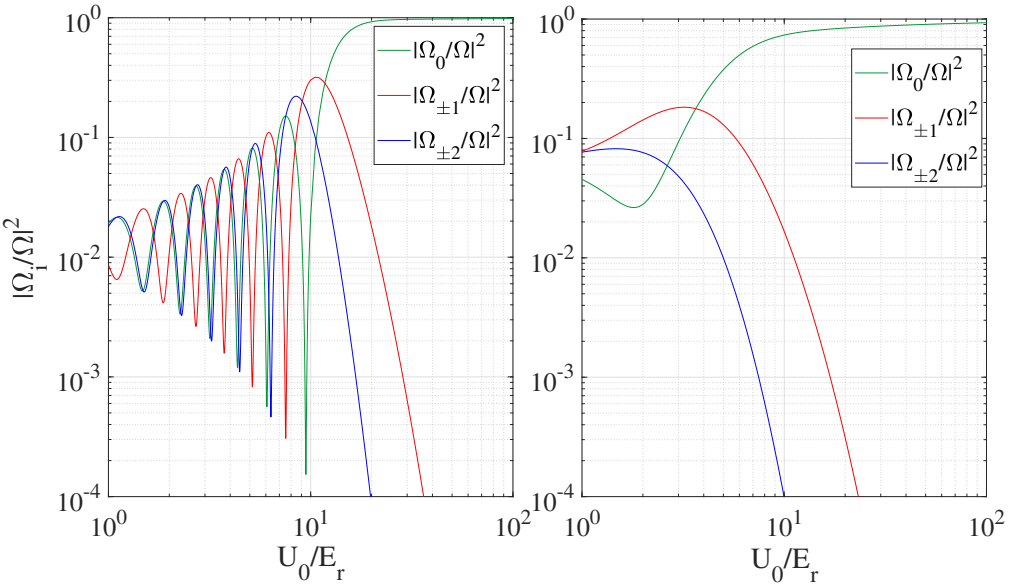


Figure 3.5: Relative coupling strengths $|\frac{\Omega_{\Delta M}}{\Omega}|^2$ of the "carrier" $\Omega_0$ and the 4 "sidebands" $\Omega_{\pm1,\pm2}$ for a blue-detuned (left) and red-detuned (right) optical lattice as a function of lattice depth. For the red-detuned lattice, the coupling strength of the carrier $\Omega_0$ quickly rises to unity with increasing lattice depth, ensuring strong trapping of the atom in a single lattice site and preventing tunneling. For the blue-detuned lattice there are strong oscillations in coupling strengths. This will allow strong coupling of the atom in $|\mathrm{W}_0\rangle$ WS state to adjecent $|\mathrm{W}_{\mathrm{m'}=\pm1,\pm2}\rangle$ states. To prevent tunnelling to these states, higher lattice depths are required for the blue-detuned lattice.

and ground state under coupling to the probe laser. The evolution is given by a set of coupled differential equations [87]

$$\begin{aligned} i\dot{a}^g_m &= \sum_{m'} \frac{\Omega^*_{m-m'}}{2} e^{-i\pi m' k_c/k} e^{i\Delta_{m-m'}t} a^e_{m'}, \\ i\dot{a}^e_m &= \sum_{m'} \frac{\Omega_{m'-m}}{2} e^{i\pi m k_c/k} e^{-i\Delta_{m'-m}t} a^g_{m'}, \end{aligned} \tag{3.8}$$

where $\mathrm{a^g_m}$ and $\mathrm{a^e_m}$ are the probability amplitudes of the ground and excited state, respectively. The detuning between different ground and excited WS states is given as $\Delta_{\mathrm{m-m'}} = \omega - \omega_{\mathrm{eg}} + (\mathrm{m} - \mathrm{m'})\Delta_{\mathrm{g}}$. The populations of the WS states are simply absolute squared values of the probability amplitudes. We will calculate these populations using the 4th order Runge-Kutta method (RK4). The resonances for different lattice depths for blue- and red-detuned optical lattice are shown in Fig. 3.6. The resonances were calculated for the central lattice site and its' nearest and second-nearest neighbouring site with each resonance appearing at the multiples of $\Delta_{\mathrm{g}}/(2\pi)$ with $\Delta_{\mathrm{g}}/(2\pi) = 866$ Hz for red-detuned and $\Delta_{\mathrm{g}}/(2\pi) = 422$ Hz for the blue-detuned lattice. These central and neighbouring resonances correspond to the central peak and the 4 "sidebands", respectively.

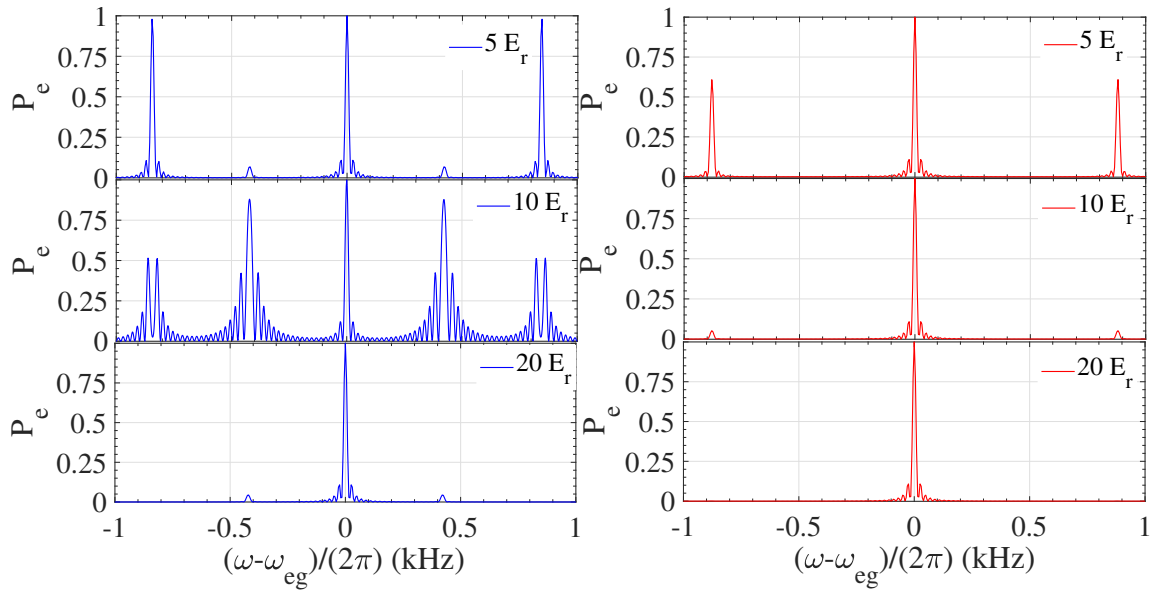


Figure 3.6: Calculated Wannier-Stark resonances for 5, 10 and 20 $E_r$ lattice depths for blue-detuned (left figure) and red-detuned (right figure) optical lattices. For the red-detuned 813 nm lattice, the sideband resonances decay quickly with increased lattice depth due to the fast rise of the relative coupling strength of the carrier on $\Omega_0$ to unity (green line in Fig.3.5 (right)). With coupling strength $\Omega_0$ near unity for 20 $E_r$, the atom can only couple from $|W_0\rangle$ to $|W_{0'}\rangle$ (see Fig. 3.4) and leaving only the central resonance for 20 $E_r$. For the blue-detuned optical lattice, there are strong oscillations in the sideband resonances. To prevent coupling of the atom into the sidebands, the lattice depth must be twice as deep compared to the red-detuned lattice (20 recoil energies for the blue-detuned lattice versus 10 recoil energies for the red-detuned lattice).

Let us once again compare the two lattices. For the red-detuned lattice (right side of Fig. 3.6), the situation seems quite clear - with increasing lattice depth the probability of finding an atom in once of the adjacent lattice sites falls off exponentially [87] and for even for very shallow lattice of just 10 $E_r$ the atom is effectively trapped in the central lattice site with strong suppression of tunnelling to side states. This is in line with Fig. 3.5 as in a red-detuned lattice the coupling strength for the carrier $\Omega_0$ is larger than any of the sidebands $\Omega_{\pm1,\pm2}$ for all 3 chosen lattice depths.

The situation is quite different for the blue-detuned lattice. For the shallowest lattice depth of 5 $E_r$, the resonance at the second-nearest neighbouring site is as strong as the resonance in the central lattice, implying strong tunneling between lattice sites. This unusual behaviour stems from the fact that for 5 $E_r$, the coupling strengths $\Omega_0$ and $\Omega_2$ are almost equal in value while $\Omega_1$ is 2 orders of magnitude smaller. This allows atoms to go from ground $W_m$ state with near equal chance to excited $W_{m'}$ or $W_{m'\pm2}$ state while spending very little time in the $W_{m'\pm1}$ as represented by small resonances at the nearest neighbour at 422 kHz. Similar behaviour appears for the 10 $E_r$ lattice with very strong resonances in the side lattice sites. However beyond this lattice depth, the coupling to the central lattice site quickly rises to

unity while coupling to sidebands plummets. And therefore, for a lattice depth of 20 $E_r$, the atom is again strongly trapped in a single lattice site with almost no probability of tunneling. Finally, it is worth noting that to achieve similar central-to-first-side band peak ratios for red- and blue-detuned optical lattice (and therefore similar trapping levels), a blue-detuned lattice requires twice the lattice depth (20 $E_r$ for a blue-detuned versus 10 $E_r$ for its red-detuned counterpart). This is in line with conclusions reached when we discussed WS states in Fig. 3.3.

## 3.2 Photoionization of atoms in blue-detuned optical lattice

In the previous sections, we've mostly talked about possible advantages of using blue magic optical lattices in optical clock operation, primarily the fact that in blue-detuned lattices atoms are loaded near minima of light intensity, reducing light-induced pertubations of the clock transition. However, before we declare victory, we have to consider possible downsides as well. One of main downsides is the possibility of single-photon photoionization of atoms by the blue magic wavelength lattice. If the energy of a blue magic wavelength photon is higher than the ionization threshold of some atomic state used in optical clock cycle, this may cause loss of atoms during the cooling/detection stage of the cycle, reducing the signal-to-noise ratio when measuring the frequency of the clock transition. The schematic energy level diagram for different transitions in clock cycle along with the ionization threshold for 390 nm light are shown in Fig. 3.7. As we can see, the $^1\mathrm{S}_0 \rightarrow {}^3\mathrm{P}_0$ clock transition is safe as both states are outside the dashed lines in Fig. 3.7, meaning that blue magic photons don't have sufficient energy to ionise atoms in either clock state. However, both the $^1\mathrm{P}_1$ and $^3\mathrm{S}_1$ state can be affected by photoionization for the blue-detuned lattice, potentially creating photoionization loss channels during both loading of the blue MOT and repumping during detection via $^3\mathrm{P}_0 \rightarrow {}^3S_1$ and $^3\mathrm{P}_2 \rightarrow {}^3S_1$ transitions. To examine how the photoionization of $^1\mathrm{P}_1$ and $^3\mathrm{S}_1$ affects the clock operation, we first measured the photoionization cross sections of the two states. To determine the $\sigma_{^3\mathrm{S}_1}$ and $\sigma_{^1\mathrm{P}_1}$ cross sections, two separate experimental methods were used. To measure $\sigma_{^1\mathrm{P}_1}$ cross section, we compared the dynamics of loading of atoms into blue magneto-optical trap with and without the presence of ionizing blue-detuned magic wavelength light. On the other hand, to measure the $\sigma_{^3\mathrm{S}_1}$ cross section, we examine the change in ground and excited clock state populations during a standard clock cycle by introducing blue-detuned magic wavelength ionizing light during the repumping in the detection phase of the clock cycle[1].

### 3.2.1 Photoionization of $^1\mathrm{P}_1$

To determine the photionization loss rate from blue magic wavelength ionizing light, we examine the loading rates of atoms into the blue MOT with and without the ionizing blue-detuned magic wavelength light. In general, the rate equation for number of atoms loaded into a magneto-optical trap is given by the following equation [92]

$$\frac{dN_{Sr}}{dt} = L_{Sr} - (\gamma_{Sr} + \gamma_p)N_{Sr} - \beta_{Sr-Sr}\int dr^3 n_{Sr}^2, \tag{3.9}$$

where $L_{Sr}$ is the loading rate of atoms into the blue MOT, $\gamma_p$ and $\gamma_{Sr}$ are the loss rate from photionization and loss rates from all other channels such as collisions with background gases and optical pumping to

[1] I should point out that I was not directly involved in this part of the experiment as the measurements of $\sigma_{^3\mathrm{S}_1}$ and $\sigma_{^1\mathrm{P}_1}$ cross sections were performed prior to my arrival at KL FAMO, primarily by Marcin Witkowski and Vijay Singh. My contribution was in calculating the loss rates from the two channels, where I also used my results from the previous section regarding Wannier-Stark states of atoms in blue magic wavelength optical lattice.

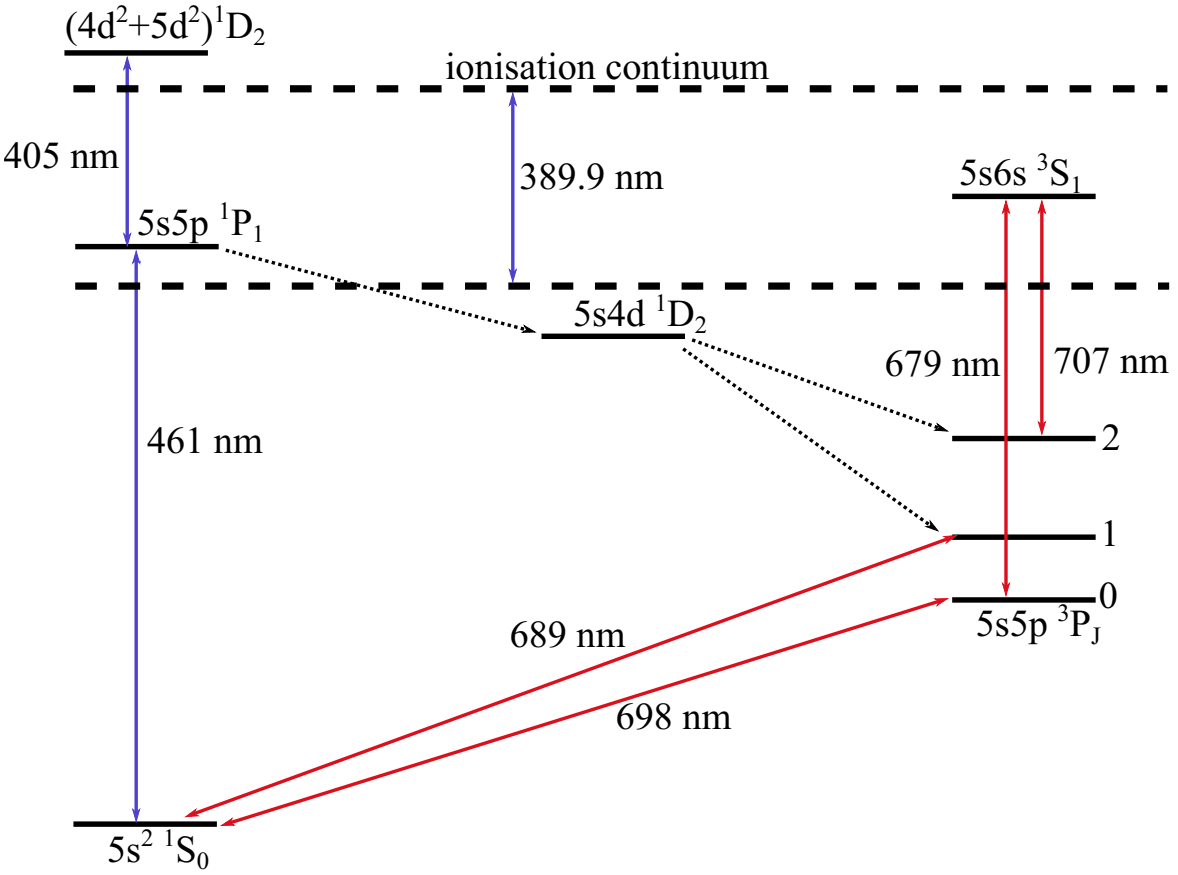


Figure 3.7: Schematic energy level diagram showing relevant optical transitions used in the basic cycle of a strontium optical lattice clock. The 405 nm wavelength corresponds to the autoionization resonance $(4d^2 + 5p^2)\ ^1D_2$. The states belonging to the area bounded by the dashed lines are potentially affected by the photionization light at 389.9 nm. Adapted from [66].

the metastable states, respectively, $\beta_{Sr-Sr}$ is the loss rate from light-assisted collisions between Sr atoms and $n_{Sr}$ is the spatial density of trapped atoms. Our experiment was run in the so-called low density regime. In this regime, the mean free path of an atom is much larger than the size of atomic cloud. Blue MOT cloud usually has a diameter of about 2 mm in diameter with around $10^8$ atoms giving a density of about $10^{11}$ cm$^{-1}$. With a collision cross-section of $10^{-13}$ cm$^{-1}$ [93], the mean free path of atom is about 100 cm which is much larger than the size of the atomic cloud. This allows us to ignore the last term in Eq. 3.9. Integrating Eq. 3.9 over time gives us the dependence of number of atoms on time of MOT loading as

$$N_{Sr}(t) = \frac{L_{Sr}}{\gamma_{Sr} + \gamma_p}(1 - e^{(\gamma_{Sr}+\gamma_p)t}). \tag{3.10}$$

Loss rate from photoionization $\gamma_\mathrm{p}$ is connected to the intensity of ionizing light $I_p$ as

$$\gamma_p = \rho_{^1P_1}\sigma_{^1P_1}\frac{I_p}{h\nu_p}, \tag{3.11}$$

where $\rho_{^1P_1}$ is the fraction of atoms in the excited $^1\mathrm{P}_1$ state and $h\nu_p$ is the photon energy of ionizing light. Before we can calculate the loss rate of $^1\mathrm{P}_1$, we still need to measure the photoionization cross section. We sequentially load two blue MOTs, one in the presence of ionizing light and one without, and record their loading curves. The sequence is shown Fig. 3.8 and the loading rates are given in Fig. 3.9. By fitting Eq. 3.10 to both loading rate curves, we found the $\gamma_{\mathrm{Sr}} + \gamma_{\mathrm{p}}$ and $\gamma_{\mathrm{Sr}}$ loss rates at which point finding the photoionization loss rate was easily calculated as their difference. The loss rates were $\gamma_{\mathrm{Sr}} = 34.08(80)\ \mathrm{s}^{-1}$ and $\gamma_{\mathrm{Sr}} + \gamma_{\mathrm{p}} = 37.9(1.5)\ \mathrm{s}^{-1}$ which corresponds to the reduction of the 1/e MOT loading time from 29.34(69) ms to 26.38(10) ms. To determine the fraction of atoms in the excited

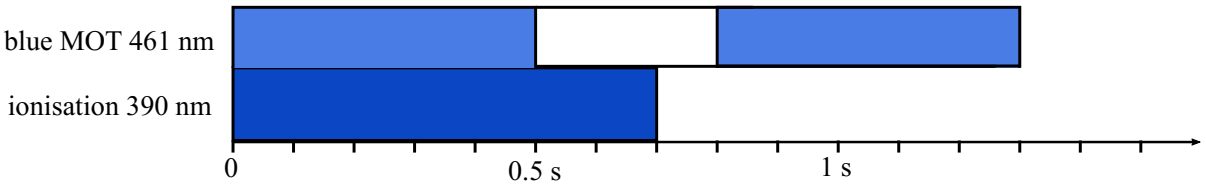


Figure 3.8: The timing sequence of the lasers used in the $^1\mathrm{P}_1$ photoionization experiment. The time of the blue MOT's loading phase is identical in each sequence. To record the background from the ionisation laser beam, it was kept on for a 200 ms longer compared to MOT's loading phase duration

$^1\mathrm{P}_1$ state, a two-state system approximation model was used

$$\rho_{^1P_1} = \frac{1}{2}\frac{\frac{I_{461}}{I_{sat}}}{\frac{I_{461}}{I_{sat}} + 4(\frac{\Delta}{\Gamma})^2 + 1}, \tag{3.12}$$

where $I_{461}$ is the total intensity from blue MOT cooling beams, $\Delta$ is laser detuning from the transition, and $I_{sat}$ and $\Gamma = 2\pi \cdot 32$ MHz are the saturation intensity and linewidth of $^1\mathrm{S}_0 \rightarrow {}^1P_1$ transition, respectively. To calculate $\rho_{^1\mathrm{P}_1}$, we assumed typical conditions in blue MOT with total intensity of blue MOT light as $I_{461} = 6 \text{ x } 30\ \mathrm{mW/cm^2}$ coming from 6 different beams, all detuned by $\Delta = 1.5\ \Gamma$. From this, Eq. 3.12 gives the fraction of atoms in the excited state to be $\rho_{^1\mathrm{P}_1} = 0.027$.
At this point we are ready to find the cross section for $^1\mathrm{P}_1$ state. To do that, we use a CCD camera to take pictures of blue MOT during interaction with ionizing light and detect the atomic distribution which is well described with a Gaussian distribution

$$N(x,y) = \frac{2N_0}{\pi r_x r_y} e^{\frac{-2x^2}{r_x^2}} e^{\frac{-2y^2}{r_y^2}}, \tag{3.13}$$

where $r_x, r_y$ are radii of blue MOT, usually around 1.2 mm. From this we can find the average intensity of ionizing beam light $\langle I_P \rangle$ seen by the atoms in blue MOT

$$\langle I_p \rangle = \int\int \frac{I(x,y)N(x,y)}{N_0} dxdy, \tag{3.14}$$

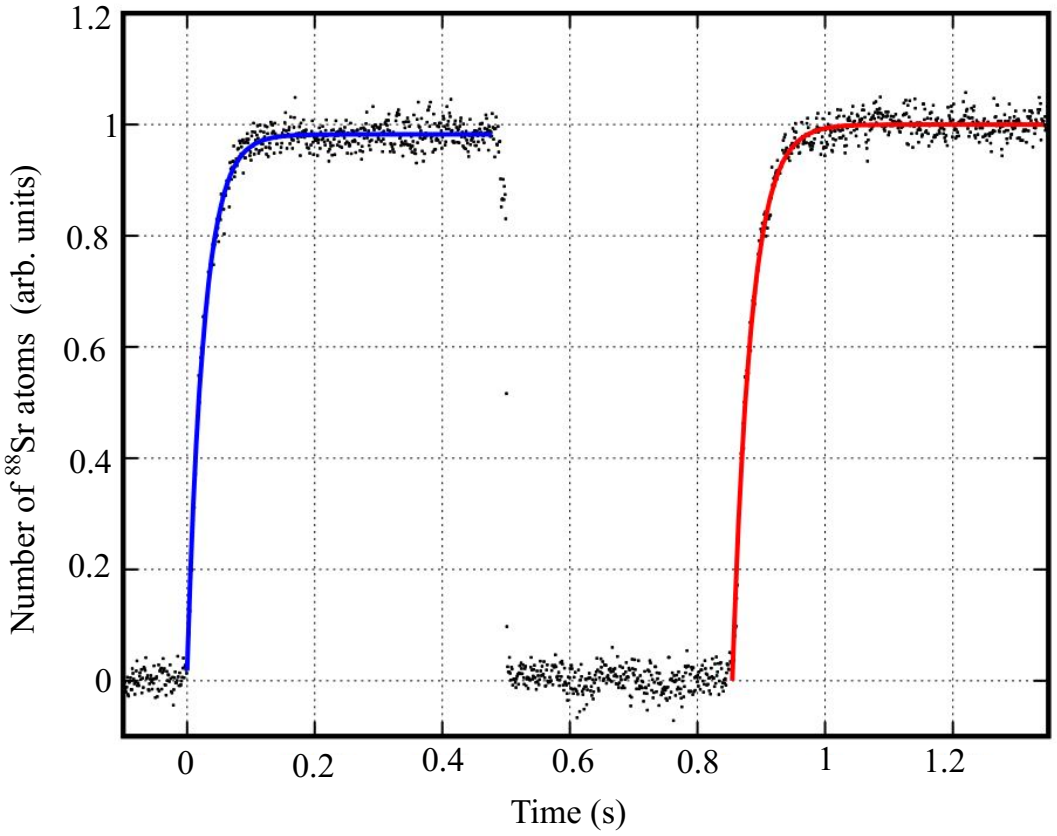


Figure 3.9: Typical fluorescence of $^{88}$Sr atoms detected while loading into the blue MOT in the presence (left) and in the absence (right) of the photoionizing 389.889 nm light. The solid blue and red lines depict fitted Eq. 3.10. Adapted from [66].

where $N_0$ is the total number of atoms in blue MOT and $I(x, y)$ and $N(x, y)$ are the distributions of intensity of ionizing light and atoms in blue MOT, respectively. Distribution of intensity of ionizing light was found by taking a picture of incoming beam with CCD camera.

We now have all the parameters needed to measure the photoionization cross section for $^1\mathrm{P}_1$ state. The results are shown in Fig. 3.10. To be sure in our method of measuring the photoionization cross section, we measure the photoionization cross section in the range from 378 nm to above 405 nm. In this range exists an autoionization resonance of $(4\mathrm{d}^2 + 5\mathrm{p}^2)\ ^1\mathrm{D}_2$ at around 405 nm. These types of asymmetric resonances appear due to interference between the background and resonant scattering process and are called Fano resonances [94].

By fitting a Fano profile to the data in Fig. 3.10, we have determined that the resonance is centered at $\lambda_\mathrm{r} = 405.196(44)\ \mathrm{nm}$ with peak value of $\sigma_\mathrm{r} = 5.20(94) \cdot 10^{-19}\ \mathrm{m}^2$. These results were consistent those previously reported [95, 96], but with our work being on cold atomic samples. Of course, our

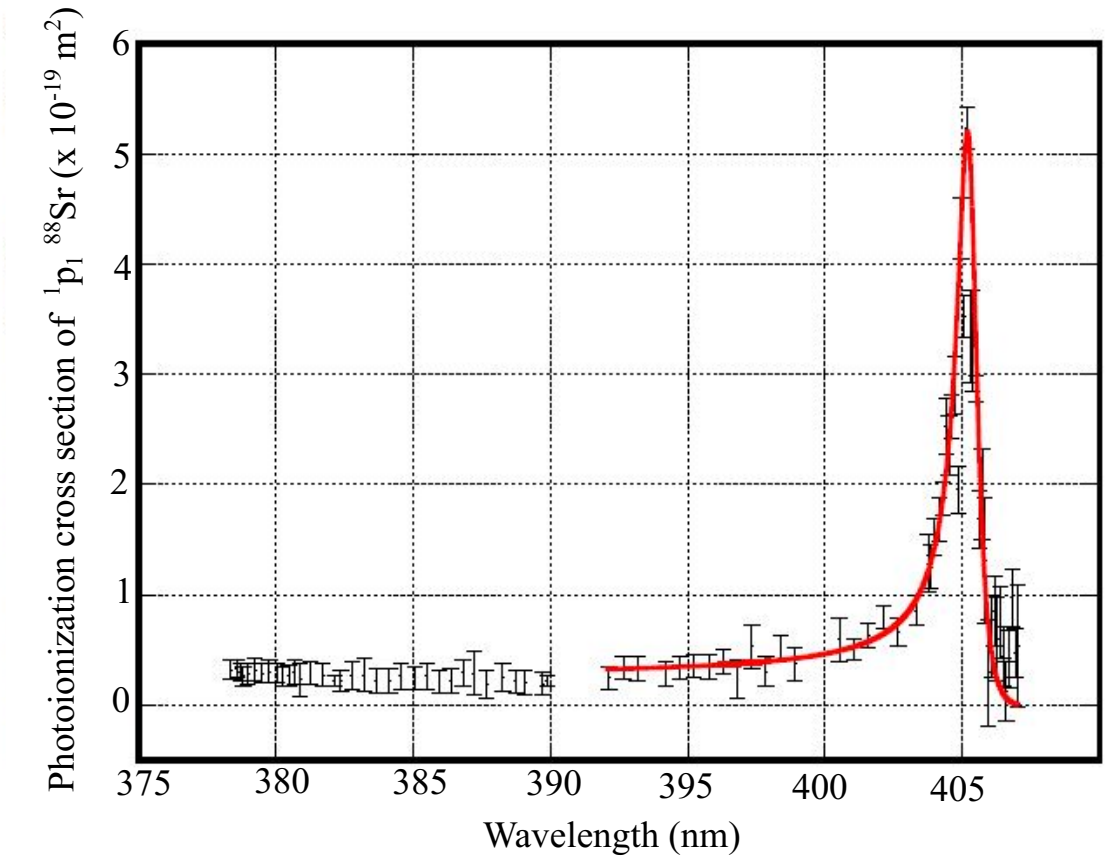


Figure 3.10: The photoionization cross section from the $^1\mathrm{P}_1$ state as a function of the wavelength of the ionizing light. The solid red line is a Fano profile fitted to the measured data. The fitting range is limited to the experimental points above 392 nm to exclude another possible resonance below 389.9 nm.

interest lies in examining the photoionization losses from blue magic wavelength light at 389.9 nm. From Fig. 3.10 we can simply ready the photoionization cross section and find it to be $2.20(50) \cdot 10^{-20}$ m$^2$. Our result is consistent with the value of $1.46(29) \cdot 10^{-20}$ m$^2$ deduced from the curve reported by Mende et al. [95] within the 20% uncertainty claimed by the author. At this point we are ready to calculate the photoionization loss rates due to blue magic wavelength light.

This is also the point where my contribution in the photoionization part of the article [66] begins as I was tasked with calculating the loss rate. Firstly, we need to remember than in the optical clock cycle the ionisation from blue magic wavelength light doesn't come from a single non-retroreflected beam but an optical lattice. We therefore must first calculate the average intensity of light in a blue-detuned optical lattice.

In my calculations I assumed we have 3 separate 1D blue-detuned optical lattices, all with the lattice depths of 20 $E_r$ (for which we have showed we have good trapping in the blue-detuned lattice). For

purposes of simplicity, I also assumed no radial dependence on intensity, focusing only on the axial direction. By averaging light intensity from this 3D optical lattice (averaged over time and space), we get an average light intensity experienced by atoms in the periodic potential of optical lattices to be $I_p^{3D} \approx 2.1 \cdot 10^8$ W/m$^2$. From Eq. 3.11 we get a loss rate of $\gamma_{^1P_1} \approx 2.4 \cdot 10^5$ s$^{-1}$.
Let us compare this photoionization loss rate with other loss channels. Assuming that blue MOT lifetime is limited by the collisions with the residual background gas molecules, the order of magnitude of the loss rate $\gamma_{Sr}$ in Eq. 3.10 in a real experimental system can be approximated by the collisional loss rate due to the collisions with $H_2$ molecules [97], which gives collisional loss rate of $\gamma_{Sr} \approx 0.4$ s$^{-1}$. Another loss channel appears due to atoms' decay into the metastable $^3P_2$ state when there are not repumpers during blue MOT loading. This loss rate is around $\gamma_{Sr} \approx 35$ s$^{-1}$[66].
We can clearly see that the photoionization loss rate from blue magic wavelength light is few orders of magnitude larger than any other loss channel. From Eq. 3.10, we see that $\gamma_p$ will lower the number of atoms by a factor of $10^5$, effectively depleting the blue MOT in the region where it overlaps with the optical lattice.
Luckily for us, the solution in this case is quite simple - one can simply reduce the lattice intensity or even turn off the lattice completely during the blue MOT phase. Temporary switching off lattice light is technically feasible, even with the power build-up cavity installed inside the vacuum setup on a low expansion glass spacer. The lattice laser can be safely switched back on and relocked during the red MOT phase, which lasts a few tens of ms. Since the red MOT phase states $^1S_0$ and $^3P_1$ are below the photoionization threshold of blue magic wavelength light, there will be no photionization of atoms by the lattice from those states.

### 3.2.2 Photionization of $^3S_1$

As mentioned above, to measure the photionization cross section of $^3S_1$ state, we used a different approach compared to the one for $^1P_1$. We measure the photionization cross section of $^3S_1$ during the detection phase of a standard optical clock cycle. The timing sequence of the laser beams used in the experiment is shown in Fig. 3.11. The sequence consists of two separate clock cycles with the first cycle having the photionization light from blue magic beam turned on during repumping in the detection phase, and the second cycle providing the background.
The cycle is designed as follows: After the atoms are cooled in the blue and red MOT phase, they are cold enough (around 1 $\mu$K) to be loaded into an optical lattice. Once loaded, they are probed by an interrogation laser pulse, long in duration compared to the Rabi oscillation frequency.
This interrogation, applied exactly at the clock transition frequency, splits the atomic population sending half of the atoms into the excited $^3P_0$ clock state while leaving the other half in the ground $^1S_0$ state. At this point, we use the 461 nm imaging probe beam to excite the atoms in the ground state to $^1P_1$ and measure their flourescence with the CCD camera. Subsequently, atoms in the $^3P_0$ are tranferred to $^1S_0$ by repumping them through $^3S_1$ using 707 nm and 679 nm laser light. After another imaging pulse at

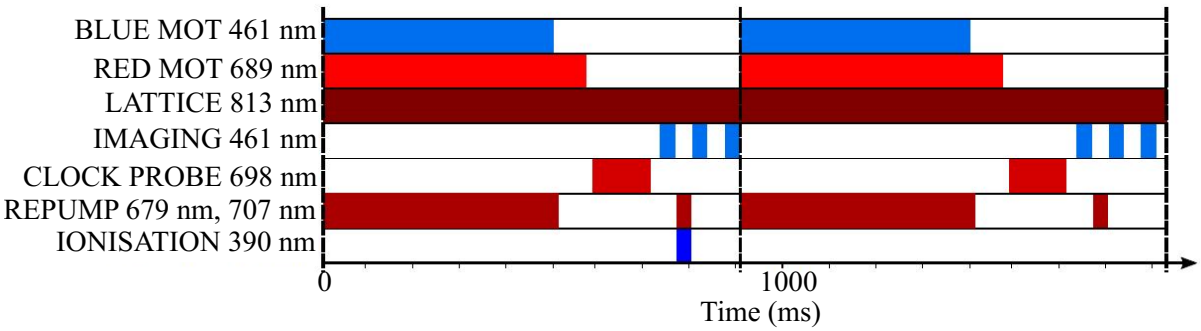


Figure 3.11: The timing sequence of the lasers used in the $^3S_1$ photionization experiment. It consists of two clock cycles, the first one (left) with added photoionizing pulse, the second one (right) providing a background. Adapted from [66].

461 nm, we again measure the flourescence of atoms with a CCD camera. This concludes the standard clock cycle as depicted on left part of Fig. 3.11. The measured flourescences are used to calculate the initial ratio of populations of the ground and excited clock state.

The crucial difference in our experiment here is adding the blue magic wavelength ionizing beam during repumping in detection phase. By adding this ionizing beam we allow the atoms to be photoionized while in $^3S_1$ state. This will be seen as a change in the population ratio of ground and excited clock state as the photionization would've removed a portion of atoms in the excited clock state from the optical lattice. To determine the photionization cross section of $^3S_1$ state we use the following equation

$$\sigma_{^3S_1} = \frac{\Delta N_e}{N_e} \frac{h\nu_p}{\langle I_P \rangle t_{eff}}, \tag{3.15}$$

where $\Delta N_e = N_e - N_e^I$ is the difference between number of atoms which are succesfully repumped from excited to the ground clock state with and without the presence of the ionizing beam, labeled as $N_e^I$ and $N_e$, respectively. $\langle I_P \rangle$ is average intensity of the photoionizing beam and $t_{eff}$ is the effective interaction time of the atoms in the $^3S_1$ state and the photoionization beam. From the transition probabilities of $^3S_1 \rightarrow {}^3P_2$ and $^3S_1 \rightarrow {}^3P_0$ [98] and natural lifetime of $^3S_1$ [99, 74] this interaction time was calculated to be $t_{eff} = 43$ ns. To ensure stability of the number of atoms throughout each experimental cycle, we monitored both ground state populations with and without the presence of the photoionization beam ($N_g^I$ and $N_g$, respectively). Any experimental point for which the difference between $N_g^I$ and $N_g$ was larger than $2\%$ was excluded from the measurement. Also, for our results be less prone to the oscillations of the number of atoms, we made the interleaved measurements randomly staggered by manual triggering of the consecutive cycles. With an ionizing beam intensity of $\langle I_P \rangle = 26270(80)$ W/m$^2$, we find the $\sigma_{^3S_1}$ photoionization cross section to be equal to $\sigma_{^3S_1} = 1.38(66) \cdot 10^{-18}$ m$^2$.

To calculate the loss rate from photionization rate from $^3S_1$, I used a similar procedure as for $^1P_1$ in previous subsection. I first calculate the intensity of blue-detuned magic wavelength light experienced

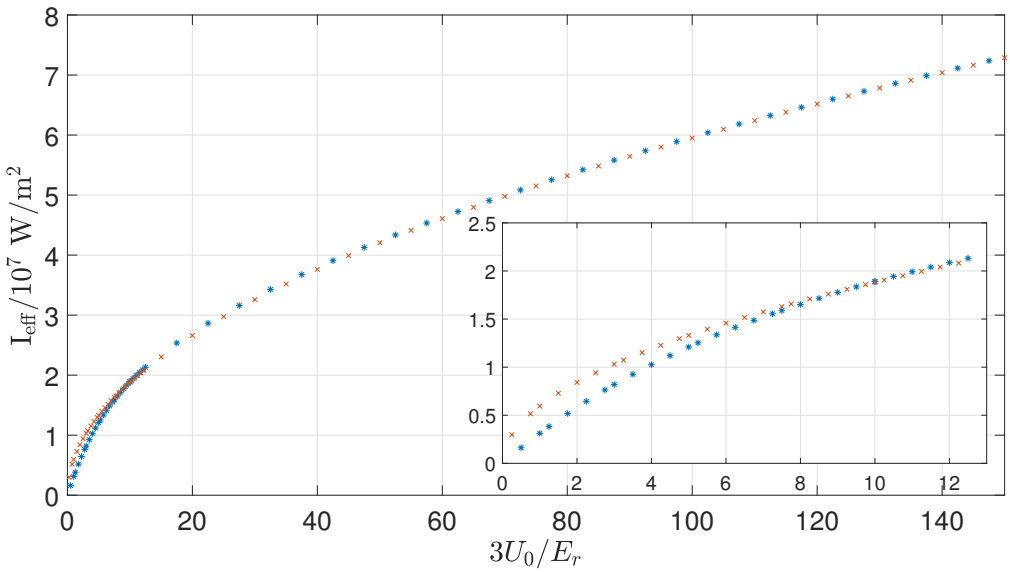


Figure 3.12: The total effective intensity $I_{eff}$ experienced by the atoms trapped in the motional ground state of a 3D blue-detuned magic wavelength optical lattice. $I_{\text{eff}}$ values were calculated for Wannier-Stark (Wannier) states for the vertical (horizontal) directions in the optical lattice (blue asterisks) and Gaussian states (orange crosses) in a harmonic potential approximation.

by the atoms in the optical lattice and then use Eq. 3.11 to find the correct loss rate. However, since in this case we have atoms in the optical lattice, I won't be calculating the average intensity like I did for $^1\text{P}_1$. Instead, I define an effective intensity $I_{\text{eff},\xi}$ which the atoms experience in the 3D optical lattice potential

$$I_{eff,\xi} = \int |\Psi_M(\xi)|^2 I(\xi) d\xi \; with \; \xi = x, y, z, \tag{3.16}$$

where $\Psi_M(\xi)$ are the Wannier (Wannier-Stark) eigenfunctions of atoms in a horizontal (vertical) optical lattice potential $I(\xi) = I_0 sin^2(k_\xi \xi)$ where $k_\xi$ is the wavevector of blue-detuned magic wavelength light and $I_0$ is the maximum intensity of light in each of 1D traps in $\xi$ direction. The total effective intensity from 3 1D optical lattices is then given by $I_{eff} = \sum_\xi I_{eff,\xi}$. Its dependence on the depth of the optical lattice is shown in Fig. 3.12 where $3U_0$ is the total amplitude of the all 3 1D lattice potentials. The blue asterisks in Fig. 3.12 represent the total effective intensity calculated for Wannier-Stark (Wannier states) for vertical (horizontal) optical lattice and the orange crosses respresent the Gaussian states in harmonic potential approximation. If we now again consider 3 independent 1D optical lattices, each with lattice depth of 20 $E_r$, this gives us effective intensity of $I_{eff} \approx 4.6 \cdot 10^7$ W/m$^2$ for total lattice depth of $U_{3D} = 3 \text{ x } 20 \; E_r = 60 \; E_r$. From Eq. 3.11 we then get the loss photionization loss rate for $^3\text{S}_1$ state to be equal to $\sigma_{^3\text{S}_1} = 1.26 \cdot 10^8$ s$^{-1}$ which is on the same order as the $^3\text{S}_1$ state decay rate due to the natural lifetime. Such large loss would effectively remove all atoms from the optical lattice during repumping in the detection phase of the optical clock cycle, making it a critical defect in using

blue-detuned optical lattices in optical clocks. A possible solution to this problem is using alternative repumping scheme through the $^3\mathrm{D}_\mathrm{J}$ state [100, 101] which are below the single-photon photoionization threshold of blue-detuned optical lattice.

# Chapter 4

# Strontium optical clock experiment in KL FAMO

The National Laboratory of Atomic, Molecular and Optical Physics (KL FAMO) in Toruń, Poland, houses two separate bosonic optical clocks, which we'll refer to as Strontium 1 (Sr 1) and Strontium 2 (Sr 2). This section will cover the redesign and upgrading done on Sr 1 clock during my stay in Toruń. The goal of the redesign was to allow for both bosonic and fermionic clock operation in Sr 1. Prior to its upgrade the optical clock was capable of only bosonic clock operation.
I feel obliged to point out that bosonic optical clock was constructed and was fully operational long before my arrival to KL FAMO. However, I have decided to put the entirety of the setup, even those parts constructed without my contributions, into this thesis to provide the full picture of our experiment. In the following sections I will, of course, do my best do differentiate between my own work and work of other members of the group, as well as state which portions of the setup were completed prior to my arrival to KL FAMO.

## 4.1 High-finesse optical cavities for 689 nm and 698 nm lasers

The key component of any optical clock setup is its high-finesse optical cavity which is used to spectrally narrow the ultra-stable lasers while also serving as a short term frequency reference. In our case, we have two such optical cavity setups, one for the 689 nm red MOT trapping laser and the other for the 698 nm clock laser. The optical cavity setups are similar in design. Both cavities are made from 100 mm long ultra-low expansion (ULE) glass with optically contacted silica mirrors and with free spectral range of 1.5 GHz. The key difference between the two cavities is the finesse of the optical cavity, which is equal to $F$=62800 for the 689 nm red MOT laser and $F$=300000 for 698 nm clock laser [28]. For the 698 nm clock laser, this provides a laser spectral linewidth below 1 Hz, which is necessary for the probing of the clock

transition. The linewidth is achieved by using a Pound-Drever-Hall (PDH) locking scheme[1]. The setup for one of the cavities is shown in Fig. 4.1[2]. The high-Q cavity is located inside a thermally-stabilized

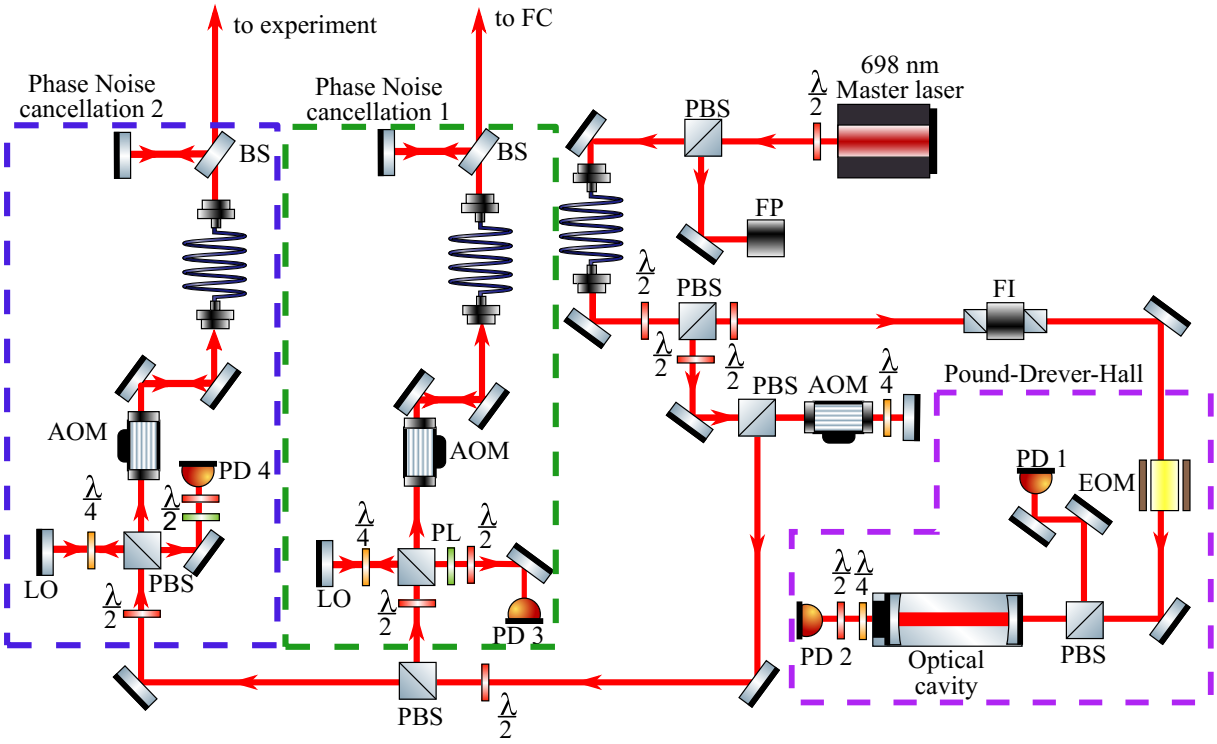


Figure 4.1: The high-finesse optical clock cavity setup for the 698 nm clock laser. A setup consisting of 698 nm clock master laser coupled into a high-finnesse optical cavity and frequency-locked via PDH method is presented. Additionally, two fiber noise-cancellation setups are shown. Abbreviations used in figure: FP-Fabry interferometer, FC- frequency comb, PBS- polarizing beam splitter, NC- noise cancellation, EOM- electro-optic modulator, AOM- accusto-optic modulator, $\frac{\lambda}{2}$- half-wave plate, $\frac{\lambda}{4}$- quarter-wave plate.

vacuum chamber which is installed on an optical breadboard. The remainder of the setup from Fig. 4.1 (aside from the laser itself) is installed on the same optical breadboard. A fraction of the light from the 698 nm laser is coupled into the high-finesse cavity and stabilized to the cavity via Pound-Drever-Hall (PDH) locking scheme [102]. The rest of the light is sent through 2 separate acousto-optic modulators (AOM) and coupled into two optical fibers. Light from one of the fibers is sent to a separate room where our frequency comb (FC) is located. There, the light from the 698 nm is used to create a beatnote signal with the frequency stabilized frequency comb. This beatnote[3] is used for monitoring and control of the laser frequency for optical clock operation. The beam from the second fiber is sent directly to the experi-

[1]Described in more detail in one of the following sections.

[2]This setup was designed and constructed prior to my arrival at KL FAMO, but I took part in upgrading it during my stay.

[3]Part of my work in upgrading of the optical clock setup.

mental setups in Sr 1 and Sr 2 where it is injected into their respective slave lasers. Additionally for each optical fibers, a phase-noise cancellation setup had been constructed which suppresses the perturbation the optical phase of the light during transfer of light through the fiber and limits the spectral broadening of light[4].

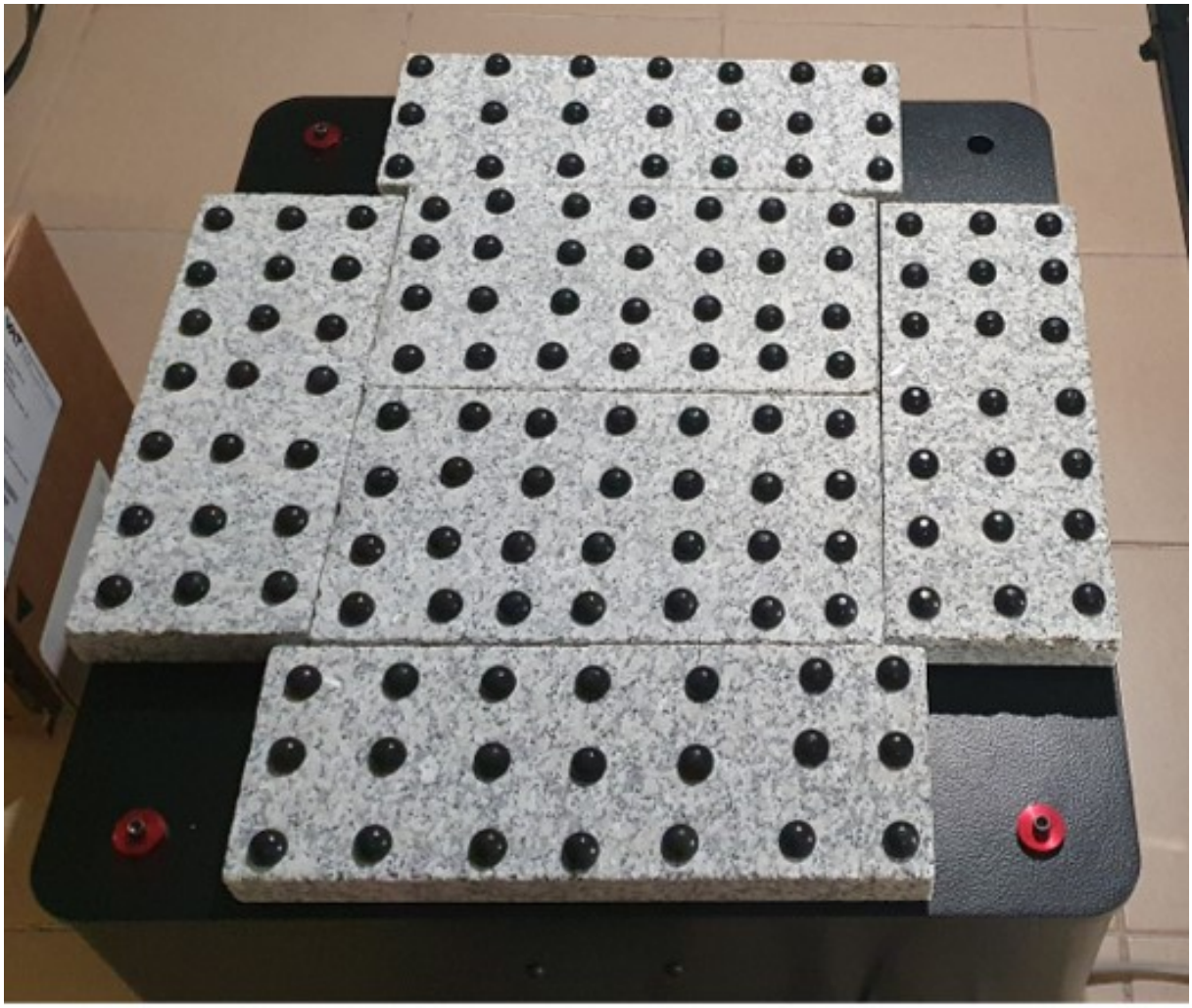

Figure 4.2: Installation of granite plates onto the anti-vibrational platform to reduce the overall load on the platform. Multiple dia-sorbothane hemisphere rubber bumpers were installed on both sides of the granite plates to ensure proper weight distribution across the entire platform.

The optical breadboard with the cavity is mounted on an anti-vibration isolation platform. A set of 6 lead plates were placed in between the breadboard and the antivibration platform to provide additional suppression of vibrations and to ensure the total weight of the setup is within the operating range of the anti-vibration platform. This entire setup was placed into an acoustic isolation chamber, thus ensuring

[4]For more details, see chapter 4.7.1.

thermal, vibrational and acoustic isolation of the high-finesse cavity from external perturbations. Regardless, during clock operation, the short- and mid-term stability (1 second to 10 second scale) of the optical clock was limited. We found that these issues arose at least partly due to the vibrations of the optical cavity. These vibrations were caused by a flaw during initial design of the cavity setup where the lead plates placed between the breadboard and the platform were effectively too heavy, pushing the total weight of the setup beyond the operational range of the anti-vibrational platform. This prevented "floating" of the anti-vibrational platform. To fix this issue, I replaced the lead plates with lighter granite plates[5], shown in Fig. 4.2. Additionally, we placed a large number of 0.75" diameter Dia-Sorbothane Hemisphere Rubber Bumpers on both sides of the granite plates to ensure proper weight distribution across the entire platform. With these improvements completed the anti-vibration platform was reinstalled into the acoustic chamber and the optical breadboard was lowered onto it. I then successfully "floated" the anti-vibration platform.

## 4.2 Vacuum setup

The schematic for the vacuum setup is shown in Fig. 4.3[6]. The setup consists of a strontium oven, a Zeeman slower with mu-metal magnetic shielding and the main vacuum chamber. The strontium oven and Zeeman slower are separated by a valve. The valve is closed if the experiment isn't operating to prevent unnecessary accumulation of strontium atoms on the windows of the vacuum chamber. The oven is made up of two connected full nipple flange fittings. On one side the nipples are closed off by a flange and the other side connected to the Zeeman slower and vacuum chamber. The two nipples are connected by copper nickel-plated gaskets. The nipple further from the chamber is used as a depository of 99.99% pure dendritic strontium.

Due to low vapor pressure of strontium at room temperature, the strontium inside the oven must be heated up to high temperature, usually in the range of 400-700 $^{o}$C. For this purpose, a heating wire is densely wound around the outer surface of the two nipples and wire ends connected to a high voltage power supply. Driving the current through the wire heats up the wire and the heat is then contact transferred to the nipples, increasing the temperature inside the nipples. Additionally, multiple temperature sensors are placed on different points along the nipple surface for monitoring and control of oven temperature. To achieve sufficiently high temperatures, the oven is thermally isolated from the environment.

The other nipple is used for creating an atomic beam of strontium atoms. Inside the nipple, a custom-made U-shape holder is placed. Dozens of stainless steel capillaries are placed and tightly packed on the inner surface of the U-shaped holder. The capillaries are 0.8 cm long with external and internal diameters of 0.03 cm and 0.02 cm, respectively. The capillaries are mutually collimated to a high degree. In this way, the capillaries serve as a collimator of the atomic beam. At their output, the capillaries collimate

[5] With assistance from other members of the POZA team

[6] Vacuum was constructed by Marcin Bober and other members of the POZA team long before my arrival to KL FAMO.

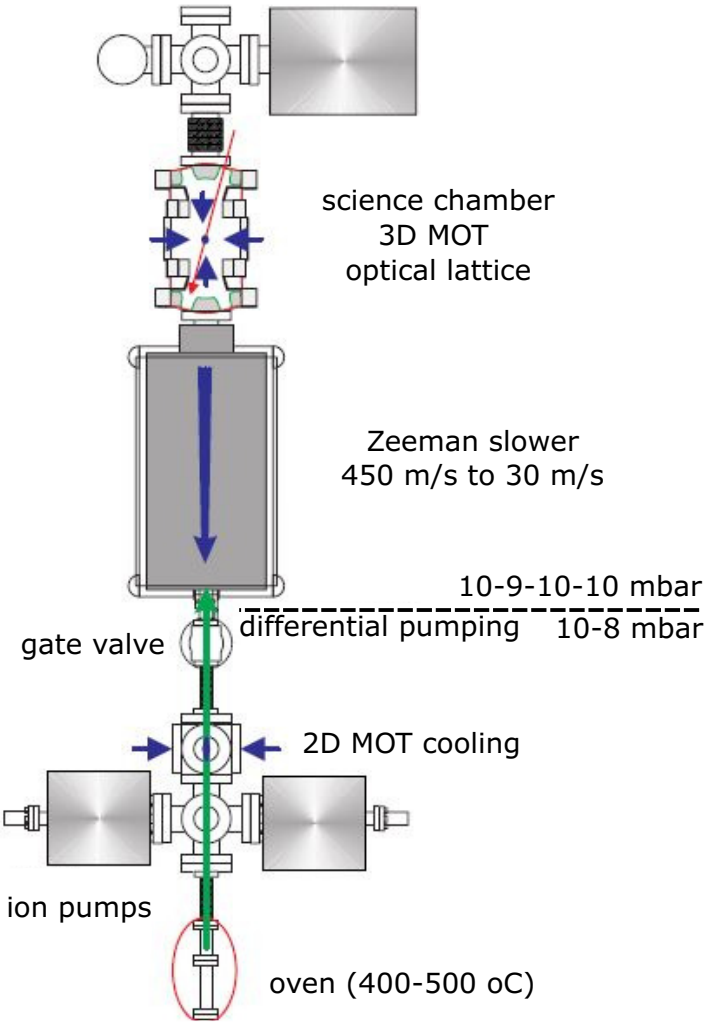


Figure 4.3: Schematic of the ultrahigh vacuum setup in KL FAMO. The setup consists of an oven, a Zeeman slower with mu-metal magnetic shielding and vacuum chamber. Blue and red arrows indicate laser beams, green arrow is the atomic beam. Taken from [28].

the atomic beam into the Zeeman slower, with flux of $10^{13}$ $\mathrm{s}^{-1}$ and beam divergence of about 25 mrad [103].

To ensure good vacuum in this section of the setup, a cross element is installed between the oven and the valve. On each side of the cross profile, and ion pump is installed, as shown in Fig. 4.3. This ensures vacuum of about $10^{-8}$ $\mathrm{mbar}$ is this part of the setup when the oven is turned on.

## 4.3 The Zeeman slower

Due to high temperature in the oven, the atoms in the atomic beam upon exiting the capillaries have a mean velocity of about $500\,\mathrm{m/s}$ producing a large Doppler shift. Therefore, any laser beam trying to slow the atoms down will need to be strongly red-detuned. In our experiment, this detuning is about $\frac{\Delta}{2\pi} = -500\,\mathrm{MHz}$ from the blue MOT transition. Additionally, such high velocity is beyond the capture velocity limit, meaning that the 3D MOT beams are incapable of cooling them down sufficiently quickly for the atoms to be trapped inside the MOT. Therefore, atoms have to be slowed down prior to their trapping. For this purpose we use the Zeeman effect inside the Zeeman slower.

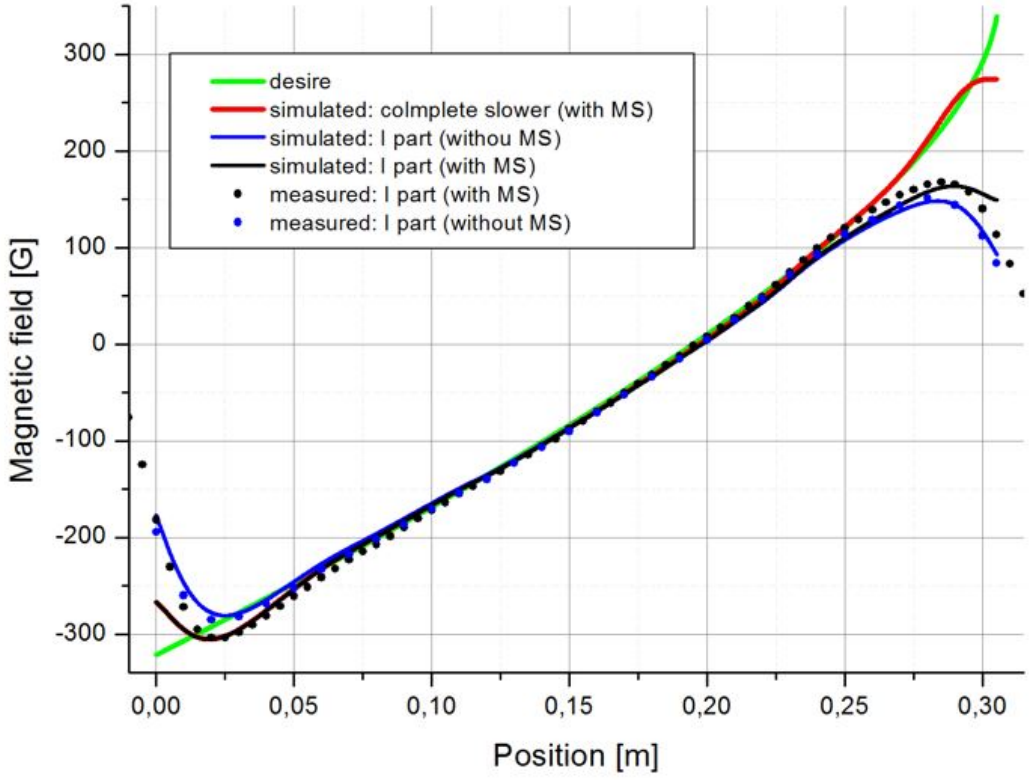


Figure 4.4: Magnetic field created by the Zeeman coils and simulated fields with and without the magnetic shielding. Two sets of coils are wound in the Zeeman slower with 3 A and 9-14 A currents running through them, respectively. Taken from [103].

The general idea behind the Zeeman slower is simple - a laser beam is red-detuned from the ${}^1\mathrm{S}_0 \rightarrow {}^1\mathrm{P}_1$ transition and counter-propagated to the atomic beam through the Zeeman slower. We then create magnetic field B(z) with a linear gradient *b'* along the path of the atomic beam, where z is direction of propagation of the atomic and laser beam. In such conditions, the laser beam will, at some position z, be detuned by $\delta^{'} = \delta + \mathrm{k}\cdot\mathrm{v} - \mathrm{b}'\mathrm{z}$ where $\mathrm{k}\cdot\mathrm{v}$ and *b'*z are Doppler and Zeeman shift, respectively. With

appropriate choice of gradient *b'*, the Zeeman shift *b'*z will be able to cancel out the Doppler shift at each point of the slower. In other words, as the atom slows down, the laser is moved out of resonance with the atomic transition due to the Doppler shift. By using the magnetic gradient, we compensate for this Doppler shift. This will ensure that the laser can continuously slow down atoms in the atomic beam. In this way, atoms in the atomic beam with velocities of few hundred meters per second will be slowed down to only few meters per second and can then be captured by the blue MOT beams in the main vacuum chamber. The magnetic field along different points of the Zeeman slower is shown in Fig. 4.4 [103]. The schematic for the Zeeman slower is shown in Fig. 4.5 [103]. The slower is a 30.5 cm long, water-cooled solenoid with a 3 A current going through the coil, producing a magnetic field with a range of 600 Gauss (from -300 G to 300 G). This field range allows slowing down of about 35-40% of the initial flux with initial velocity as high as 450 m/s. By the time the atomic beam reaches the main vacuum chambers, atoms are slowed down to about 31 m/s and can be loaded into the blue MOT. Obviously, the use of such

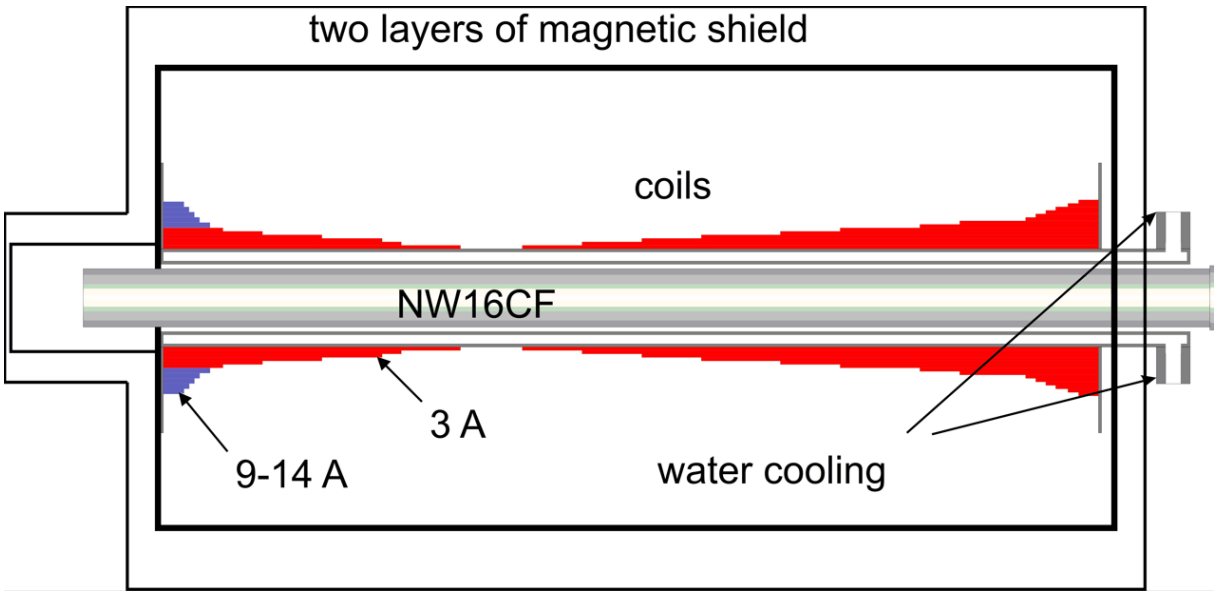


Figure 4.5: Schematic design of the Zeeman slower. Coil length is 30.5 cm with inner diameter of 32 mm. Taken from [103].

high magnetic field would have a negative impact on clock operation as we wish for our atoms to be free of any perturbation by electric or magnetic field while clock is in operation. For this purpose a special two-layer magnetic shield made from pure iron and mu-metal layer was designed. This shield prevents the magnetic field of the coils of the Zeeman slower from penetrating to the chamber where the cooling and trapping of strontium in the blue MOT is performed, while also allowing for a higher field gradient to be created at the end of the slower. More details on design of the Zeeman slower is available in [103]. The vacuum chamber is a stainless steel Kimball-Physics extended spherical octagon with windows with anti-reflection coating. The MOT gradient field is produced by two solenoids in anti-Helmholtz configuration in custom-made holders which are installed along the main axis of the chamber. The solenoids

are water-cooled to protect the coils wire from damage. The solenoids produce a gradient field of about $60\ \mathrm{G/cm}$. Additionally, 3 sets of compensation coils in Helmholtz configuration are placed in 3 orthogonal directions (x,y,z) to compensate any stray magnetic field. Finally, during the upgrade to enable both bosonic and fermionic clock operation, we installed an additional set of magnetic coils. These coils are to be used during optical pumping in the fermionic clock operation cycle.

## 4.4 Blue MOT on $^1\mathrm{S}_0 \rightarrow {}^1\mathrm{P}_1$ transition

The relevant transition frequencies and laser detunings for the $^1\mathrm{S}_0 \rightarrow {}^1\mathrm{P}_1$ transition for $^{88}\mathrm{Sr}$ and $^{87}\mathrm{Sr}$ are given in Fig. 4.6 while the experimental setup is shown in Fig. 4.7. The transition frequencies of two

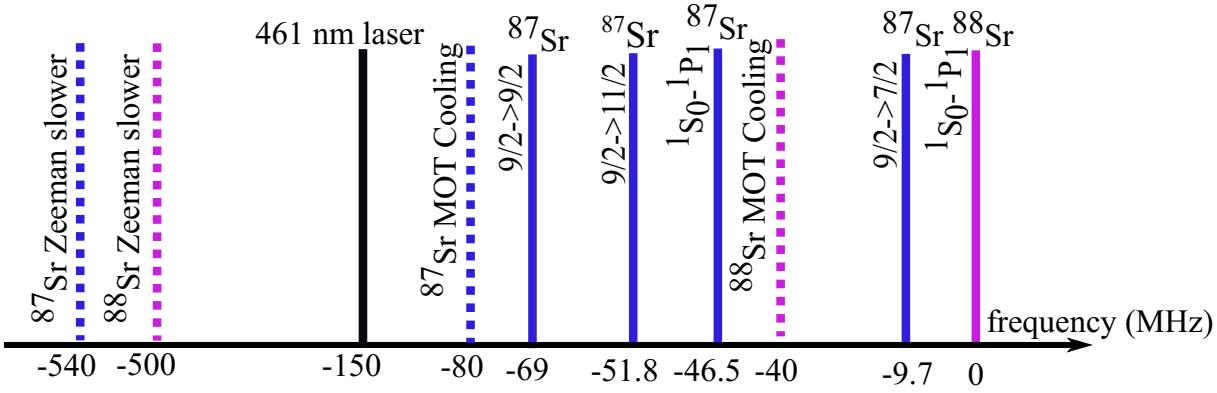


Figure 4.6: Relevant frequencies for $^{88}\mathrm{Sr}$ and $^{87}\mathrm{Sr}$ blue MOT operation. Frequencies of different laser beams and isotope shifts of different $^1\mathrm{S}_0 \rightarrow {}^1\mathrm{P}_1$ hyperfine transitions of $^{87}\mathrm{Sr}$ are all given relative to the $^1\mathrm{S}_0 \rightarrow {}^1\mathrm{P}_1$ transition of $^{88}\mathrm{Sr}$. The solid purple (blue) lines represent detunings of different bosonic (fermionic) blue MOT transition(s). The dashed purple (blue) lines represent detunings of 3D MOT and Zeeman slower beams needed for bosonic (fermionic) blue MOT operation. The black line is the detuning of the 461 nm laser.

isotopes are separated by 46.5 MHz [6] with a linewidth of the atomic transition of 32 MHz [103].
For blue MOT cooling we use a 922 nm Toptica TA-SHG 100 laser. A master laser diode at 922 nm is fed into a tapered amplifier which increases the light output to about 1.5 W of power. The light is then frequency doubled in a resonant doubling cavity in bow-tie arrangement producing around 400 mW of 461 nm light. The 461 nm master laser is then frequency locked to $^1\mathrm{S}_0 \rightarrow {}^1\mathrm{P}_1$ transition with a frequency-shifted saturation spectroscopy [104]. By placing AOM 1 in the path of the beam used for saturation spectroscopy, we effectively create a frequency shifter, allowing us to the change the frequency lock point of the 461 nm laser. Additionally, three seperate AOMs are used for the flourescence probe beam, Zeeman slower and 3D MOT cooling (AOMs 2, 3 and 4 in Fig. 4.7, respectively). Frequencies of AOMs used in Fig. 4.6 and detunings of corresponding beams from the bosonic $^1\mathrm{S}_0 \rightarrow {}^1\mathrm{P}_1$ transition are given in Table 4.1.

| AOM | AOM RF shift (MHz) | laser beam | beam $\delta$ $^{88}$Sr (MHz) | beam $\delta$ $^{87}$Sr (MHz) |
|---|---|---|---|---|
| 1 | 2 x -75 (-95) | saturation spectroscopy | -150 | -140 |
| 2 | 2 x -175 | Zeeman slower | -500 | -490 |
| 3 | 1 x 110 | 3D blue MOT | -40 | -30 |
| 4 | 2 x -75 | flourescence probe | 0 | 0 |

Table 4.1: AOM RF shifts of different AOMs from Fig. 4.7 and detunings $\delta$ from $^1S_0 \rightarrow {}^1P_1$ transition of different beams used in bosonic (fermionic) blue MOT stage. The detunings in 4th and 5th column are given relative to the bosonic and fermionic blue MOT transition frequencies, respectively. Additionally, the detunings for different beams in 4th and 5th column are aproximate values as detuning of each beam can be tuned to optimize the number of atoms in the blue MOT.

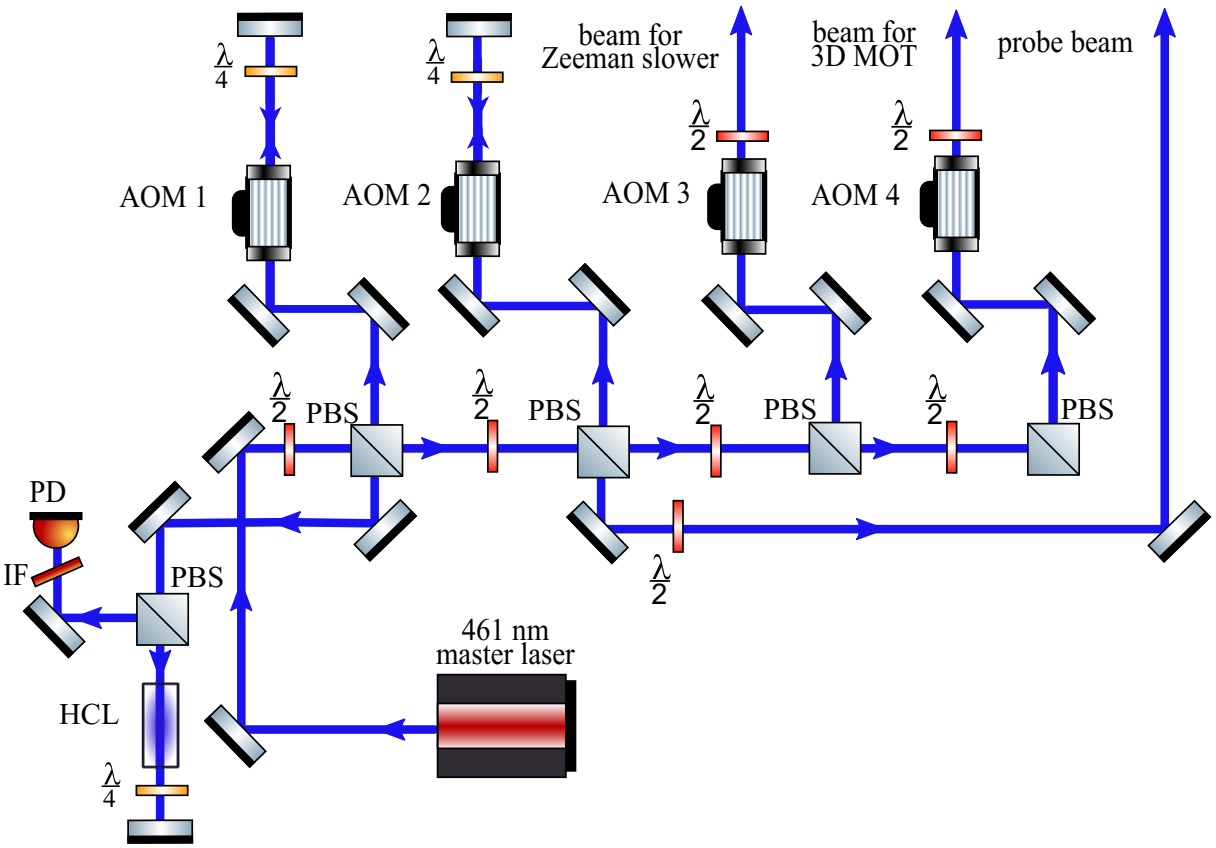


Figure 4.7: Experimental setup for blue MOT in KL FAMO. A 461 nm laser is locked to a frequency shifted saturation spectroscopy. Three separate beams (Zeeman slower beam, 3D MOT beam, floures-cence probe beam) used in different stages of clock operations are detuned from blue MOT transition by three separate AOMs. Beam detunings and AOM RFs are given in Table 4.1. Abbreviations: AOM- acousto-optic modulator, PBS- polarising beam splitter, IF- interference filter, PD- photodiode, $\frac{\lambda}{2}$- half wave plate, $\frac{\lambda}{4}$- quarter wave plate.

The idea behind our setup design was the following - we wanted to enable quick and simple swapping between fermionic and bosonic clock operation. This meant we need to be able to swap quickly between fermions and bosons at each stage of clock operation. For blue MOT cooling, the isotope shift between the $^1S_0 \rightarrow {}^1P_1$ of $^{88}Sr$ and $^1S_0, F = 9/2 \rightarrow {}^1P_1, F = 11/2$ blue MOT transitions of $^{87}Sr$ is 51.8 MHz. This means that for swapping between the isotopes we would like to shift the detunings of the different laser beams (3D MOT beam, Zeeman beam, flourescence beam) by the same amount to ensure the same detuning conditions (4th and 5th column in Table 4.1) when loading the bosonic and fermionic blue MOT. This is done with the use of AOM 1 in Fig. 4.7. By changing the AOM 1 RF between -75 (for bosons) and -95 MHz (for fermions), we change the frequency lock point of the 461 nm laser. This way we ensure that for both isotopes, the laser is detuned by the about the same amount (-150 MHz for bosons and -140 for fermions) from their respective blue MOT cooling transitions. This allows us to keep the RF of AOMs 2, 3 and 4 the same for both fermionic and bosonic blue MOT. The final detunings for each specific beam used in blue MOT (Zeeman slower, 3D MOT cooling, flourescence probe beam) for bosonic and fermionic blue MOT are given in 4th and 5th column of Table 4.1. Note that these are approximate values as detuning of each beam can be changed to maximize the number of atoms in the blue MOT.

For Zeeman slower beam this means a total detuning of about $\delta_{\text{Zeeman}} = -500$ MHz from the $^{88}Sr$ $^1S_0 \rightarrow {}^1P_1$ transition. The beam has a power of 30 mW and spatial width (FWHM) of 2.2 cm achieved by use of achromatic lenses, giving a beam intensity of about $2\ \mathrm{mW/cm^2}$.

For the 3D MOT we use a beam detuned by about $-1\Gamma$ (40 MHz) from the cooling transition. The total power of the beam after AOM 4 is around 60 mW with spatial width (FWHM) of 2.2 cm. After the AOM, the blue MOT beam is merged with the red MOT cooling and stirring beams on dichroic nonpolarising beamsplitter and split into 3 independent retro-reflected beams using half-wave plates and polarizing beamsplitter (PBS) cubes. This gives a beam intensity of about $1.5\ \mathrm{mW/cm^2}$ for each pair of retroreflected beams.

The third and final beam is the flourescence beam used as a probe for measurement of populations in the ground and excited state of clock transition. This beam is detuned back to resonance of the $^1S_0 \rightarrow {}^1P_1$ transition after passing through AOM 2 in Fig. 4.7.

## 4.5 Red MOT cooling on $^1S_0 \rightarrow {}^3P_1$ transition

As we discussed in previous chapters, fermionic red MOT cooling is more complicated due to hyperfine structure and requires an additional stirring laser, as well as optical pumping during detection phase. An experimental setup with these new requirements in mind was designed and constructed in KL FAMO. My personal contribution was the construction of the stirring and optical pumping parts of the experiment. Red MOT cooling, stirring and optical pumping part of the experiment is shown in Fig. 4.9. The detunings of different laser beams in red MOT and isotopic shifts of $^{87}Sr$, both relative to $^1S_0 \rightarrow {}^3P_1$

transition of $^{88}$Sr are given in Fig. 4.8. The RFs of different AOMs in Fig. 4.9 and detunings of bosonic (fermionic) red MOT beams are given in Table 4.2.

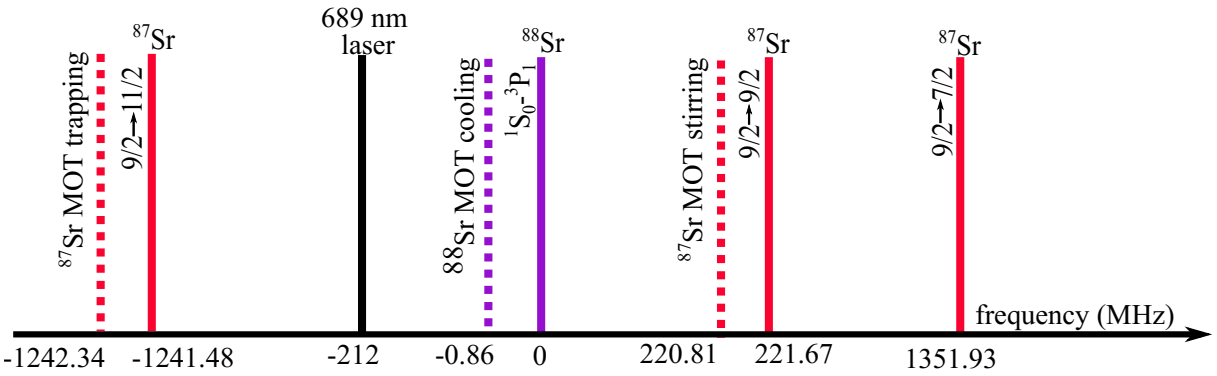


Figure 4.8: Relevant frequencies for $^{88}$Sr and $^{87}$Sr red MOT operation. Frequencies of different laser beams and isotope shifts of different $^1\mathrm{S}_0 \rightarrow {}^3\mathrm{P}_1$ hyperfine transitions of $^{87}$Sr are all given relative to the $^1\mathrm{S}_0 \rightarrow {}^3\mathrm{P}_1$ transition of $^{88}$Sr. The solid purple (red) lines represent detunings of different bosonic (fermionic) red MOT transition(s). The dashed purple (red) lines represent detunings of 3D MOT trapping and stirring (for fermions) beams needed for bosonic (fermionic) blue MOT operation. The black line is the detuning of the 689 nm laser.

| AOM | AOM RF shift (MHz) | laser beam | beam $\delta$ $^{88}$Sr (MHz) | beam $\delta$ $^{87}$Sr (MHz) |
|---|---|---|---|---|
| 5 | 2 x -111 | injection to slave lasers | -434 | -434 |
| 6 | 2 x 216.57 | $^{88}$Sr cooling ( $^{87}$Sr stirring ) | -0.86 | -0.86 |
| 7 | 2 x 217 | $^{87}$Sr optical pumping | / | 0 |
| 8 | 2 x 217 | $^{87}$Sr optical pumping | / | 0 |
| 9 | 2 x -250 | $^{87}$Sr trapping | / | / |
| 10 | 2 x -265.17 | $^{87}$Sr trapping | N/A | -0.86 |

Table 4.2: AOM RF shifts of different AOMs from Fig. 4.9 and detunings $\delta$ from $^1\mathrm{S}_0 \rightarrow {}^3\mathrm{P}_1$ transition(s) of different beams used in bosonic (fermionic) red MOT stage. The detunings in 4th and 5th column are given with respect to the relevant transitions used in bosonic and fermionic red MOT, respectively.

Light from a 689 nm master laser is frequency-locked to a high finesse cavity, shifted by AOM by $2\,\mathrm{x} - 106$ MHz (not depicted in Fig. 4.9.) from the bosonic $^1\mathrm{S}_0 \rightarrow {}^3\mathrm{P}_1$ transition of $^{88}$Sr, transferred through a single-mode polarization-maintaining fiber and delivered to experiment setup shown in Fig. 4.9.

Let us now consider what are the detunings of our 689 nm master laser compared to relevant transitions for bosonic (fermionic) red MOT. Before passing through any AOMs shown in Fig. 4.9, the 689 nm light is detuned by $-212$ MHz from $^{88}$Sr cooling transition, $-433.6$ MHz from $^{87}$Sr stirring transition, and $+1029.44$ MHz from $^{87}$Sr cooling transition. Now, in lieu with blue MOT setup described in previous

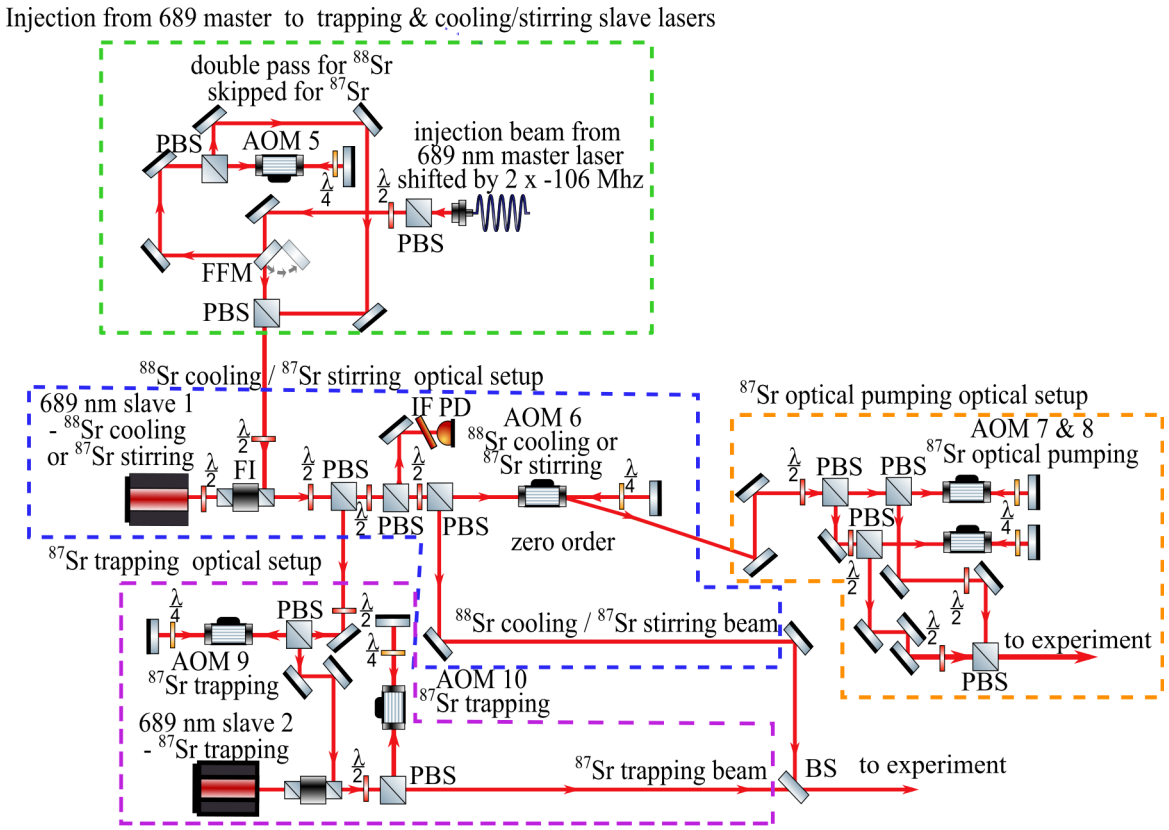


Figure 4.9: Experimental setup for red MOT in KL FAMO. The setup is separated into 4 sections. First section (green dashed box) is used for injection of the 689 nm master laser beam into two slave lasers used for $^{88}$Sr cooling / $^{87}$Sr stirring and $^{87}$Sr trapping. The remaining sections (blue, purple and orange dashed box) are the $^{88}$Sr cooling / $^{87}$Sr stirring, $^{87}$Sr trapping and $^{87}$Sr optical pumping optical setups, respectively. More details on each section can be found in main text. Abbreviations: FFM-flip-flop mirror, AOM- acousto-optic modulator, PBS- polarising beam splitter, IF- interference filter, PD-photodiode, $\frac{\lambda}{2}$- half wave plate, $\frac{\lambda}{4}$- quarter wave plate.

chapter, we wish to able to swap between bosonic and fermionic red MOT as quickly and painlessly as possible. To do just that, we decided to use a single laser for either bosonic cooling or fermionic stirring and optical pumping. This laser is labeled as 689 nm slave 1 in Fig. 4.9. To swap between the two isotopes we simply put (remove) a flip-flop (FFM) mirror (see green box in Fig. 4.9) to use the laser for bosonic cooling (fermionic stirring).

To have bosonic cooling, we put the flip-flop mirror in path of the beam and send the beam through AOM 5 (green dashed box in Fig. 4.9). After the AOM, the beam is red-detuned by $-434$ MHz from $^1\mathrm{S}_0 \rightarrow {}^3\mathrm{P}_1$ transition. The light is then injected into the 689 nm slave 1 laser.

For fermionic stirring, the flip-flop mirror is removed, skipping the double pass on AOM 5, and the beam is directly injected into 689 nm slave 1 laser. The beam is then again detuned by $-434$ MHz, this time from the $^1\mathrm{S}_0, \mathrm{F} = 9/2 \rightarrow {}^3\mathrm{P}_1, \mathrm{F}' = 9/2$ stirring transition.

From this point on, bosonic cooling and fermionic stirring beam follow the same path. By using AOM 6, we shift the laser frequency back near $^1S_0 \rightarrow {}^3P_1$ resonance, leaving the laser red-detuned by about $0.856$ MHz. This AOM is used for both the broadband (BB) and single frequency red MOT phase. In the BB phase, AOM 6 is modulated by $\omega_{\mathrm{mod}} = 0.8$ MHz where $\omega_{\mathrm{mod}}$ is the frequency modulation imposed on the AOM[7]. This broadens the linewidth of the red MOT laser, ensuring efficient transfer of atoms between blue and red MOT. During the single frequency (SF) phase the modulation is turned off and the laser is detuned closer to resonance to about -1 $\Gamma$ from the transition. After the double pass through AOM 6, the light is merged with the $^{87}$Sr trapping beam and sent to the experiment.
Additionally, for fermionic clock operation, the zero order after the first pass through AOM 6 isn't blocked, but instead used for optical pumping. The beam is split on a beamsplitter and each of the split beams sent through AOMs 7 and 8, respectively. This brings the beams used for optical pumping to resonance with the fermionic stirring transition. The beams are then merged and sent to the experiment.
For fermionic trapping, we use 689 nm slave 2 laser. A part of light from fermionic stirring laser is split and injected into the fermionic trapping laser after going through AOM 9. The output light from slave 2 is sent through AOM 10, red-detuning the laser by 0.856 MHz from the $F = 9/2 \rightarrow F' = 11/2$ fermionic trapping transition. For broadband (BB) red MOT phase, AOM 10 is modulated by modulation frequency of $\omega_{\mathrm{mod}} = 0.8$ MHz. For the SF red MOT phase, the modulation is turned off.

## 4.6 Red-detuned 813 nm dipole trap

Once the atoms are sufficiently cooled down using the two-stage cooling, they are loaded into the optical lattice. To produce a sufficiently deep dipole trap we use the optical setup shown of Fig. 4.10. Light from a high-power pump laser capable of producing up to 14 W of power at 532 nm is coupled into a 4 mirror Ti:Sa ring laser. At the output of the Ti:Sa laser, about 2.5W of 813 nm light is produced. A small fraction of Ti:Sa light is taken and coupled into a Ti:Sapphires' internal reference cavity for monitoring and locking of the laser frequency. This internal lock, however, is not sufficiently tight for the Ti:Sa to be used in optical clock operation. To resolve this issue, I designed and constructed a separate locking scheme where I locked the Ti:Sa to our RF-locked frequency comb. The method was the following - light from the Ti:Sa is split into three separate beams. Two of the beams, with a small fraction of the total power of the 813 nm light, are sent through a double pass (AOM 11 in Fig. 4.10) and through fiber (FB 1) to wavelength meter (WM). The part of the beam going through the AOM is then coupled into a separate fiber (FB 2).
At the fiber output, I built an optical beatnote setup between Ti:Sa and the frequency comb. The beatnote setup produced a 38 MHz beatnote signal, as shown in Fig. 4.11. The beatnote is then filtered, amplified and sent onto a mixer along side a 102 MHz signal from a signal generator. The new beatnote, now

[7]This means the detuning is swept by $\omega_{\mathrm{mod}}/2$ on each side, from -1.256 MHz to -0.456 MHz. Here it is important to we make sure that even with modulation we do not cross to the blue side of the transition.

at 140 MHz, is again filtered, amplified and sent to a home-made digital phase comparator. A separate signal generator, used as a local oscillator (LO), sends another 140 MHz signal to the phase comparator. This leaves only the phase difference between the two inputs at the comparator output. The output is sent to a PI controller which is then used to lock the Ti:Sa laser frequency to the frequency comb[8].

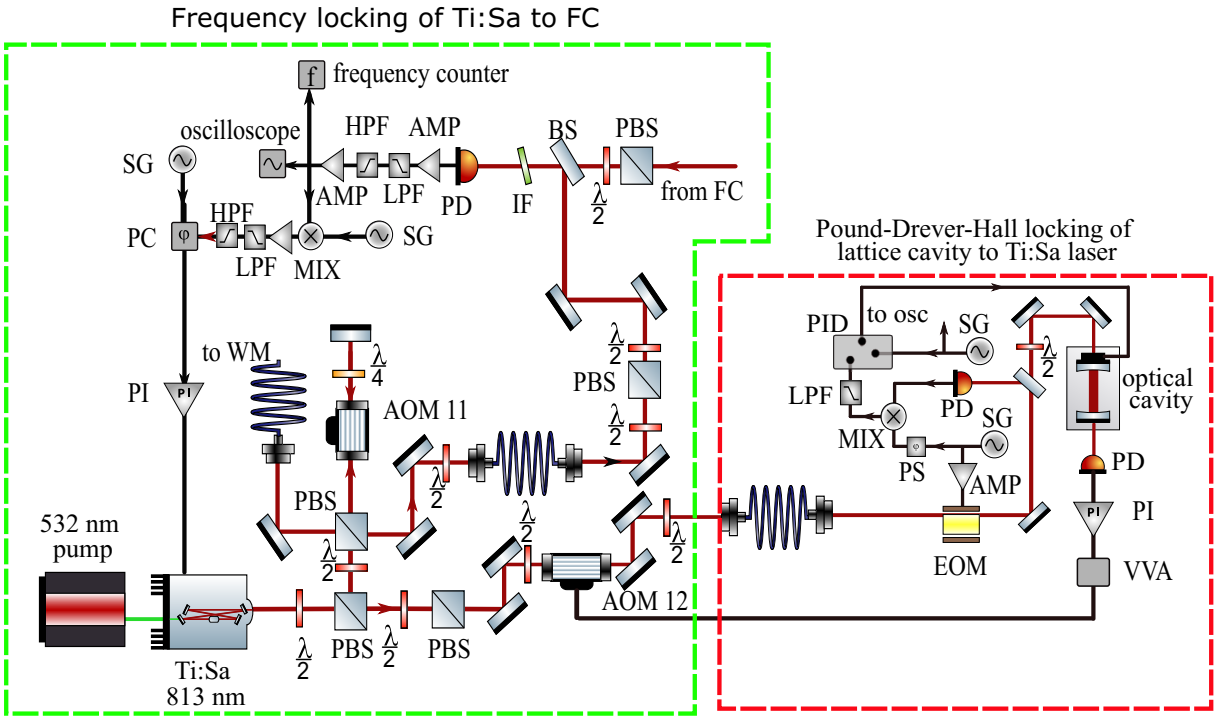


Figure 4.10: Optical setup for the 813 nm dipole trap. A Ti:Sa 813 nm laser, pumped by a 532 nm pump, is locked to the optical frequency of the RF-locked frequency comb. Additionally the optical cavity setup used to load atoms in the optical lattice in optical clock operation is presented. The length of the optical cavity is locked to the Ti:Sa laser using a Pound-Drever-Hall stabilisation technique [105]. Abbreviations used in figure: FC- frequency comb, PBS- polarizing beam splitter, EOM- electro-optic modulator, AOM- acousto-optic modulator, $\frac{\lambda}{2}$- half-wave plate, $\frac{\lambda}{4}$- quarter-wave plate, LPF- low pass filter, HPF- high pass filter, AMP- operational amplifier, PD- photodiode, IF- interference filter, LO- local oscillator, MIX-mixer, SG- signal generator, PI(D)- proportional-integral–(derivative) controller, PC- phase comparator, PS- phase shifter, VVA- variable voltage attenuator, FB- optical fiber, osc- oscilloscope.

### 4.6.1 Optical cavity Pound-Drever-Hall frequency locking

Major part of 813 nm light is sent through AOM 12 in Fig. 4.10, coupled into a polarization-maintaining single-mode fiber and transferred to the experiment. With coupling transfer efficiency of about 80%, there is around 350-400 mW of 813 nm light at the output of the fiber. This light goes through a single

[8]Prior to my arrival at KL FAMO, the Ti:Sa laser was locked using a transfer cavity. The cavity would be locked onto the 689 nm laser and then the 813 nm Ti:Sa would be locked onto the cavity.

pass EOM and is coupled into the power build-up cavity. The mirrors of the vertical optical lattice are placed outside the vacuum chamber. The cavity has a finesse of around 100. To lock the power build-up cavity to 813 nm light we use a standard Pound-Drever-Hall (PDH) technique [105, 106]. In Pound-Drever-Hall lock, light passes through a electro-optic modulator (EOM), is reflected from the mirrors of the lattice cavity and is detected by the photodetector (PD). The PD signal is mixed with the signal from the signal generator. This generator is used to both drive the EOM and serve as the local oscillator for the mixer. The mixed signal is filtered by a LPF filter and sent to the PID controller. The phase shifter (PS) is used to match the phases of the two signal going into the mixer. The error signal from the PID unit is sent to the piezoelectric transducer on one of the mirrors of the lattice cavity, locking the cavity length to the frequency of the Ti:Sa laser.

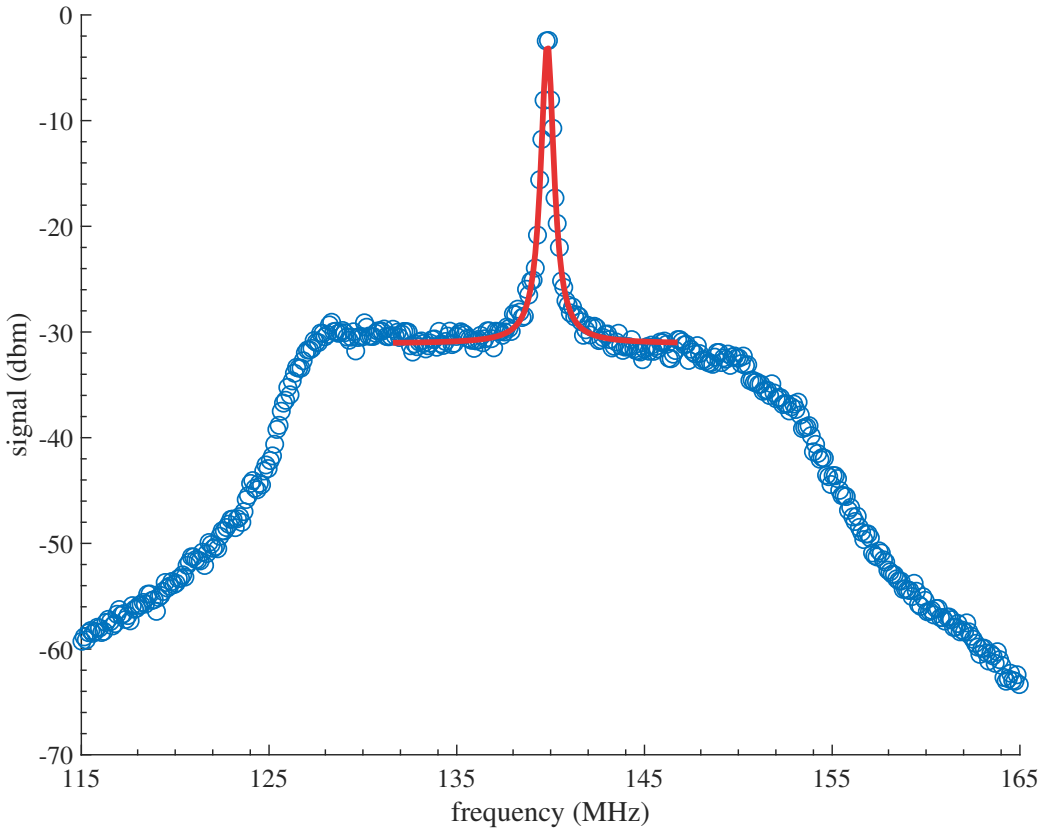


Figure 4.11: Beat of 813 nm Ti-Sa laser with the frequency comb, represented by blue points. The beatnote is centered at 140 MHz. By fitting a Lorentzian function, represented by solid red line, to the points, I determined the width (FWHM) of the beatnote to be equal to 420 kHz, coming mostly from the width of the Ti-Sa laser.

## 4.7 The clock transition spectroscopy

The atoms are finally loaded into the optical lattice and we are ready to perform the high-precision spectroscopy of the clock transition and digitally lock our clock laser to the clock transition. The relevant transitions for bosonic and fermionic clock spectroscopy are given in Fig. 4.12. Similar to the red and

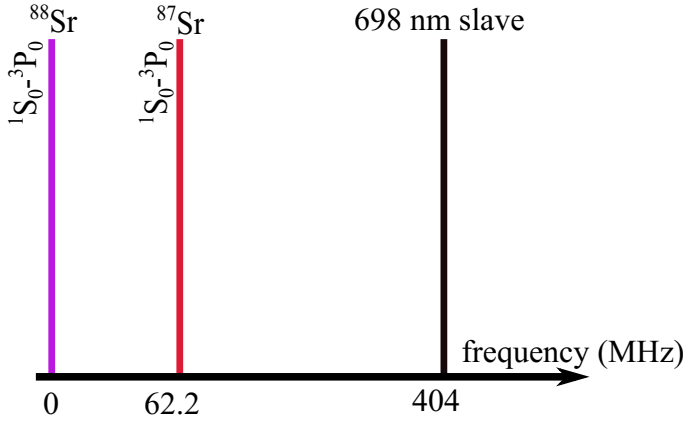


Figure 4.12: Relevant atomic clock frequencies for $^{88}$Sr and $^{87}$Sr. The frequency of the 698 clock laser (black line) and the isotope shift of the fermionic clock transition (red line) are given relative to the frequency of the bosonic clock transition (purple line)

blue MOT optical setups, here we also want to be able to swap between bosonic and fermionic clock spectroscopy as simple as possible. The 698 nm master laser is frequency-locked to a high-finesse optical cavity (neither are depicted in Fig. 4.13) and then the light from the master laser is transferred to Sr 1 experiment via a single-mode polarization-maintaining fiber and injected into the 698 nm slave laser shown in Fig. 4.13. The injected light is shifted by +404 MHz and +342 MHz from the bosonic and fermionic $^1\mathrm{S}_0 \rightarrow {}^3\mathrm{P}_0$ clock transition, respectively.
For fermionic spectroscopy, the 698 nm beam is sent through AOMs 14 and 15. This shifts the laser frequency by total of 342 MHz, bringing the laser frequency in resonance with the fermionic clock transition. For bosonic spectroscopy, we use a double-pass AOM (AOM 16) to bring the frequency of the laser light back onto the clock transition frequency. The two clock interrogation beams are then merged on beamsplitter (BS 2) and sent to the experiment.

### 4.7.1 Phase noise cancellation

As one might note from the sheer size of the few previous experimental setups, optical clocks are very complex systems, often spanning across multiple optical tables. This brings up the question of methods of transferring optical light across different tables. Here, optical fibers become an essential tool, offering great flexibility in experiment design with their ability to deliver laser beams with high stability of laser modes and stable polarization [107]. As such they have broad scientific and industrial applications, ca-

pable of delivering light across thousands of kilometers [108, 109].

Optical fibers, however, are also very sensitive to environmental factors such as acoustic vibrations or temperature variations. These factors perturb the optical phase of the light inserted into the fiber causing significant spectral broadening on the order of a few hundred Hz. Generally, phase noise perturbations in fibers usually aren't of significant consequence when dealing with experiments with relevant linewidths on kHz or MHz level, and can even be beneficial for sensor applications. However, they are a serious obstacle in transfer of ultra-narrow linewidth laser light with high spectral purity such as the one required for ultra-high precision spectroscopy in optical clocks [109].

The basic principle behind phase noise cancellation comes from the fact that the phase noise acquired

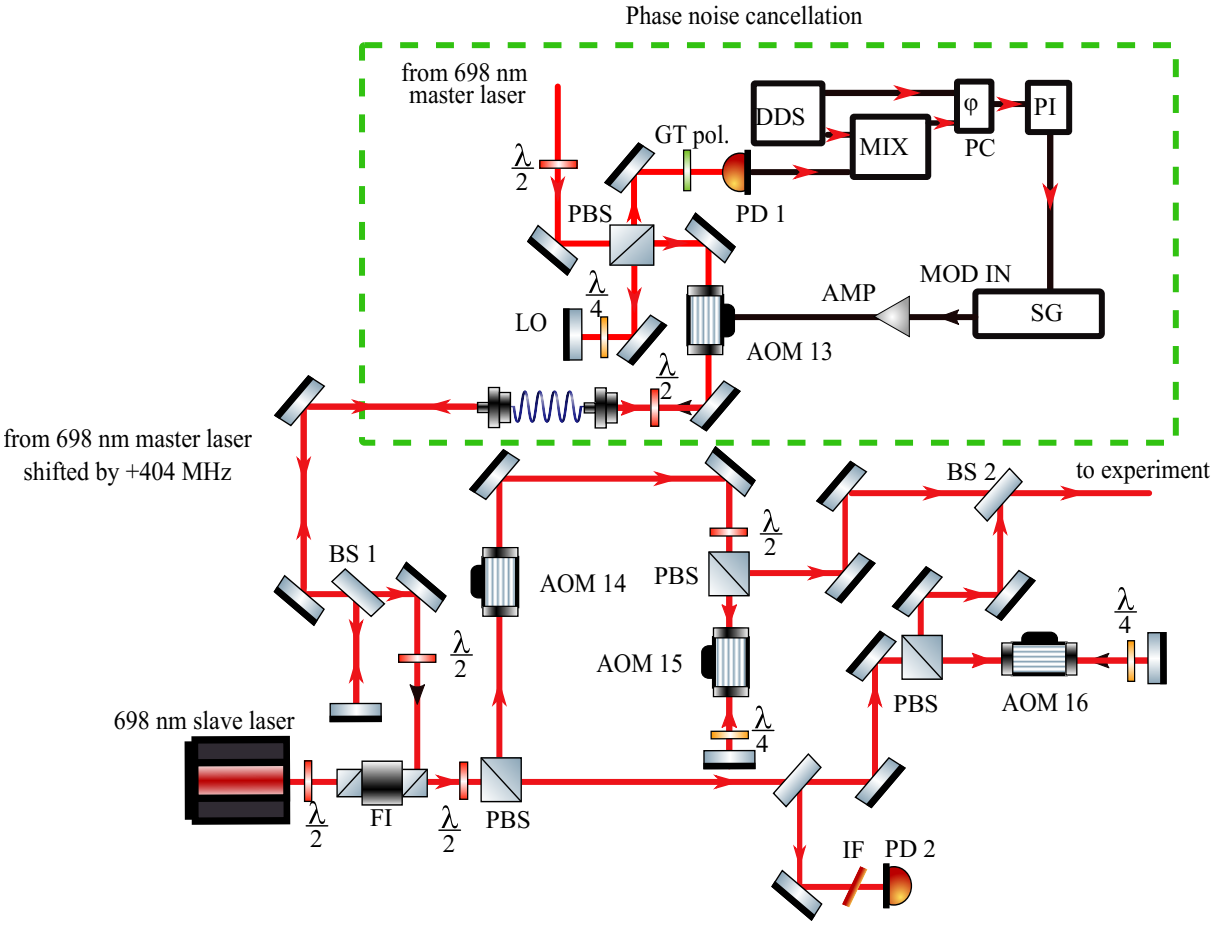


Figure 4.13: Experimental setup for clock spectroscopy with phase noise cancellation. The setup enables a clock spectroscopy for both fermionic and bosonic strontium. Abbreviations: PBS- polarising beam splitter, GT pol.- Glam-Taylor polariser, LO- local oscillator, BS- beam splitter, AOM- acousto-optic modulator, IF- interference filter, FI- Faraday isolator, PD- photodetector, $\frac{\lambda}{2}$- half-wave plate, $\frac{\lambda}{4}$- quarter-wave plate, DDS- direct digital synthesiser, MIX- mixer, PC- phase comparator, PI- proportional–integral controller, SG- signal generator, AMP- operational amplifier.

during fiber transfer is independent from direction of light propagation. Therefore, light propagated through a fiber and retroreflected back through will have simply twice the phase noise of single-transit light. The retroreflected phase-noise affected signal can then be compared with the original input signal. A heterodyne beatnote of these two signals will produce a signal with twice the phase noise. By pre-modulating the phase of input light with the negative of the phase noise, one can effectively completely remove the phase noise generated by the transfer through the fiber.

To cancel the phase noise acquired by transfer of light through optical fibers and other optical elements, a phase noise cancellation setup is used. One such setup was constructed in Sr 1 setup in KL FAMO and is shown in the green dashed box in Fig. 4.13. Light from a 698 nm master laser (not shown in Fig. 4.13) is split on a polarising beamsplitter. A fraction of the light is retroreflected on a mirror serving as a local oscillator (LO). The rest of the light is sent through an AOM (AOM 13 in Fig. 4.13) and coupled into a polarization-maintaining single-mode optical fiber. At the output from the fiber, a small fraction of light is split on a beam splitter (BS 1) and reflected back through the fiber. On the way back, the light again goes through AOM 13 and is then merged with the light from the local oscillator and sent onto a photodiode. The frequency of the beatnote generated on the photodiode is 2 x RF of AOM 13, coming from the double pass through the AOM. In our case the frequency of the beatnote will be 160 MHz. The beatnote will also have twice the phase noise due to the double transfer through the fiber.

At this point the beatnote is downconverted to 20 MHz using a DDS signal generator and a mixer. The 20 MHz beatnote is sent to the phase comparator where the signal is divided by 4 to produce a 5 MHz signal. By dividing the signal, we increase the capture range of the servo controller. A separate 5 MHz signal, serving as a local oscillator, is also sent from the DDS to the phase comparator. This leaves only the phase noise on the output from the comparator. Output from the phase comparator is sent to the PID controller. The PID controller receives this error signal and, using the PID parameters, generates a correction signal which is sent to the frequency modulation input of the RF generator used to drive the AOM. This frequency modulation compensates for any phase noise induced by the fiber, allowing the light to be transferred through the fiber noise-free.

# Chapter 5

# Characterization of the fermionic optical clock

As the title would imply, this section presents the preliminary results on our road to fermionic clock, from the blue MOT all the way to atoms in the optical lattice. We expect, all things being equal, a order of magnitude less atoms (and therefore less flourescence) in our fermionic clock compared to the bosonic one due to the fact that the natural abundance of $^{87}$Sr is about 10 times less than $^{88}$Sr atoms. This means that, along with ensuring sufficiently low temperature of fermions at each stage, we'll have to take great care to maximize the number of $^{87}$Sr atoms in our MOT and optical lattice to have sufficient signal for clock operation. In addition, for the sake of comparison, we will present also the results of bosonic clock, measured for similar experimental conditions.

## 5.1 Fermionic blue MOT

The number of atoms in an atomic ansamble as a function of the loading time in MOT is given as [92]

$$N_{Sr}(t) = \frac{L_{Sr}}{\gamma_{Sr}}(1 - e^{\gamma_{Sr}t}); \tag{5.1}$$

where $L_{Sr}$ is the loading rate of atoms into the blue MOT, $\gamma_{\mathrm{Sr}}$ are the loss rates from different channels such as collisions with background gases and optical pumping to the metastable states [66] and $N_{Sr}(\mathrm{t}=0)$=0[1]. The blue MOT flourescence as a function of loading time in MOT for both fermionic and bosonic blue MOT is shown in Fig. 5.1. Since blue MOT flourescence is directly proportional to the number of atoms, the figure shows the dependence of number of atoms in MOT as function of loading time. The comparison between bosonic and fermionic blue MOT is possible due to the unique design

[1] A similar equation was derived and discussed in more detail in section 3.2.1 when we've discussed photoionization loss rates of different states in a blue-detuned magic wavelength lattice.

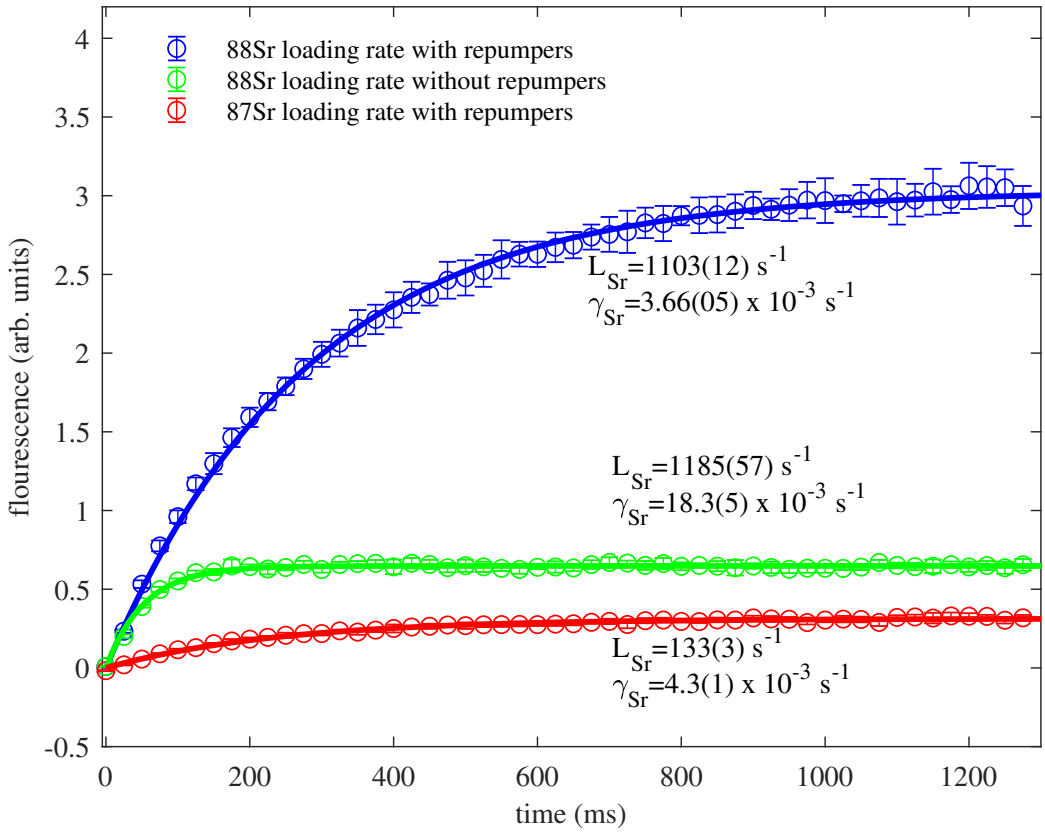


Figure 5.1: Number of atoms as a function of loading time for fermionic and bosonic blue MOTs. Red points represent number of atoms as a function of loading time in fermionic blue MOT while blue and green points respresent number of atoms in bosonic blue MOT with and without repumpers as a function of loading time, respectively. In the steady state the total number of atoms in the fermionic blue MOT is an order of magnitude lower than the bosonic one due to a lower loading rate. This is expected when we remember that there is a large difference in natural abundanuces of the two isotopes in strontium. Additionally, we can also see that the without repumpers bosonic blue MOT will have a larger loss rate as atoms can escape the cooling cycle via $^1D_2$ and get stuck in the $^3P_2$ state. To determine the loading rate $L_{Sr}$ and loss rate $\gamma_{\mathrm{Sr}}$, Eq. 5.1 was fitted to the measured datasets.

.

of our blue MOT setup which enables quick swapping between bosonic and fermionic blue MOT. From Fig. 5.1, we see that the flourescence in steady state of fermionic $^{87}$Sr blue MOT is about an order of magnitude lower than its' bosonic counterpart as the fermionic blue MOT loading rate is about ten times lower than the bosonic one. This is expected when we remember that the difference in natural abundances of the two isotopes is also about an order of magnitude. To determine the loading and loss rate in Fig. 5.1, Eq. 5.1 was fitted to the datasets. We see that the number of atoms in bosonic blue MOT, with and without repumpers being turned on during loading, is about half an order of magnitude lower when

the repumpers are turned off. The difference in number of atoms comes from a larger loss rate when there are no repumpers during the loading stage. This lack of repumpers allows the atoms to get stuck in the $^3\mathrm{P}_2$ state and escape the cooling cycle. This can provide us with baseline expectations of the ratio of flourescences of fermions and bosons in optical lattice. Since fermionic blue MOT has 10 times less atoms than the bosonic one, assuming similar efficiencies of transferring of fermions and bosons from blue to red MOT and then from red MOT to the optical lattice, we would expect the number of fermions in the lattice would also be about 10 times smaller than its bosonic counterpart.

## 5.2 Fermionic red MOT

Once the loading fermionic blue MOT is complete the next stage is red MOT cooling. Red MOT cooling is done via the two stage broadband+single frequency (BB+SF) cooling scheme which employs a combination of two lasers - one for trapping and another for stirring and optical pumping.
As a reminder, in the broadband red MOT stage, the linewidth of the red MOT laser(s) is broadened. In our experiment, this is done by modulating the frequency of an AOM used in red MOT setup. This needs to be done due to the large difference in natural linewidths of the blue and red MOT transitions. By using the modulated red MOT phase, we match the Doppler profiles of blue and red MOTs ensuring efficient transfer of atoms between the two MOTs. During single frequency stage, the modulation is turned off and the only the linewidth of the laser remains. Without the BB phase, the SF phase of red MOT would be able to capture only a small fraction of blue MOT atoms.
Before we proceed further, it would be beneficial to clear up the nomenclature used in the following section. Generally, in the initial sections of this thesis where we described the theory behind cooling of bosonic strontium, we would use terms like "cooling transition", "cooling beam", "cooling laser" and so forth. This nomenclature is somewhat incomplete as the "cooling" laser is also crucial in trapping of atoms in the MOT, but as there is a single laser performing both roles at each stage of the cooling (be it blue MOT or red MOT), this isn't of great importance.
The situation is quite different for fermionic red MOT. Here we have two separate lasers. One of the lasers used drives the $^1\mathrm{S}_0, \mathrm{F} = 9/2 \rightarrow\ ^3\mathrm{P}_1, \mathrm{F}' = 9/2$ and the other drives the $^1\mathrm{S}_0, \mathrm{F} = 9/2 \rightarrow\ ^3\mathrm{P}_1, \mathrm{F}' = 11/2$ transition. Naming either of these lasers as the "cooling laser" would imply that the other one does not participate in cooling of atoms, which is simply wrong, as both lasers fulfill that role. We will therefore keep the nomenclature used in the initial paper by Katori [80] and refer to these two lasers as "stirring" and "trapping" laser to highlight the different roles they perform. The one driving the $^1\mathrm{S}_0, \mathrm{F} = 9/2 \rightarrow\ ^3\mathrm{P}_1, \mathrm{F}' = 9/2$ transition "stirs" the atoms through different ground magnetic sublevels, and the one driving $^1\mathrm{S}_0, \mathrm{F} = 9/2 \rightarrow\ ^3\mathrm{P}_1, \mathrm{F}' = 11/2$ traps the atoms in the MOT. With that out of the way, let's return to our red MOT.
Our goal at this stage remains the same as with blue MOT: find the experimental parameters which give the maximum flourescence from the cloud, i.e. give the largest number of trapped atoms in the red MOT.

To achieve just that, we mimic the approach used to load bosons into red MOT - align and overlap the

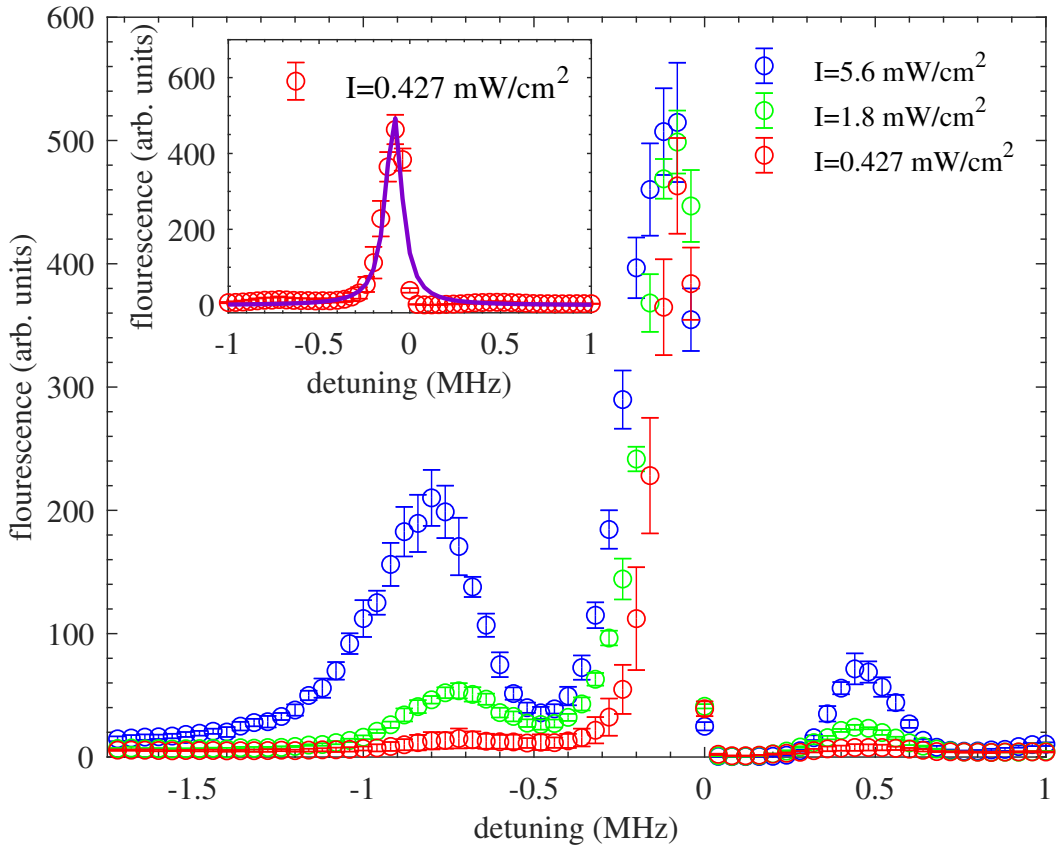


Figure 5.2: Spectroscopy of $^1S_0 \rightarrow {}^3P_1$ transition for different total intensities of trapping beam. The frequency of bosonic red MOT cooling beam was scanned with AOM. Flourescence of atoms as a function of detuning from the resonance of the trapping transition (represented by blue, red and green points for three different trapping beam intensities) was measured by CCD camera. The horizontal axis is given as detuning of the red MOT laser frequency from the calculated resonance of the red MOT transition, with detuning $\delta = 0$ corresponding to the resonance of the red MOT transition. The inset shows the flourescence for the lowest intensity of the trapping beam. The solid purple line is a Lorentzian fit to the measured flourescence.

red MOT beams with the zero point of the magnetic gradient and compensate any stray magnetic fields via the compensation coils. Additionally, we can use the red MOT AOMs to change the red MOT beam power and laser frequency in other to optimize cooling of the atoms and maximise the flourescence. To load atoms into the red MOT, we have to bring the frequencies of our trapping and stirring laser beams to (or near) the frequencies of the trapping and stirring transition. In other words, we need to find out which RFs to put onto the red MOT AOMs in Fig. 4.9.

For this purpose, frequency of either the trapping or stirring laser was scanned by AOM whose RF fre-

quency and power are controlled by a Direct Digital Synthesizer (DDS) board. While the frequency of one of the lasers was scanned, the frequency and power of the other laser was kept constant. The frequency scans over their respective transitions were performed for different beam intensities of the scanned laser. These scans were done during the single frequency stage, where the of frequency and RF power of the AOM used in scanning were controlled by the DDS.

Note that this type of spectroscopy was also done for the blue MOT in previous section. However in that case, finding the fermionic blue MOT cooling transition was straightforward. The blue MOT transition is very wide and its isotope shift is on the same order as the width of the transition. Additionally, the blue MOT is usually very large (around 2 cm in diameter or more) and easily seen by the naked eye. So to load blue MOT, it was possible to simply scan AOM 1 in Fig. 4.7 and watch into the vacuum chamber until the fermionic blue MOT appeared.

The situation is quite different for the red MOT. The natural linewidth of red MOT transition(s) is 7.6 kHz, and the isotope shifts of the relevant transitions are hundred of MHz apart. Combined with the small size of the red MOT (usually on the order of 100 micrometers) and low sensitivity of the eye to near IR wavelengths, loading the red MOT comes a more complicated matter. This is why we decided to perform flourescence spectroscopies for both the stirring and trapping transition in fermionic red MOT. The scan across the stirring (trapping) transition is done by changing the frequency of AOM 6 (10) in Fig. 4.9 and measuring the flourescence of the red MOT. When it comes to fermions, we perform a flourescence spectroscopy where the frequency of either the stirring or trapping laser is scanned over their respective transition and the flourescence produced by atoms in the red MOT is measured on a CCD camera. Four separate spectroscopies were performed - spectroscopy of the stirring $\mathrm{F} = 9/2 \rightarrow \mathrm{F}' = 9/2$ transition with trapping laser on/off and spectroscopy of the trapping $\mathrm{F} = 9/2 \rightarrow \mathrm{F}' = 11/2$ transition with the stirring laser on and off. Additionally, for comparison purposes, we perform a spectroscopy of the bosonic $^1\mathrm{S}_0 \rightarrow {}^3\mathrm{P}_1$ cooling transition. For each scan we change the beam power of the scanned laser by changing the input RF amplitude on the respective AOM. To analyze the results, we will again compare the bosonic versus the fermionic case.

We begin our analysis with the simplest result - the spectroscopy of the bosonic $^1\mathrm{S}_0 \rightarrow {}^3\mathrm{P}_1$ transition in SF red MOT phase, shown in Fig. 5.2. This spectroscopy represents the "standard" spectroscopy of the red MOT transition. The spectroscopy was measured for 3 different red MOT beam intensities where intensities correspond to total red MOT beam intensity, i.e. the intensity before the beams are split in 3 orthogonal direction for the 3D MOT cooling. For the lowest of the three measured intensities ($\mathrm{I} = 0.427\ \mathrm{mW/cm^2}$) we have a single peak corresponding to the $^1\mathrm{S}_0 \rightarrow {}^3\mathrm{P}_1$ transition. A Lorentzian peak-function was fit to the spectroscopy line gives a FWHM linewidth of 106 kHz (purple line in inset in Fig. 5.2). The Lorentzian was chosen as the increase in linewidth compared to natural linewidth mostly comes from powerbroadening due to low saturation intensity of $^1\mathrm{S}_0 \rightarrow {}^3\mathrm{P}_1$ which is equal to $3\ \mu\mathrm{W/cm^2}$. For beam intensity of $\mathrm{I} = 0.427\ \mathrm{mW/cm^2}$ and natural linewidth of 7.6 kHz, the power-broadened linewidth is equal to 91 kHz. This is fairly close to the experimentally measured linewidth of

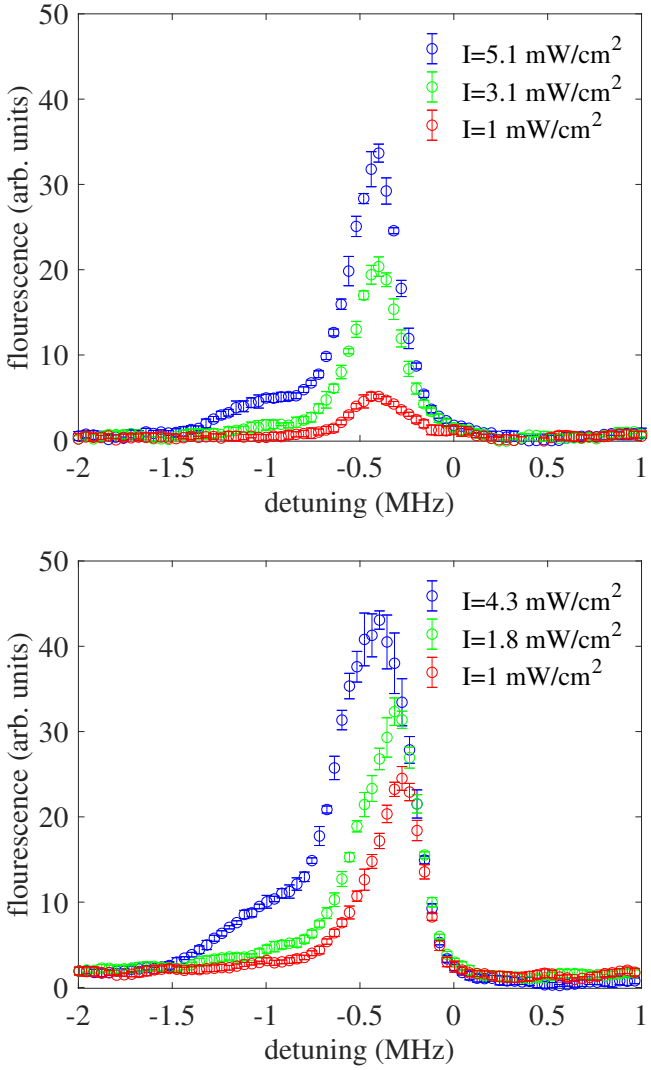


Figure 5.3: Spectroscopy over the $F = 9/2 \rightarrow F' = 9/2$ stirring transition with the trapping beam during SF red MOT being either turned off (top figure) or turned on (bottom figure). The frequency of fermionic red MOT trapping beam was scanned with AOM. Flourescence of atoms as a function of detuning from the resonance of the stirring transition (represented with blue, red and greeen points for three different total intensity of the stirring beam, respectively), was measured by CCD camera. The spectroscopy was performed for different total beam intensities of the stirring laser beam. The horizontal x axis represents the frequency detuning of the stirring laser from the calculated resonant frequency of the stirring tranisition. In bottom figure, the trapping laser was left on and at resonance of the trapping transition.

106 kHz.

Further increase of boson red MOT cooling beam intensities brings increased power broadening and the rise of additional sidepeaks. Theory of magneto-optical trapping states that atoms are always trapped in

the minimum (zero) of the magnetic field. However, due to imperfect symmetry of the anti-Helmholtz coils, unbalanced intensities and polarisations of the counter-propagating cooling beams, atoms are generally slightly shifted from this minima of the magnetic field [110].

The shift of magneto-sensitive transitions of the magnetic sublevels of $^1\mathrm{S}_0, \mathrm{m_j} = 0 \rightarrow ^3\mathrm{P}_1, \mathrm{m_j} = \pm 1$ is 2.1 MHz/G [110]. For spectroscopy in Fig. 5.2 we used gradient field of 16 G/cm. Therefore, even a 100 $\mu$m shift of the red MOT from zero of the magnetic field would shift the $\mathrm{m_j} = \pm 1$ sublevels of $^3\mathrm{P}_1$ by about 600 kHz. This would account for the sidebands seen in Fig. 5.2.

For purposes of SF phase of red MOT, the red MOT cooling laser is detuned by about $-1\Gamma$ (7.6 kHz). The number of atoms, directly proporational to the flourescence in Fig. 5.2, doesn't change significantly near the $\delta \approx 0$ resonance for the 3 given intensities. Therefore, even the lowest intensity of $\mathrm{I} = 0.427\ \mathrm{mW/cm^2}$ is sufficiently high for SF red MOT phase of the clock cycle.

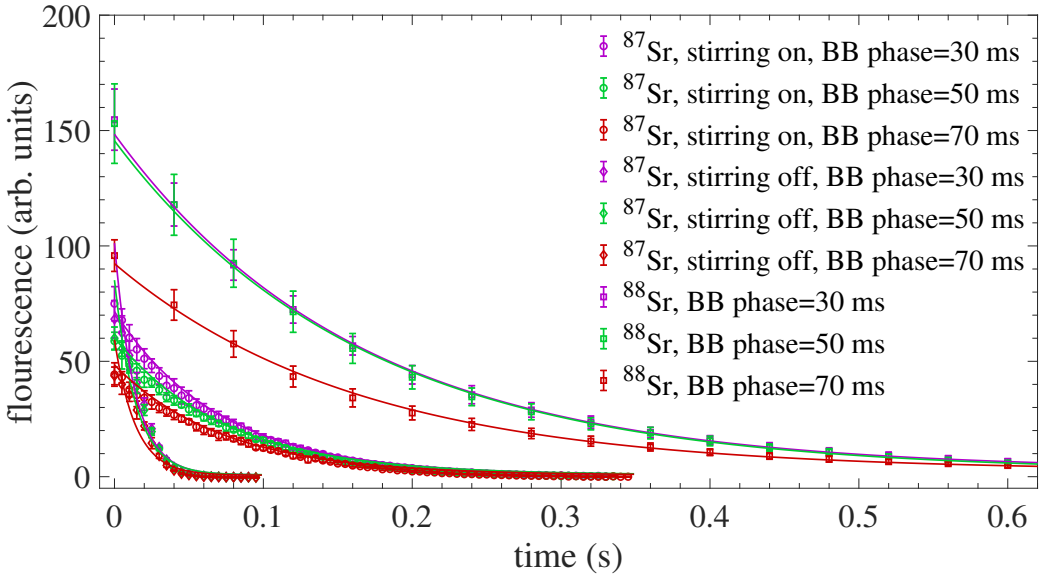


Figure 5.4: The flourescence of atoms (proportional to the number of atoms) in the fermionic SF red MOT phase as a function of the duration of the SF red MOT phase was measured. The flourescence was measured for three different loading times of BB red MOT (30, 50 and 70 ms represented by purple, green and red points, respectively). The circles and diamonds correspond to the flourescence of atoms with and without stirring during the SF red MOT phase. The gradient of magnetic field was ramped linearly from 4 G/cm to 12 G/cm during the BB red MOT phase. For comparison purposes, flourescence of atoms in bosonic SF red MOT as a function of the duration of the SF red MOT phase was also measured. The flourescence was measured for 3 different BB red MOT phase duration of 30, 50 and 70 ms (represented by purple, green and red squares), respectively. An exponentially decaying function was fitted to all datasets and decay times were determined.

Now that we have examined the bosonic red MOT spectroscopy, let us turn our attention to the fermionic case. The spectroscopy of the stirring $\mathrm{F} = 9/2 \rightarrow \mathrm{F}' = 9/2$ transition for different stirring beam inten-

sities is shown in Fig. 5.3. In Fig 5.3 (top) the trapping beam was turned off, while in Fig 5.3 (bottom) the trapping beam was turned on and its frequency set to the $\mathrm{F} = 9/2 \rightarrow \mathrm{F}' = 11/2$ resonance. By comparing the fermionic spectroscopy with the bosonic one in Fig. 5.2, one may note a few key differences. Firstly, there are no distinctly separate sidebands. For the $^1\mathrm{S}_0, \mathrm{F} = 9/2 \rightarrow {}^3\mathrm{P}_1, \mathrm{F}' = 9/2$ transition, shift of magneto-sensitive sublevels $\mathrm{m_F}$ are in the range of 0.04 MHz/G (for $\mathrm{m_F} = 1/2$) to 0.39 MHz/G (for $\mathrm{m_F} = 9/2$) [111]. Assuming similar shift in position of 100 $\mu$m of the red MOT from zero of magnetic field, the splitting of the magnetic sublevels would be at most 100 kHz (for the 0.39 MHz/G splitting of $\mathrm{m_F} = 9/2$ sublevel of the excited red MOT state) for our experimental conditions. Additionally, the spectroscopies of the stirring transition are significantly broader that their bosonic counterparts. For the lowest intensities used ($\mathrm{I} = 1\ \mathrm{mW/cm^2}$ in Fig. 5.3 (top)), we get a linewidth of about 380 kHz, where again a Lorentian fit function for the lowest beam intensity was used. This linewidth of 380 kHz is almost 4 times as broad compared to the bosonic 106 kHz. Of course, some of this additional broadening can be contributed to high levels of powerbroadening as we did use about twice as much intensity per beam compared to the bosonic case[2]. However, if one were to assume this broadening of the linewidth to arrise purely from powerbroadening, beam intensity of $\mathrm{I} = 1\ \mathrm{mW/cm^2}$ would give a power-broadened linewidth of 140 kHz, not the 380 kHz in our spectroscopy. A possible explanation of the additional broadening is the shift of the magnetic hyperfine sublevels, particularly the stretched $\mathrm{m_F} = 9/2$. Again, for optical clock operation, we mostly care about maximizing the number of atoms in our red MOT (and achieving sufficiently low temperatures) to ensure efficient loading of atoms in the optical lattice.

The next step would be the flourescence spectroscopy of the trapping transition with the stirring laser turned on/off. I have performed the spectroscopies of the trapping transition with and without the stirring laser turned on and was able to locate the resonant frequency of the transition. However, the resonance of the trapping transition was part of a more complex spectroscopical structure. This spectroscopical structure was similar to those shown in [112, 113, 114, 115, 116] where the spectroscopy was reported to be a combination of Raman-Zeeman resonances [116, 117] and recoil-induced resonances [114, 117]. As the discussion of the Raman-Zeeman and recoil-induced resonances would be beyond the scope of this thesis, I have elected to not include the spectroscopies of the trapping transition into this thesis.

In the final step of the characterization of the red MOT, we wished to examine the decay of the flourescence of single frequency red MOT as function of the duration of SF red MOT, following the approach laid out in Katori et al. [58, 63]. This decay was measured in the following way - atoms were loaded into blue MOT and then transferred into broadband red MOT. The magnetic field gradient during BB red MOT was ramped linearly from 4 G/cm to 12 G/cm. At that point, the magnetic field gradient is kept at 12 G/cm and the SF phase of red MOT begins. I then measured the decay in flourescence of SF red MOT as a function of the duration of SF red MOT with t=0 in Fig. 5.4 corresponding to the starting point of SF red MOT phase. This was done for 3 different BB MOT loading times (30, 50 and 70 ms) for fermionic SF red MOT, both with and without the stirring laser turned on during SF phase. Stirring laser total beam

[2]We did this purely to ensure sufficient flourescence for the case when the trapping beam is turned off, cf. red graph in Fig. 5.3(top).

intensity was equal to $1.84\ \mathrm{mW/cm^2}$ and its frequency kept on the stirring transition resonance during SF phase.

Finally, for comparison purposes, I also measured the decay in flourescence of bosonic red MOT in the SF phase with the same ramp of magnetic gradient for the three BB MOT loading times of 30, 50 and 70 ms. These decays in flourescence are shown in Fig. 5.4. For each measurement of decay in flourescence an exponential decay function of the form $\mathrm{y} = \mathrm{y_0} + \mathrm{Ae^{-t/\tau}}$ was fitted, from which decay time $\tau$ (referred to as trap lifetime in [58]) was determined. The decay times for different BB MOT loading times are given in Table. 5.1. The flourescence decay times of SF phase of fermionic MOT when stirring is turned on ($\tau \approx 75$ ms) is about five times as long compared to the decay times with stirring beam turned off ($\tau \approx 14$ ms). Additionally, the flourescence decay of bosonic MOT is about twice as long as the flourescence decay times of SF phase of fermionic MOT when stirring is turned on. These ratios match well with those reported in [58, 63] where decay times of 600 ms, 410 ms and 77 ms for bosonic MOT and fermionic MOT with and without stirring beam turned on, respectively, are reported. The differences in absolute values can be attributed to different vacuum background pressures in our setup and the one reported in [58, 63].

The following steps in getting the fermionic optical clock operational involve loading atoms in into the optical lattice and performing the high-precision spectroscopy of the optical clock transition. As of the writing of this thesis, that work is still in progress by the POZA group in KL FAMO.

| BB red MOT loading time (ms) | $^{87}$Sr decay time $\tau$ with stirring beam off (ms) | $^{87}$Sr decay time $\tau$ with stirring beam on (ms) | $^{88}$Sr decay time $\tau$ (ms) |
|---|---|---|---|
| 30 | 13.6(1) | 73(1) | 164(2) |
| 50 | 14.2(1) | 73(2) | 167(1) |
| 70 | 14.2(1) | 74(2) | 164(1) |

Table 5.1: The decay times of flourescence for fermionic SF red MOT with stirring beam turned on and off for different BB MOT loading times (30, 50 and 70 ms) are shown. Additionally, for comparison, the decay times of bosonic SF red MOT for the same BB loading times is also given. The decay time of fermionic MOT with stirring beam turned on is about 7 times higher than with stirring beam turned off. Additionally, the decay time of fermionic MOT with stirring beam turned on is also about half as long as its bosonic counterpart. These results match well with those reported in [58, 63].

# Chapter 6

# Evaluation of systematic shifts of bosonic optical clock (Sr 1)

The quality of an specific optical clock is measured through two parameters - the optical clocks' *stability* and *accuracy*. As explained in the introduction of the thesis, stability of the optical clock tells us how the measured optical clock frequency changes cycle-to-cycle and is usually represented using the Allan statistics. The accuracy of an optical clock tells us how far our measurement of absolute frequency of the clock transition is from the true theoretical value of the transition frequency. This frequency shift between experimental and theoretical value comes from a variety of different physical effects such as Zeeman effect, AC Stark effect, black-body radiation, probe light shift and others. The shift is usually represented in the form of an accuracy budget where contributions of above mentioned effects to the overall shift are evaluated. In the following sections we will provide accuracy budget of the bosonic $^{88}$Sr optical clock at KL FAMO described in previous sections. This accuracy budget was measured during our recent international clock campaign in March 2022. The accuracy budget will also be compared with a previous campaign from 2015. The following subsections will evaluate contributions from different effects to accuracy. We'll examine each effect individually and evaluate its contribution to overal shift of experimentally measured absolute frequency of $^{88}$Sr clock transition from its theoretical value.

## 6.1 Linear and quadratic Zeeman shift

The Zeeman shift is the result of coupling of atomic total magnetic momentum $\mu$ with an external magnetic field B, shifting the energy levels of the atom. The Hamiltonian of this interaction is given as

$$\hat{H_Z} = -\hat{\mu} \cdot B, \tag{6.1}$$

where $\hat{\mu}$ is the operator of total angular momentum. The total angular momentum has three components: orbital ($\mu_{\mathrm{L}} = -\frac{\mu_{\mathrm{B}} \mathrm{g_l} \hat{\mathrm{L}}}{\hbar}$), spin ($\mu_{\mathrm{S}} = -\frac{\mu_{\mathrm{B}} \mathrm{g_s} \hat{\mathrm{S}}}{\hbar}$) and nuclear ($\mu_{\mathrm{S}} = -\frac{\mu_{\mathrm{B}} \mathrm{g_I} \hat{\mathrm{I}}}{\hbar}$) magnetic momentum, where $\mu_{\mathrm{B}}$ is the Bohr magneton and $\mathrm{g_L}$ and $\mathrm{g_S}$ are the orbital and spin Landé factors, respectively. The Landé factors are approximately equal to $\mathrm{g_L} \approx 1$ and $\mathrm{g_S} \approx 2$, respectively. Since the nuclear quantum number I for bosons is zero, nuclear magnetic momentum for bosons doesn't contribute the Zeeman shift. In section

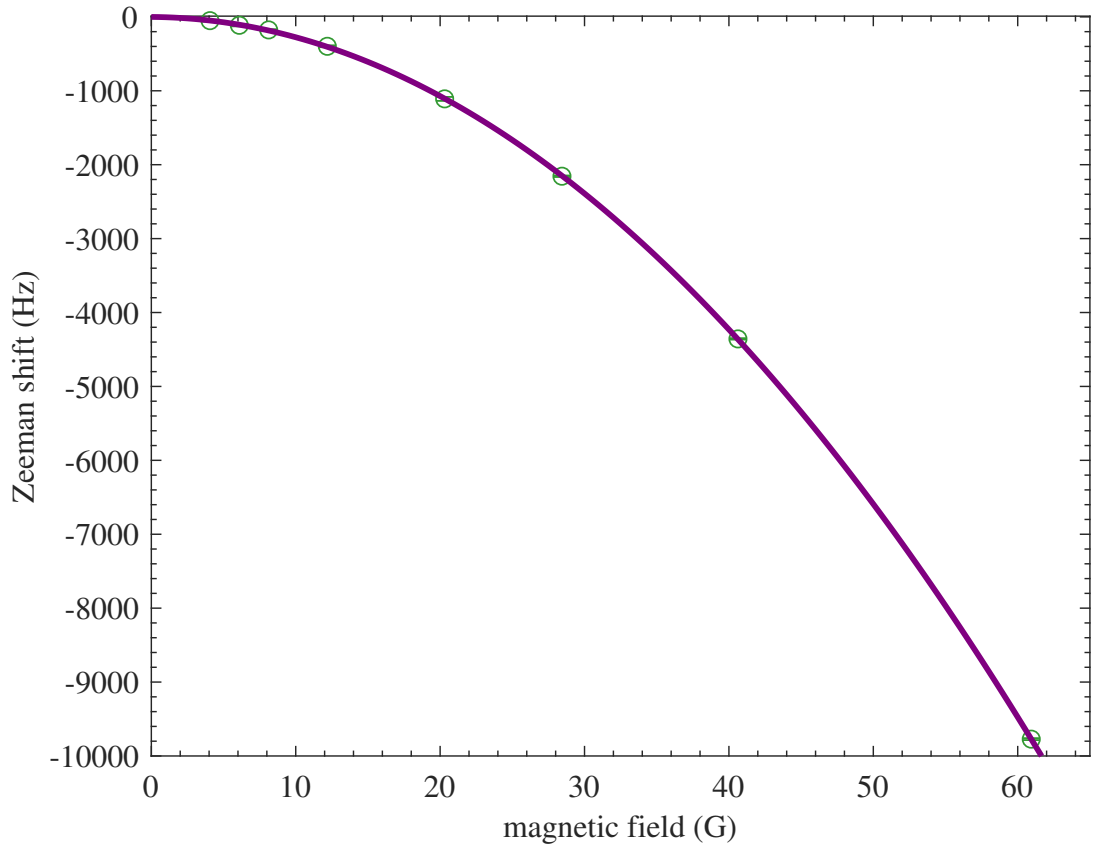


Figure 6.1: Depedence of the quadratic Zeeman shift of the clock transition as a function of magnetic field, measured during an international campaign in March of 2022. Green points correspond to measurements of the Zeeman shift of the clock transition as a function of the magnetic field. A quadratic function, represented by solid purple line, was fitted to the measured data from which the second order Zeeman shift was evaluated at -177.7(2.9) Hz for magnetic field of B=8 G used during the campaign.

2.9, we've discussed how the forbidden bosonic clock transition becomes allowed by using a strong bias field which couples $^3\mathrm{P}_0$ and $^3\mathrm{P}_1$. We also mentioned that the use of this strong magnetic field will affect our accuracy budget. Let us now consider how the Zeeman shift due to the strong bias field will affect the $^1\mathrm{S}_0 \rightarrow {}^3\mathrm{P}_0$ clock transition.

The first order Zeeman shift is given as $\Delta\nu_{\mathrm{Z}}^{(1)} = \delta\mathrm{g}\mu_{\mathrm{B}}\mathrm{m_F}\mathrm{B}/\mathrm{h}$ where $\delta\mathrm{g}$ is the differential Landé factor which appears due hyperfine mixing between different states. Obviously, since $^{88}\mathrm{Sr}$ doesn't have hyper-

fine structure, the first order zeeman shift is zero. Therefore, the first contributing order of Zeeman shift is the 2nd order Zeeman shift which scales with the square of the magnetic field B. The quadratic Zeeman shift comes from the fact that both clock states have the same angular momentum J=0 with significant contribution of fine structure splitting from LS coupling. The quadratic shift is equal to

$$\Delta\nu_Z^2 = -\frac{2\alpha^2\mu_B^2}{3\Delta\nu_s h^2}B^2 = aB^2, \tag{6.2}$$

where $h\Delta\nu_s$ is the energy splitting between $^3\mathrm{P}_1$ and $^3\mathrm{P}_0$ states whose interaction is the biggest contributor the quadratic Zeeman shift since they are the two fine states closest in energy. To calibrate the quadratic Zeeman shift, we apply different values of magnetic field B, measure the shift of clock transition and perform 2nd order polynomial fit as shown in Fig. 6.1. We find the shift to be equal to -177.7(2.9) Hz for typical working conditions, consistent with results from a previous campaign in 2015 [118].

## 6.2 Lattice light shift

As we stated in a previous chapter, the light-atom interaction during the clock transition interrogation will induce a light shift of the clock transition. There are two light shifts induced in our clock - one from the optical lattice and another from the probe beam. We'll discuss the light shift from the optical lattice in this section and leave the probe beam light shift for the next section. The lattice light shift appears due to the interaction between the atoms and the trapping laser light from the optical lattice. This shift is given by Eq. 2.23 and depends on the difference in polarizability of the two clock states

$$\omega = \omega_0 - \frac{1}{4}\Delta\alpha(\omega_l)E^2 - \frac{1}{64}\Delta\gamma(\omega_l)E_0^4. \tag{6.3}$$

The lattice light shift was a significant hurdle in the early days of neutral atom optical clocks. The reason is the following: to ensure high-precision spectroscopy of the clock transition, we have to suppress the recoil shift from photons that are being absorbed by the atoms during clock transition interrogation. This suppression is done by loading atoms in the optical lattice in the Lamb-Dicke regime, as explained in previous chapters. The Lamb-Dicke regime, however, requires deep optical lattices, usually a few hundred recoil energies. Due to high detuning of the magic wavelength for any atomic transition in strontium, this in turn requires high intensity of light inside the dipole trap, usually dozens of $\mathrm{W/cm^2}$. Due to different polarizabilities of the ground and excited clock state at a given wavelength, the lattice AC Stark effect would heavily perturb the clock transition by shifting the clock states. The solution to this problem was ingeniously provided by Katori in 2003 [80] who suggested using an an optical lattice at the magic wavelength. At this wavelength, the polarizabilities of two clock states are the same and the lattice AC Stark shift vanishes. Such a optical lattice was achieved by Katori's group in 2005 [119].

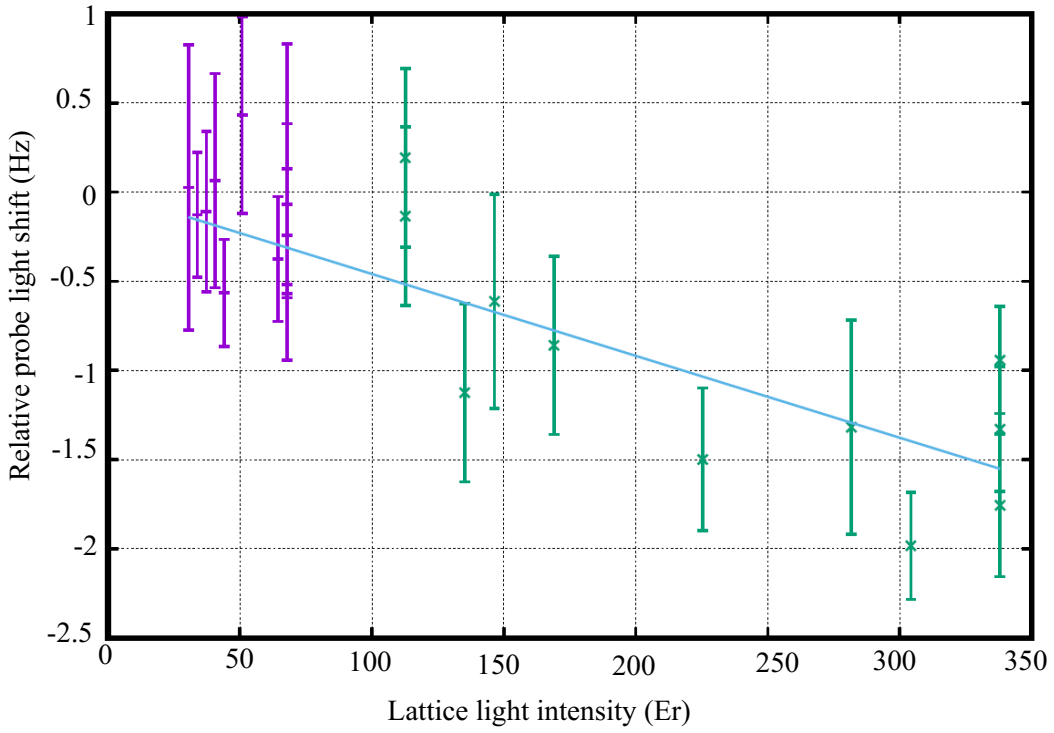


Figure 6.2: Dependence of the lattice light shift as a function of lattice light intensity. Violet and green points corresponds to measurements in Sr 1 and Sr 2, respectively. A linear function, represented by solid blue line, was fitted on the measured data sets. The lattice light shift was found to be equal to -0.34(47) Hz. Taken from [118] from the 2015 campaign.

Experimentally, the lattice light shift is evaluated by measuring the clock transition at different lattice depths. Evaluation of this lattice light shift is shown in Fig. 6.2. The lattice light shift was found to be equal to -0.34(47) Hz [118].

## 6.3 Probe light shift

The AC Stark shift doesn't come just from the far-detuned optical lattice, but also from the probe light used during interrogation of the $^1S_0 \rightarrow {}^3P_0$ transition. Here we need to remember that, while the probe beam intensity is not very high, the probe is at 698 nm which is not a magic wavelength for strontium and the polarizabilities of the clock states are different. This difference in polarizabilities is sufficiently large to induce a measurable probe light shift. In terms of probe beam intensities required to interrogate the clock transition, fermions require low intensities, usually in the $\mu W/cm^2$ as the fermion clock transition saturation intensity is $I_{sat} = 0.4\ pW/cm^2$ [63]. However, bosons require much higher probe

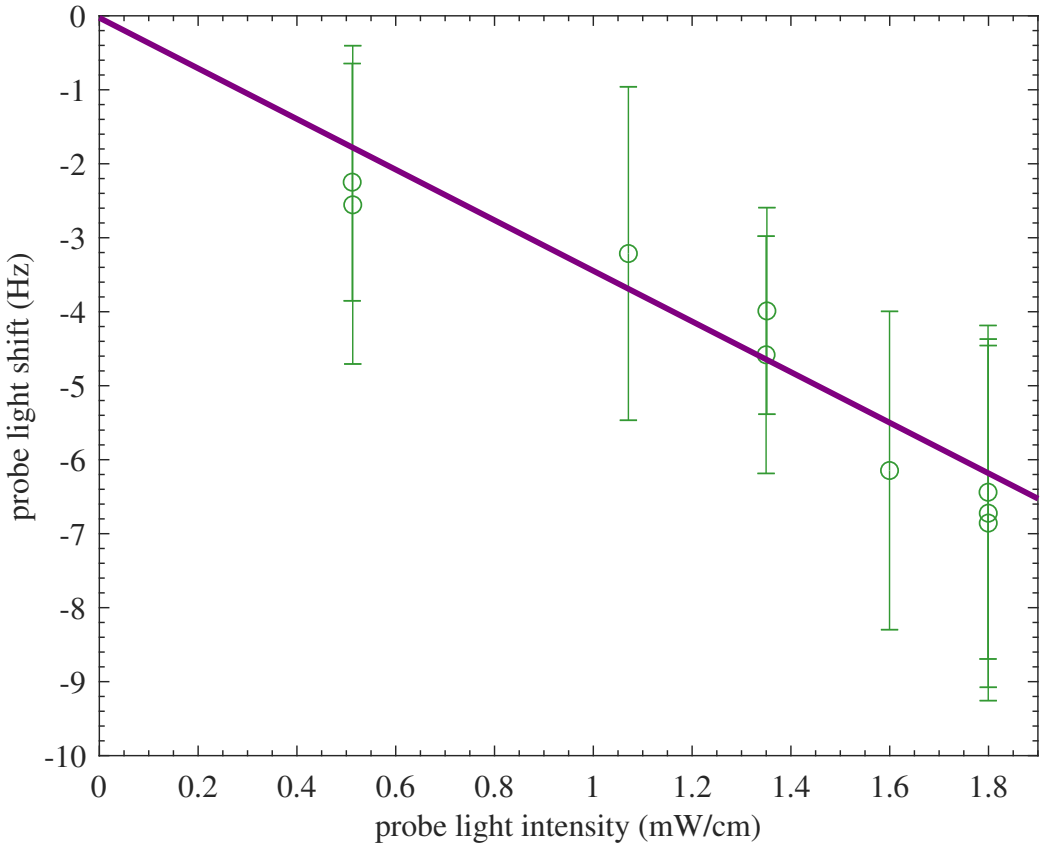


Figure 6.3: Dependence of the probe light shift as a function of probe light intensity. Green points correspond to measurements of the probe light shift of the clock transition as a function of the probe beam intensity. A linear function, represented by solid purple line, was fitted on the measured data sets. The shift was found to be equal to -6.51(75) Hz, consistent with the 2015 campaign.

light intensity of about $I_p \approx 400\,\mathrm{mW/cm^2}$ [120]. This high intensity again comes from the lack of bosonic hyperfine structure. Generally, it is possible to reduce the required intensity by increasing the bias magnetic field during interrogation. This makes it a balancing act between the probe light shift and the quadratic Zeeman shift. Evaluation of the probe light shift performed during the 2022 campaign is shown in Fig. 6.3. The probe light shift, represented by green points, was measured for different probe light intensities. A linear function, represented by solid purple line, was fitted to the measured data and the probe light shift was found to be equal to -6.51(75) Hz, again consistent with results from the 2015 campaign.

## 6.4 Density shift

One of the main advantages of neutral atoms optical clocks over their ion counterparts is the ability of interrogating many atoms simultaneously, increasing signal-to-noise ratio and improving clock stability. On the other hand, this also allows atoms within the optical lattice to interact with each other, inducing an interaction related shift.

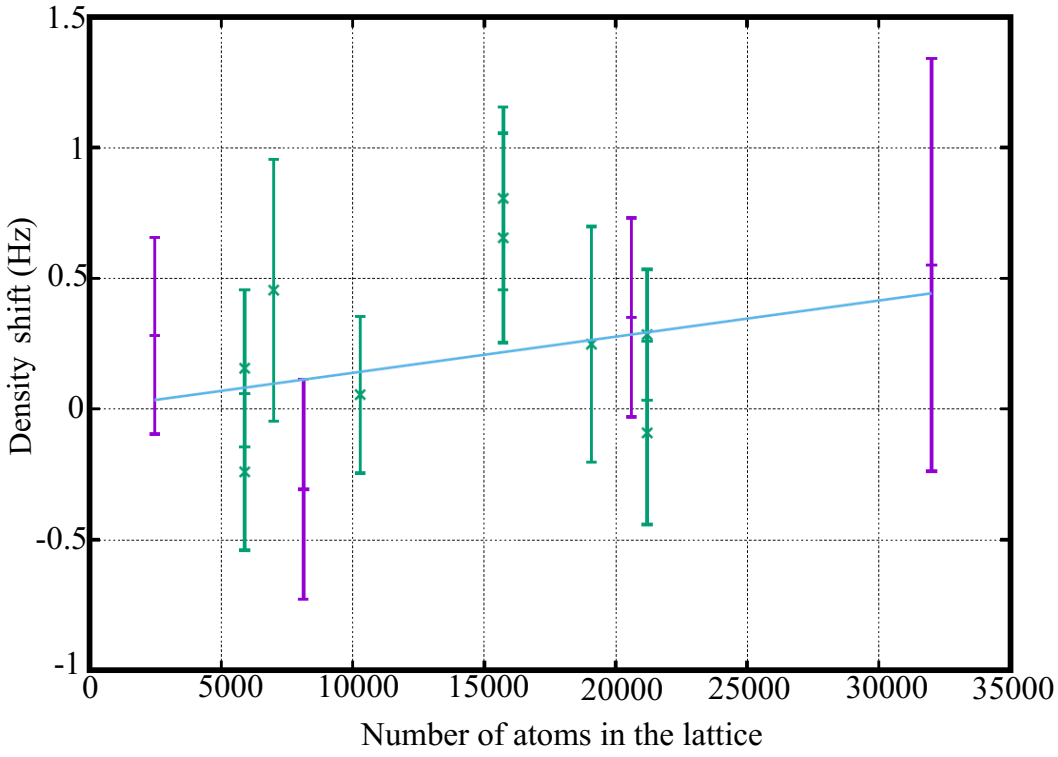


Figure 6.4: Dependence of density shift as a function of number of atoms in the optical lattice. Violet and green points correspond to measurements of density shift in Sr 1 and Sr 2, respectively. A linear function, represented by solid blue line, was fitted to the measured data and the shift was found to be equal to 0.35(52) Hz. Taken from [118] from the 2015 campaign.

This shift is significantly reduced for fermions where the lowest order s-wave scattering is forbidden due to Fermi exclusion principle and is one of the main advantages of using fermionic optical clock over a bosonic one. Also, higher order p-scattering is allowed in fermionic optical clock, but is strongly suppressed for sufficiently cold atomic samples due to the height of the centrifugal barrier [2]. Of course, since we are operating a bosonic optical clock here, there is no Fermi exclusion principle and s-wave scattering is allowed. This creates a larger density shift for the bosonic optical clock than it does for the fermionic one. To limit the perturbations of the clock transition by the density shift, we use a large waist of the optical lattice (of about 75 $\mu$m) and trap only few bosons per lattice site. The density shift was

measured by changing the number of atoms in the optical lattice. The density shift as a function of the number of atoms in the optical lattice is shown in Fig. 6.4. The density shift as a function of the number of atoms in the lattice was measured during the 2015 campaign and found to be equal to 0.35(52) Hz [118].

## 6.5 Collisional effects

Aside from collisions between different strontium atoms within the optical lattice, we also must consider the collisions of lattice atoms with the background gas. In case of ultra-high vacuum, most such collisions occur from interactions with hydrogen which is being released by the stainless steel chamber. The collisions kick strontium atoms out of the optical lattice and thus prevent them from being used in the clock frequency detection. However, this interaction will also induce a phase shift in the unscattered atoms. This shift can be assessed by using the approach given in [121]. And, while [121] focuses on Cs-He collisions, it can be adapted to apply to strontium as well. Along with knowing the $C_6$ van der Waals coeficients, which are similar for strontium and caesium, we also need to know the lifetime of atoms in the lattice, which in our case was 1.5s (cf. Fig 2.7). In our case, we expect the collisional shift not to be larger than 0.0(1) Hz.[1]

## 6.6 Black body radiation

The black body radiation (BBR) shift arises from the thermal radiation at temperature T of atoms' surroundings and resulting light shift. The biggest contribution to BBR at $\mathrm{T} = 300$ K is at $\lambda \approx 10\ \mu m$ as given by Wien's law with the largest portion of this shift coming from the electric dipole (E1) transition. The BBR shift can be written in two components:

$$\Delta\nu_{BBR} = \Delta\nu_{stat}\left(\frac{T}{T_0}\right)^4 + \Delta\nu_{dyn}\left(\frac{T}{T_0}\right)^6 + \mathcal{O}(T^8), \tag{6.4}$$

where $\Delta\nu_{\mathrm{stat}}$ and $\Delta\nu_{\mathrm{dyn}}$ are the static and dynamic BBR shift, respectively.

The static shift comes from the difference in polarizabilities of the clock states and the mean thermal field of the surrounding environment, while the dynamic BBR shift comes from the frequency dependence of the polarizability of each clock state and is calculated by integration over the entire BBR frequency spectrum. The dynamic BBR shift contribution to the total BBR shift is usually on the order of a few percent for Sr [122]. The static and dynamic BBR shifts were determined experimentally to be $\Delta\nu_{\mathrm{stat}} = -2.13023(6)$ Hz and $\Delta\nu_{\mathrm{dyn}} = -147.6(23)$ mHz [81], in good agreement with theoretical values calculated by Safronova et al. [124]. The method of evaluating the BBR shifts consists of precise

[1] This assessment was made by using results in [5] and accounting for the fact that our lattice lifetime is about an order of magnitude shorter than what was reported in there.

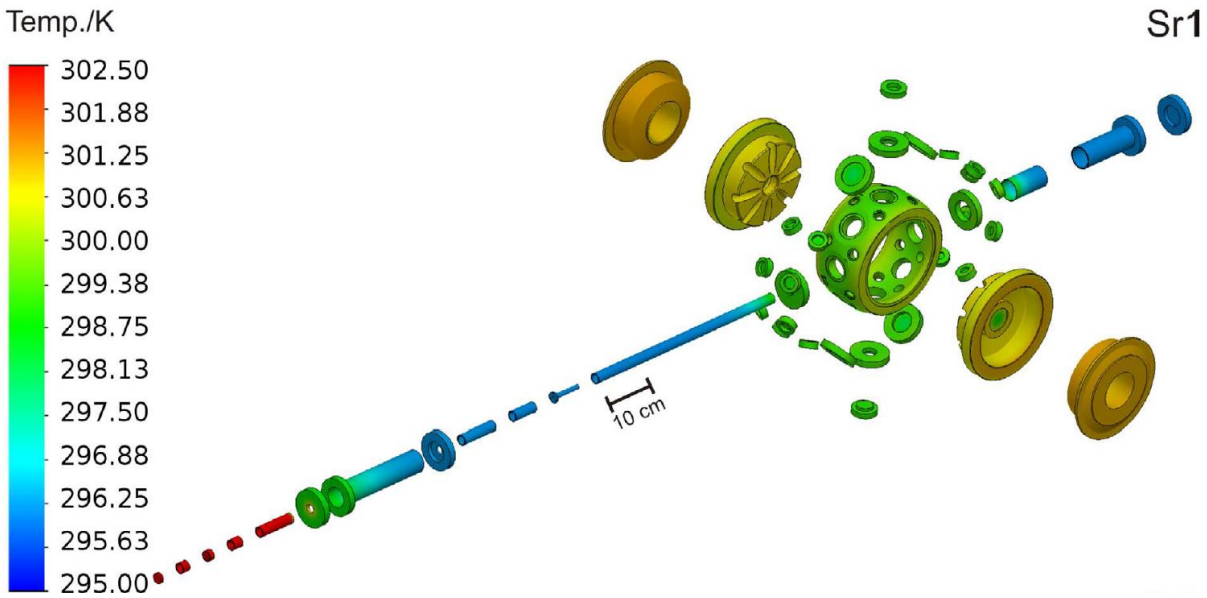


Figure 6.5: The simulated temperature distribution of the vacuum systems and theirs surroundings. The temperature of crucial points of the vacuum system was monitored during the experiment cycle by calibrated thermistors. The acquired data are used to calculate the temperature distribution of the system by a finite elements stationary thermal simulation. Note that for the sake of clarity the temperature of the strontium ovens (above 770 K) is not included in the temperature legend. Taken from [123].

measurements of temperature with temperature sensors at different points of the vacuum setup. In the simplest approach, the temperature of the hottest and coldest parts of the vacuum setup is measured. Usually, the hottest points of the vacuum setup are near the magnetic coils which, while cooled, still heat their surroundings and the coolest point somewhere far from the coils. At this point we simply assume that the effective temperature seen by the atoms is within those extremes. Additional BBR shift may also come from the strontium oven which is usually heated to $\mathrm{T} \approx 500\ ^{\circ}\mathrm{C}$ to ensure sufficient atom flux for clock operation as well as the windows of the vacuum chamber which have higher emissivity than the rest of the vacuum setup. Possible solutions to reduction of BBR shift is the use of cryogenic chamber cooled to $\mathrm{T} = 95\ \mathrm{K}$ in which atoms are then trapped and interrogated, reducing the BBR shift to $\nu_{\mathrm{BBR}} = -22\ \mathrm{mHz}$ [27]. Another possible solution is the installation of a thermal radiation "shield" with exceptional temperature uniformity, provided by highly thermally-conductive materials and platinum resistance temperature sensors to provide accurate absolute temperature of the shield [125]. The simulated temperature distribution of the vacuum systems and their surroundings in Sr 1 is shown in Fig. 6.4. The temperature of the different points of the vacuum system was measured during the clock cycle by calibrated thermistors. The measured data was used to calculate the temperature distribution of the system. The BBR shift, measured during the 2015 campaign [118], was found to be equal to -2.210(75) Hz.

## 6.7 Gravitational red shift

As given by Einstein' theory of general relativity, clocks at different gravitational potentials tick at different rates. This shift is called gravitational red shift and depends on the local height of the optical clock over the Geoid:

$$\frac{\Delta\nu}{\nu_0} = \frac{g\Delta h}{c^2}. \tag{6.5}$$

So two optical clocks at different heights, connected by a phase-coherent link, will see a fractional frequency difference between them. With their high sensitivity to gravitational changes, optical clocks have already been used to test the theory of general relativity [126, 127, 128]. A network of optical clocks could use be used to map the geo-potential of Earth, providing us with the "true" shape of our planet [129, 130, 131]. In the case of our optical clock, the height of the clock compared to the geoid is equal to 50(2) meters and the gravimetrically measured local value of the gravitational acceleration is equal to $9.8127208(26)\ \mathrm{m/s^2}$. This gives the gravitational red shift of 2.34(10) Hz [118].

## 6.8 Accuracy budget

The accuracy budget, as measured during our international 2022 campaign, is given in Table 6.1. All shifts and their uncertainties are given in Hz. I feel obliged to point out that two effects with highest contributions to the accuracy budget were explictly measured during the 2022 campaign - the quadratic Zeeman and the probe light shift. The remainder of the reported effects (aside from BBR shift) are at least one order of magnitude lower than the two highest contributing effects and therefore do not significantly change the accuracy budget and so were taken from the previous 2015 campaign.

| Effect | Shift (uncertainty) (Hz) |
|---|---|
| Quadratic Zeeman | -177.7(2.9) |
| Probe light shift | -6.51(75) |
| Lattice light shift | -0.34(47) |
| BBR shift | -2.210(75) |
| Density shift | 0.35(52) |
| Gravitational redshift | 2.34(10) |
| DDS and electronics | 0.00(16) |
| UTC(AOS)—UTC | -0.40(43) |
| **Total** | **-184.4(2.1)** |

Table 6.1: Evaluation of systematic shifts of bosonic optical clock in Sr 1 lab for standard experimental conditions performed during our international 2022 clock campaign. Total resulting shift of -184.4(2.1) Hz is consistent with the results from 2015 campaign [118].

# Chapter 7

# Conclusion

This thesis presents the work I've done during my three year stay at the Institute of Physics at the Nicolaus Copernicus University in Toruń, Poland. During this period, my work was partially focused on the study of feasibility of using blue magic wavelength optical lattices at 390 nm in strontium optical clocks. Most papers available on blue magic wavelength optical lattices, starting with [77], focus on determination of the magic wavelength and theoretical benefits of using blue magic wavelength lattices in reduction of lattice shifts. Our work, however, focused on experimental requirements such as lattice depths needed to ensure Lamb-Dicke regime, possible roadblocks in terms of photoionization of atoms out the lattice during clock cycle and ways to mitigate them. We believe this work will provide valuable and in some cases critical insight into implementation of blue magic wavelength lattices in optical clock setups.
Additionally, during my stay I worked on upgrading of the existing experimental setup with the goal of improving the stability and accuracy of our existing setups. My primary contribution is the work I've done on upgrading one the existing bosonic optical clock to enable both fermionic and bosonic optical clock operation. I fully upgraded our experimental setup and was able to bring the fermionic clock fully operational up to the single frequency red MOT stage, with other members continuing my work after my departure from POZA group. It is our hope to able to run our fermionic and bosonic clocks in a simultaneous (intermittent) manner and perform measurements of the fermionic clock transition frequency by comparison with its bosonic counterpart. Finally, the thesis presents (in form of published articles) the work I've done on examinations of interaction of rubidium atoms with a frequency comb as part of the Quantum technologies group at the Center for Advanced Laser Techniques at the Institute of Physics in Zagreb, Croatia. Our work focused on using frequency combs to cool down atoms in $^{85}\mathrm{Rb}$ and $^{87}\mathrm{Rb}$ MOTs as well as the examination of frequency-comb-induced radiation pressure force in dense atomic clouds. With this work, we aimed to present the versatility of the frequency comb, provide it an active role in the lab and show it can be more than just an "optical ruler". We hope that our work will broaden the applications of the frequency comb and bring it to new and exciting frontiers in the years to come.

# Curriculum vitae

Domagoj Kovačić was born in Zagreb, Croatia on January 13th, 1992. From 2007 to 2011 he attended "Archdiocesan Classical Gymnasium" high school in Zagreb. In 2011 he enrolled at the Department of Physics at the Faculty of Science in Zagreb, in an integrated undergraduate and graduate study of research physics. He graduated in 2017 with a masters' degree in Physics. The master thesis is titled "Generation of supercontinuum in nonlinear optical fiber" and was done at the Institute of Physics in Zagreb under supervision of dr. sc. Damir Aumiler. Since February 2018 he is employed at the Institute of Physics as a research assistant. Since the same year he's enrolled in the doctoral study of Atomic, Molecular and Optical Physics at the Faculty of Science in Zagreb. Since 2019 he's enrolled into the Interdisciplinary Doctoral Studies in Physical Sciences program at the Faculty of Physics, Astronomy and Informatics at the Nicolaus Copernicus University in Toruń.

As a dual PhD student at the University in Zagreb and Nicolaus Copernicus University in Toruń, he is a member of the Quantum Technologies group under the leadership of dr.sc. Ticijana Ban at the Institute of Physics in Zagreb and the Polish optical atomic clock group under the leadership of prof.hab. Michał Zawada at the Institute of Physics in Toruń. He was the recipient of the TEAM "A next-generation world-wide quantum sensor network with optical atomic clocks" (TEAM/2017-4/42/styp16) scholarship funded by Foundation for Polish Science (pl. Fundacja na rzecz Nauki Polskiej). He was also the recipient of the Opus 13 "Study of magic and magic-zero wavelength in optical lattice clocks with blue-detuned lattice" (UMO-2017/25/B/ST2/000429) scholarship funded by the National Science Centre (pl. Narodowe Centrum Nauki). During his doctoral study he was a teaching assistant at the Faculty of Science for experimental courses Physics Lab 1 and Physics Lab 2. He participated in popular science events.

# Appendix A - published articles

Research Article | Vol. 30, No. 12 / 6 Jun 2022 / Optics Express 21423
Optics EXPRESS

# Photoionization cross sections of ultracold $^{88}$Sr in $^1P_1$ and $^3S_1$ states at 390 nm and the resulting blue-detuned magic wavelength optical lattice clock constraints

MARCIN WITKOWSKI,[1,*] SŁAWOMIR BILICKI,[1] MARCIN BOBER,[1] DOMAGOJ KOVAČIĆ,[1,2] VIJAY SINGH,[1] ARA TONOYAN,[1,3] AND MICHAŁ ZAWADA[1]

[1] *Institute of Physics, Faculty of Physics, Astronomy and Informatics, Nicolaus Copernicus University, Grudziądzka 5, PL-87-100 Toruń, Poland*
[2] *Institute of Physics, Bijenička cesta 46, 10000 Zagreb, Croatia*
[3] *Institute for Physical Research, National Academy of Sciences of the Republic of Armenia, Ashtrarak-2, 0203, Armenia*
[*] *marcin_w@umk.pl*

**Abstract:** We present the measurements of the photoionization cross sections of the excited $^1P_1$ and $^3S_1$ states of ultracold $^{88}$Sr atoms at 389.889 nm wavelength, which is the magic wavelength of the $^1S_0$-$^3P_0$ clock transition. The photoionization cross section of the $^1P_1$ state is determined from the measured ionization rates of $^{88}$Sr in the magneto-optical trap in the $^1P_1$ state to be $2.20(50)\times10^{-20}$ m$^2$, while the photoionization cross section of $^{88}$Sr in the $^3S_1$ state is inferred from the photoionization-induced reduction in the number of atoms transferred through the $^3S_1$ state in an operating optical lattice clock to be $1.38(66)\times10^{-18}$ m$^2$. Furthermore, the resulting limitations of employing a blue-detuned magic wavelength optical lattice in strontium optical lattice clocks are evaluated. We estimated photoionization induced loss rates of atoms at 389.889 nm wavelength under typical experimental conditions and made several suggestions on how to mitigate these losses. In particular, the large photoionization induced losses for the $^3S_1$ state would make the use of the $^3S_1$ state in the optical cycle in a blue-detuned optical lattice unfeasible and would instead require the less commonly used $^3D_{1,2}$ states during the detection part of the optical clock cycle.



## 1. Introduction

Optical atomic clocks have proven to be excellent research instruments in various fields ranging from ultra-precise metrology [1–5], tests of fundamental physics [5,6] to searches for new matter in astrophysics [7–10]. Along with improving atomic optical clocks, the factors limiting their performance have become increasingly important. The perturbing effects induced by the environment, like light shifts [11], black-body radiation (BBR) shifts [12], and collisional shifts [13], are matters of growing experimental concern. Several solutions have been implemented to counteract these undesirable effects, like Pauli blocking mechanism [14,15], temperature decreasing through cryogenic systems [16], and light shift cancellation by magic-wavelength-based optical traps [17,18].

A blue-detuned optical trap has been proposed as an alternative to commonly used red-detuned optical traps [19]. In blue-detuned optical traps, atoms are confined near the minimum of light intensity, leading to a significant reduction of light-induced perturbations. On the other hand, if the energy of the blue-detuned trapping light photon is above the atomic ionization threshold, it may lead to atomic losses. Moreover, they were proposed together with the red-detuned conveyor

#460554 https://doi.org/10.1364/OE.460554
Journal © 2022 Received 6 Apr 2022; revised 30 Apr 2022; accepted 9 May 2022; published 31 May 2022

Optics EXPRESS

belt optical lattice as a way to realize an active optical atomic clock based on superradiance [20]. In the present work, we analyze the feasibility of the blue-detuned magic wavelength for the optical trapping of strontium atoms and possible atomic losses due to photoionization.

A blue-detuned magic wavelength for the $^1S_0$-$^3P_0$ clock transition in $^{87}Sr$ was experimentally determined to be 389.889(9) nm [19]. While these blue-detuned magic wavelength photons do not have sufficient energy to ionize the atoms directly from the strontium clock ($^1S_0$ and $^3P_0$) states, other states that are involved during the normal operation of the strontium optical lattice clock are potentially affected by the photoionization (see the region between the dashed lines in Fig. 1). For instance, the first stage of cooling down the atoms before loading them into the optical lattice is generally based on the $^1S_0$-$^1P_1$ transition (460.9 nm in Fig. 1), and the repumping during detection is based on the $^3P_0$-$^3S_1$ and $^3P_2$-$^3S_1$ transitions (679.3 nm and 707.2 nm, respectively, in Fig. 1) [21–23].

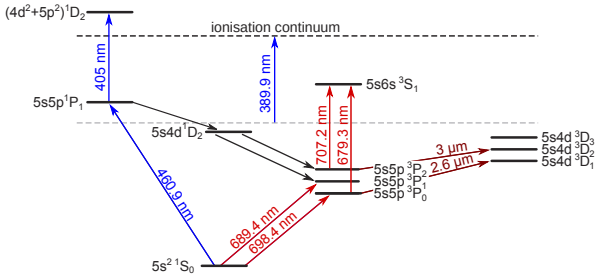


**Fig. 1.** Schematic energy level diagram showing relevant optical transitions used in the basic cycle of a strontium optical lattice clock. The 460.9 nm transition is used in the first stage of cooling and for imaging of atoms. The 689.4 nm transition is used in the next cooling stages and the optical pumping in fermionic isotopes. The 707.2 nm and 679.3 nm transitions are used to repump the $^3P_0$ and $^3P_2$ states. The 698.4 nm transition is the clock transition. The 405 nm wavelength corresponds to the autoionization resonance $(4d^2+5p^2)^1D_2$. The states belonging to the area bounded by the dashed lines are potentially affected by the photoionization light at 389.9 nm. The 3 µm and 2.6 µm transitions can be used as an alternative repumping scheme.

To determine photoionization cross sections for $^1P_1$ and $^3S_1$ levels, we used two different experimental methods. To investigate the photoionization effect on the $^1P_1$ state, we compared the dynamics of loading atoms into the magneto-optical trap (MOT) with and without the ionizing blue-detuned magic wavelength 389.889 nm light, alternately. To measure the photoionization cross section for $^3S_1$ state, we detect atomic losses from the optical lattice trap induced by the presence of an ionization laser beam at blue-detuned magic wavelength during the strontium optical lattice clock operation. The results of both measurements were used to analyze how the photoionization by the blue-detuned magic wavelength light affects the performance of the optical atomic clocks under typical experimental conditions. Since the magic wavelength does not depend heavily on the particular isotope, as was shown for the red-detuned magic wavelength of Sr at 813 nm [24], we based our research on a more abundant bosonic $^{88}Sr$ isotope without limiting the generality of our results.

Optics EXPRESS

## 2. Experiment

### 2.1. Experimental setup

The photoionization experiment has been performed on the Sr optical lattice atomic clock setup described in detail in [25] operating on $^{88}$Sr bosonic isotope. A basic cycle of this clock consists of cooling and loading atoms into a 1D red-detuned optical lattice trap, an interrogation of the clock transition by an ultra-stable clock laser, and detection of the resulting atomic population in the ground ($^1$S$_0$) and the excited ($^3$P$_0$) clock states [21]. Cooling and loading of atoms into the optical lattice trap are achieved by two consecutive MOTs, operating on the $^1$S$_0$-$^1$P$_1$ (blue MOT) and $^1$S$_0$-$^3$P$_1$ (red MOT) transitions, respectively. The clock $^1$S$_0$-$^3$P$_0$ transition is interrogated by the $\pi$-pulse Rabi excitation. The clock cycle is concluded by the detection phase that measures the ratio of populations in $^1$S$_0$ and $^3$P$_0$ states with the help of an electron shelving scheme [26], including fluorescence imaging on $^1$S$_0$-$^1$P$_1$ transition and optical pumping on $^3$P$_0$-$^3$S$_1$ and $^3$P$_2$-$^3$S$_1$ transitions.

The photoionization laser beam is synthesized via frequency doubling of a TiSa tunable laser light inside a bow-tie enhancement cavity. The resulting laser beam is spatially filtered with polarization-maintaining single-mode fibre and expanded by sets of lenses to either $\sigma_x$=7.034(85) mm and $\sigma_y$=6.07(30) mm or $\sigma_x$=2.19(11) mm and $\sigma_y$=1.88(12) mm beam waist radii and directed on atoms trapped by the blue MOT or the optical lattice trap, respectively. The diameter of the ionization beam is much larger than the typical dimensions of atomic clouds, i.e., 2.4 mm × 2.4 mm and 157 µm × 66 µm for blue MOT and the optical lattice, respectively. The frequency of the ionizing laser is stabilized to a wavemeter through an analogue feedback loop with an accuracy better than 100 MHz.

### 2.2. Photoionization of the $^1P_1$

To determine photo-induced losses from the $^1$P$_1$ state due to blue-detuned magic 389.889 nm light, we analyzed the fluorescence signal at 461 nm emitted by $^{88}$Sr atoms during the blue MOT loading phase. To ensure that the $^1$P$_1$ is the only possible ionized state, the repumping laser beams for the $^3$P$_0$ and $^3$P$_2$ states were switched off (see Fig. 1). The photoionization cross section $\sigma_{^1\mathrm{P}_1}$ was determined by comparing the loading rates of the MOT fluorescence with and without the photoionizing 389.889 nm light. This technique has proven very efficient in measuring absolute ionization cross sections of trapped atoms [27,28].

The rate equation for the number of atoms $N_{\mathrm{Sr}}$ loaded into the MOT can be expressed as [29]

$$\frac{dN_{\mathrm{Sr}}}{dt} = L_{\mathrm{Sr}} - (\gamma_{\mathrm{Sr}} + \gamma_P) N_{\mathrm{Sr}} - \beta_{\mathrm{SrSr}} \int dr^3 n_{\mathrm{Sr}}^2, \tag{1}$$

where $L_{\mathrm{Sr}}$ is the MOT loading rate, $\gamma_{\mathrm{Sr}}$ is the combined loss coefficient due to collisions with background gases, optical pumping to the metastable states and other possible single atom losses, $\gamma_P$ is the loss coefficient due to photoionization, $\beta_{\mathrm{SrSr}}$ is the loss coefficient due to light-assisted collisions between Sr atoms, and $n_{\mathrm{Sr}}$ is the spatial density of trapped atoms. In this approach, photoionization is considered as another mechanism of losses, linearly dependent on the number of atoms. The approach is valid if the photoionizing beam does not modify the density distribution of the MOT (e.g., by a dipole force), which is always fulfilled in our setup.

The experiment was performed in the low-density regime, which means that the mean free path of the atoms is larger than the size of the trapped atomic cloud. A typical number of strontium atoms in a blue MOT of a diameter of ~2 mm is ~6×10$^8$ [25]. It gives an atomic density of ~10$^{11}$ cm$^{-3}$. Using the $^{88}$Sr collision cross-section of 10$^{-13}$ cm$^2$ [30], the mean free path of the atoms trapped in the blue MOT is ~100 cm, which is very large compared to the size of the MOT. The low-density regime enables us to neglect the last term in Eq. (1) as the collisions between

Optics EXPRESS

trapped atoms are negligible. This yields the simplified rate equation

$$\frac{dN_{\mathrm{Sr}}}{dt} = L_{\mathrm{Sr}} - (\gamma_{\mathrm{Sr}} + \gamma_P) N_{\mathrm{Sr}}. \tag{2}$$

Integration of Eq. (2) over time gives the formula for the dependence of the number of atoms on time during MOT loading

$$N_{\mathrm{Sr}}(t) = \frac{L_{\mathrm{Sr}}}{\gamma_{\mathrm{Sr}} + \gamma_P} \left(1 - \exp\left(-\left(\gamma_{\mathrm{Sr}} + \gamma_P\right) t\right)\right), \tag{3}$$

where $N_{\mathrm{Sr}}(t = 0) = 0$.

The loss coefficient $\gamma_P$ is related to the intensity $I_P$ of the ionizing light through the expression

$$\gamma_P = \rho_{^1\mathrm{P}_1} \sigma_{^1\mathrm{P}_1} \frac{I_P}{h\nu_P}, \tag{4}$$

where $\rho_{^1\mathrm{P}_1}$ is the fraction of atoms in $^1\mathrm{P}_1$ excited state, $\sigma_{^1\mathrm{P}_1}$ is the photoionization cross section, and $I_P/h\nu_P$ is the ionizing photon flux. The frequency $\nu_P$ is determined with the type B standard uncertainty $u(\nu_P)$ derived from the accuracy of the wavemeter. To find the value of the $\gamma_P$ coefficient, two blue MOT loading curves were recorded sequentially in the presence and absence of the photoionization laser beam (see Fig. 2). By fitting Eq. (3) independently to both curves, we obtained loading rates $\gamma_{\mathrm{Sr}}$ and $\gamma_{\mathrm{Sr}} + \gamma_P$, and determined $\gamma_P$ by their difference. The typical loading curves detected in the experiment are presented in Fig. 3. For these curves, the loss coefficients are $\gamma_{\mathrm{Sr}}$=34.08(80) $\mathrm{s}^{-1}$ and $\gamma_{\mathrm{Sr}} + \gamma_P$=37.9(1.5) $\mathrm{s}^{-1}$, which corresponds to the reduction of the 1/e MOT loading time from 29.34(69) ms to 26.4(1.0) ms. To block the scattered light from the ionization laser, the blue MOT fluorescence was filtered by a 461 nm interference filter and then focused on a photodiode.

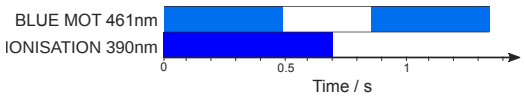


**Fig. 2.** The timing sequence of the lasers used in the $^1\mathrm{P}_1$ photoionization experiment. The time of the blue MOT's loading phase is identical in each sequence. To record the background from the ionization laser beam, it was kept on for a 200 ms longer compared to MOT's loading phase duration.

To determine the fraction of atoms in the excited state $\rho_{^1\mathrm{P}_1}$, a model for two-level system was used

$$\rho_{^1\mathrm{P}_1} = \frac{1}{2} \frac{I_{461}/I_{sat}}{I_{461}/I_{sat} + 4(\Delta/\Gamma)^2 + 1}, \tag{5}$$

where $I_{461}$ is the total intensity of the blue MOT trapping laser light, $I_{sat}$ is the $^1\mathrm{S}_0$-$^1\mathrm{P}_1$ transition saturation intensity (427 $\mathrm{W/m^2}$), $\Gamma$ is the natural decay rate of the excited $^1\mathrm{P}_1$ state ($2\pi \times 32$ MHz) and $\Delta$ is the trapping laser detuning from resonance (typically $2\Gamma$). The population fraction of the atoms in $^1\mathrm{P}_1$ state was varied by changing the trapping laser intensity. To calibrate the trapping laser intensity, a small portion of the trapping 461 nm laser light was uncoupled before splitting and sent to a photodetector to monitor the intensity $I_{461}$.

The detuning $\Delta$ was continuously measured by an optical frequency comb. The related uncertainties $u(I_{461})$ and $u(\Delta)$ were determined as standard deviations of their means. The intensity of the trapping laser light and its detuning from the resonance were continuously recorded by data acquisition software. The trapping beam is expanded to a diameter of 2 cm and is split into three retro-reflected beams. The typical value of the total intensity of the blue

Optics EXPRESS

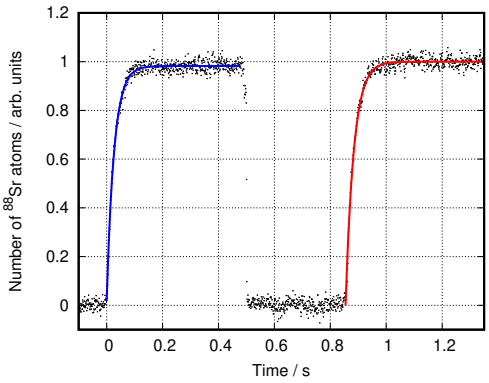


**Fig. 3.** Typical fluorescence of $^{88}$Sr atoms detected while loading into the blue MOT in the presence (left) and in the absence (right) of the photoionizing 389.889 nm light. The solid blue and red lines depict fitted Eq. (3).

MOT trapping laser light seen by atoms, taking into account losses on viewports and optics, is $I_{461} = 6{\times}30$ W/m$^2 \approx 0.42\ I_{sat}$. The methods that calibrate population dependence on the MOT beams intensity, described e.g., in [28,31], are not used here since they require laser light intensities exceeding the saturation of the transition. Instead, the measured values of $I_{461}$ and $\Delta$ are directly used in Eq. (5).

### 2.3. *Photoionization of the* $^3S_1$

To measure the photoionization cross section of $^3$S$_1$ state at 389.889 nm, we employed a different experimental approach. The experiment was performed during the standard clock cycle of the strontium optical lattice clock described in detail elsewhere [25]. The timing sequence of the laser beams used in the experiment is shown in Fig. 4. After sequential cooling in blue and red MOT Sr, atoms are transferred into the 1D vertical red-detuned magic wavelength optical lattice at 813 nm and interrogated by an ultrastable clock laser. The clock laser is locked to the $^1$S$_0$-$^3$P$_0$ transition in the second, independent strontium optical lattice clock. The clock laser interrogation pulse, long with respect to the transition Rabi frequency, is applied exactly on the transition centre frequency and excites one-half of the atoms ($N_e$) to the $^3$P$_0$ state while the rest of the atoms ($N_g$) remain in the ground $^1$S$_0$ state. Subsequently, after that, Sr atoms initially excited to the $^3$P$_0$ state are pumped back to the ground state through the $^3$S$_1$, $^3$P$_1$, and $^3$P$_2$ states with 679.3 nm and 707.2 nm transitions (see Figs. 1 and 4). The number of previously excited atoms $N_e$ is then determined by the second imaging pulse at 461 nm. The detection is concluded by a background image of the empty trap.

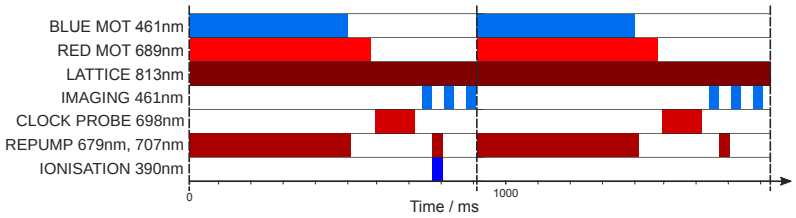


**Fig. 4.** The timing sequence of the lasers used in the $^3$S$_1$ photoionization experiment. It consists of two clock cycles, the first one (left) with an added photoionizing pulse, the second one (right) providing a background.

Optics EXPRESS

A pulse of the photoionizing beam added during the repumping phase of the first clock cycle opens a new channel of losses due to photoionization from the $^3S_1$ state. Therefore, it decreases repumping efficiency and, consequently, reduces the number of atoms recorded by the second imaging pulse. The photoionization cross section $\sigma_{^3S_1}$ is inferred from the photoionization-induced reduction in the number of atoms $\Delta N_e = N_e - N_e^I$, where $N_e^I$ and $N_e$ are the excited-state $^3P_0$ populations detected sequentially in the presence (the first cycle in Fig. 4) and absence of the photoionization beam (the second cycle in Fig. 4), respectively.

## 3. Results

### 3.1. Photoionization cross section at blue magic wavelength

The photoionization cross section $\sigma_{^1P_1}$ was determined from the loss coefficient $\gamma_P$ and characteristics of both the blue MOT and the ionizing beam. The atomic distribution in the blue MOT detected by a CCD camera is well described by the Gaussian-like profile

$$N(x,y) = \frac{2N_0}{\pi r_x r_y} \exp\left(\frac{-2x^2}{r_x^2}\right) \exp\left(\frac{-2y^2}{r_y^2}\right), \tag{6}$$

where $r_x, r_y$ are MOT radii (about 1.2 mm, typically). The averaged intensity of the ionizing light $\langle I_P \rangle$ seen by atoms in the blue MOT is given by

$$\langle I_P \rangle = \int\int \frac{I(x,y)N(x,y)}{N_0} dxdy, \tag{7}$$

where $N_0$ is the total number of atoms in the MOT, and $I(x,y)$ and $N(x,y)$ are distributions of the intensity of the beam and the atoms, respectively. The intensity profile of the photoionizing beam was determined by a CCD beam profiler measurement and corrected with the coefficient of transmission through the vacuum chamber viewports. The intensity of the ionizing light was power-locked and continuously monitored by a photodiode, and the related uncertainty $u(I_P)$ was calculated as a standard error of the mean of the recorded photodiode readout. The photodiode was calibrated based on the uncertainties related to the atomic distribution, namely $u(r_x)$ and $u(r_y)$.

The photoionization cross section $\sigma_{^1P_1}$ was calculated according to Eq. (4) by combining the measured values of the excited state fraction $\rho_{^1P_1}$, loss coefficient $\gamma_P$, and the intensity $\langle I_P \rangle$, monitored and recorded during measurements. We recorded 12 to 20 pairs of MOT loading curves sequentially with (the first curve) and without the photoionization beam (the second curve) for each wavelength of the photoionization beam separately. For each pair of curves, we determined the ionization loss rate $\gamma_P$ as the difference $(\gamma_{Sr} + \gamma_P) - \gamma_{Sr}$, where $\gamma_{Sr} + \gamma_P$ and $\gamma_{Sr}$ were determined by fitting the Eq. (3) to the first or the second curve, respectively. The uncertainty $u(\gamma_P)$ was calculated independently for each wavelength as the standard deviation of the mean. Finally, the uncertainty of the photoionization cross section $u(\sigma_{^1P_1})$ was calculated as a combined standard uncertainty with several independent quantities, namely $u(\gamma_P)$, $u(I_P)$, $u(\Delta)$, $u(I_{461})$, and $u(\nu_p)$.

To verify our experimental method, we extended the range of photoionization wavelengths to cover the autoionization resonance $(4d^2 + 5p^2)^1D_2$ near 405 nm [32–34]. This way, we enabled comparison with previous measurements of the autoionization resonance performed with different experimental approaches [35,36]. The measurements of $\sigma_{^1P_1}$ were carried out for wavelengths in a range from 378.4 nm to 407 nm. The results are shown in Fig. 5.

By fitting a Fano profile [37] to the measured points, we determined the position of the resonance and its peak value to be $\lambda_R$=405.196(44) nm and $\sigma_R$=5.20(94)×10$^{-19}$ m$^2$, respectively. To exclude another possible resonance observed on the high energy wing of the measured photoionization spectra, the fitting range was limited to the experimental points above 392 nm.

Optics EXPRESS

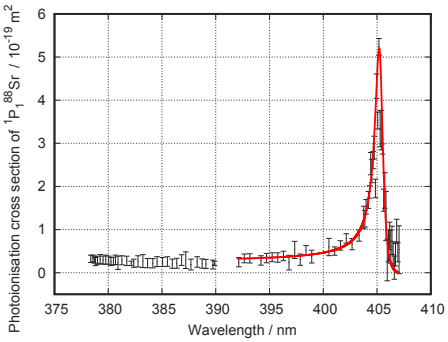


**Fig. 5.** The photoionization cross section from the $^1P_1$ state as a function of the wavelength of the ionizing light. The solid red line is a Fano profile fitted to the measured data. The fitting range is limited to the experimental points above 392 nm to exclude another possible resonance below 389.9 nm.

The gap in results between 390 nm and 392 nm is due to technical problems related to the locking of TiSa laser within the corresponding range. Our results are consistent with the results presented previously by Mende *et al.* ($\lambda_R$=405.213(2) nm, $\sigma_R$ = 5.6(1.1)×10$^{-19}$ m$^2$) [35] and by Sami-ul-Haq *et al.* ($\lambda_R$= 405.177(16) nm, $\sigma_R$=5.45(98)×10$^{-19}$ m$^2$) [36]. Note that previous measurements, unlike ours, did not involve cold atomic samples.

At the blue magic 389.889 nm wavelength, the photoionization cross section is equal to 2.20(50)×10$^{-20}$ m$^2$ (see Fig. 5). Our result is consistent with the value deduced from the curve reported by Mende *et al.* [35] 1.46(29)×10$^{-20}$ m$^2$, within the 20% uncertainty claimed by the author. In our case, the most significant factor contributing to the uncertainty of $\sigma_{^1P_1}$ comes from the fluctuation of the number of atoms loaded into the blue MOT. The atom number fluctuation affects the fitting uncertainty, however, as the statistical error, it is averaged, and it does not contribute to the final result, only to its uncertainty.

In the second set of experiments, the photoionization cross section from the $5s6s\,^3S_1$ excited state was determined by

$$\sigma_{^3S_1} = \frac{\langle \Delta N_e \rangle}{\langle N_e \rangle} \frac{h\nu_P}{\langle I_P \rangle t_{\rm int}}, \tag{8}$$

where $\langle N_e \rangle$ and $\langle \Delta N_e \rangle$ are the averaged excited state $^3P_0$ population and its averaged photoionization-induced reduction during the repumping through the $^3S_1$ state, respectively, $\langle I_P \rangle$ is the averaged intensity of the photoionization radiation seen by atoms in the optical lattice calculated according to Eq. (7), and $t_{\rm int}$ is the interaction time between photoionization beam and the atoms in the $^3S_1$ state. The value of $t_{\rm int}$ = 43 ns was determined on the basis of both $^3S_1 \rightarrow {}^3P_2$ and $^3S_1 \rightarrow {}^3P_0$ transition probabilities [38] and the natural lifetime of the $^3S_1$ state [39,40]. Additionally, in calculating the interaction time $t_{\rm int}$, we included repumping to the excited $^3S_1$ state back from $^3P_2$ and $^3P_0$ states. The ionization beam was power-locked with an intensity of 26270(80) W/m$^2$ at the Gaussian-profile peak. The $e^{-2}$ diameters of the beam (2.19(11)×1.88(12) mm) are much larger than the dimensions of the illuminated atomic cloud (157(10) µm x 66(6) µm). To ensure the stability of the number of atoms throughout each experimental cycle, we monitored both ground-state populations $N_g$ and $N_g^I$ independently. The experimental points satisfying the relation $(N_g - N_g^I)/N_g \rangle 2\%$ were excluded resulting in 3292 points left for further analysis. To be less prone to the oscillations of the number of atoms, we made the interleaved measurements randomly staggered by the manual triggering of consecutive cycles.

The determination of the cross section $\sigma_{^3S_1}$ based on Eq. (8) yields $\sigma_{^3S_1}$ = 1.38(66)×10$^{-18}$ m$^2$. The uncertainty of the $\sigma_{^3S_1}$ was calculated as the combined standard uncertainty involving the

Optics EXPRESS

uncertainties $u(\langle Ne\rangle)$, $u(\langle \Delta Ne\rangle)$, $u(\langle I_P\rangle)$, and $u(\nu_P)$. The frequency type B uncertainty $u(\nu_P)$ is derived from the resolution of the wavemeter. All the other terms are calculated as the standard deviations of their means.

### 3.2. *Study of feasibility: strontium optical clock with blue-detuned magic wavelength optical lattice*

In this section, we use our measured photoionization cross sections of $^1P_1$ and $^3S_1$ states to estimate the impact of the loss of the atoms from these states due to the ionization in a blue-detuned magic wavelength optical lattice on an optical strontium clock operation and suggest possible mitigation measures.

As mentioned above, in a blue-detuned magic wavelength optical lattice, atoms are confined at the minima of light intensity as opposed to a red-detuned magic wavelength optical lattice. However, the atoms cannot be trapped in a simple 1D blue-detuned magic wavelength lattice trap because they will escape along the radial directions. Confinement in all three orthogonal directions can be achieved, for instance, by a 3D optical lattice trap, made up of three independent 1D optical lattices [41]. Moreover, a 3D optical lattice will reduce the influence of interactions between atoms on the optical clock's accuracy [42].

To reach the accuracy goal of state-of-the-art optical lattice clocks, all frequency shifts connected with motional effects must be suppressed. When each atom is confined in a single lattice site to a region much smaller than the wavelength of the clock probing laser, and any tunnelling between sites is negligible, the Doppler and recoil shifts are suppressed, and the atoms are in the Lamb-Dicke regime [43,44]. This implies different limits on minimal required potential depth depending on the direction of the probing of the clock transition by a clock laser beam, either horizontal or vertical. On the other hand, higher potential means higher losses due to photoionization.

#### 3.2.1. Horizontal direction

In a horizontal periodic potential, the states with the same vibrational quantum number in different potential wells are degenerated in energy, amplifying tunnelling between the wells. This will spread out the spatial wave functions of the atoms so that they are not localized to a single well and create a band structure in their energy spectrum. This yields, depending on the initial state of the atoms in the trap, a broadening and a shift of the atomic transition of the order of the bandwidth of the lowest energy band of the system [45]. Figure 3 of [45] shows the corresponding bandwidth with the bandwidth in units of the recoil energy $E^{\mathrm{rec}}$ associated with the absorption or emission of a photon of the lattice light and in Hz units calculated for 813 nm magic wavelength.

Since the recoil energy scales like $k^2$, where $k$ is the wavenumber of the lattice light, in the blue-detuned lattice, for instance, the bandwidth of $\sim$ 1 mHz, corresponding to the $10^{-17} - 10^{-18}$ accuracy range, requires the potential depth above $\sim 125\ E^{\mathrm{rec}}$.

#### 3.2.2. Vertical direction

For a vertical clock laser probe beam, the approach from the previous subsection is no longer valid due to the presence of gravity. In the periodic potential in an accelerated frame, energies of atoms in adjacent lattice sites are shifted, and the Hamiltonian no longer supports bound states. This means that an atom in a vertical optical lattice will eventually tunnel to a continuum. Fortunately, the timescale of this process increases exponentially with lattice depth [45], and this is not an issue with the lattice depths considered here. Therefore, we must adopt the formalism of Wannier-Stark states [46]. The external Hamiltonian of an atom with mass $m$ in a vertical

Optics EXPRESS

lattice optical trap of the depth $U_{0z}$ is given as

$$\hat{H} = \frac{\hbar^2 \hat{\kappa}^2}{2m} + \frac{U_{0z}}{2}[1 - \cos(2k\hat{z})] + mg\hat{z}, \tag{9}$$

where $\kappa$ is the atom quasimomentum in z-direction. The eigenstates of this Hamiltonian are called Wannier-Stark states $|W_M\rangle$, where $M$ denotes $m$th well of the lattice. We have constructed the Wannier-Stark state as the sum of Wannier states in different lattice sites (i.e., the eigenstates of Hamiltonian in Eq. (9) without gravity) where every Wannier function is weighed by the appropriate Bessel function [47]. Figure 6 shows the spatial representation of Wannier-Stark states $|W_0\rangle$ centred around site $M = 0$ for different values of the lattice depth $U_{0z}$. The states are calculated for 390 nm blue-detuned lattice and, for comparison, for widely-used 813 nm red-detuned lattice. In both cases, we assumed that the tunnelling between different energy bands is negligible, i.e., the atom can only tunnel between lattice sites of the ground energy band.

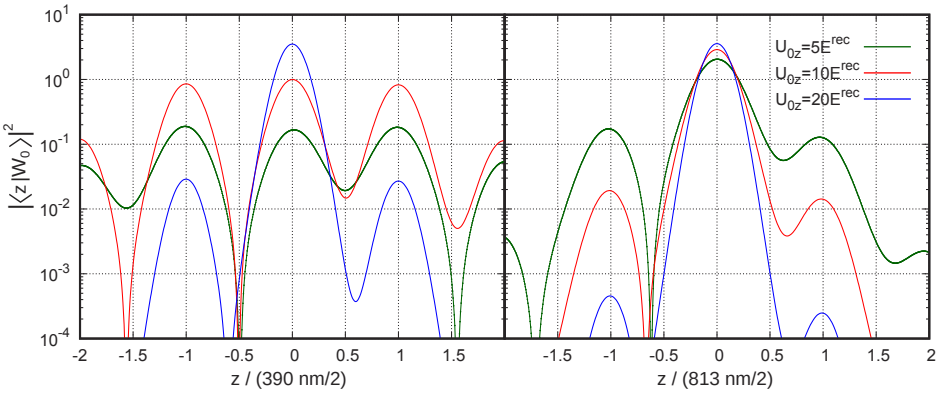


**Fig. 6.** Wannier-Stark states in position representation for different lattice depths for 390 nm (left) and 813 nm (right) magic wavelength lattices.

As seen in Fig. 6, for an 813 nm red-detuned optical lattice, the Wannier-Stark state consists of a main central peak and two smaller "revival" peaks in the adjacent wells, even for shallow lattices. These revival peaks decay quickly with increasing lattice depth, with revival peaks being hundred times smaller at lattice depths of 10 $E_z^{\text{rec}}$ and the wave function being practically localized to one lattice site [45]. To achieve similar ratios of the main and side peaks for a 390 nm blue-detuned lattice, the lattice should be at least twice as deep, i.e., $U_{0z} = 20\ E^{\text{rec}}$ because of the shorter distance between lattice sites and thus smaller energy shifts in the adjacent sites.

To examine the effects of coupling the Wannier-Stark states to their neighbors by the $^1S_0$-$^3P_0$ probe beam, we consider the Wannier-Stark ladder of states with an internal two-level energy structure $\left(|g, W_M\rangle, |e, W_M^{'}\rangle\right)$. The Wannier-Stark ladder is a set of Wannier-Stark states with one $|W_M\rangle$ state in each lattice site. Wannier-Stark states in the adjacent lattice sites are separated in energy by $\hbar\Delta_g$ corresponding to the change in gravitational potential between sites. For Sr, this separation between adjacent sites is equal to $\frac{\Delta_g}{2\pi} = 417$ Hz for 390 nm blue-detuned lattice. The energy difference between the ground $|g\rangle$ state and the excited $|e\rangle$ state of the atom is given by $\hbar\omega_{eg}$. The probe beam couples the $|g, W_M\rangle$ and $|e, W_M^{'}\rangle$ states with different coupling strengths $\Omega_{\Delta M}$, where $\Delta M = M^{'} - M = 0$ and $\Delta M \neq 0$ for coupling of WS states in the same lattice site and for coupling to neighboring lattice sites, respectively. This coupling corresponds to a translation in momentum space $e^{ik_c z}$ [45]:

$$\Omega_{\Delta M} = \Omega\langle W_M|e^{ik_c\hat{z}}|W_{M'}\rangle, \tag{10}$$

Optics EXPRESS

where $k_c$ is the wavevector of the coupling probe laser and $\Omega$ is the Rabi frequency. The relative coupling strengths $|\frac{\Omega_{\Delta M}}{\Omega}|^2$ of the "carrier" $\Omega_0$ and the first 4 "sidebands" $\Omega_{\pm1,\pm2}$ as a function of lattice depth are shown in Fig. 7 (left). For very shallow optical lattices with depths below $15E^{\text{rec}}$ the couplings show strong oscillations similar to those in [48]. For higher lattice depths, couplings to neighboring lattice sites rapidly decay and the atom becomes trapped in a single lattice with strong suppression of tunnelling between sites. Additionally, Fig. 7 (left) shows that for shallow lattice it is possible to choose different ratios of coupling parameters $\frac{\Omega_0}{\Omega_{1,2}}$ by tight control of lattice depth. This control over coupling parameters allows engineering of the extent of atomic wavefunctions through the adjustment of trap depth and thereby lowering the collisional frequency shifts arising the on-site p-wave and neighboring-site s-wave interactions, as done for 813 nm optical lattice [49]. For lattice depth of $20E^{\text{rec}}$, coupling strengths to the nearest and second-nearest lattice site are $10^{-2}$ and $10^{-4}$ times weaker than coupling between the ground $|g, W_M\rangle$ and excited $|g, W_M\rangle$ WS state in the same lattice site.

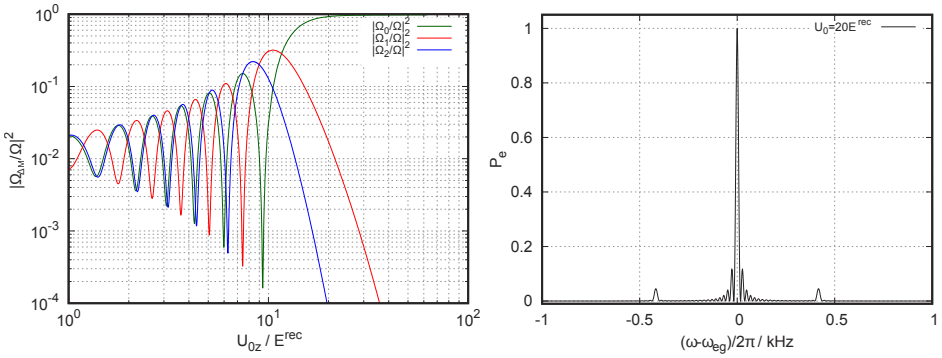


**Fig. 7.** (left) Relative coupling strengths $|\frac{\Omega_{\Delta M}}{\Omega}|^2$ of the carrier ($\Delta M = 0$) and first 4 sidebands ($\Delta M = \pm1$, $\Delta M = \pm2$) as a function of lattice depth for a blue-detuned optical lattice. (right) Transition probability $P_e$ of the $^1S_0$-$^3P_0$ clock transition for effective Rabi frequency $\Omega_0/2\pi = 10$ Hz and $\pi$-pulse interaction time of 50 ms when the initial state is a pure Wannier-Stark state and $U_0 = 20\ E^{\text{rec}}$.

To calculate the populations of the ground and excited WS states, we considered the evolution of the different states under coupling to the probe laser by numerically solving the set of differential equations [45]

$$\begin{aligned} i\dot{a}^g_M &= \sum_{M'} \frac{\Omega^*_{M-M'}}{2} e^{-i\pi M' k_c/k} e^{i\Delta_{M-M'}t} a^e_{M'}, \\ i\dot{a}^e_M &= \sum_{M'} \frac{\Omega_{M'-M}}{2} e^{i\pi M k_c/k} e^{-i\Delta_{M'-M}t} a^g_{M'}, \end{aligned} \tag{11}$$

where $a^g_M$ and $a^e_M$ are the probability amplitudes of the ground and excited state, respectively, and $\Delta_{M-M'} = \omega - \omega_{eg} + (M - M')\Delta_g$. In these calculations we assume that the atom can only tunnel to the nearest lattice site and the initial state is a pure WS state.

The computed resonances for a blue-detuned vertical optical lattice with depth of $20E^{\text{rec}}$, an effective Rabi frequency $\Omega_0/2\pi = 10$ Hz and interaction time of 50 ms are shown in Fig. 7 (right). The central resonance corresponds to the clock transition frequency $\omega_{eg}$ and two frequency sidebands located at $\pm\Delta_g/2\pi$ arise from weak tunnelling of atoms to neighboring sites and are completely symmetric with respect to the central resonance.

The results presented in Fig. 7 shows that the blue-detuned vertical lattice with depth of $20E^{\text{rec}}$ has similar level of suppression of the tunelling and of the effects of the atom dynamics as the

Optics EXPRESS

$10E^{rec}$ deep red-detuned optical lattice [45]. To hold the atoms in a 3D blue-detuned magic lattice, it is required that the energies of the first few lattice states are smaller than the lattice depth. The 20 $E^{rec}$ trap depth corresponds to around 14 μK and it is sufficiently deep to hold atoms cooled down by using the $^1S_0$-$^3P_1$ (red MOT) transition — typical temperatures achieved in the last cooling stage are of the order of 1 μK.

#### 3.2.3. Photoionization losses due to blue magic lattice

The previous subsections show that the minimal required optical trap potential depth for an effective operation of an optical strontium clock based on the blue-detuned 390 nm magic wavelength is on the order of 20 $E^{rec}$, assuming vertical probing of the clock transition. Now we want to estimate the losses due to the presence of the 3D blue-detuned lattice potential during a commonly used optical strontium clock operation cycle.

To characterize the photoionization losses, we consider two parts of the clock cycle when atoms are being cooled and trapped by the blue MOT and when the atoms are already loaded into the optical lattice. We assume that the 3D lattice potential is present during the whole clock cycle.

#### 3.2.4. Atoms trapped in the blue MOT

The photoionization losses can lower the total number of the atoms loaded into the blue MOT, which would decrease the number of atoms transferred into the 3D optical lattice trap and consequently lower the signal-to-noise ratio of the observed clock line. In the blue MOT phase atoms are cooled and trapped through the $^1P_1$ state. About 0.002% of atoms escape the closed cooling transition $^1S_0 \leftrightarrow {}^1P_1$ and must be repumped. Typically, the repumping through the $^3S_1$ state is chosen [50]. However, as the photoionization of the $^3S_1$ state by the blue-detuned light at 390 nm is significant, a different repumping scheme, e.g., through the $^3D$ state [51,52], is preferable.

In most of the present realizations of optical lattice clock, the centres of the blue MOT and the lattice trap overlap and the waist of the 1D optical lattice is much smaller than the atomic cloud trapped in the blue MOT. At the same time, with some notable exceptions [53], the optical lattice is shallow in comparison with the temperature of blue MOT atoms and they can freely pass the optical lattice area. Therefore, any losses due to photoionization in the blue MOT due to the blue magic 3D lattice can appear only when atoms are passing the optical lattice region.

To estimate the losses, we assume a typical blue MOT condition with maximum total intensity of the trapping beams equal to $I_{461} = 6{\times}30$ W/m$^2$ and their detuning from atomic resonance $\Delta = 1.25\Gamma$, and use Eq. (5) to calculate the relative population of atoms in the $^1P_1$ state, $\rho_{^1P_1} \approx 0.027$.

For the specific case of equal depths of all three blue detuned 1D lattices, and each of the depths equals to 20 $E^{rec}$ considered in the previous subsection, the intensity (averaged over time and space) of the 390 nm light experienced by the atoms passing the optical lattices periodic potentials, is $\sim 2.1 \times 10^8$ W/m$^2$. The resulting loss coefficient (Eq. (4)) is equal to $\gamma_P \approx 2.4 \times 10^5$ s$^{-1}$.

Assuming that blue MOT lifetime is limited by the collisions with the residual background gas molecules, the order of magnitude of the loss coefficient $\gamma_{Sr}$ in rate Eqs. (1–3) in real experimental system can be approximated by the collisional loss rate due to the collisions with $H_2$ reported in [54], resulting in $\gamma_{Sr} \approx 0.4$ s$^{-1}$ at the vacuum of $10^{-9}$ mbar. The loss rate connected with atoms' decay to metastable $^3P_2$ state in the case of operating blue MOT without repumpers is around 35 s$^{-1}$. Therefore, Eq. (3) shows that the blue MOT will be effectively depleted in the region where it overlaps with the 3D optical lattice trap made of three 20 $E^{rec}$ deep 1D optical lattices.

To overcome this loss of atoms, one can reduce the lattice intensity or even turn off the lattice beams during the blue MOT phase. Temporary switching off lattice light is technically feasible,

Optics EXPRESS

e.g., with the power build-up cavity installed inside the vacuum setup on a low expansion glass spacer. The lattice laser can be safely switched back on and relocked during the red MOT phase, which lasts a few tens of ms. Another possibility is to store cold atoms during the blue MOT phase in the dark $^3P_2$ state [55] or to use cold atomic beam loading directly the red MOT [56].

#### 3.2.5. Atoms trapped in the 3D optical lattice

After the interrogation of the clock transition, the populations of the ground and excited states are determined using the optical repumping through the $^1P_1$ and $^3S_1$ states, as discussed before. The effective intensity of the ionizing light seen by an atom trapped in the motional ground state of the optical lattice is determined by the modulus of its wave function $\psi$, approximated in horizontal and vertical directions by Wannier and Wannier-Stark states, respectively. Due to the short lifetimes of the atoms in the $^3S_1$ state, the spatial distribution of the atoms is determined by their preceding, metastable $^3P_0$ state (the short lifetime prevents changing the shape of the distribution in the new potential corresponding to the $^3S_1$ state polarizability before they decay to the lower states, which are not susceptible to photoionization). The $^{88}$Sr atoms have the same polarizabilities in the $^3P_0$ and $^1S_0$ states at the optical trapping magic wavelength (at 389.889 nm these polarizabilities are equal to 459 a.u. as calculated using the data in Ref. [57]), therefore in our calculations, we have used numerically calculated Wannier and Wannier-Stark states for a given potential scaled in the units of $E^{\mathrm{rec}}$.

The effective intensity from 1D lattice along $\zeta$ axis is calculated by

$$I_{\mathrm{eff},\zeta} = \int |\psi(\zeta)|^2 I(\zeta) d\zeta, \text{ with } \zeta = x, y, z, \tag{12}$$

where $I(\zeta) = I_{0\zeta} \sin^2(k_\zeta \zeta)$ is the standing wave intensity distribution and $I_{0\zeta}$ is the maximum intensity of each of 1D traps in $\zeta$ direction. It should be pointed out that the effective intensity $I_{\mathrm{eff},\zeta}$ is calculated differently than the average intensity $I_P$ from Eq. (7). $I_P$ is the average intensity of light from a single non-reflected photoionization beam with Gaussian intensity distribution, whereas the $I_{\mathrm{eff},\zeta}$ is the effective intensity which induces photoionization of atoms in the ground Wannier or Wannier-Stark state of the blue-detuned optical lattice periodic potential.

Figure 8 depicts the dependence of the total effective intensity in 3D lattice $I_{\mathrm{eff}} = \sum_\zeta I_{\mathrm{eff},\zeta}$ on the total amplitude of the potential $3U_0$. The blue crosses depict the values numerically calculated for Wannier-Stark (Wannier) states for the vertical (horizontal) directions in an optical lattice. In general, for deep enough optical lattice traps the calculations can be greatly simplified by approximating the system in Eq. (12) by a harmonic potential and its Gaussian ground states, which yields a square-root dependence of the effective intensity on the lattice potential (red crosses).

In the considered lattice consisting of three independent 1D lattices, each 20 $E^{\mathrm{rec}}$ deep, the $I_{\mathrm{eff}} \sim 4.6 \times 10^7$ W/m$^2$. To calculate the rate of losses for $^3S_1$ state, we replace in Eq. (4) the average intensity $I_P$ with the effective intensity $I_{\mathrm{eff}}$. The resulting rate of losses of atoms in the $^3S_1$ state due to photoionization is $1.26 \times 10^8$ s$^{-1}$, which is of the order of the $^3S_1$ state decay rate due to the natural lifetime. Such a large loss rate significantly limits the applicability of the blue magic lattice with a $^3S_1$-based repumping scheme. A possible solution is to employ an alternative repumping scheme through the $^3D_{1,2}$ states (see Fig. 1). As these $^3D$ states lie below the photoionization threshold for blue-detuned optical lattice, they are not affected by the photoionization induced losses from 390 nm wavelength light. However, the high IR wavelengths of 2.6 µm for the $^3P_0$-$^3D_1$ and 3 µm for the $^3P_2$-$^3D_2$ transition make the use of these transitions experimentally challenging as the lasers at these wavelengths are often not readily available. Additionally, the longer lifetimes of $\tau_{^3D_1} = 2.18(1)$ µs for $^3D_1$[1] and $\tau_{^3D_2} = 12.7$ µs for $^3D_2$ state (the value deduced from the energy diagram in [51]) would require longer repumping times during the detection of the clock transition.

Optics EXPRESS

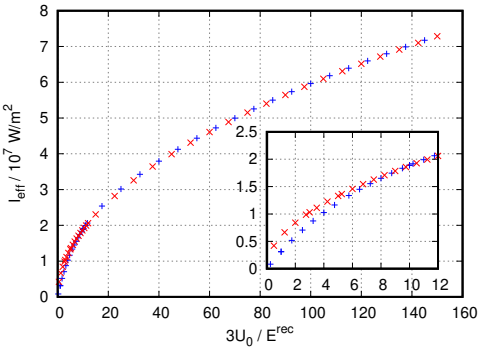


**Fig. 8.** The total effective intensity $I_{\text{eff}}$ experienced by the atoms trapped in the motional ground state of a 3D blue-detuned magic wavelength optical lattice. $I_{\text{eff}}$ values were calculated for Wannier-Stark (Wannier) states for the vertical (horizontal) directions in the optical lattice (blue crosses) and Gaussian states (red crosses) in a harmonic potential approximation.

#### 3.2.6. AC Stark shift from independent 1D lattices

To prevent interference between independent 1D lattices, small frequency detunings must exist between the light of each of the 1D lattices. While the detuning from the magic wavelength of the 1D lattice optical clock would add a considerable light shift to the clock frequency, in the 3D lattice the effective light shift can be still controlled at the required level. One can assume that the 1D optical lattice in the clock laser interrogation axis can be precisely tuned to the magic wavelength. With blue detuned optical lattice, all higher-order effects will be suppressed as atoms are trapped close to the intensity minimum. According to our calculations, a trapping depth of 20 $E^{\text{rec}}$ is enough for clock operations in the vertical direction. Tunnelling in horizontal directions do not have to be suppressed that well, and we assume individual trap depth to be 20 $E^{\text{rec}}$ as well. With the vertical lattice tuned to the magic wavelength, the required minimal detuning of two other individual lattice beams is determined by the atomic oscillation period and thus by the trap frequency. For a trapping depth of 20 $E^{\text{rec}}$, the trap frequency is around 135 kHz. With detuning around a few times the trap frequency, we can assume that potential can trap atoms efficiently. Both horizontal lattice beams can be detuned to opposite sides of magic wavelength, which in case of identical intensity and almost perfectly linear light shift scaling around magic wavelength [19] should cancel out individual light shifts. If we assume detuning of plus and minus 500 kHz of each horizontal lattice beam and a relative intensity difference of 3%, the induced effective light shift from detuning from both horizontal lattice beams can be controlled to the level of around $1 \times 10^{-19}$. For both horizontal lattices detuned by 1 MHz and an intensity mismatch of 5%, the induced effective light shift is still around $5 \times 10^{-19}$. For this estimation, we use the dependence of the intensity seen by atoms calculated in subsection 3.2.3.

## 4. Conclusion

In conclusion, we have determined the values of the $^{88}$Sr photoionization cross section at blue-detuned magic wavelength 389.889 nm to be 2.20(50)×$10^{-20}$ m$^2$ and 1.38(66)×$10^{-18}$ m$^2$, for the excited states $^1$P$_1$ and $^3$S$_1$, respectively. Additionally, we have measured the photoionization cross section for the $^1$P$_1$ state in a range from 378.4 nm to 407 nm and determined the position and the peak value of the autoionization resonance (4d$^2$+5p$^2$) $^1$D$_2$ to be 405.196(44) nm and 5.20(94)×$10^{-19}$ m$^2$, respectively. These results are consistent with the results previously reported [35,36], which, unlike ours, did not involve cold atomic systems.

Optics EXPRESS

To examine the potential feasibility of the blue-detuned magic wavelength strontium optical lattice trap, we have estimated photoionization-induced atomic losses in a three-dimensional optical lattice trap operating at the minimal intensity required to fulfil the Lamb-Dicke regime [43,44] for the clock transition. For a 3D lattice with lattice depths of $20E^{\mathrm{rec}}$ we found the rate of photoionization losses for $^1P_1$ and $^3S_1$ to be $\gamma_P \approx 2.4 \times 10^5$ s$^{-1}$ and $1.26 \times 10^8$ s$^{-1}$, respectively, and we have compared these losses with other channels of atomic losses during the standard operation of an optical lattice strontium clock. We also make several suggestions on mitigating the photoionization losses for $^1P_1$ and $^3S_1$ states, thus ensuring that neither of these loss channels is a critical defect for a blue-detuned lattice clock. In particular, the large photoionization loss rate in the blue-detuned optical lattice makes the use of $^3S_1$ state in the optical clock cycle unfeasible and would instead require the use of the less commonly $^3D_1$ state which, while feasible, adds additional experimental difficulties due to the high IR wavelengths of the relevant $^3P_0$-$^3D_1$ and $^3P_2$-$^3D_2$ transitions. Interestingly, the non-destructive measurements of the clock transition probability(e.g., [58,59]), assuming a different way of repumping, still seem compatible with the blue-detuned trap. The non-destructive measurements that utilize 461 nm light assume that the excited level is not populated thanks to detuning and low power of the local oscillator and probe beams (down to ~30 uW at the waist of ~75 um and detuning of ~2 GHz in the newest experiments, that corresponds to the relative population of atoms in the $^1P_1$ state, $\rho_{^1P_1} \approx 0.00025$), because any atom in the excited $^1P_1$ state in the optical lattice is lost from the relatively shallow optical trap.

Moreover, the schemes of a continuous superradiant optical active clocks that were proposed in [20] and related works that use a blue-detuned magic wavelength to realize the Lamb-Dicke regime are not using either the first-stage cooling or excitation readout in the presence of the blue-detuned optical lattice, therefore their feasibility is not affected by high photoionization cross sections. The losses can, however, impact newer proposals, that would improve the proposed scheme by including repumping of superradianting atoms by external incoherent pumping [60,61].

**Funding.** H2020 Future and Emerging Technologies (No 820404, iqClock project); The European Metrology Programme for Innovation and Research (EMPIR) Programme cofinanced by the Participating States and from the European Union's Horizon 2020 Research and Innovation Programme (EMPIR 17FUN03 USOQS); Fundacja na rzecz Nauki Polskiej (TEAM/2017-4/42); Narodowe Centrum Nauki (2017/25/B/ST2/00429, 2017/25/Z/ST2/03021).

**Acknowledgments.** The measurements were performed at the National Laboratory FAMO (KL FAMO) in Toruń, Poland, and were supported by a subsidy from the Polish Ministry of Science and Higher Education.

**Disclosures.** The authors declare no conflicts of interest.

**Data availability.** Data underlying the results presented in this paper are available in the open data repository [62].

## References

1. T. Nicholson, S. Campbell, R. Hutson, G. Marti, B. Bloom, R. McNally, W. Zhang, M. Barrett, M. Safronova, G. Strouse, W. L. Tew, and J. Ye, "Systematic evaluation of an atomic clock at $2 \times 10^{-18}$ total uncertainty," Nat. Commun. **6**(1), 6896 (2015).
2. M. Schioppo, R. C. Brown, W. F. McGrew, N. Hinkley, R. J. Fasano, K. Beloy, T. H. Yoon, G. Milani, D. Nicolodi, J. A. Sherman, N. B. Phillips, C. W. Oates, and A. D. Ludlow, "Ultrastable optical clock with two cold-atom ensembles," Nat. Photonics **11**(1), 48–52 (2017).
3. C. Lisdat, G. Grosche, and N. Quintin, *et al.*, "A clock network for geodesy and fundamental science," Nat. Commun. **7**(1), 12443 (2016).
4. J. Grotti, S. Koller, and S. Vogt, *et al.*, "Geodesy and metrology with a transportable optical clock," Nat. Phys. **14**(5), 437–441 (2018).
5. M. Takamoto, I. Ushijima, N. Ohmae, T. Yahagi, K. Kokado, H. Shinkai, and H. Katori, "Test of general relativity by a pair of transportable optical lattice clocks," Nat. Photonics **14**(7), 411–415 (2020).
6. P. Delva, J. Lodewyck, and S. Bilicki, *et al.*, "Test of Special Relativity Using a Fiber Network of Optical Clocks," Phys. Rev. Lett. **118**(22), 221102 (2017).
7. P. Wcisło, P. Morzyński, M. Bober, A. Cygan, D. Lisak, R. Ciuryło, and M. Zawada, "Experimental constraint on dark matter detection with optical atomic clocks," Nat. Astron. **1**(1), 0009 (2017).

Optics EXPRESS


8. P. Wcisło, P. Ablewski, and K. Beloy, *et al.*, "New bounds on dark matter coupling from a global network of optical atomic clocks," Sci. Adv. **4**(12), eaau4869 (2018).
9. B. M. Roberts, P. Delva, and A. Al-Masoudi, *et al.*, "Search for transient variations of the fine structure constant and dark matter using fiber-linked optical atomic clocks," New J. Phys. **22**(9), 093010 (2020).
10. C. J. Kennedy, E. Oelker, J. M. Robinson, T. Bothwell, D. Kedar, W. R. Milner, G. E. Marti, A. Derevianko, and J. Ye, "Precision metrology meets cosmology: Improved constraints on ultralight dark matter from atom-cavity frequency comparisons," Phys. Rev. Lett. **125**(20), 201302 (2020).
11. C. Shi, J.-L. Robyr, U. Eismann, M. Zawada, L. Lorini, R. Le Targat, and J. Lodewyck, "Polarizabilities of the $^{87}$Sr clock transition," Phys. Rev. A **92**(1), 012516 (2015).
12. T. Middelmann, S. Falke, C. Lisdat, and U. Sterr, "High Accuracy Correction of Blackbody Radiation Shift in an Optical Lattice Clock," Phys. Rev. Lett. **109**(26), 263004 (2012).
13. K. Gibble, "Scattering of Cold-Atom Coherences by Hot Atoms: Frequency Shifts from Background-Gas Collisions," Phys. Rev. Lett. **110**(18), 180802 (2013).
14. K. Gibble and B. J. Verhaar, "Eliminating cold-collision frequency shifts," Phys. Rev. A **52**(4), 3370–3373 (1995).
15. S. Gupta, Z. Hadzibabic, M. W. Zwierlein, C. A. Stan, K. Dieckmann, C. H. Schunck, E. G. M. van Kempen, B. J. Verhaar, and W. Ketterle, "Radio-Frequency Spectroscopy of Ultracold Fermions," Science **300**(5626), 1723–1726 (2003).
16. I. Ushijima, M. Takamoto, M. Das, T. Ohkubo, and H. Katori, "Cryogenic optical lattice clocks," Nat. Photonics **9**(3), 185–189 (2015).
17. H. Katori, M. Takamoto, V. G. Pal'chikov, and V. D. Ovsiannikov, "Ultrastable Optical Clock with Neutral Atoms in an Engineered Light Shift Trap," Phys. Rev. Lett. **91**(17), 173005 (2003).
18. I. Ushijima, M. Takamoto, and H. Katori, "Operational Magic Intensity for Sr Optical Lattice Clocks," Phys. Rev. Lett. **121**(26), 263202 (2018).
19. M. Takamoto, H. Katori, S. I. Marmo, V. D. Ovsiannikov, and V. G. Pal'chikov, "Prospects for Optical Clocks with a Blue-Detuned Lattice," Phys. Rev. Lett. **102**(6), 063002 (2009).
20. G. A. Kazakov and T. Schumm, "Active optical frequency standard using sequential coupling of atomic ensembles," Phys. Rev. A **87**(1), 013821 (2013).
21. A. D. Ludlow, M. M. Boyd, J. Ye, E. Peik, and P. O. Schmidt, "Optical atomic clocks," Rev. Mod. Phys. **87**(2), 637–701 (2015).
22. M. Takamoto, F.-L. Hong, R. Higashi, and H. Katori, "An optical lattice clock," Nature **435**(7040), 321–324 (2005).
23. A. D. Ludlow, M. M. Boyd, T. Zelevinsky, S. M. Foreman, S. Blatt, M. Notcutt, T. Ido, and J. Ye, "Systematic study of the $^{87}$Sr clock transition in an optical lattice," Phys. Rev. Lett. **96**(3), 033003 (2006).
24. T. Takano, R. Mizushima, and H. Katori, "Precise determination of the isotope shift of $^{88}$Sr-$^{87}$Sr optical lattice clock by sharing perturbations," Appl. Phys. Express **10**(7), 072801 (2017).
25. M. Bober, P. Morzyński, and A. Cygan, *et al.*, "Strontium optical lattice clocks for practical realization of the metre and secondary representation of the second," Meas. Sci. Technol. **26**(7), 075201 (2015).
26. H. G. Dehmelt, "Monoion oscillator as potential ultimate laser frequency standard," IEEE Trans. Instrum. Meas. **IM-31**(2), 83–87 (1982).
27. T. P. Dinneen, C. D. Wallace, K.-Y. N. Tan, and P. L. Gould, "Use of trapped atoms to measure absolute photoionization cross sections," Opt. Lett. **17**(23), 1706–1708 (1992).
28. M. Witkowski, R. Munoz-Rodriguez, A. Raczyński, J. Zaremba, B. Nagórny, P. S. Żuchowski, R. Ciuryło, and M. Zawada, "Photoionization cross sections of the $5S_{1/2}$ and $5P_{3/2}$ states of Rb in simultaneous magneto-optical trapping of Rb and Hg," Phys. Rev. A **98**(5), 053444 (2018).
29. C. Gabbanini, S. Gozzini, and A. Lucchesini, "Photoionization cross section measurement in a Rb vapor cell trap," Opt. Commun. **141**(1-2), 25–28 (1997).
30. G. Ferrari, R. E. Drullinger, N. Poli, F. Sorrentino, and G. M. Tino, "Cooling of Sr to high phase-space density by laser and sympathetic cooling in isotopic mixtures," Phys. Rev. A **73**(2), 023408 (2006).
31. M. H. Shah, H. A. Camp, M. L. Trachy, G. Veshapidze, M. A. Gearba, and B. D. DePaola, "Model-independent measurement of the excited fraction in a magneto-optical trap," Phys. Rev. A **75**(5), 053418 (2007).
32. P. Ewart and A. F. Purdie, "Laser ionization spectroscopy of Rydberg and autoionization levels in Sr I," J. Phys. B **9**(15), L437–L441 (1976).
33. P. Esherick, "Bound, even-parity $J = 0$ and $J = 2$ spectra of Sr," Phys. Rev. A **15**(5), 1920–1936 (1977).
34. M. Baig, M. Yaseen, R. Ali, A. Nadeem, and S. Bhatti, "Near-threshold photoionization spectra of strontium," Chem. Phys. Lett. **296**(3-4), 403–407 (1998).
35. W. Mende, K. Bartschat, and M. Kock, "Near-threshold photoionization from the Sr I $(5s5p)^1P_1^o$ state," J. Phys. B: At., Mol. Opt. Phys. **28**(12), 2385–2393 (1995).
36. S. ul Haq, S. Mahmood, N. Amin, Y. Jamil, R. Ali, and M. A. Baig, "Measurements of photoionization cross sections from the 5s5p $^1P_1$ and 5s6s $^1S_0$ excited states of strontium," J. Phys. B: At., Mol. Opt. Phys. **39**(7), 1587–1596 (2006).
37. U. Fano, "Effects of Configuration Interaction on Intensities and Phase Shifts," Phys. Rev. **124**(6), 1866–1878 (1961).
38. G. García and J. Campos, "Transition probabilities for triplet levels of Sr(I)," J. Quant. Spectrosc. Radiat. Transfer **39**(6), 477–483 (1988).

Optics EXPRESS


39. G. Jöhnsson, C. Levinson, A. Persson, and C. G. Wahlström, "Natural radiative lifetimes in the $^1P_1$ and $^1F_3$ sequences of Sr I," Z. Rev. A **316**, 255–258 (1984).
40. S. G. Porsev, A. D. Ludlow, M. M. Boyd, and J. Ye, "Determination of Sr properties for a high-accuracy optical clock," Phys. Rev. A **78**(3), 032508 (2008).
41. S. Will, *From Atom Optics to Quantum Simulation. Interacting Bosons and Fermions in Three-dimensional Optical Lattice Potentials* (Springer-Verlag Berlin Heidelberg, 2013).
42. S. L. Campbell, R. B. Hutson, G. E. Marti, A. Goban, N. Darkwah Oppong, R. L. McNally, L. Sonderhouse, J. M. Robinson, W. Zhang, B. J. Bloom, and J. Ye, "A fermi-degenerate three-dimensional optical lattice clock," Science **358**(6359), 90–94 (2017).
43. R. H. Dicke, "The effect of collisions upon the doppler width of spectral lines," Phys. Rev. **89**(2), 472–473 (1953).
44. D. J. Wineland and W. M. Itano, "Laser cooling of atoms," Phys. Rev. A **20**(4), 1521–1540 (1979).
45. P. Lemonde and P. Wolf, "Optical lattice clock with atoms confined in a shallow trap," Phys. Rev. A **72**(3), 033409 (2005).
46. G. H. Wannier, "Wave functions and effective hamiltonian for bloch electrons in an electric field," Phys. Rev. **117**(2), 432–439 (1960).
47. M. Glück, A. R. Kolovsky, and H. J. Korsch, "Wannier-Stark resonances in optical and semiconductor superlattices," Phys. Rep. **366**(3), 103–182 (2002).
48. G. Tackmann, B. Pelle, A. Hilico, Q. Beaufils, and F. Pereira dos Santos, "Raman-laser spectroscopy of wannier-stark states," Phys. Rev. A **84**(6), 063422 (2011).
49. T. Bothwell, C. Kennedy, A. Aeppli, D. Kedar, J. Robinson, E. Oelker, A. Staron, and J. Ye, "Resolving the gravitational redshift across a millimetre-scale atomic sample," Nature **602**(7897), 420–424 (2022).
50. I. Courtillot, A. Quessada-Vial, A. Brusch, D. Kolker, G. D. Rovera, and P. Lemonde, "Accurate spectroscopy of Sr atoms," Eur. Phys. J. D **33**(2), 161–171 (2005).
51. P. G. Mickelson, Y. N. M. de Escobar, P. Anzel, B. J. DeSalvo, S. B. Nagel, A. J. Traverso, M. Yan, and T. C. Killian, "Repumping and spectroscopy of laser-cooled Sr atoms using the (5s5p)3P2–(5s4d)3D2 transition," J. Phys. B: At., Mol. Opt. Phys. **42**(23), 235001 (2009).
52. S. Zhang, P. Ramchurn, M. Menchetti, Q. Ubaid, J. Jones, K. Bongs, and Y. Singh, "Novel repumping on 3P0 → 3D1 for Sr magneto-optical trap and Landé g factor measurement of 3D1," J. Phys. B: At., Mol. Opt. Phys. **53**(23), 235301 (2020).
53. X. Baillard, M. Fouché, R. L. Targat, P. G. Westergaard, A. Lecallier, Y. L. Coq, G. D. Rovera, S. Bize, and P. Lemonde, "Accuracy evaluation of an optical lattice clock with bosonic atoms," Opt. Lett. **32**(13), 1812–1814 (2007).
54. M. Abdel-Hafiz, P. Ablewski, and A. Al-Masoudi, *et al.*, "Guidelines for developing optical clocks with $10^{-18}$ fractional frequency uncertainty," arXiv:1906.11495 (2019).
55. S. Stellmer, M. K. Tey, B. Huang, R. Grimm, and F. Schreck, "Bose-Einstein Condensation of Strontium," Phys. Rev. Lett. **103**(20), 200401 (2009).
56. C.-C. Chen, S. Bennetts, R. G. Escudero, B. Pasquiou, and F. Schreck, "Continuous Guided Strontium Beam with High Phase-Space Density," Phys. Rev. Appl. **12**(4), 044014 (2019).
57. X. Zhou, X. Xu, X. Chen, and J. Chen, "Magic wavelengths for terahertz clock transitions," Phys. Rev. A **81**(1), 012115 (2010).
58. G. Vallet, E. Bookjans, U. Eismann, S. Bilicki, R. L. Targat, and J. Lodewyck, "A noise-immune cavity-assisted non-destructive detection for an optical lattice clock in the quantum regime," New J. Phys. **19**(8), 083002 (2017).
59. R. Hobson, W. Bowden, A. Vianello, I. R. Hill, and P. Gill, "Cavity-enhanced non-destructive detection of atoms for an optical lattice clock," Opt. Express **27**(26), 37099–37110 (2019).
60. C. Hotter, D. Plankensteiner, L. Ostermann, and H. Ritsch, "Superradiant cooling, trapping, and lasing of dipole-interacting clock atoms," Opt. Express **27**(22), 31193–31206 (2019).
61. A. Bychek, C. Hotter, D. Plankensteiner, and H. Ritsch, "Superradiant lasing in inhomogeneously broadened ensembles with spatially varying coupling [version 2; peer review: 2 approved]," Open Res. Europe **1**, 73 (2021).
62. W. Marcin, B. Sławomir, M. Bober, D. Kovačić, V. Singh, A. Tonoyan, and M. Zawada, "Photoionisation losses in a strontium optical lattice clock operating at blue-detuned magic wavelength light," (2022), RepOD https://doi.org/10.18150/LQ6WUK.

Research Article Vol. 39, No. 5 / May 2022 / Journal of the Optical Society of America B 1411

Journal of the Optical Society of America B

OPTICAL PHYSICS

# Frequency-comb-induced radiation pressure force in dense atomic clouds

Mateo Kruljac,* Danijel Buhin, Domagoj Kovačić, Vjekoslav Vulić, Damir Aumiler, and Ticijana Ban

*Institute of Physics, Bijenička cesta 46, 10000 Zagreb, Croatia*
**Corresponding author: mkruljac@ifs.hr*

*Received 1 December 2021; revised 28 March 2022; accepted 28 March 2022; posted 28 March 2022; published 22 April 2022*

**We investigate the frequency-comb-induced radiation pressure force acting on a cloud of cold $^{87}$Rb atoms. Reduction and spectral broadening of the frequency comb force are observed as the cloud's optical thickness is increased. Since the radiation pressure force is uniquely determined by light scattered by an atomic cloud, we discuss different scattering mechanisms and point to the shadow effect as the dominant mechanism affecting the FC-induced force in resonantly excited dense atomic clouds. Our results improve the understanding of the interaction of frequency comb light with many-atom ensembles, which is essential for novel frequency comb applications in simultaneous multispecies cooling and self-ordering, multimode quantum memories, and quantum computing.** 

https://doi.org/10.1364/JOSAB.449798

## 1. INTRODUCTION

Investigation of light scattered from an ensemble of cold atoms illuminated by a continuous wave (cw) laser has been a fruitful platform for studying light–matter interactions [1–5]. Cooperative scattering by an ensemble of resonant systems has been studied in detail by Dicke [6], which led to understanding of super-radiance and collective level shifts. Since the scattered intensity is directly mapped to the radiation pressure force, several experiments studied the cw-induced radiation pressure force on a cold atomic cloud in order to capture the signature of cooperative effects [7–10]. The later studies, however, indicated that specific effects observed in cw laser radiation pressure force may not always be a signature of cooperativity but a result of different scattering mechanisms such as attenuation of the probe light, diffraction and refraction, multiple scattering, etc. [11,12].

In contrast with the extensive studies using cw lasers, the investigations of light scattered from an ensemble of cold atoms illuminated by a mode-locked femtosecond laser, i.e., a frequency comb (FC), are scarce in the literature. FCs are unique sources of light with novel applications in laser–atom interaction studies that extend from FC cooling [13–16] and self-ordering [17] to multimode quantum memories [18,19] and quantum computing [20,21]. In the time-domain, frequency combs are represented by a train of phase-stabilized ultrashort pulses; in the frequency domain, their spectrum consists of a large number of equidistant narrow lines, i.e., comb modes.

When the excitation of atoms is considered, a single mode within the comb spectrum will act as a cw laser. The FC-atom interaction will, on the other hand, generally be much more complex, as many comb lines (modes) that are present in the comb spectrum can simultaneously interact with the atoms [16]. In general, when atoms are excited by a train of ultrashort pulses from a mode-locked laser, coherent accumulation of population and coherence will occur in the condition when the atomic relaxation times are longer than the laser repetition period [22–24]. The coherent effects depend on the comb spectrum and the atomic energy levels. It is therefore not trivial to make conclusions on the nature of the FC–atom interaction in specific applications, such as the determination of FC-induced radiation pressure force on atoms. The FC-induced force on single atoms can readily be calculated using the optical Bloch equations and the Ehrenfest theorem [14]; however, this approach becomes increasingly complex in dense atomic ensembles, where the radiation pressure force starts to differ from the single-atom force. This can be achieved even for the optical thickness of the order of 1 for on-resonance excitation.

In this paper, we investigate the FC-induced radiation pressure force acting on a dense cloud of cold atoms with an on-resonance optical thickness up to 20. Reduction and spectral broadening of the frequency comb force are observed as the cloud's optical thickness is increased. We discuss the role of diffuse, Mie, and cooperative scattering in the measured FC-induced force, using theoretical models developed for the radiation pressure force induced by the cw laser excitation. We show that the FC-induced radiation pressure force is predominately affected by the progressive attenuation of the light



0740-3224/22/051411-08 Journal 

intensity within the cloud due to diffuse scattering of light. We identify the so-called shadow effect as the dominant mechanism affecting the FC-induced force in dense atomic clouds. Our results provide better understanding of the frequency comb excitation of dense clouds of multilevel atoms. The results support the considerations in [11] for the case of the cw-induced force, thus verifying the analogy between the frequency comb and cw laser excitation of an atomic ensemble.

## 2. EXPERIMENT

A simplified scheme of the experimental setup for the preparation of a cold $^{87}$Rb cloud and its characterization using absorption imaging as well as the setup for FC force measurement using fluorescence imaging is shown in Fig. 1(a).

**Preparation of a cloud of cold atoms.** A cold $^{87}$Rb cloud is loaded from a background vapor in a stainless-steel vacuum chamber with AR-coated viewports for 780 nm light, using a standard six-beam configuration in a magneto-optical trap (MOT). The pressure level in the chamber is around $10^{-8}$ mbar. The preparation of a cold cloud of a given optical thickness is achieved in three consecutive stages: MOT loading, temporal dark MOT, and repumping stage. In the first stage, we load the MOT for 6 s, with the cooling laser detuned $-3.5\Gamma$ from the $^{87}$Rb $|5S_{1/2};\, F=2\rangle \rightarrow |5P_{3/2};\, F'=3\rangle$ transition, and the repumper laser in resonance with the $|5S_{1/2};\, F=1\rangle \rightarrow |5P_{3/2};\, F'=2\rangle$ transition, generating a cloud of $\approx 4\cdot 10^7$ atoms at a temperature of around 50 μK and a $1/e^2$ radius of $\approx 0.8$ mm. Here, $\Gamma = 2\pi\cdot 6.07$ MHz is the natural linewidth of the $|5S_{1/2}\rangle \rightarrow |5P_{3/2}\rangle$ transition [25]. For a large number of loaded atoms, multiple scattering of cooling/trapping light results in an effective repulsive force between atoms, thus limiting the achievable high densities. To further increase the density of the cloud in the experiment, we introduce an additional, so-called dark MOT stage, as explained in detail in [26]. In this second stage, we apply a 15 ms long temporal dark MOT, where we reduce the power of the repumper laser to 10 μW (1% of initial power) and the detuning of the cooling laser to $-2\Gamma$, leaving other parameters unchanged. As a result, the atoms are pumped into the $F=1$ ground (dark) state, causing an increase of the cloud density and, consequently, of the optical thickness. Finally, we increase the power of the repumper laser to 1.5 mW and tune the cooling laser to $-7\Gamma$, in order to re-cool and compress the cloud into a spherical shape while pumping all the atoms back into the $F=2$ ground state in the third repumping stage that lasts 1 ms. After preparing the cold cloud, we measure its optical thickness, $b(y,z)$, using the standard absorption imaging technique on the $|5S_{1/2};\, F=2\rangle \rightarrow |5P_{3/2};\, F'=3\rangle$ transition. We probe the spatial intensity distribution of a weak probe propagating in the $x$ direction with no cloud present, $I_0(y,z)$, and passing through a $^{87}$Rb cloud, $I(y,z)$, and calculate the optical thickness given by $b(y,z) = -\ln[I(y,z)/I_0(y,z)]$. For an atomic cloud of a Gaussian density distribution, $b(y,z)$ will also have a Gaussian shape. By fitting a 2D Gaussian to the measured $b(y,z)$, we extract the optical thickness at the center of the cloud, $b_{\text{peak}}$. On-resonance optical thickness, $b_0$, is calculated using $b_0 = b_{\text{peak}}\cdot(1+4\delta_{\text{img}}^2/\Gamma^2)$, where $\delta_{\text{img}}$ is the detuning of the probe laser frequency used for absorption imaging. On-resonance optical thickness is defined as $b_0 = \sigma_0 \int_{-\infty}^{\infty} n(x, y=z=0)\mathrm{d}x$, where $\sigma_0$ is the on-resonance

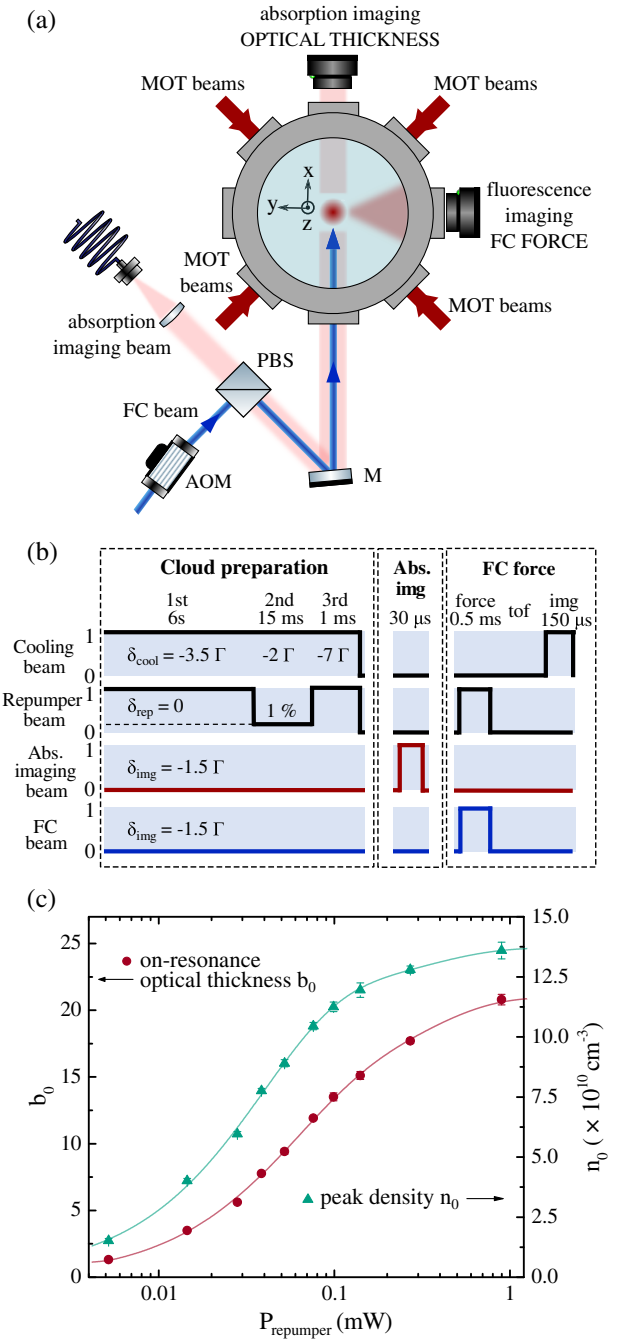


**Fig. 1.** (a) Simplified experimental scheme. Two pairs of MOT beams are shown, while the third pair is propagating along the $z$ axis. The absorption imaging beam and the FC beam are co-propagated in the $x$ axis. The optical thickness is measured using the absorption imaging camera, while the FC force is measured using the fluorescence imaging camera. During the measurement of optical thickness, the FC beam is blocked. M is a mirror; PBS is a polarizing beam splitter. (b) Experimental sequence showing the cloud preparation, followed by either absorption imaging or FC force measurement. (c) On-resonance optical thickness (red circles) and cloud peak density (green triangles) as a function of the repumper laser power during the MOT loading stage. Solid lines represent a guide for the eye.

cross section [25], and $n(x, y, z)$ is the spatial density of the cloud. The experimental sequence is shown in Fig. 1(b), where the cloud preparation stage is presented, followed by either absorption imaging of the cloud to measure its optical thickness or by the FC force measurement, since one of the beams has to be blocked, as shown in Fig. 1(a).

In order to vary the optical thickness of the cloud, we change the power of the repumper laser in the MOT loading stage, leaving the dark MOT and the repumping stage parameters unchanged. This change in the loading stage also affects other cloud parameters, such as size, number of atoms, and temperature. This does not affect the accuracy of optical thickness determination since it is measured directly by absorption imaging; nevertheless, a detailed characterization of all cloud parameters has been made. In Fig. 1(c), the peak density, $n_0 = n(x = y = z = 0)$, and on-resonance optical thickness, $b_0$, are shown as a function of the repumper laser power in the MOT loading stage. For the given range of powers, the cloud temperature varies from 35 μK to 75 μK, measured using a standard time-of-flight (TOF) technique [27].

**FC force measurement.** The FC is generated by frequency doubling an Er:fiber mode-locked femtosecond laser (TOPTICA FFS) operating at 1560 nm with a repetition rate of $f_{rep} = 80.495$ MHz. The frequency-doubled spectrum is centered around 780 nm with an FWHM of about 5 nm and a total output power of 76 mW. The FC spectrum consists of a series of sharp lines, i.e., comb modes [28]. The optical frequency of the $n$th comb mode is given by $f_n = n \cdot f_{\mathrm{rep}} + f_0$, where $f_0$ is the offset frequency. In our experiment, we actively stabilize $f_{\mathrm{rep}}$ and $f_n$ by giving feedback to the cavity length and pump power of the mode-locked laser, thus indirectly fixing $f_0$. The frequency of the $n$th comb mode is varied by scanning $f_0$ while keeping $f_{\mathrm{rep}}$ fixed. A detailed description of the FC stabilization and scanning scheme is presented in our recent papers [14,15].

The measurement sequence starts after the preparation of a cloud of a given optical thickness and is similar to the one described in our recent works [14,15]. At $t = 0$, we turn off the MOT cooling beams and switch on the linearly polarized FC beam. The total power of the FC beam on the atoms is 25 mW and the beam size ($1/e^2$) is 4.5 mm, resulting in the power and intensity per comb mode of about 75 μW and 9μW/cm$^2$, respectively. The MOT repumper laser is left on to continuously pump the atoms out of the $|5S_{1/2};\ F = 1\rangle$ ground level and has no measurable mechanical effect. The quadrupole magnetic field is also left on. We let the comb interact with the cold cloud for 0.5 ms. During this time, the center of mass (CM) of the cloud accelerates in the FC beam direction ($+x$ direction) due to the FC force. The FC and repumper beams are then switched off, and the cloud expands freely for a variable time, after which we switch on the MOT cooling beams for 0.15 ms and image the cloud's fluorescence with a camera to determine its CM displacement.

It is worth noting here that the approaches to change the optical thickness of the cloud by changing the repumper laser power immediately after the dark MOT stage used in [7], and by changing the cloud's expansion time before interaction as used in [1], are not applicable in our case of the FC excitation. In the first approach, only a fraction of atoms are transferred from $|5S_{1/2};\ F = 1\rangle$ to $|5S_{1/2};\ F = 2\rangle$ ground level after the dark MOT, depending on the repumper laser power. Atoms remaining in the $|5S_{1/2};\ F = 1\rangle$ level and atoms in $|5S_{1/2};\ F = 2\rangle$ could be simultaneously excited by different comb modes, which would result in a complex lineshape of the measured FC force. In the second approach, the size of the FC beam should be bigger than the size of the expanding cloud, which cannot be achieved in our setup due to the low power per comb mode.

## 3. RESULTS AND DISCUSSION

### A. FC Force as a Function of Cloud Density

Hyperfine energy levels of $^{87}$Rb and the relevant optical transitions for the FC excitation are shown in Fig. 2(a). In Fig. 2(b), we show the measured FC force, $F_{\mathrm{FC}}^N$, as a function of the FC detuning $\delta$, which we define as the detuning of the $n$th comb mode from the $|5S_{1/2};\ F = 2\rangle \rightarrow |5P_{3/2};\ F' = 3\rangle$ transition, for different peak cloud densities, $n_0$. Due to the nature of the comb spectrum, the FC radiation pressure force is periodic with respect to the comb detuning with a period equal to $f_{\mathrm{rep}}$. Two distinct peaks appear in one $f_{\mathrm{rep}}$ scan, reflecting the interaction with three comb modes, as explained in detail in our recent work [14]. The peak at $\delta = 0$ is due to the $n$th comb mode being in resonance with the $|5S_{1/2};\ F = 2\rangle \rightarrow |5P_{3/2};\ F' = 3\rangle$ transition, whereas the peak at $\delta \approx -25.5$ MHz is due to the $(n-3)$rd mode being in resonance with the $|5S_{1/2};\ F = 2\rangle \rightarrow |5P_{3/2};\ F' = 2\rangle$ transition and the $(n-5)$th mode with the $|5S_{1/2};\ F = 2\rangle \rightarrow |5P_{3/2};\ F' = 1\rangle$ transition. For completeness, Fig. 2(c) shows the calculated FC force, $F_{\mathrm{FC}}^1$, obtained by summing the contributions from three hyperfine transitions. The FC force is calculated for a single atom; details of the calculation can be found in [14].

As the cloud density increases, broadening and reduction of both FC force peaks are observed. However, these effect are not equally pronounced for both peaks, as can be seen from the ratio of the peaks at $\delta = 0$ and $\delta \approx -25.5$ MHz. The peak ratio decreases with increasing density, as can be seen from the inset in Fig. 2(b). For applications of multiline excitation, it is thus important to consider that, for a sample of fixed density, as is usually prepared in most experiments, broadening and reduction of the FC radiation pressure force will vary for different transitions. The peak ratio of 2.8 is expected when $n_0$ approaches zero, as it reflects the ratio of the $|5S_{1/2};\ F = 2\rangle \rightarrow |5P_{3/2};\ F' = 3\rangle$ and $|5S_{1/2};\ F = 2\rangle \rightarrow |5P_{3/2};\ F' = 2\rangle$ transition dipole moments [25]. This can be easily understood given the well-known result that the force broadening and reduction due to collective effects in many-atom ensembles depend on the optical thickness rather than the density [29]. Since the optical thickness is defined through the cross-section $\sigma_0 = \hbar\omega\Gamma/(2I_{\mathrm{sat}})$, where $I_{\mathrm{sat}}$ is the saturation intensity that depends on the dipole moment of the relevant transition [25], the two peaks have different optical thicknesses for a given density and therefore different factors of force reduction, which directly affects the peak ratio. In the following sections, we will therefore present and analyze the dependence of the FC force on the optical thickness for each force peak separately.

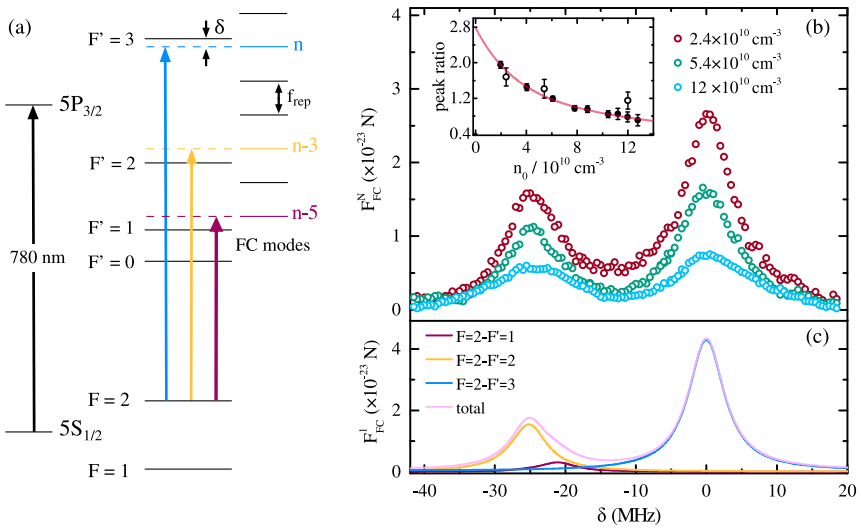


**Fig. 2.** (a) Hyperfine energy levels of $^{87}$Rb D2 line (780 nm) and the relevant optical transitions for the FC excitation. (b) Measured FC force, $F_{\mathrm{FC}}^{N}$, as a function of the FC detuning $\delta$, for different peak densities $n_0$. Inset shows the ratio of the FC peak forces at $\delta = 0$ and $\delta \approx -25.5$ MHz, where the symbols are experimental data and the line represents a guide for the eye. Full circles correspond to averaged multiple scans, as described in the experimental section. Empty circles correspond to peak ratios of the scans shown in (b), which were taken without averaging and thus have larger errors. (c) Calculated FC force, $F_{\mathrm{FC}}^{1}$, as a function of the FC detuning $\delta$. The total FC force (violet line) is obtained by summing the force contributions from three $|5S_{1/2};\ F = 2\rangle \rightarrow |5P_{3/2};\ F' = 1,\ 2,\ 3\rangle$ hyperfine transitions [14].

### B. FC Force as a Function of Cloud Optical Thickness

Figure 3 shows the measured FC force, $F_{\mathrm{FC}}^{N}$, as a function of the FC detuning $\delta$ for different on-resonance optical thicknesses $b_0$. In the case of the $|5S_{1/2};\ F = 2\rangle \rightarrow |5P_{3/2};\ F' = 3\rangle$ transition, $b_0$ is measured directly as described in Section 2 and is divided by 2.8 to obtain $b_0$ relevant for the $|5S_{1/2};\ F = 2\rangle \rightarrow |5P_{3/2};\ F' = 2\rangle$ transition.

The measured FC forces, arising from the $|5S_{1/2};\ F = 2\rangle \rightarrow |5P_{3/2};\ F' = 3\rangle$ transition show a Lorentzian lineshape in the whole range of measured $b_0$ [Fig. 3(a)]. In the case of the $|5S_{1/2};\ F = 2\rangle \rightarrow |5P_{3/2};\ F' = 2\rangle$ transition, the FC forces deviate from the Lorentzian lineshape [Fig. 3(b)] due to the $|5S_{1/2};\ F = 2\rangle \rightarrow |5P_{3/2};\ F' = 1\rangle$ FC force contribution positioned in the blue wing of the peak, as indicated in Fig. 2(b).

For a given $b_0$, a Lorentzian function is fitted to the experimental data. For the $|5S_{1/2};\ F = 2\rangle \rightarrow |5P_{3/2};\ F' = 2\rangle$ transition, we fit only to the data on the red side of the curve, where the influence of the $|5S_{1/2};\ F = 2\rangle \rightarrow |5P_{3/2};\ F' = 1\rangle$ transition is negligible. While the FC force offset should be zero, experimentally we see a small offset due to inaccuracies in determination of the initial and final position of the cloud's CM, from which the force is determined. The value of this offset depends on the optical thickness since the imaging signal-to-noise depends on the cloud parameters. However, the relative offset is around 10% of the peak force value (at $\delta = 0$) for all optical thicknesses in the case of $F = 2 \rightarrow F' = 3$ transition and around 15% of the peak force value (at $\delta = -25.5$ MHz) in the case of $F = 2 \rightarrow F' = 2$ transition. The small FC force offset is subtracted from all experimental data shown in Figs. 3 and 4.

The FC force broadening and reduction are clearly observed for both peaks shown in Figs. 3(a) and 3(b) and are presented in more detail in Fig. 4.

### C. FC Force Broadening and Reduction

Figure 4(a) shows the measured (symbols) FC force linewidths, $\Gamma_{\mathrm{FC}}^{N}$, as a function of $b_0$. For a given $b_0$, $\Gamma_{\mathrm{FC}}^{N}$ is obtained from the fit of a Lorentzian function to the measured FC force spectra as shown in Fig. 3(a) for the $|5S_{1/2};\ F = 2\rangle \rightarrow |5P_{3/2};\ F' = 3\rangle$ transition and in Fig. 3(b) for $|5S_{1/2};\ F = 2\rangle \rightarrow |5P_{3/2};\ F' = 2\rangle$ transitio. We observe an increase of the FC force linewidth with increasing $b_0$. For small $b_0$, the increase is linear, while the curve starts to flatten as the $b_0$ is increased. In the limit $b_0 \rightarrow 0$, the FC linewidth of $\Gamma = 2\pi \cdot 6.07$ MHz is expected, as it reflects the natural linewidth of the $^{87}$Rb $|5S_{1/2}\rangle \rightarrow |5P_{3/2}\rangle$ transition [25]. For the largest $b_0 = 20.8$ achieved in the experiment, the FC force linewidth of 2.5 $\Gamma$ is measured.

Figure 4(b) shows the measured (symbols) reduction of the FC force, $F_{\mathrm{FC}}^{N}(\delta)/F_{\mathrm{FC}}^{1}(\delta)$, as a function of $b_0$. $F_{\mathrm{FC}}^{N}(\delta)$ are obtained from the measured FC force spectra as shown in Fig. 3(a) (for $\delta = 0$ and $\delta = -\Gamma$) in the case of the $|5S_{1/2};\ F = 2\rangle \rightarrow |5P_{3/2};\ F' = 3\rangle$ transition and in Fig. 3(b) (for $\delta = -25.5$ MHz and $\delta = -25.5\mathrm{MHz} - \Gamma$) in the case of the $|5S_{1/2};\ F = 2\rangle \rightarrow |5P_{3/2};\ F' = 2\rangle$ transition. The single-atom force $F_{\mathrm{FC}}^{1}(\delta)$ is obtained by fitting Eq. (2) to the measured data with $F_{\mathrm{FC}}^{1}(\delta)$ as a free parameter (see the following paragraph for details). A reduction of the FC force with increasing $b_0$ is observed. The force reduction is larger when the relevant comb mode is resonant with a given atomic transition, i.e., when the $n$th comb mode in resonance with the $|5S_{1/2};\ F = 2\rangle \rightarrow |5P_{3/2};\ F' = 3\rangle$ transition ($\delta = 0$), and the $(n-3)$rd with the $|5S_{1/2};\ F = 2\rangle \rightarrow |5P_{3/2};\ F' = 2\rangle$ transition ($\delta = -25.5$ MHz). These data also show that both atomic

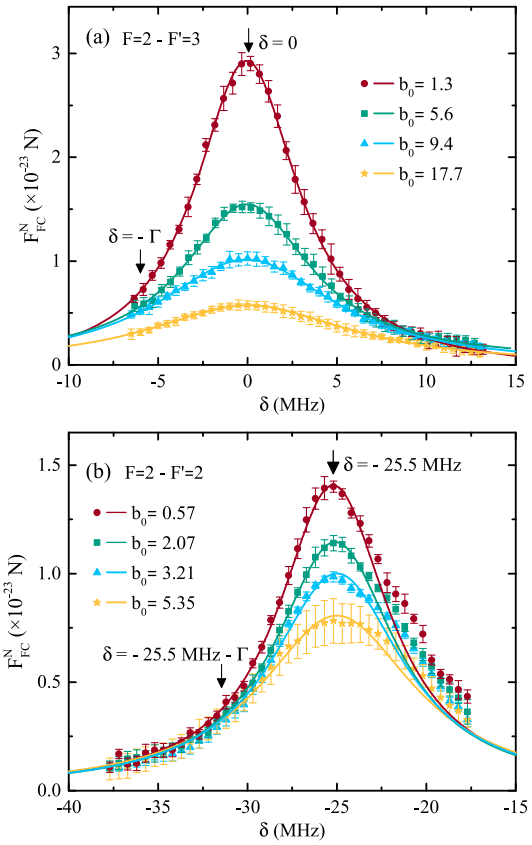


**Fig. 3.** Measured FC force (symbols) as a function of detuning $\delta$ for different optical thicknesses $b_0$. (a) FC force is due to the $n$th comb mode being in resonance with the $|5S_{1/2};\ F=2\rangle \rightarrow |5P_{3/2};\ F'=3\rangle$ transition. (b) FC force is due to the $(n-3)$ rd mode being in resonance with the $|5S_{1/2};\ F=2\rangle \rightarrow |5P_{3/2};\ F'=2\rangle$ transition and the $(n-5)$th mode with the $|5S_{1/2};\ F=2\rangle \rightarrow |5P_{3/2};\ F'=1\rangle$ transition. For the $|5S_{1/2};\ F=2\rangle \rightarrow |5P_{3/2};\ F'=2\rangle$ transition, we fit only to the data on the red side of the curve, where the influence of the $|5S_{1/2};\ F=2\rangle \rightarrow |5P_{3/2};\ F'=1\rangle$ transition is negligible. A solid line shows a Lorentzian fit to the experimental data. The arrows show detunings that were chosen to show dependences on $b_0$ in Fig. 4(b).

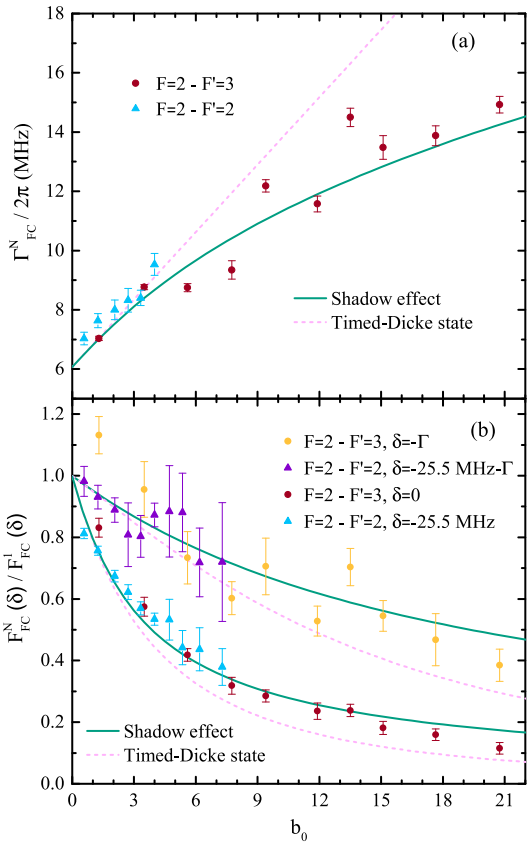


**Fig. 4.** (a) Measured (symbols) and calculated FC force linewidth in the presence of shadow (solid line) and cooperative (dashed line) effects, using Eqs. (2) and (3), respectively, as a function of $b_0$. (b) Measured (symbols) and calculated FC force reduction as a function of $b_0$ at $\delta=0$ and $\delta=-\Gamma$ in the case of $|5S_{1/2};\ F=2\rangle \rightarrow |5P_{3/2};\ F'=3\rangle$ transition, and $\delta=-25.5$ MHz and $\delta=-25.5$ MHz $-\Gamma$ in the case of $|5S_{1/2};\ F=2\rangle \rightarrow |5P_{3/2};\ F'=2\rangle$ transition.

transitions follow the same dependence on the optical thickness (both on- and off-resonance). For the largest $b_0=20.8$ achieved in the experiment, the FC force reduction of almost 90% is measured.

In addition to the measured data, the calculated FC force linewidths and FC force reduction are shown in Figs. 4(a) and 4(b) by solid and dashed lines. The calculations are performed for our experimental parameters using the theoretical models developed for the cw-induced radiation pressure force [11]. By doing so, we considered a single-comb mode participating in the interaction as a cw laser. This consideration is reasonable given that the FC pulse repetition rate, $f_{\mathrm{rep}}$, is much larger than the natural linewidth of the relevant transition, $\Gamma$; thus, the scattering rate of the neighboring comb modes is strongly reduced due to the $(2\pi f_{\mathrm{rep}}/\Gamma)^2$ dependence [13–15].

A detailed derivation of the average cw radiation pressure force resulting from the excitation of N atoms by a resonant laser can be found in [30] and is given by

$$F=\frac{\hbar k_0\Gamma}{4\pi N}\int_0^{2\pi}\mathrm{d}\phi\int_0^{\pi}\mathrm{d}\theta\,\sin\theta(1-\cos\theta)\,I_s(\theta,\phi). \quad \textbf{(1)}$$

$I_s(\theta,\phi)$ is the scattered far-field intensity, and $\theta,\phi$ determine the direction of the scattered photons. Equation (1) shows that the angular pattern of the scattered intensity uniquely determines the radiation pressure force; thus, to understand the force, it is necessary to discuss different scattering mechanisms relevant to our experimental conditions. Light scattering by an atomic cloud illuminated by a resonant laser can be decomposed into several contributions [11]: (a) the background radiation composed of diffuse scattering by all atoms, which is incoherent in the sense that the phase of the scattered wave is random from one to another realization of atomic positions; (b) a forward lobe arising from diffraction of the incident beam from the cloud, i.e., Mie scattering in the single scattering order. This contribution is coherent in the sense that the scattered wave has a well-defined phase. (c) The coherent backscattering cone that arises from constructive interference during multiple scattering.

A full microscopic model built on a set of equations of $N$ coherently coupled dipoles (CD) can be used to calculate the scattering intensity [1,3,29]. This quantum model captures

incoherent and coherent contributions, including all scattering orders, and can be extended to include atomic motion. However, due to computational complexity, the CD model is limited to small samples and, as such, is beyond the scope of this paper.

Another approach is to use semiclassical models to understand different scattering contributions and their influence on the radiation pressure force. To investigate these contributions, we will follow the analysis developed in [11] for the cw-induced force and extend it beyond the limit of $b < 1$.

Diffuse scattering has two contributions to the force. The first one is called the "shadow effect" and comes as a result of progressive attenuation of light intensity through the cloud due to diffuse scattering. It can be explained by the Beer–Lambert law, i.e., the exponential decrease of the intensity results in broadening and reduction of the overall radiation pressure force. The force reduction arising from the shadow effect can be calculated from [11]

$$\frac{F_{\text{shadow}}}{F_1} = \frac{\text{Ein}(b)}{b}, \tag{2}$$

where $\text{Ein}(b)$ is the entire function given by $\text{Ein}(z) = \int_0^z dx(1-e^{-x})/x$, with $b = b_0/(1+4\delta^2/\Gamma^2)$, and $F_1$ the single-atom radiation pressure force. We calculate $F_{\text{shadow}}$ spectra as a function of $b_0$ for our experimental parameters, from which we extract the $F_{\text{shadow}}(\delta)$ and $F_{\text{shadow}}$ linewidths. In order to obtain $F^1_{\text{FC}}(\delta)$, we fit Eq. (2) to the measured FC force data as a function of $b_0$ for a given detuning $\delta$, $F^N_{\text{FC}}(\delta)$, with $F^1_{\text{FC}}(\delta)$ as a free fitting parameter. Then, the determined $F^1_{\text{FC}}(\delta)$ is then used as a scaling factor for normalization of all $F^N_{\text{FC}}(\delta)$ forces shown in Fig. 4(b). The calculated force linewidth and reduction as a function of $b_0$ resulting from the shadow effect are shown in Figs. 4(a) and 4(b) by solid green lines. The calculated values show good agreement with the measured data for both on- and off-resonant excitation.

The second contribution to the force due to diffuse scattering is a consequence of the first one, i.e., since the light intensity is larger at the entrance of the cloud than at the exit, more light is scattered in the backward than in the forward direction. This causes an anisotropy of the emission pattern, which slightly increases the radiation pressure force. This anisotropy can numerically be simulated using a random walk approach [11] and becomes significant only at large optical thicknesses. Based on [31], we estimate that, for the largest $b_0 = 20.8$ achieved in the experiment, the force, including corrections due to anisotropy is around 10% larger than the $F_{\text{shadow}}$, i.e., $F_{\text{diffuse}} = F_{\text{shadow}} + F_{\text{anis}} \approx 1.1 F_{\text{shadow}}$. This correction is within the uncertainty of the experimental data.

The contribution to the force due to diffraction of the incident beam can be calculated for clouds of small optical thickness [32] employing the Mie scattering approach [11]. As stated in [33,34], this contribution is significant for very small atomic clouds ($kR \approx 10$) and for probe lasers tuned far-off resonance; it is therefore negligible for condition used in our experiment, i.e., large cloud ($kR > 1000$) and on-resonant excitation. Here, $k$ is the wavevector and $R$ is rms (sigma) radius of a cloud of a Gaussian density distribution.

The coherent backscattering contribution cannot be calculated using semiclassical models but requires the full microscopic CD model [11,29,35,36]. However, as predicted in [11], its contribution is also negligible for large clouds ($kR > 1000$) and on-resonant excitation such as in our experiment.

Because of its importance in the earlier experimental and theoretical papers [7,9,11,35], we also mention an alternative approach used to investigate the radiation pressure force. It describes the force reduction as a consequence of coherent collective (i.e., cooperative) scattering of atomic dipoles. This cooperative contribution to the force can be calculated using a mean-field approach inspired by the timed-Dicke state (TDS). This model assumes that all atoms are driven by the unperturbed laser beam, i.e., the atoms acquire the phase of the laser, and all have the same excitation probabilities. It neglects reabsorption of photons by other atoms and works in conditions of small probe laser intensity or large detunings. The TDS approach has become widely used in recent years, as it provides an explanation of experimental results on superradiance [6,37], a hallmark of cooperative effects. Cooperative radiation pressure force, $F_{\text{TDS}}$ was studied in detail in [7,9] and can be calculated from

$$\frac{F_{\text{TDS}}}{F_1} = \frac{4\delta^2+\Gamma^2}{4\delta^2+(1+b_0/8)^2\Gamma^2}\left[1+\frac{b_0}{16(k_0R)^2}\right], \tag{3}$$

where $R$ is the cloud radius, and $F_1$ is the single atom force. We calculate $F_{\text{TDS}}$ spectra as a function of $b_0$ for our experimental parameters, from which we extract the $F_{\text{TDS}}(\delta)$ and $F_{\text{TDS}}$ linewidths. The calculated values are shown in Figs. 4(a) and 4(b) by dashed violet lines. The TDS force agrees with measured data for small $b_0$ and coincides with the shadow effect curve up to $b_0 \approx 3$. However, at larger $b_0$, the TDS model predicts a linear increase of the force linewidth, which is not supported by our experimental results, as it does not include multiple scattering effects that can induce the flattening of the force linewidth curve at large $b_0$ [9]. On the other hand, the good agreement of the force reduction calculated from the shadow and TDS models [Fig. 4(b)] even for intermediate $b_0$ explains why, in earlier studies [7], the reduction of the force was attributed to atomic cooperativity. However, the results of the force broadening given in Fig. 4(a) clearly indicate that this agreement can be misleading and point to the shadow effect as the dominant contribution to the force in dense atomic clouds. In the conditions when the atoms are resonantly excited by the frequency comb, the beam attenuation due to diffuse scattering is the dominant physical mechanism defining the radiation pressure force, and the atomic cooperativity effects are negligible. This conclusion is in good agreement with measurements of super-radiance, where super-radiant enhancement was observed only for mid- to large detunings, while tuning the probe close to resonance results in suppression of super-radiant (cooperative) behavior [37].

## 4. CONCLUSION

In conclusion, we have measured the frequency-comb-induced radiation pressure force acting on a cold $^{87}$Rb cloud as a function of the optical thickness of the cloud. We observed reduction and broadening of the frequency comb force as the optical thickness increases. As the scattered intensity is directly mapped

to the radiation pressure force, we discuss different scattering mechanisms and their contributions to the force. For our experimental conditions, we show that a single scattering mechanism dominates the radiation pressure force. It comes as a result of progressive attenuation of light intensity in the cloud due to diffuse scattering of light, i.e., the shadow effect. We also review the cooperative timed-Dicke state approach used in earlier experiments to investigate the radiation pressure force. Theoretical models for cw radiation pressure force in the presence of shadow and cooperative effects developed in [7,11], respectively, are used to describe the measured frequency comb force. The measured and the calculated force broadening and reduction arising as results of the shadow effect are in good agreement. The cooperative force agrees with measured data for small $b_0$; however. the behavior of force linewidth and force reduction at larger $b_0$ is not supported by the experiment. This points to the shadow effect as the dominant contribution to the force modification in resonantly excited atomic clouds with an on-resonance optical thickness up to 20, i.e., a simple semiclassical model can be used to reproduce the measured force broadening and reduction. In order to observe the signature of the cooperative effects in the radiation pressure force, it would be necessary to work in the parametric regime where the beam attenuation due to diffuse scattering is negligible, such as in large detunings from the atomic resonance.

Our results confirm the analogy between the cw and a single-comb-mode interaction, i.e., the influence of the off-resonance comb modes on the comb–atom interaction is minor and can be neglected, even in the case of increased cloud optical thickness.

The results presented in this paper contribute to the understanding of scattering of the frequency comb light by an ensemble of cold atoms, thus paving the way toward novel frequency comb applications in the field of cooling, quantum communication, and light–atom interfaces based on structured and disordered atomic systems.

**Funding.** Hrvatska Zaklada za Znanost (IP-2018-01-9047).

**Acknowledgment.** The authors acknowledge Neven Šantić for reading the manuscript and providing constructive comments as well as for his early contribution to the development of cold atoms experiment. In addition, the authors acknowledge Ivor Krešić for the early contribution to the development of theoretical models as well as Grzegorz Kowzan and Piotr Masłowski for their contribution to the frequency comb stabilization.

**Disclosures.** The authors declare no conflicts of interest.

**Data availability.** Data underlying the results presented in this paper are not publicly available at this time but may be obtained from the authors upon reasonable request.

## REFERENCES

1. S. Bromley, B. Zhu, M. Bishof, X. Zhang, T. Bothwell, J. Schachenmayer, T. L. Nicholson, R. Kaiser, S. F. Yelin, M. D. Lukin, A. M. Rey, and J. Ye, "Collective atomic scattering and motional effects in a dense coherent medium," Nat. Commun. **7**, 11039 (2016).
2. J. Pellegrino, R. Bourgain, S. Jennewein, Y. Sortais, A. Browaeys, S. Jenkins, and J. Ruostekoski, "Observation of suppression of light scattering induced by dipole-dipole interactions in a cold-atom ensemble," Phys. Rev. Lett. **113**, 133602 (2014).
3. S. D. Jenkins, J. Ruostekoski, J. Javanainen, S. Jennewein, R. Bourgain, J. Pellegrino, Y. R. P. Sortais, and A. Browaeys, "Collective resonance fluorescence in small and dense atom clouds: comparison between theory and experiment," Phys. Rev. A **94**, 023842 (2016).
4. S. Balik, A. L. Win, M. D. Havey, I. M. Sokolov, and D. V. Kupriyanov, "Near-resonance light scattering from a high-density ultracold atomic $^{87}$Rb gas," Phys. Rev. A **87**, 053817 (2013).
5. J. Rui, D. Wei, A. Rubio-Abadal, S. Hollerith, J. Zeiher, D. M. Stamper-Kurn, C. Gross, and I. Bloch, "A subradiant optical mirror formed by a single structured atomic layer," Nature **583**, 369–374 (2020).
6. R. H. Dicke, "Coherence in spontaneous radiation processes," Phys. Rev. **93**, 99 (1954).
7. T. Bienaimé, S. Bux, E. Lucioni, P. Courteille, N. Piovella, and R. Kaiser, "Observation of a cooperative radiation force in the presence of disorder," Phys. Rev. Lett. **104**, 183602 (2010).
8. S. Bux, E. Lucioni, H. Bender, T. Bienaimé, K. Lauber, C. Stehle, C. Zimmermann, S. Slama, P. Courteille, N. Piovella, and R. Kaiser, "Cooperative scattering by cold atoms," J. Mod. Opt. **57**, 1841–1848 (2010).
9. P. W. Courteille, S. Bux, E. Lucioni, K. Lauber, T. Bienaimé, R. Kaiser, and N. Piovella, "Modification of radiation pressure due to cooperative scattering of light," Eur. Phys. J. D **58**, 69–73 (2010).
10. J. Chabé, M. Rouabah, L. Bellando, T. Bienaimé, N. Piovella, R. Bachelard, and R. Kaiser, "Coherent and incoherent multiple scattering," Phys. Rev. A **89**, 043833 (2014).
11. R. Bachelard, N. Piovella, W. Guerin, and R. Kaiser, "Collective effects in the radiation pressure force," Phys. Rev. A **94**, 033836 (2016).
12. W. Guerin, M. O. Araújo, and R. Kaiser, "Subradiance in a large cloud of cold atoms," Phys. Rev. Lett. **116**, 083601 (2016).
13. D. Kielpinski, "Laser cooling of atoms and molecules with ultrafast pulses," Phys. Rev. A **73**, 063407 (2006).
14. N. Šantić, D. Buhin, D. Kovačić, I. Krešić, D. Aumiler, and T. Ban, "Cooling of atoms using an optical frequency comb," Sci. Rep. **9**, 2510 (2019).
15. D. Buhin, D. Kovačić, F. Schmid, M. Kruljac, V. Vulić, T. Ban, and D. Aumiler, "Simultaneous dual-species laser cooling using an optical frequency comb," Phys. Rev. A **102**, 021101 (2020).
16. A. M. Jayich, X. Long, and W. C. Campbell, "Direct frequency comb laser cooling and trapping," Phys. Rev. X **6**, 041004 (2016).
17. V. Torggler, I. Krešić, T. Ban, and H. Ritsch, "Self-ordering and cavity cooling using a train of ultrashort pulses," New J. Phys. **22**, 063003 (2020).
18. I. Krešić, M. Kruljac, T. Ban, and D. Aumiler, "Electromagnetically induced transparency with a single frequency comb mode probe," J. Opt. Soc. Am. B **36**, 1758–1764 (2019).
19. D. Main, T. M. Hird, S. Gao, I. A. Walmsley, and P. M. Ledingham, "Room temperature atomic frequency comb storage for light," Opt. Lett. **46**, 2960–2963 (2021).
20. D. Hayes, D. N. Matsukevich, P. Maunz, D. Hucul, Q. Quraishi, S. Olmschenk, W. Campbell, J. Mizrahi, C. Senko, and C. Monroe, "Entanglement of atomic qubits using an optical frequency comb," Phys. Rev. Lett. **104**, 140501 (2010).
21. G. Maltese, M. I. Amanti, F. Appas, G. Sinnl, A. Lemaître, P. Milman, F. Baboux, and S. Ducci, "Generation and symmetry control of quantum frequency combs," npj Quantum Inf. **6**, 13 (2020).
22. D. Felinto, C. A. C. Bosco, L. Acioli, and S. Vianna, "Coherent accumulation in two-level atoms excited by a train of ultrashort pulses," Opt. Commun. **215**, 69–73 (2003).
23. A. Marian, M. C. Stove, J. R. Lawall, D. Felinto, and J. Ye, "United time-frequency spectroscopy for dynamics and global structure," Science **306**, 2063–2068 (2004).
24. D. Aumiler, T. Ban, H. Skenderović, and G. Pichler, "Velocity selective optical pumping of Rb hyperfine lines induced by a train of femtosecond pulses," Phys. Rev. Lett. **95** (2005).
25. D. A. Steck, Rubidium 87 D line data, revision 2.2.2 (2021).
26. W. Ketterle, K. B. Davis, M. A. Joffe, A. Martin, and D. E. Pritchard, "High densities of cold atoms in a dark spontaneous-force optical trap," Phys. Rev. Lett. **70**, 2253 (1993).
27. I. Yavin, M. Weel, A. Andreyuk, and A. Kumarakrishnan, "A calculation of the time-of-flight distribution of trapped atoms," Am. J. Phys. **70**, 149 (2002).
28. S. T. Cundiff and J. Ye, *Femtosecond Optical Frequency Comb: Principle, Operation and Applications* (Springer, 2005).
29. B. Zhu, J. Cooper, J. Ye, and A. M. Rey, "Light scattering from dense cold atomic media," Phys. Rev. A **94**, 023612 (2016).

30. T. Bienaimé, R. Bachelard, J. Chabé, M. Rouabah, L. Bellando, P. W. Courteille, N. Piovella, and R. Kaiser, "Interplay between radiation pressure force and scattered light intensity in the cooperative scattering by cold atoms," J. Mod. Opt. **61**, 18–24 (2014).
31. W. Guerin, M. T. Rouabah, and R. Kaiser, "Light interacting with atomic ensembles: collective, cooperative and mesoscopic effects," J. Mod. Opt. **64**, 895–907 (2017).
32. M. Rouabah, M. Samoylova, R. Bachelard, P. W. Courteille, R. Kaiser, and N. Piovella, "Coherence effects in scattering order expansion of light by atomic clouds," J. Opt. Soc. Am. A **31**, 1031–1039 (2014).
33. H. Bender, C. Stehle, S. Slama, R. Kaiser, N. Piovella, C. Zimmermann, and P. W. Courteille, "Observation of cooperative Mie scattering from an ultracold atomic cloud," Phys. Rev. A **82**, 011404 (2010).
34. R. Bachelard, P. Courteille, R. Kaiser, and N. Piovella, "Critical behavior in porous media flow," Europhys. Lett. **97**, 14004 (2012).
35. T. Bienaimé, M. Petruzzo, D. Bigerni, N. Piovella, and R. Kaiser, "Atom and photon measurement in cooperative scattering by cold atoms," J. Mod. Opt. **58**, 1942–1950 (2011).
36. J. Javanainen, J. Ruostekoski, B. Vestergaard, and M. R. Francis, "One-dimensional modeling of light propagation in dense and degenerate samples," Phys. Rev. A **59**, 649 (1999).
37. M. Araújo, I. Krešić, R. Kaiser, and W. Guerin, "Superradiance in a large and dilute cloud of cold atoms in the linear-optics regime," Phys. Rev. Lett. **117**, 073002 (2016).

Rapid Communications

# Simultaneous dual-species laser cooling using an optical frequency comb

D. Buhin,[1] D. Kovačić,[1] F. Schmid,[2] M. Kruljac,[1] V. Vulić,[1] T. Ban,[1] and D. Aumiler[1,*]
[1]*Institute of Physics, Bijenička cesta 46, 10000 Zagreb, Croatia*
[2]*Max-Planck-Institut für Quantenoptik, 85748 Garching, Germany*

(Received 2 June 2020; accepted 27 July 2020; published 25 August 2020)

We demonstrate 1D simultaneous laser cooling of $^{87}$Rb and $^{85}$Rb atoms using an optical frequency comb. By adjusting the pulse repetition frequency and the offset frequency, the frequency comb spectrum is tuned to ensure that two distinct frequency comb modes are simultaneously red-detuned from the cooling transitions, one mode for each species. Starting from a precooled cloud of $^{85,87}$Rb atoms at above-Doppler temperatures, we show simultaneous cooling of both species down to the Doppler temperature using two counter-propagating $\sigma^+$ and $\sigma^-$ polarized beams from the frequency comb. The results indicate that simultaneous dual-species frequency comb cooling does not affect the cooling characteristics of individual atomic species. The results of this work imply that several atomic species could be cooled simultaneously using a single frequency comb source. This comb-based multichannel laser cooling could bring significant advances in multispecies atom interferometers for space applications and in the study of multispecies interactions.

DOI: 10.1103/PhysRevA.102.021101

Optical frequency combs (FCs) are unique light sources with applications ranging from metrology [1] and high-resolution spectroscopy [2,3] to quantum communication and processing [4]. In the time domain, the output of a FC is a train of phase-stable ultrashort pulses of typically high peak power. This allows for efficient frequency conversion and other nonlinear interactions. The spectrum of a FC consists of a series of equally spaced narrow spectral lines. Owing to these unique properties, FCs have been proposed as potential light sources for laser cooling of atoms with strong cycling transitions in the vacuum ultraviolet (VUV) [5–7]. This part of the spectrum, and thus some of the most prevalent atomic species, has so far remained inaccessible to laser cooling since generating continuous wave (cw) laser radiation in the VUV is extremely challenging.

Cooling of atoms and ions using FCs has recently been demonstrated. Jayich *et al.* [7] achieved FC Doppler cooling of precooled rubidium atoms on the two-photon transition at 778 nm. Davila-Rodriguez *et al.* [6] showed FC Doppler cooling of trapped magnesium ions on a single-photon transition in the UV. Ip *et al.* [8] demonstrated loading, cooling and crystallization of hot ytterbium ions, and Šantić *et al.* [9] demonstrated cooling of rubidium atoms on a single-photon transition at 780 nm. A recent theoretical work by our group [10] investigated simultaneous FC cooling in multiple cooling channels and has shown that simultaneous cooling of $^{40}$K, $^{85}$Rb, and $^{87}$Rb can be achieved using a single FC by appropriate selection of comb parameters.

In this work, we demonstrate simultaneous FC cooling of $^{85}$Rb and $^{87}$Rb atoms. We believe that the application of FC multichannel cooling could bring significant advances in multispecies atom interferometers (AIs). Simultaneous dual-species AIs pave the way for future ground and space experiments dedicated to testing the weak equivalence principle, also known as the universality of free fall [11–13]. Current design for space applications is based on the $^{85}$Rb and $^{87}$Rb dual-species interferometer which employs four amplified diode laser modules at 780 nm, offset locked to the rubidium spectroscopy referenced frequency doubled Telecom laser, for cooling and manipulation of atoms [14]. Multispecies AIs offer extended dynamic measurement ranges [15] which could increase the sensitivity and resolution of instruments. To our knowledge, three- (and more) species AIs have so far not been demonstrated, most likely due to the complexity of the laser systems required. In this context, we believe that the application of FCs with multispecies cooling capabilities could lead to a breakthrough in the development of multispecies AIs for space applications.

Dual- and multispecies magneto-optical traps (MOTs) are an experimental tool for investigating atomic interactions. They are a starting point for the production of quantum degenerate mixtures [16–19] as well as for the formation of heteronuclear cold molecules [20,21]. FC multichannel cooling could greatly reduce the complexity of multispecies MOT experimental systems by replacing a series of cw lasers with a single FC source, where different comb modes can serve as cooling and repumper lasers. One notable simplification of the experiment involves replacing a large number of feedback loops (one for each cw laser) with only two feedback loops that can stabilize and phase-lock all lines within the FC spectrum. FC cooling would therefore allow cooling of different atomic species by highly phase-coherent comb modes which could bring new insights into the physics of heteronuclear cold collisions and molecules formation [10,22].

Our apparatus consists of a dual-species MOT in which $\approx 1 \times 10^6$ $^{85}$Rb atoms and $\approx 3 \times 10^6$ $^{87}$Rb atoms are simultaneously loaded from a background vapor in a stainless steel

*aumiler@ifs.hr



 

chamber. The MOT relies on four independent frequency-stabilized cw lasers arranged in a standard six-beam configuration, which together with a quadrupole magnetic field creates the trapping potential for both species. To ensure that the MOTs are well overlapped, the cooling beams for both species are delivered through a single optical fiber. A detailed description of the experimental setup can be found in Ref. [23]. In typical experimental conditions, we obtain two clouds of cold $^{85}$Rb and $^{87}$Rb atoms with temperatures in the range of 200–300 $\mu$K. The clouds typically have $1/e^2$ radii of $\approx 0.8$ mm, and their centers of mass overlap to within 5% of their radii. Such overlapped pre-cooled clouds of $^{85}$Rb and $^{87}$Rb atoms represent the initial sample for all measurements presented in this work.

The FC is generated by frequency doubling an Er:fiber mode-locked laser (TOPTICA FFS) operating at 1550 nm with a nominal repetition rate $f_{\mathrm{rep}} = 80.5$ MHz. $f_{\mathrm{rep}}$ tuning range of 50 kHz can be achieved by adjusting the laser cavity length using an integrated stepper motor and a piezotransducer. The frequency-doubled spectrum used in the experiment is centered around 780 nm with a FWHM of about 5 nm and a total power of 68 mW. The FC spectrum consists of a series of sharp lines, i.e., comb modes [24]. The optical frequency of the $n$th comb mode is given by $f_n = n\, f_{\mathrm{rep}} + f_0$, where $f_{\mathrm{rep}}$ is the laser repetition rate and $f_0$ is the offset frequency.

In our experiment, we actively stabilize $f_{\mathrm{rep}}$ and $f_n$ by giving feedback to the cavity length and pump power of the mode-locked laser, thus indirectly fixing $f_0$. The $n$-th comb mode, $f_n$, is phase-locked to a frequency-shifted cw reference laser (ECDL, Moglabs CEL002), which is locked to the $^{87}$Rb $|5S_{1/2}; F = 2\rangle \rightarrow |5P_{3/2}; F' = 3\rangle$ transition. The frequency shift of the cw reference laser is achieved by an acousto-optic modulator (AOM) in a double pass configuration. $f_{\mathrm{rep}}$ is stabilized to a low-noise synthesizer which is referenced to a rubidium frequency standard. A detailed description of the FC stabilization scheme is presented in our recent paper [9].

In order to achieve simultaneous cooling of two atomic species, two distinct modes within the comb spectrum must be simultaneously red detuned from the cooling transitions of the atomic species [10]. Careful tailoring of the FC spectrum (choosing $f_{\mathrm{rep}}$ and $f_0$) is therefore crucial for the successful realization of FC cooling. In our experiment, $f_{\mathrm{rep}}$ is fixed during the measurements and set to $f_{\mathrm{rep}} = 80.495$ MHz, while $f_0$ is scanned by adjusting the heterodyne beat frequency between the cw reference laser and the $n$th comb mode. This way it is possible to control the detuning of the $n$-th comb mode with respect to the $^{87}$Rb $|5S_{1/2}; F = 2\rangle \rightarrow |5P_{3/2}; F' = 3\rangle$ transition. The heterodyne beat frequency can be continuously changed over a range of 5–30 MHz by changing the frequency of the local oscillator, so four separate scans with different cw reference laser frequency shifts are performed and subsequently merged to fully scan $f_n$ by one $f_{\mathrm{rep}}$.

We start the investigation of simultaneous interaction of the FC with cold $^{85}$Rb and $^{87}$Rb atoms by measuring the FC radiation pressure force. The experimental setup and the measurement sequence used are similar to the ones described in our recent work [9]. A single circularly polarized FC beam is sent through an AOM for fast switching, and is then directed to the center of the dual-species MOT. The total power of the FC beam on the atoms is 10 mW and the beam size (FWHM) is 2.7 mm, resulting in the power and intensity per comb mode of about 0.3 $\mu$W and 3.6 $\mu$W/cm$^2$, respectively.

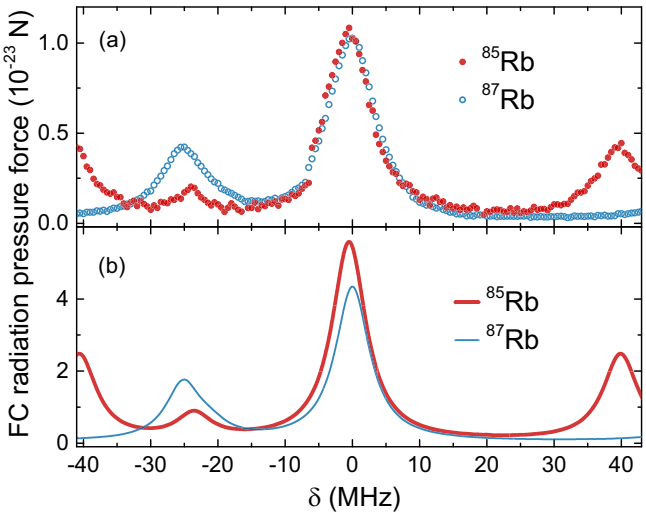


FIG. 1. Measured (a) and calculated (b) FC radiation pressure force as a function of comb detuning $\delta$ for $^{85}$Rb (red) and $^{87}$Rb (blue) atoms. $\delta$ denotes the detuning of the $n$th comb mode from the $^{87}$Rb $|5S_{1/2}; F = 2\rangle \rightarrow |5P_{3/2}; F' = 3\rangle$ transition. The calculated FC force in (b) includes contributions from three $^{85}$Rb $|5S_{1/2}; F = 3\rangle \rightarrow |5P_{3/2}; F' = 2, 3, 4\rangle$ and three $^{87}$Rb $|5S_{1/2}; F = 2\rangle \rightarrow |5P_{3/2}; F' = 1, 2, 3\rangle$ hyperfine transitions (shown separately in Ref. [26]).

The measurement sequence starts with the preparation of cold $^{85}$Rb and $^{87}$Rb clouds. At $t = 0$ we turn off the MOT cooling beams, and switch on the FC beam. The MOT repumper lasers are left on continuously to optically pump the atoms out of the $^{85}$Rb $|5S_{1/2}; F = 2\rangle$ and $^{87}$Rb $|5S_{1/2}; F = 1\rangle$ ground states. They are arranged in a counter-propagating configuration with the intensity predominantly in the direction perpendicular to the FC beam propagation, and have no measurable mechanical effect (see Ref. [23] for a detailed scheme of the optical setup). The quadrupole magnetic field is also left on. We let the comb interact with the cold clouds for 2 ms. During this time the centers of mass of both clouds accelerate in the FC beam direction ($+x$ direction) due to the FC radiation pressure force. The FC beam and repumper lasers are then switched off, and the clouds expand freely for 2 ms, after which we switch on the MOT cooling beams for 0.15 ms and image the cloud fluorescence with a camera. Fluorescence images are recorded separately for the $^{85}$Rb and $^{87}$Rb atoms. This basic measurement sequence is repeated 6 times, and the resulting fluorescence images are then averaged for each isotope. The cloud center of mass displacement in the $+x$ direction is determined from the images, providing information on the cloud acceleration and the FC radiation pressure force. In Fig. 1, we show the measured (a) and calculated (b) FC force for both isotopes as a function of the FC detuning $\delta$, which is defined as the detuning of the $n$th comb mode from the $^{87}$Rb $|5S_{1/2}; F = 2\rangle \rightarrow |5P_{3/2}; F' = 3\rangle$ transition. Due to the nature of the comb spectrum, the

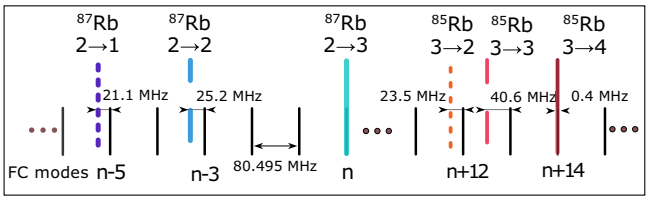


FIG. 2. Relative positions of comb lines within the FC spectrum with respect to the $^{85}$Rb $|5S_{1/2};F=3\rangle \rightarrow |5P_{3/2};F'=2,3,4\rangle$ and $^{87}$Rb $|5S_{1/2};F=2\rangle \rightarrow |5P_{3/2};F'=1,2,3\rangle$ hyperfine transitions for the FC parameters used in the experiment. Note that, when the $n$-th comb mode is resonant with the $^{87}$Rb $|5S_{1/2};F=2\rangle \rightarrow |5P_{3/2};F'=3\rangle$ transition, the $(n+14)$-th comb mode is 0.4 MHz blue detuned from (i.e., almost in resonance with) the $^{85}$Rb $|5S_{1/2};F=3\rangle \rightarrow |5P_{3/2};F'=4\rangle$ transition.

FC radiation pressure force is periodic with respect to comb detuning with period equal to $f_{\mathrm{rep}}$.

The FC radiation pressure force induced on the $^{85,87}$Rb atoms, shown in Fig. 1(b), is the total force obtained by summing the contributions from three hyperfine transitions. The force is calculated numerically by solving the optical Bloch equations that describe the excitation of six-level $^{85,87}$Rb atoms by the FC [25] and subsequently using the Ehrenfest theorem. More details on the comb force calculation are given in Ref. [23]. The overall agreement of the measured and calculated comb force in Fig. 1 is satisfactory. The relative positions of the peaks, as well as the ratios between them are well reproduced for both species. The calculated force is, however, about four times larger than the measured force, and a small broadening of around 1 MHz is observed in the measured peaks. This discrepancy can be attributed to several effects that were not taken into account in the theoretical model, such as stray magnetic fields, finite comb mode linewidth, and in particular the spatial beam profile. These results are in line with the measured and calculated FC force on $^{87}$Rb atoms in our recent work [9]. The deviation of the measured and calculated force around $\delta \approx 0$ will be clarified in the following paragraphs.

In order to understand the relative positions of the comb force peaks in Fig. 1, it is instructive to study in more detail the hyperfine energy level structure of $^{85,87}$Rb atoms with respect to the FC spectrum. Figure 2 schematically depicts the positions of the comb modes with respect to the three $^{85}$Rb $|5S_{1/2};F=3\rangle \rightarrow |5P_{3/2};F'=2,3,4\rangle$ and the three $^{87}$Rb $|5S_{1/2};F=2\rangle \rightarrow |5P_{3/2};F'=1,2,3\rangle$ hyperfine transitions that are relevant for the atom-comb interaction. When the $n$-th comb mode is resonant with the $^{87}$Rb $|5S_{1/2};F=2\rangle \rightarrow |5P_{3/2};F'=3\rangle$ transition, the $(n+14)$th mode is 0.4 MHz blue detuned from the $^{85}$Rb $|5S_{1/2};F=3\rangle \rightarrow |5P_{3/2};F'=4\rangle$ transition. Taking into account that the natural linewidth of both hyperfine transitions is $\Gamma = 2\pi \times 6.07$ MHz [26,27], the above condition ensures simultaneous excitation of the cooling transitions of both $^{85}$Rb and $^{87}$Rb atoms by the FC. These two excitations contribute to the peak around $\delta \approx 0$ in Fig. 1. The peak at $\delta \approx -25.5$ MHz for $^{87}$Rb is due to the $(n-3)$rd mode being in resonance with the $|5S_{1/2};F=2\rangle \rightarrow |5P_{3/2};F'=2\rangle$ transition, and the $(n-5)$th mode in resonance with the $|5S_{1/2};F=2\rangle \rightarrow |5P_{3/2};F'=1\rangle$ transition. For $^{85}$Rb, the peak at $\delta \approx -23.5$ MHz is due to the $(n+12)$-th comb mode being in resonance with the $|5S_{1/2};F=3\rangle \rightarrow |5P_{3/2};F'=2\rangle$ transition, whereas the peaks at $\delta \approx -40$ MHz and $\delta \approx 40$ MHz are due to the $(n+13)$th and $(n+12)$th modes, respectively, being in resonance with the $|5S_{1/2};F=3\rangle \rightarrow |5P_{3/2};F'=3\rangle$ transition.

The largest force is obtained for both isotopes for $\delta \approx 0$, where simultaneous excitation of the $^{87}$Rb and $^{85}$Rb cooling transitions is achieved by the $n$th and $(n+14)$th comb mode, respectively. As the intensities of these two modes are approximately equal, the larger calculated force for $^{85}$Rb reflects the larger transition dipole matrix elements for this transition of $\sqrt{3/2} \times 3.584 \times 10^{-29}$ C m [27], compared to $\sqrt{7/6} \times 3.584 \times 10^{-29}$ C m [26] for $^{87}$Rb. The actual situation is more complex, as can be seen in the experimental results, where the measured comb force for $\delta \approx 0$ is equal for both species. Due to the circular polarization of the FC beam and the presence of stray magnetic fields, the $^{85}$Rb $|5S_{1/2};F=3;m_F=+3\rangle \rightarrow |5P_{3/2};F'=4;m_F=+4\rangle$ and $^{87}$Rb $|5S_{1/2};F=2;m_F=+2\rangle \rightarrow |5P_{3/2};F'=3;m_F=+3\rangle$ stretched transitions dominate all other Zeeman hyperfine transitions. As these two transitions have equal transition dipole matrix elements of $\sqrt{1/2} \times 3.584 \times 10^{-29}$ C m [26,27], the resulting comb force is the same for both isotopes. This could be accounted for in the force calculations by including all Zeeman hyperfine transitions into the optical Bloch equations, but this is rather cumbersome and beyond the scope of this paper.

FC cooling in one dimension is achieved by using two counter-propagating $\sigma^+$ and $\sigma^-$ polarized beams. We first prepare the pre-cooled clouds of $^{85}$Rb and $^{87}$Rb atoms in a dual-species MOT. Then we turn off the MOT cooling beams and turn on the FC beams. The weak cw repumper lasers are left on, as well as the quadrupole magnetic field. Since the clouds are in the center of the quadrupole field, the magnetic field is $B \approx 0$. The FC beams are left on for the FC cooling time $t_{\mathrm{FC}}$, after which they are switched off, and the clouds are left to expand freely for several ms. After a given expansion time, we switch on the MOT cooling beams and image the cloud fluorescence with a camera separately for each species. A series of alternating time-of-flight (TOF) images of $^{85}$Rb and $^{87}$Rb clouds are taken in this way at different expansion times. We then determine the cloud widths by fitting a Gaussian distribution to the spatial distribution of the atoms in the clouds. The obtained cloud widths as a function of expansion time $\sigma(t)$ give an accurate measure of the cloud temperature by fitting the expression $\sigma(t) = \sqrt{\sigma_0^2 + \frac{k_B T}{m} t^2}$ [28,29], where $\sigma_0$ is the cloud width at $t = 0$ (when the FC beams are switched off), $k_B$ is the Boltzmann constant, $m$ is the atomic mass, and $T$ is the cloud temperature. We repeat the measurement sequence 10 times and average the results to obtain the average temperature and its statistical uncertainty.

Temperatures obtained by FC cooling of $^{85}$Rb and $^{87}$Rb as a function of comb detuning are shown in Fig. 3. The total power of the FC beams on the atoms is 20 mW with a beam size (FWHM) of 2.7 mm, resulting in the power and intensity per comb mode of 0.6 $\mu$W and 7.2 $\mu$W/cm$^2$, respectively. $t_{\mathrm{FC}} = 3$ ms and TOF images are taken for expansion

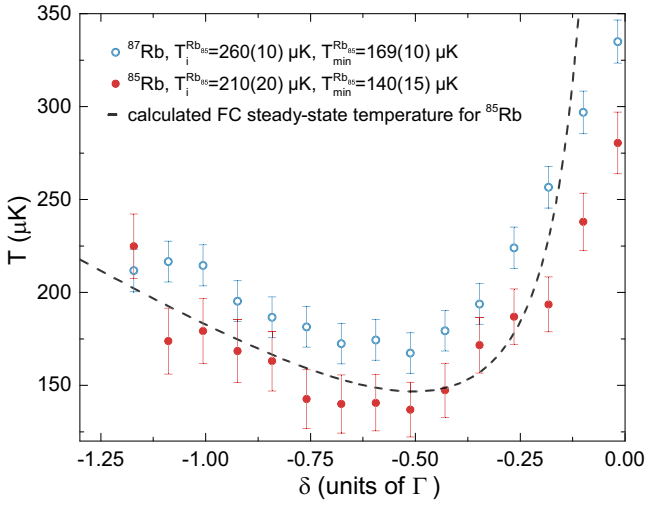


FIG. 3. Temperatures obtained by simultaneous FC cooling of $^{85}$Rb (red circles) and $^{87}$Rb (blue circles) as a function of the comb detuning. $\delta$ denotes the detuning of the $n$th comb mode from the $^{87}$Rb $|5S_{1/2};F=2\rangle \rightarrow |5P_{3/2};F'=3\rangle$ transition. The initial cloud temperatures are $T_i = 210(20)$ $\mu$K for $^{85}$Rb and $T_i = 260(10)$ $\mu$K for $^{87}$Rb, and the FC cooling time is $t_{\mathrm{FC}} = 3$ ms. For $^{85}$Rb the steady-state temperature, which approaches the Doppler temperature, is achieved for $\delta \approx -\Gamma/2$. Due to the higher $T_i$ for $^{87}$Rb, the steady-state is not achieved during the applied cooling time leading to slightly higher measured temperatures. In general, equal temperature dependence on the comb detuning is obtained for both isotopes. The dashed line indicates the $^{85}$Rb temperature calculated for the relevant experimental parameters using the relation (17) in Ref. [10], i.e., the steady-state temperature obtained for the simple model of 1D FC cooling of two-level atoms.

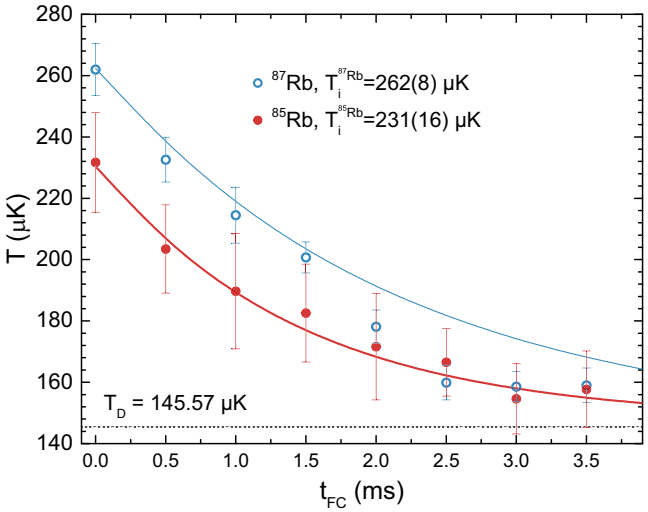


FIG. 4. Temperatures obtained by simultaneous FC cooling of $^{85}$Rb (red circles) and $^{87}$Rb (blue circles) as a function of FC cooling time $t_{\mathrm{FC}}$. The initial cloud temperatures are $T_i = 231(16)$ $\mu$K for $^{85}$Rb and $T_i = 262(8)$ $\mu$K for $^{87}$Rb, with comb detuning $\delta = -\Gamma/2$. As the FC cooling time is increased, the cloud temperature decreases from the initial value $T_i$ prepared in the MOT phase and approaches the Doppler limited steady-state temperature on the time scale of a few ms. Solid lines represent the theoretical estimate for the dependence of the cloud temperature on the FC cooling time (see text for details of the model).

times between 6–11 ms. The initial cloud temperatures of $T_i = 210(20)$ $\mu$K for $^{85}$Rb and $T_i = 260(10)$ $\mu$K for $^{87}$Rb are chosen in order to make the data for the two isotopes clearly distinguishable on the graph. For the same cloud initial temperatures $T_i$, the measured FC cooling temperatures for the two isotopes would overlap within the measurement error. The measured temperatures approach $T_i$ for large comb detunings. FC cooling is observed when there is a mode in the comb spectrum that is red detuned from a cooling transition, i.e., when the $n$th comb mode is red detuned from the $^{87}$Rb $|5S_{1/2};F=2\rangle \rightarrow |5P_{3/2};F'=3\rangle$ transition, and simultaneously the $(n+14)$th mode is red detuned from the $^{85}$Rb $|5S_{1/2};F=3\rangle \rightarrow |5P_{3/2};F'=4\rangle$ transition. The dashed line in Fig. 3 indicates the steady-state 1D FC cooling temperature for the case of two-level atoms, calculated using relation (17) from Ref. [10] and relevant experimental parameters: $^{85}$Rb $|5S_{1/2};F=3\rangle \rightarrow |5P_{3/2};F'=4\rangle$ transition dipole matrix element of $\sqrt{3/2} \times 3.584 \times 10^{-29}$ C m, $\Gamma = 2\pi \times 6.07$ MHz, pulse electric field amplitude $E_0 = 0.9 \times 10^5$ V/m, pulse duration $T_P = 300$ fs, pulse area $\theta = \pi/78$, and $f_{\mathrm{rep}} = 80.495$ MHz. The agreement between the measured $^{85}$Rb temperatures and the 1D FC cooling temperatures calculated for the simple two-level atom model is quite satisfactory. As expected, deviations due to heating are observed when the comb detuning approaches 0.

The lowest temperature is observed for $\delta \approx -\Gamma/2$, and approaches the Doppler temperature (145.57 $\mu$K [27]) for $^{85}$Rb. The lowest measured temperature for $^{87}$Rb in Fig. 3 is slightly higher than the Doppler temperature due to the higher initial temperature. In this case the steady state temperature is not yet reached after $t_{\mathrm{FC}}$. This is illustrated in Fig. 4 where $^{85}$Rb and $^{87}$Rb FC cooling temperatures are shown as a function of the FC cooling time. $T_i = 231(16)$ $\mu$K for $^{85}$Rb and $T_i = 262(8)$ $\mu$K for $^{87}$Rb. Temperatures are measured for $\delta = -\Gamma/2$, i.e., for the $n$th comb mode 3 MHz red detuned from the $^{87}$Rb $|5S_{1/2};F=2\rangle \rightarrow |5P_{3/2};F'=3\rangle$ transition and the $(n+14)$th mode 2.6 MHz red detuned from the $^{85}$Rb $|5S_{1/2};F=3\rangle \rightarrow |5P_{3/2};F'=4\rangle$ transition. The cloud temperatures decrease from the initial value prepared in the MOT phase and approach the Doppler limit after a few ms of FC cooling. As expected, the steady state temperature is reached sooner when increasing the comb mode intensity and lowering the initial cloud temperature.

The solid lines in Fig. 4 represent the theoretical estimates for the cloud temperatures as a function of $t_{\mathrm{FC}}$, based on a simple model in which the comb mode responsible for cooling is considered a cw laser (of the same frequency), and the atomic system is considered a two-level system. The model relies on determining the time evolution of the cloud atomic velocity distribution by solving the Fokker-Planck equation for different interaction times, with the radiation pressure force and the diffusion coefficient calculated using standard low-intensity theory for two-level atoms in 1D (see for example Ref. [30]; more details on the model can be found in Ref. [9]). The following parameters were used: cw laser intensity of

7.2 $\mu$W/cm$^2$ (corresponding to the intensity per comb mode), transition dipole matrix elements $\sqrt{3/2} \times 3.584 \times 10^{-29}$ C m and $\sqrt{7/6} \times 3.584 \times 10^{-29}$ C m for $^{85}$Rb and $^{87}$Rb, respectively, and $\delta = -\Gamma/2$. This simple model well describes the behavior of the measured temperatures, confirming the analogy between FC and cw laser cooling, in line with the results of our previous work [9]. The minimum temperature observed in our FC cooling experiment is limited by the low comb mode intensity (about two orders of magnitude lower than the saturation intensity). Our previous investigations have shown that, in order to achieve sub-Doppler temperatures, the comb mode intensity must be increased by a factor of 40 [9]. Based on the analogy of FC and cw laser cooling, we have estimated this sub-Doppler threshold by measuring the temperature as a function of cw laser intensity in the case of cw laser cooling. Aside from reaching sub-Doppler temperatures, using high comb mode intensities should also enable FC cooling directly from a room temperature atomic gas [10].

In conclusion, we have demonstrated simultaneous cooling of $^{85}$Rb and $^{87}$Rb atoms by using two comb modes from the same FC spectrum. Simultaneous cooling of two types of atoms does not affect the cooling of each type, which can be seen from the comparison of FC cooling of $^{87}$Rb in the case of dual-species cooling (this work) and single-species cooling (Ref. [9]). In addition, we see no evidence that the action of other comb modes within the FC spectrum deteriorates the final FC cooling temperature. The minimum observed temperature is limited by the comb mode intensity. We confirm the analogy between simultaneous laser cooling of multiple atomic species using a FC and multiple independent cw lasers, in line with Ref. [9], thus verifying the potential application of the FC for simultaneous multichannel cooling. We believe that the results of this work should contribute to the development of multispecies AIs for space applications. This could be achieved with available fiber-based combs that have already been used in space applications [31], and can provide mW-level power per comb mode [32]—sufficient to enable direct frequency comb cooling from room temperature to sub-Doppler temperatures. Moreover, there is clear potential in utilizing the rapidly developing chip-based microresonator FC technology [33–35] that can currently provide $>$ 1 mW per comb mode at high repetition rates in the gigahertz (GHz) range [36]. In addition, we foresee the application of the results of our work in the experimental investigations of multiatom interactions and creation of multispecies cold molecules.

The authors acknowledge support from the Croatian Science Foundation (Project Frequency comb cooling of atoms - IP-2018-01-9047). F. Schmid acknowledges support from the Deutscher Akademischer Austauschdienst (DAAD) and the Croatian Ministry of Science and Education under the German-Croatian bilateral project. The authors thank T. Udem for reading the manuscript and providing constructive comments. In addition, the authors acknowledge Neven Šantić for early contribution to the development of cold atoms experiment and Ivor Krešić for the early contribution to the development of theoretical models, as well as Grzegorz Kowzan and Piotr Maslowski for their contribution to the frequency comb stabilization.

[1] J. Ye, H. Schnatz, and L. W. Hollberg, IEEE J. Sel. Top. Quantum Electron **9**, 1041 (2003).
[2] N. Picque and T. W. Hänsch, Nat. Photonics **13**, 146 (2019).
[3] P. Maslowski, K. C. Cossel, A. Foltynowicz, and J. Ye, Cavity-enhanced direct frequency comb spectroscopy, in *Cavity-Enhanced Spectroscopy and Sensing*, edited by G. Gagliardi and H.-P. Loock, Springer Series in Optical Sciences Vol. 179 (Springer, Berlin, Heidelberg, 2014).
[4] G. Maltese, M. I. Amanti, F. Appas *et al.*, npj Quantum Inf. **6**, 13 (2020).
[5] D. Kielpinski, Phys. Rev. A **73**, 063407 (2006).
[6] J. Davila-Rodriguez, A. Ozawa, T. W. Hänsch, and T. Udem, Phys. Rev. Lett. **116**, 043002 (2016).
[7] A. M. Jayich, X. Long, and W. C. Campbell, Phys. Rev. X **6**, 041004 (2016).
[8] M. Ip, A. Ransford, A. M. Jayich, X. Long, C. Roman, and W. C. Campbell, Phys. Rev. Lett. **121**, 043201 (2018).
[9] N. Šantić, D. Buhin, D. Kovačić, I. Krešić, D. Aumiler, and T. Ban, Sci. Rep. **9**, 2510 (2019).
[10] D. Aumiler and T. Ban, Phys. Rev. A **85**, 063412 (2012).
[11] A. Bonnin, N. Zahzam, Y. Bidel, and A. Bresson, Phys. Rev. A **88**, 043615 (2013).
[12] L. Zhou, S. Long, B. Tang, X. Chen, F. Gao, W. Peng, W. Duan, J. Zhong, Z. Xiong, J. Wang, Y. Zhang, and M. Zhan, Phys. Rev. Lett. **115**, 013004 (2015).
[13] J. Williams, S. Chiow, N. Yu, and H. Müller, New J. Phys. **18**, 025018 (2016).
[14] T. Schuldt, C. Schubert, M. Krutzik *et al.*, Exper. Astron. **39**, 167 (2015).
[15] A. Bonnin, C. Diboune, N. Zahzam, Y. Bidel, M. Cadoret, and A. Bresson, Appl. Phys. B **124**, 181 (2018).
[16] G. Modugno, M. Modugno, F. Riboli, G. Roati, and M. Inguscio, Phys. Rev. Lett. **89**, 190404 (2002).
[17] H. Hara, Y. Takasu, Y. Yamaoka, and J. M. Doyle, and Y. Takahashi, Phys. Rev. Lett. **106**, 205304 (2011).
[18] V. D. Vaidya, J. Tiamsuphat, S. L. Rolston, and J. V. Porto, Phys. Rev. A **92**, 043604 (2015).
[19] K. W. Madison, Y. Wang, A. M. Reym, and K. Bongs, *Annual Review of Cold Atoms and Molecules*, Vol. 1 (World Scientific Publishing Co. Pte. Ltd. Singapore, 2013).
[20] L. D. Carr, D. DeMille, R. V. Krems, and J. Ye, New J. Phys. **11**, 055049 (2009).
[21] C. R. Menegatti, B. S. Marangoni, and L. G. Marcassa, Laser Phys. **18**, 1305 (2008).
[22] C. Chin, R. Grimm, P. Julienne, and E. Tiesinga, Rev. Mod. Phys. **82**, 1225 (2010).
[23] See Supplemental Material at http://link.aps.org/supplemental/10.1103/PhysRevA.102.021101 for detailed description of the dual-species magneto-optical trap and the theoretical model for the calculation of the FC radiation pressure force.

[24] J. Ye and S. T. Cundiff (Eds.), *Femtosecond Optical Frequency Comb: Principle, Operation and Applications* (Springer Science + Business Media, Inc., Boston, 2005).
[25] T. Ban, D. Aumiler, H. Skenderović, and G. Pichler, Phys. Rev. A **73**, 043407 (2006).
[26] D. A. Steck, Rubidium 87 D Line Data, http://steck.us/alkalidata/rubidium87numbers.pdf.
[27] D. A. Steck, Rubidium 85 D Line Data, http://steck.us/alkalidata/rubidium85numbers.pdf.
[28] T. M. Brzozowski, M. Maczynska, M. Zawada, J. Zachorowski, and W. Gawlik, J. Opt. B: Quantum Semiclass. Opt. **4**, 62 (2002).
[29] I. Yavin, M. Weel, A. Andreyuk, and A. Kumarakrishnan, Am. J. Phys. **70**, 149 (2002).
[30] H. J. Metcalf, and P. van der Straten, Laser Cooling and Trapping (Springer, New York, 2001).
[31] M. Lezius *et al.*, Optica **12**, 1381 (2016).
[32] X. Li, M. A. R. Reber, C. Corder, Y. Chen, and P. Zhao, Rev. Sci. Instrum. **87**, 093114 (2016).
[33] T. J. Kippenberg, R. Holzwarth, and S. A. Diddams, Science **332**, 555 (2011).
[34] T. Tanabe, S. Fujii, and R. Suzuki, Jpn. J. Appl. Phys. **58**, SJ0801 (2019).
[35] A. A. Savchenkov, D. Eliyahu, W. Liang, V. S. Ilchenko, J. Byrd, A. B. Matsko, D. Seidel, and L. Maleki, Opt. Lett. **38**, 2636 (2013).
[36] X. Xue, P.-H. Wang, Y. Xuan, M. Qi, and A. M. Weiner, Laser Photonics Rev. **11**, 1600276 (2017).

SCIENTIFIC REPORTS

OPEN

# Cooling of atoms using an optical frequency comb

N. Šantić, D. Buhin, D. Kovačić, I. Krešić, D. Aumiler & T. Ban

Received: 19 October 2018
Accepted: 21 December 2018
Published online: 21 February 2019

**We report on laser cooling of neutral rubidium atoms by using a single mode of a frequency comb. Cooling is achieved on a dipole-allowed transition at 780 nm in a one-dimensional retro-reflected beam geometry. Temperatures are measured using standard time-of-flight imaging. We show the dependence of the temperature on the cooling time, intensity and detuning of the frequency comb. The lowest temperature achieved is approximately equal to the Doppler temperature and is limited by the intensity of the comb mode driving the cooling transition. Additionally, we verify the analogy between frequency comb and continuous-wave laser cooling. Our work is a step towards laser cooling of atoms with strong cycling transitions in the vacuum ultraviolet, such as hydrogen, deuterium and antihydrogen, where generation of continuous-wave laser light is limited by current laser technology. Achieving efficient cooling at these wavelengths would significantly improve the precision of optical frequency standards, enable measurements of fundamental constants with unprecedented accuracy, improve tests of charge, parity, and time reversal symmetry, and open the way to achieving quantum degeneracy width new atomic species.**

Laser cooling and trapping brings atomic physics to one of the most exciting frontiers in science, with applications ranging from atom interferometry[1] and optical frequency standards[2] to high precision spectroscopy and ultracold chemistry[3,4]. Regardless of their great importance, laser cooling techniques are still limited to atoms with a simple energy level structure and closed transitions accessible by currently available continuous wave (CW) laser sources.

There are two main obstacles that prevent the extension of laser cooling techniques to a variety of atomic species and molecules. The first is associated with difficulties in creating CW laser light in the vacuum ultraviolet (VUV). The absence of such light sources hampers cooling of simple atoms such as hydrogen, deuterium and antihydrogen that exhibit single-photon transitions suitable for laser cooling in the VUV. For example, cooling of hydrogen and antihydrogen using the strong cycling, single photon 1s-2p transition requires Lyman-alpha radiation at 121 nm, which is far below the limit imposed by the phase matching condition in nonlinear crystals[5]. The second obstacle is associated with the complex level structure of many atoms and all molecules, which permits decay of an excited state into a number of lower lying metastable states, widely separated in energy. Efficient cooling of those species requires multiple repumping lasers which makes the system inefficient and experimentally very challenging[6].

The aforementioned issues can be addressed using mode-locked femtosecond (fs) or picosecond (ps) lasers with high pulse repetition rates which produce optical frequency combs (FCs). Due to their pulsed light emission, FCs provide high peak powers needed for efficient frequency conversion via nonlinear crystals[7] or high harmonic generation[8,9]. Simultaneously, FCs preserve long coherence times needed for efficient laser cooling since their spectrum consists of a series of narrow, phase coherent frequency lines. Mode-locked ps lasers have been used to decelerate specific velocity groups in atomic beams that were in resonance with frequency comb modes[10], and to compress the velocity distribution of an atomic beam[11]. On the other hand, few ps long pulses have been used for broadband laser cooling of ions in the condition when the atomic relaxation time is shorter than the time period of the mode-locked laser[12]. A laser cooling scheme that uses ultrafast pulse trains to cool simple atoms in the VUV as well as complex atoms and molecules is proposed in the work of Kielpinski[13]. The author proposes driving two-photon transition with pulse trains in order to cool atoms with transitions in the VUV. To address cooling of complex atoms and molecules, the author proposes to modulate the original FC at several adjustable RF frequencies via electro-optical modulators. Cooling of atoms on a single-photon transition using a FC has previously been proposed in the work of our group[14]. There, a theory to quantitatively describe the cooling process, based on the interaction of two-level atoms with two counterpropagating pulse trains, is developed and used to derive the

Institute of Physics, Zagreb, 10000, Croatia. D. Buhin and D. Kovačić contributed equally. Correspondence and requests for materials should be addressed to T.B. (email: ticijana@ifs.hr)

123

radiative force and steady-state temperature. We also showed that simultaneous laser cooling in multiple cooling channels can be achieved using a single frequency comb source.

Along the lines of these proposals, the first experiments that demonstrate FC cooling of atoms and ions have recently appeared in the literature[5,15,16]. Jayich *et al.*[15] demonstrate FC Doppler cooling of pre-cooled rubidium atoms on the two-photon transition at 778 nm in a 1D counterpropagating geometry. The authors achieved cooling through a coherent process in which multiple excitation pathways are excited by different combinations of comb modes. In the second experiment[5], the authors demonstrate FC Doppler cooling of trapped magnesium ions on a single-photon transition in the UV by using a frequency tripled comb. And just recently, Ip *et al.*[16] demonstrated loading, cooling and crystallization of hot ytterbium ions using an optical frequency comb due to phonon lasing of the ion's harmonic motion in the trap which is driven by the blue-detuned comb teeth.

In this work we demonstrate cooling of rubidium atoms on a dipole-allowed transition at 780 nm by using a FC. To the best of our knowledge, this is the first demonstration of FC cooling of neutral atoms on a single-photon transition. We prepare a cold sample of rubidium atoms that we further cool with the FC in a 1D retro-reflected geometry, achieving a minimum temperature close to the Doppler temperature, $T_D = 146\,\mu$K[17]. We verify the analogy between FC and CW cooling by replacing the FC with a CW laser in the same experimental geometry, whose intensity matches that of a single comb mode. A simple theoretical model was applied to model our experimental findings, in an approach where one comb line mimics a CW laser interacting with a two-level rubidium atom.

## Results

Our apparatus consists of a standard magneto-optical trap (MOT) for $^{87}$Rb atoms. A cold rubidium cloud is loaded from background vapor in a stainless steel chamber. The MOT is realized by intersecting six CW laser beams, which, together with the anti-Helmholtz produced quadrupole magnetic field, create the trapping potential. Fluorescence imaging of the cloud is performed with a camera aligned along a horizontal axis. In typical experimental conditions we obtain a cloud 1.6 mm in diameter, which contains $\approx 10^8$ atoms. By changing the detuning of the MOT beams we are able to prepare a cloud with temperatures in the range of 50–300 μK. Such a cold cloud represents the initial sample for all our measurements presented in this work.

The FC is generated by frequency doubling an Er:fiber mode-locked laser (TOPTICA FFS) operating with a repetition rate $f_{rep} = 80.5$ MHz, an output power of $P \approx 230$ mW, and a ≈130 nm broad (FWHM) spectrum centered around 1560 nm. The frequency-doubled spectrum used in the experiment is centered around 780 nm with a FWHM of about 5 nm and a total power of 76 mW. Approximately 90000 comb lines are contained under the FC spectral envelope. The FC is stabilized to a CW reference laser (ECDL, Moglabs CEL002) locked to the $^{87}$Rb$|5S_{1/2}; F=2\rangle \rightarrow |5P_{3/2}; F'=3\rangle$ transition, while the pulse train repetition frequency is locked to a stable microwave reference. A brief technical description of the FC stabilization is outlined in Methods.

**FC radiation pressure force.** The efficiency of Doppler cooling depends critically on the scattering rate, since a scattering event changes the atomic momentum, on average, by one photon recoil. Hence, in order to determine the FC scattering rate we measure the FC radiation pressure force on cold Rb atoms. A single linearly polarized FC beam is sent through an acousto-optic modulator (AOM) for fast switching, and is then directed to the center of the MOT where the cold cloud of Rb atoms is prepared. A total power of 18 mW was used with a beam FWHM of 2.7 mm, giving a FC intensity of about 0.01 mW/cm$^2$ per comb mode. The measurement sequence starts with the preparation of a cold $^{87}$Rb cloud and the FC beam off. At $t = 0$ we turn off the MOT beams, and switch on the FC beam. The weak repumper light is left on continuously to optically pump the atoms out of the $|5S_{1/2}; F=1\rangle$ ground state. It propagates perpendicular to the FC, is arranged in a counter-propagating configuration, and has no measurable mechanical effect. We let the FC interact with the cold cloud for 1 ms. During this time the cloud center of mass (CM) accelerates along the FC beam propagation axis ($+x$-direction) due to the FC radiation pressure force. At $t = 1$ ms the FC beam and repumper are switched off, and the cloud expands freely for 5 ms. At $t = 6$ ms the MOT beams are turned on and the cloud fluorescence is imaged with a camera to determine the cloud's centre of mass displacement in the $x$ direction, $\Delta x_{CM}$. We then use $\Delta x_{CM}$ to calculate the acceleration of the cloud, which, using the Rb atom mass, finally gives the FC force. This measurement is performed for different relative detunings of the comb lines with respect to the hyperfine transitions, the average of 4 consecutive measurements is shown in Fig. 1(b).

As the FC spectrum consists of identical, regularly spaced comb lines, we characterize the FC spectrum by the detuning $\delta$ of the $n$-th comb mode from the $|5S_{1/2}; F=2\rangle \rightarrow |5P_{3/2}; F'=3\rangle$ transition. Accordingly, the measured FC force dependence on comb detuning, $F_{FC}(\delta)$, shown in Fig. 1(b,c) repeats every $f_{rep} = 80.5$ MHz. Two distinct peaks appear in one $f_{rep}$ scan reflecting the interaction with three comb modes, as shown schematically in Fig. 1(a). The peak at $\delta = 0$ is due to the $n$-th comb mode being in resonance with the $|5S_{1/2}; F=2\rangle \rightarrow |5P_{3/2}; F'=3\rangle$ transition, whereas the peak at $\delta \approx -4.2\,\Gamma$ is due to the $(n-3)$-rd mode being in resonance with the $|5S_{1/2}; F=2\rangle \rightarrow |5P_{3/2}; F'=2\rangle$ transition, and the $(n-5)$-th mode in resonance with the $|5S_{1/2}; F=2\rangle \rightarrow |5P_{3/2}; F'=1\rangle$ transition. Here, $\Gamma = 2\pi \times 6.0666$ MHz[17], and refers to the natural line width of the $^{87}$Rb $|5S_{1/2}\rangle \rightarrow |5P_{3/2}\rangle$ transition. The contributions to the FC force coming from transitions to different hyperfine states being in resonance with different comb modes are expressed more clearly in the results of calculations of the FC force shown in Fig. 1(c), where contributions of relevant transitions are explicitly given. The calculated FC force is obtained by numerically solving the optical Bloch equations describing the excitation of six-level $^{87}$Rb atoms by a FC[18], and subsequently using the Ehrenfest theorem. More details on the FC force calculation are given in Methods.

The agreement between measured and calculated FC force in Fig. 1(b,c) is reasonable. Relative positions of the two peaks are well reproduced, though there is a small but noticeable broadening of the measured peaks, which we attribute to Zeeman splitting due to the stray magnetic fields. It is worth noting that similar line broadening has also been observed in[15], whereas a detailed analysis of all possible systematic sources of errors which affect line broadening and shifts in FC spectroscopy can be found in[19]. The comparison of the areas under the measured

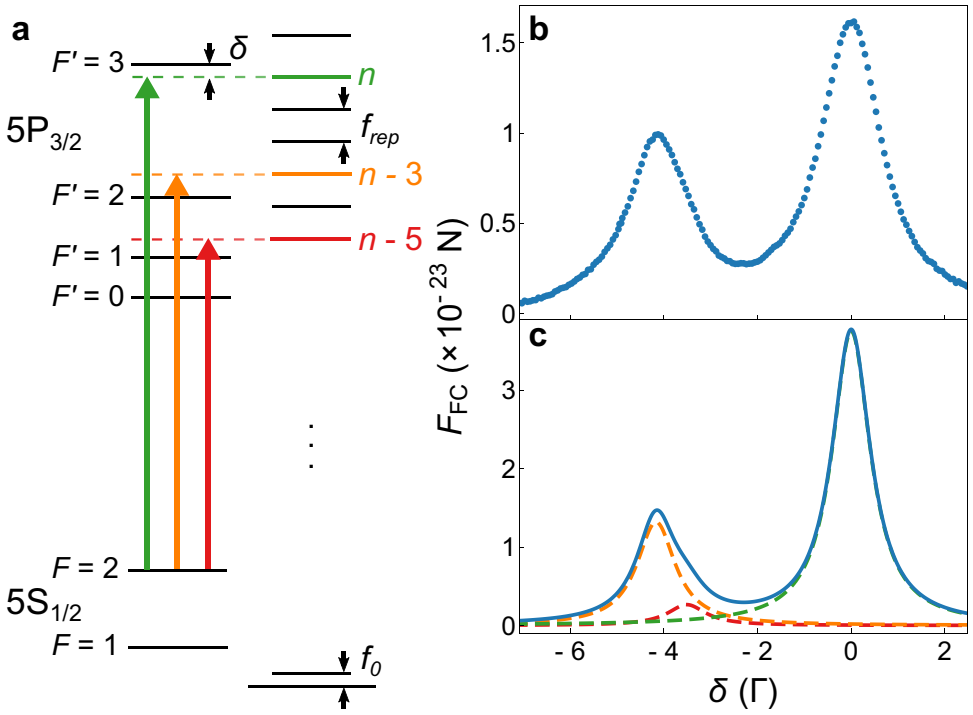


**Figure 1.** Scheme of relevant $^{87}$Rb energy levels and FC modes (**a**). Measured (**b**) and calculated (**c**) FC force as a function of detuning. The total force in (**c**), blue line, reflects the interaction with three comb modes: the $n$-th comb mode with the $|5S_{1/2}; F=2\rangle \rightarrow |5P_{3/2}; F'=3\rangle$ transition (green dashed line); the $(n-3)$-rd mode resonance with the $|5S_{1/2}; F=2\rangle \rightarrow |5P_{3/2}; F'=2\rangle$ transition (orange dashed line); and the $(n-5)$-th mode resonance with the $|5S_{1/2}; F=2\rangle \rightarrow |5P_{3/2}; F'=1\rangle$ transition (red dashed line).

and calculated force curve gives the factor 1.3, i.e. calculated force is 30% larger than measured. This agreement is satisfactory given that there are no free parameters in the calculations. In addition, calculations do not account for all the physical parameters of the experiment such as the stray magnetic fields, finite laser linewidth, and the laser beam profile.

The largest force is measured when the $n$-th comb mode is resonant with the standard cooling transition for $^{87}$Rb, i.e., the right peak in Fig. 1(b), for which $\Delta x_{CM} = 0.6$ mm is obtained. During 1 ms of FC interaction time the atoms are accelerated with a constant acceleration of 110 m/s$^2$ and acquire a velocity of 0.11 m/s. From the measured force, we calculate an on resonance scattering rate of $\gamma_{scat} = 18600\ s^{-1}$. Although the measured FC scattering rate is nearly three times larger than the value for a two-photon FC excitation, reported in Jayich *et al.*[15], both works show comparable performance in term of the peak force, since the momentum transferred per two-photon excitation is about two times the momentum transferred per a single photon excitation. This clearly suggests that FC cooling via one-photon excitation is viable, and could therefore be a good choice when pursuing cooling of atoms and ions with dipole allowed transitions in the VUV spectral region.

**FC cooling.** In order to achieve FC cooling in one dimension, we retro-reflect the FC beam. Two counter-propagating FC beams are carefully overlapped in the centre of the MOT, and specific care is taken to slightly focus the retro-reflected beam in order to match its intensity to the incoming FC beam intensity. Prior to entering the MOT chamber $\lambda/4$ waveplates are put in the beam path, so as to achieve a $\sigma^+$-$\sigma^-$ polarization configuration.

The measurement sequence for studying FC cooling starts by preparing a cold rubidium cloud in the MOT. At $t=0$ the MOT beams are switched off. The weak CW repumper laser is again left on. A quadrupole magnetic field with a gradient of 11.3 G/cm remains on during the measurements. Since the cloud is in the centre of the quadrupole field, the magnetic field is $B \approx 0$. At $t = 100\ \mu$s the FC beams are turned on. The FC beams are on for a time $t_{FC}$ (typically 3 ms), which we call the FC cooling time, after which the FC beams are switched off, and the cloud is left to expand freely for several ms before it is imaged with the camera. A series of time-of-flight (TOF) images are taken in this way at different expansion times. We fit our measured atomic distributions to the two dimensional Gaussian function characterized by $\sigma_x$ and $\sigma_y$, which are related to the widths of the cloud along the x and y direction, respectively. The obtained spatial width of the cloud $\sigma_x$ as a function of the expansion time gives an accurate measure of the cloud temperature by fitting to the expression $\sigma(t)^2 = \sigma_0^2 + \frac{kT}{m}t^2$[15], where $t=0$ is the time when the FC cooling laser is switched off. We repeat the measurement protocol 4 times for a given expansion time, and subsequently average the results to obtain the temperature.

Temperatures obtained by TOF measurements as a function of $\delta$ are shown in Fig. 2, where $\delta$ is the detuning of the $n$-th comb mode from the $|5S_{1/2}; F=2\rangle \rightarrow |5P_{3/2}; F'=3\rangle$ transition. A total power of the FC beam entering the MOT chamber was 21 mW and a beam FWHM of 2.8 mm were used, giving 0.6 $\mu$W power and 0.011 mW/cm$^2$ intensity per comb mode. The initial cloud temperature is $T_i = 240\ \mu$K, and the FC cooling time is $t_{FC} = 3$ ms.

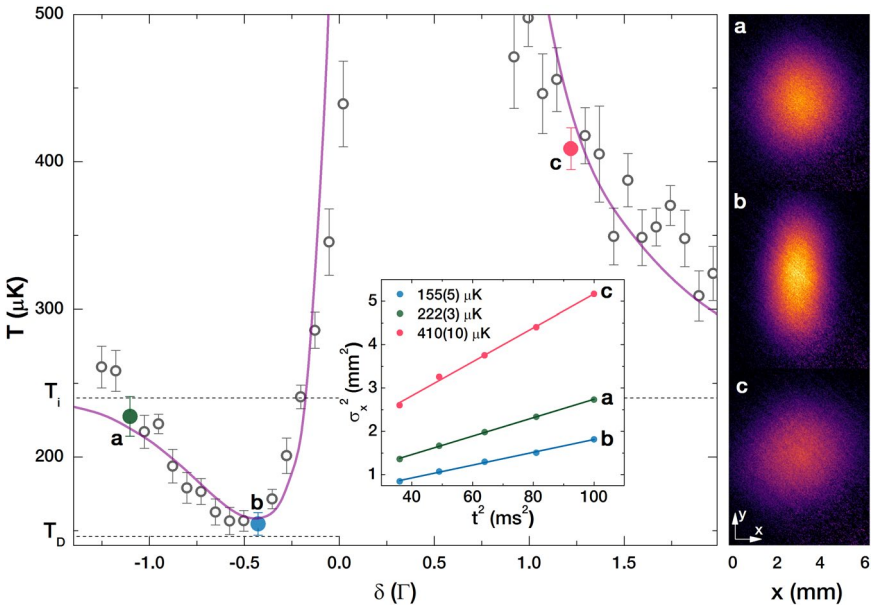


**Figure 2.** Temperature obtained by TOF after 1D FC cooling as a function of FC detuning. The right panel shows three TOF images taken after 6 ms expansion time for a FC detuning that corresponds to the cloud's temperature that is close to the initial temperature - green data point (**a**), lowest obtained - blue data point (**b**), higher than the initial temperature - red data point (**c**). Corresponding TOF data for 6–10 ms expansion times are given in the inset. A cloud with an initial temperature of $T_i = 240\,\mu$K, a FC cooling time of 3 ms, and a comb mode intensity of 0.01 mW/cm$^2$ were used. Solid line - theoretical model for relevant experimental parameters.

The measured temperatures approach the initial cloud temperature for large $\delta$. FC cooling is observed for the $n$-th comb mode red detuned from the $|5S_{1/2}; F=2\rangle \rightarrow |5P_{3/2}; F'=3\rangle$ transition, with the lowest temperature of 155(5) $\mu$K is observed for $\delta \approx -\Gamma/2$. Heating is observed when the $n$-th comb mode is blue detuned from the resonance transition. Figure 2(a) shows the TOF image at 6 ms of expansion time for $\delta = -1.1\,\Gamma$, green data point, where the obtained cloud temperature is close to the initial temperature, see green slope in the inset. The measured width (FWHM) of the cloud along the $x$-axis which is relevant for 1D FC cooling is 2.75 mm.

The lowest temperature is observed for $\delta \approx -\Gamma/2$, blue data point, i.e., when there is a comb ($n$-th comb) detuned by $\approx -3$ MHz from the $^{87}$Rb $|5S_{1/2}; F=2\rangle \rightarrow |5P_{3/2}; F'=3\rangle$ transition. The corresponding TOF image, at 6 ms of expansion time, is shown in Fig. 2(b). As a consequence of the FC cooling the cloud FWHM along the $x$-axis is decreased to 2.17 mm. The temperature given by the slope in the inset is 155(5) $\mu$K. This temperature is, within measured uncertainty, in agreement with the predictions for the comb cooling Doppler temperature given in the works of Aumiler *et al.*[14] and Ip *et al.*[16] for our experimental parameters $\delta = -\Gamma/2$, $\theta = \pi/160$, $T_R = 12.5$ ns and $\zeta = 1$.

For a blue-detuned comb we observe heating, obtaining temperatures higher than the initial temperature, red data point and red slope in the inset. Correspondingly, the TOF image shown in Fig. 2(c) shows an increased cloud FWHM along the $x$-axis of 3.8 mm. The changes in the cloud temperature (along the $x$-axis) with the FC detuning are accompanied with the increase of the temperature in the $y$-axis, i.e., perpendicular to the FC cooling beams, due to the heating caused by spontaneous emission. The signature of this heating along the $y$-axis is evident in the increase of the cloud FWHM along the $y$-axis. Of the ones shown, the largest FWHM along the $y$-axis of 4.33 mm is obtained for the TOF image shown in Fig. 2(b) since the most efficient excitation (and consequently more spontaneous emission) is obtained for this detuning.

As the FC cooling time is increased, the cloud temperature decreases from the initial value prepared in the MOT phase, $T_i$, and the Doppler limited steady state temperature is achieved after a few ms of FC cooling time. In Fig. 3(a) the dependence of cloud temperature on the FC cooling time is shown, with an initial cloud temperature $T_i = 237\,\mu$K, $\delta = -2/3\,\Gamma$, and single comb mode intensity of 0.01 mW/cm$^2$. The steady state is achieved faster for higher comb mode intensities.

The dependence of the measured temperature on the intensity of the comb mode for a cloud with an initial temperature $T_i = 250\,\mu$K, FC cooling time of 3.5 ms, and for $\delta = -2/3\,\Gamma$ is shown in Fig. 3(b). Temperatures close to the Doppler temperature are obtained for a wide range of intensities, and an insignificant reduction in temperature is observed when the comb mode intensity approaches zero. Such behavior is a consequence of the very low comb mode intensities which are below 1% of the saturation intensity, $I_s$, for the $|5S_{1/2}; F=2\rangle \rightarrow |5P_{3/2}; F'=3\rangle$ transition[17] and a limited FC interaction time.

## Discussion

The results shown in Fig. 2 imply that the FC cooling is equivalent to the CW laser cooling, since a comb line red-detuned from the cooling transition is needed to obtain cooling. We verify this analogy by performing the same measurements with two counter-propagating CW beams replacing the FC beams, keeping all experimental parameters identical, with the two CW laser beams having intensity equal to the intensity of the relevant comb mode. The

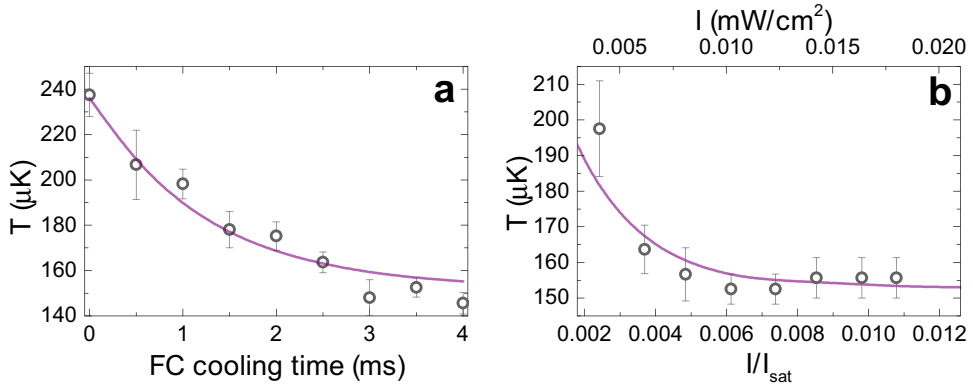


**Figure 3.** (**a**) The decrease in cloud temperature due to FC cooling as a function of the FC cooling time for an initial cloud temperature $T_i = 237\,\mu$K, $\delta = -2/3\Gamma$, and single comb mode intensity of 0.01 mW/cm$^2$. (**b**) The dependence of the measured temperature on the intensity of the comb mode for a cloud with an initial temperature $T_i = 250\,\mu$K, a FC cooling time of 3.5 ms and $\delta = -2/3\Gamma$. A theoretical model for relevant experimental parameters is also shown (solid line).

obtained temperatures are comparable to the temperatures measured in the case of FC cooling. With respect to this, FC cooling observed in our experiment can be interpreted as single comb mode cooling, i.e., only the $n$-th comb mode is relevant for cooling, while other comb modes do not contribute to cooling or significant heating of the atoms. This is in agreement with the estimation that the scattering rates of neighboring comb modes[13] are reduced by a factor of $(\Gamma/2\pi f_{rep})^2$, which in our experiment gives a factor of 0.0055. This rapid falloff of scattering rate with detuning ensures that, althougth there are many comb lines, the dominant contribution to the total scattering rate comes from the single, near-resonant comb line. In addition, this is in line with the measurement of the FC radiation pressure force, Fig. 1, where it is shown that only one comb mode, the $n$-th comb mode, participates in the excitation of the $|5S_{1/2}; F=2\rangle \rightarrow |5P_{3/2}; F'=3\rangle$ cooling transition. This also rules out the concern that the interaction with the $|5S_{1/2}; F=2\rangle \rightarrow |5P_{3/2}; F'=1,2\rangle$ resonances, Fig. 1, from which the (n − 3)rd and (n − 5)th comb mode are ≈25 MHz blue detuned, contributes to heating and degrades the minimal observed temperature. In order to model the measured temperatures, we consider the $n$-th comb mode as a CW laser and use the analytical formulas for the calculation of radiation pressure force and diffusion coefficients[20,21]. With these parameters we numerically solve the Fokker-Planck equation for a given FC interaction (cooling) time and extract the atomic velocity distribution after the interaction with the FC, from which the cloud temperature is then obtained. The calculated temperatures, for relevant experimental parameters, are shown in Figs 2 and 3 by solid lines. The agreement between theory and experiment is satisfactory. More details on the temperature calculation are given in Methods.

As seen in Fig. 3(b), our experiment is performed in the low intensity regime ($I \ll I_s$) that sets the limit of the observed temperature to the Doppler temperature. In order to achieve sub-Doppler temperatures, i.e., temperatures below 146 $\mu$K, the intensity of the comb mode must be increased by a factor of 40. This sub-Doppler threshold was obtained by measuring the temperature as a function of CW laser intensity in the case of CW laser cooling, and it is in agreement with the sub-Doppler threshold given in J. Dalibard and Y. Castin[22]. This leads to the conclusion that sub-Doppler cooling can be achieved with a FC of total output power about 840 mW. Such FC power levels are commercially available, thus the future demonstration of FC sub-Doppler cooling can be anticipated.

## Conclusion

We have demonstrated Doppler cooling of neutral rubidium atoms on a single-photon transition using a single comb line of a frequency comb. The analogy between FC (single comb line) and CW laser cooling is verified by performing the same measurements using a CW laser of appropriate intensity. The minimum temperature obtained is limited by the low intensity in the comb mode relevant for cooling rather than with the residual heating from adjacent comb modes. We believe that in future experiments the power per comb line can easily be increased by more than two orders of magnitude, which should allow cooling to temperatures approaching the recoil limit, thus opening the possibility of laser cooling of species that require light in the VUV spectral region and enabling their use in quantum optics experiments and their applications.

## Methods

**Frequency comb stabilization.** The spectrum of the frequency comb (FC) consists of a series of sharp lines, e.g. comb modes[23]. The optical frequency of the $n$-th comb mode is given by $f_n = nf_{rep} + f_0$, where $f_{rep}$ is the laser repetition frequency and $f_0$ is the offset frequency. Stabilization of the FC requires stabilization of these two degrees of freedom. In our experiment, we actively stabilize $f_n$ and $f_{rep}$. We stabilize a FC to a CW reference laser (ECDL, Moglabs CEL002) locked to the $^{87}$Rb $|5S_{1/2}; F=2\rangle \rightarrow |5P_{3/2}; F'=3\rangle$ transition.

The laser repetition frequency, $f_{rep}$, is a radio frequency (RF) signal of ≈80.5 MHz. It is detected with a high-speed photodiode and referenced to a rubidium frequency standard referenced low-noise synthesizer. The obtained error signal is used to actively stabilize $f_{rep}$ by feedback to the Er:fiber laser intracavity piezoelectric-transducer-mounted mirror.

The optical frequency of the $n$-th comb mode, $f_n$, is stabilized to an external cavity diode laser (ECDL) which is stabilized to the $^{87}$Rb $|5S_{1/2}; F=2\rangle \rightarrow |5P_{3/2}; F'=3\rangle$ cooling transition using polarization spectroscopy. $f_n$ is phase locked to the stabilized ECDL by using heterodyne spectroscopy. A fraction of the ECDL light ($\approx$10 mW) and a fraction of the FC light ($\approx$1 mW) are co-propagated and directed first onto a grating to spatially filter the unwanted comb modes to reduce background noise, and then onto a fast photodiode. The measured signal, $f_{beat}$, is a radio frequency signal in the range of 0–40 MHz. It is also referenced to a rubidium frequency standard referenced low-noise synthesizer. The obtained error signal is used for stabilization of $f_n$ via feedback to the Er:fiber laser current.

By changing the reference frequency for the beat note stabilization, it is possible to change the detuning of the *n-th* comb mode, $\delta$, from the the $|5S_{1/2}; F=2\rangle \rightarrow |5P_{3/2}; F'=3\rangle$ transition. The available range for a continuous change of the beat frequency is $f_{beat}$ = 5–30 MHz, so three scans with different detunings of the reference ECDL are measured and subsequently merged to obtain the total scan of 58 MHz shown in Fig. 1(b), while only one detuning of the reference ECDL is sufficient for the FC scan shown in Fig. 2.

The stability of the FC is evaluated by measuring the optical heterodyne beat note between the FC and an additional ECDL laser stabilized to a two-photon transition in rubidium, which serves as a length primary standard. The length primary standard laser is stabilized to the two-photon transition in $^{87}$Rb $|5S_{1/2}; F=2\rangle \rightarrow |5D_{5/2}; F'=4\rangle$ using a dither lock. The error signal is generated from the laser induced fluorescence (LIF) at 420 nm produced by rubidium atoms contained in a glass cell heated to $\approx$110 °C, where a photomultiplier tube collects the LIF and generates an adequate signal. The measured Allan deviation which determines the upper limit on the stability of our FC is $\approx$3 kHz for an integration time of 10 s.

**Theoretical model for the FC radiation pressure force calculation.** We model the electric field $E_T(t)$ of a FC by[24]

$$E_T(t) = \left[\sum_{m=0}^{\infty} \varepsilon(t - mT_R)e^{im\Phi_R}\right]e^{i\omega_L t}, \tag{1}$$

where $\varepsilon(t) = E_0\, sech\,(1.763t/T_p)$ is the single pulse envelope, $T_p$ is the pulse length, $T_R$ is the laser repetition period, $\Phi_R$ is the roundtrip phase acquired by the laser within the cavity and the laser spectrum is centered at $\omega_L + \Phi_R/T_R$. In addition to the FC beam we include a CW beam with amplitude $E_{cw}$, to model the repumper laser. For the simulation results presented in Fig. 1(c) we have used: $E_0 = 5\times10^4$ V/m, $T_p$ = 300 fs, $1/T_R$ = 80.54 MHz and $\Phi_R = 0$ for the FC beam and $E_{cw}$ = 40 V/m with a detuning of −100 MHz from the $|5S_{1/2}; F=1\rangle \rightarrow |5P_{3/2}; F'=2\rangle$ transition for the CW repumper beam. This corresponds to experimental values within measured uncertainty.

Dynamical evolution of the internal atomic states interacting with the FC field $E_T$ and the CW field $E_{cw}$ is modeled by optical Bloch equations (OBEs). The description of an OBE model for two-level atoms interacting with a FC is given e.g. in Ilinova *et al.*[25]. In our calculations we take into account the full hyperfine level structure of the $D_2(5S_{1/2} \rightarrow 5P_{3/2})$ line of $^{87}$Rb, i.e. a total of 6 levels, see Fig. 1. This results in a system of 21 coupled differential equations for the independent elements $\rho_{ij}(t)$ of the density matrix, which are solved numerically. To calculate the steady state values of an optical coherence, we average the solution for a pulse train consisting of 150 pulses over the duration of final 5 pulses. The Doppler shift due to pushing by the FC is neglected due to small velocity acquired (see description of Fig. 1).

We calculate the force $F_{FC}$ exerted on an atom by a FC pulse train propagating in the $+x$-direction by using the Ehrenfest theorem. The atom-light interaction is approximated to arise solely due to the three near-resonant comb modes. The effective on-resonance Rabi frequency of the $n$-th comb mode is given by $\Omega_n = \mu E_n^{eff}/\hbar$, where $\mu = \sqrt{7/6}\cdot 3.584\cdot 10^{-29}$ C·m is the transition dipole matrix element, and $E_n^{eff}$=3.1 V/m is the effective electric field amplitude of the $n$-th comb mode. As the powers in the neighboring comb modes are approximately equal, Rabi frequencies of the three modes differ solely due to different coupling strengths of their respective transitions. Ratios of the Rabi frequencies are thus $\eta_{n-5} = \Omega_{n-5}/\Omega_n = \sqrt{1/14}$ and $\eta_{n-3} = \Omega_{n-3}/\Omega_n = \sqrt{5/14}$[17]. Coupling of the FC to the $F=1$ ground state is neglected due to majority of population being in the $F=2$ ground state, as confirmed by simulations. Following Ilinova *et al.*[25], the total FC force on a single atom is now given by

$$F_{FC} = \hbar k\Omega_n(\eta_{n-5}\, Im(\rho_{21'}) + \eta_{n-3}\, Im(\rho_{22'}) + Im(\rho_{23'})), \tag{2}$$

where $k$ is the laser wavenumber and $\rho_{ij'}$ is an optical coherence of the transition $F=i \rightarrow F'=j'$.

**Theoretical model for a comb mode cooling.** In order to model the measured temperatures, we consider the $n$-th comb mode as a CW laser. Temperature is extracted from the width of the atomic velocity distribution obtained after a given interaction time with the laser. Since the atomic velocity distribution after the interaction can still be considered as Maxwell-Boltzman, the temperature is calculated using the relation $mv_{rms}^2 = k_B T$ where $m$ is the mass of rubidium atom, $v_{rms}$ is the standard deviation of the corresponding Gaussian function, $k_B$ is Boltzman constant, and $T$ is the temperature.

The atomic velocity distribution after a given interaction time is calculated by employing the Fokker-Planck equation[20]:

$$\frac{\partial\rho(v,\,t)}{\partial t} = -\frac{1}{m}\frac{\partial}{\partial v}(F(v)\rho(v,\,t)) + \frac{1}{m^2}\frac{\partial^2}{\partial v^2}(D(v)\rho(v,\,t)), \tag{3}$$

where $v$ is the velocity of the atom, $t$ is the interaction time, $\rho(v, t)$ is the atomic velocity distribution, $F(v)$ and $D(v)$ are velocity dependent radiation pressure force and diffusion coefficient, respectively.

Radiation pressure force and diffusion coefficients are calculated using standard low-intensity theory for a two-level atom in one dimension[20].

Total force from two counter-propagating light beams interacting with the $^{87}$Rb $|5S_{1/2}; F=2\rangle \rightarrow |5P_{3/2}; F'=3\rangle$ transition is equal to the sum of the contributions of the two counter-propagating beams:

$$F(v) = \frac{\hbar k^2 \delta \Gamma \Omega^2 v}{\left(\frac{\Omega^2}{2} + \frac{\Gamma^2}{4} + (\delta - kv)^2\right)\left(\frac{\Omega^2}{2} + \frac{\Gamma^2}{4} + (\delta + kv)^2\right)}. \tag{4}$$

The Rabi frequency, $\Omega$, is defined by the amplitude of the light electric field, transition dipole matrix element and reduced Planck constant, $k = 2\pi/780\ \mathrm{nm}^{-1}$ is the wave number, and $\delta$ is detuning from the atomic resonance frequency[17].

The diffusion coefficient is calculated from:

$$D(v) = \frac{\hbar^2 k^2 \Gamma \Omega^2 \left(\frac{\Omega^2}{2} + \frac{\Gamma^2}{4} + \delta^2 + (kv)^2\right)}{2\left(\frac{\Omega^2}{2} + \frac{\Gamma^2}{4} + (\delta - kv)^2\right)\left(\frac{\Omega^2}{2} + \frac{\Gamma^2}{4} + (\delta + kv)^2\right)}. \tag{5}$$

We numerically solve the Fokker-Planck equation for a given set of parameters: atom-light interaction time, $t_{FC}$, the amplitude of the light electric field, $E_0$, and detuning, $\delta$, and calculate the final atomic velocity distribution from which the temperature of the cloud after the interaction with the light beam is obtained. This temperature corresponds to the temperature measured by TOF spectroscopy, and it is shown by solid lines in Figs 2 and 3. For the simulation results presented in Fig. 2 we used $E_0 = 6\,\mathrm{V/m}$ and $t_{FC} = 3$ ms, while for the simulation results presented in Fig. 3(a,b) $E_0 = 8.2\,\mathrm{V/m}$, $\delta = -2/3\,\Gamma$ and $t_{FC} = 3.5$ ms are used, respectively. These results corresponds to the measured values within the measured uncertainty.

## Data Availability

The data that support the findings of this study are available from the corresponding author on reasonable request.

## References


1. Cronin, A. D., Schmiedmayer, J. & Pritchard, D. E. Optics and interferometry with atoms and molecules. *Reviews of Modern Physics* **81**, 1051–1129, https://doi.org/10.1103/RevModPhys.81.1051 (2009).
2. Bloom, B. J. *et al.* An optical lattice clock with accuracy and stability at the 10(−18) level. *Nature* **506**, 71–75, https://doi.org/10.1038/nature12941 (2014).
3. Ospelkaus, S. *et al.* Quantum-state controlled chemical reactions of ultracold potassium-rubidium molecules. *Science* **327**, 85317, http://science.sciencemag.org/content/327/5967/853 (2010).
4. Knoop, S. *et al.* Magnetically controlled exchange process in an ultracold atom-dimer mixture. *Phys. Rev. Lett.* **104**, 05321, https://doi.org/10.1103/PhysRevLett.104.053201 (2010).
5. Davila-Rodriguez, J., Ozawa, A., Hänsch, T. W. & Udem, T. Doppler cooling trapped ions with a uv frequency comb. *Phys. Rev. Lett.* **116**, 043002, https://doi.org/10.1103/PhysRevLett.116.043002 (2016).
6. Barry, J. F., McCarron, D. J., Norrgard, E. B., Steinecker, H. & DeMille, D. Magneto-optical trapping of a diatomic molecule. *Nature* **512**, 286–289, https://doi.org/10.1038/nature13634 (2014).
7. Peters, E. *et al.* A deep-uv optical frequency comb at 205 nm. *Opt. Express* **17**, 9183–9190, https://doi.org/10.1364/OE.17.009183 (2009).
8. Yost, D. C. *et al.* Vacuum-ultraviolet frequency combs from below-threshold harmonics. *Nature Physics* **5**, 815, https://doi.org/10.1038/nphys1398 (2009).
9. Bernhardt, B. *et al.* Vacuum ultraviolet frequency combs generated by a femtosecond enhancement cavity in the visible. *Opt. Lett.* **37**, 503, https://doi.org/10.1364/OL.37.000503 (2012).
10. Strohmeier, P. *et al.* Na-atom beam deceleration by a mode-locked laser. *Optics Communications* **73**, 451, https://doi.org/10.1016/0030-4018(89)90460-4 (1989).
11. Watanabe, M. *et al.* Velocity control of an yb beam by a frequency-doubled mode-locked laser. *J. Opt. Soc. Am. B* **13**, 2377, https://doi.org/10.1364/JOSAB.13.002377 (1996).
12. Blinov, B. B. *et al.* Broadband laser cooling of trapped atoms with ultrafast pulses. *J. Opt. Soc. Am. B* **23**, 1170, https://doi.org/10.1364/JOSAB.23.001170 (2006).
13. Kielpinski, D. Laser cooling of atoms and molecules with ultrafast pulses. *Phys. Rev. A* **73**, 063407, https://doi.org/10.1103/PhysRevA.73.063407 (2006).
14. Aumiler, D. & Ban, T. Simultaneous laser cooling of multiple atomic species using an optical frequency comb. *Phys. Rev. A* **85**, 063412, https://doi.org/10.1103/PhysRevA.85.063412 (2012).
15. Jayich, A. M., Long, X. & Campbell, W. C. Direct frequency comb laser cooling and trapping. *Phys. Rev. X* **6**, 041004, https://doi.org/10.1103/PhysRevX.6.041004 (2016).
16. Ip, M. *et al.* Phonon lasing from optical frequency comb illumination of trapped ions. *Phys. Rev. Lett.* **121**, 043201, https://doi.org/10.1103/PhysRevLett.121.043201 (2018).
17. Steck, D. A. Rubidium 87 d line data. *figshare*, http://steck.us/alkalidata/rubidium87numbers.pdf (2015).
18. Ban, T., Aumiler, D., Skenderović, H. & Pichler, G. Mapping of the optical frequency comb to the atom-velocity comb. *Phys. Rev. A* **73**, 043407, https://doi.org/10.1103/PhysRevA.73.043407 (2006).
19. Marian, A., Stowe, M. C., Lawall, J. R., Felinto, D. & Ye, J. United time-frequency spectroscopy for dynamics and global structure. *Science* **306**, 2063, https://doi.org/10.1126/science.1105660 (2004).
20. Metcalf, H. J. & van der Straten, P. *Laser Cooling and Trapping*. Springer Science and Business Media (2001).
21. Dalibard, J. & Cohen-Tannoudji, C. Laser cooling below the doppler limit by polarization gradients: simple theoretical models. *Journal of the Optical Society of America B* **6**, 2023–2045, https://doi.org/10.1364/JOSAB.6.002023 (1989).
22. Dalibard, J. & Castin, Y. Laser cooling from the semi-classical to the quantum regime. *figshare*, http://www.phys.ens.fr/dalibard/publi2/varenna1992.pdf (1992).
23. Ye, J. & Cundiff, S. T. *Femtosecond Optical Frequency Comb: Principle, Operation and Applications*. (Springer, US, 2005).
24. Xu, L. *et al.* Route to phase control of ultrashort light pulses. *Optics Letters* **21**, 2008, https://doi.org/10.1364/OL.21.002008 (1996).

25. Ilinova, E., Ahmad, M. & Derevianko, A. Doppler cooling with coherent trains of laser pulses and a tunable velocity comb. *Phys. Rev. A* **84**, 033421, https://doi.org/10.1103/PhysRevA.84.033421 (2011).

## Acknowledgements
The authors acknowledge support from the Croatian Science Foundation (Project Frequency-Comb-induced OptoMechanics - IP-2014-09-7342). In addition, the authors would like to warmly acknowledge Grzegorz Kowzan and Piotr Masłowski for their expert contribution to the frequency comb stabilization.

## Author Contributions
N.Š., T.B. and D.A. conceived the experiments, N.Š., D.B. and D.K. conducted the experiments, N.Š., D.B., D.K. and T.B. analyzed the results, I.K. and D.A. developed the theoretical models and performed calculations. All authors reviewed the manuscript.

## Additional Information
**Competing Interests:** The authors declare no competing interests.

**Publisher's note:** Springer Nature remains neutral with regard to jurisdictional claims in published maps and institutional affiliations.

# References


[1] M. Boyd, "High precision spectroscopy of strontium in an optical lattice: Towards a new standard for frequency and time", PhD thesis, 2002.

[2] A. Ludlow, "Strontium optical lattice clock: Optical spectroscopy with sub-hertz accuracy", PhD thesis, 2008.

[3] P, Westergaard, "Strontium optical lattice clock: In quest of the ultimate performance", PhD thesis, 2010.

[4] R. L. Targat, "Horloge à réseau optique au strontium : une 2ème génération d'horloges à atomes froids", PhD thesis, 2011.

[5] S. Bilicki, "Strontium optical lattice clocks: clock comparisons for timescales and fundamental physics applications", PhD thessis, 2018.

[6] S. Stellmer, "Degenerate quantum gases of strontium", PhD thesis, 2019.

[7] M. J. Martin, "Quantum metrology and many-body physics: Pushing the frontier of the optical lattice clock", PhD thesis, 2013.

[8] T. Nicholson, S. Campbell, R. Hutson, E. Marti, B. Bloom, R. McNally, W. Zhang, M. Barrett, M. Safronova, G. Strouse, W. Tew, and J. Ye, "Systematic evaluation of an atomic clock at 2 x $10^{-18}$ total uncertainty", *Nature Communications*, vol. 6, p. 6896, 2015-04, 2015.

[9] L. Essen and J. V. L. Parry, "An atomic standard of frequency and time interval: A cæsium resonator", *Nature*, vol. 176, pp. 280–282, 1955.

[10] J. Guena, M. Abgrall, D. Rovera, P. Laurent, B. Chupin, M. Lours, G. Santarelli, P. Rosenbusch, M. E. Tobar, R. Li, K. Gibble, A. Clairon, and S. Bize, "Progress in atomic fountains at LNE-SYRTE", *IEEE Transactions on Ultrasonics, Ferroelectrics, and Frequency Control*, vol. 59, no. 3, pp. 391–409, 2012.

[11] W. J. Riley, "Handbook of frequency stability analysis", 2008.

[12] W. Paul, "Electromagnetic traps for charged and neutral particles", *Rev. Mod. Phys.*, vol. 62, pp. 531–540, Jul 1990.

[13] T. Rosenband, D. B. Hume, P. O. Schmidt, C. W. Chou, A. Brusch, L. Lorini, W. H. Oskay, R. E. Drullinger, T. M. Fortier, J. E. Stalnaker, S. A. Diddams, W. C. Swann, N. R. Newbury, W. M.

Itano, D. J. Wineland, and J. C. Bergquist, "Frequency ratio of $Al^+$ and $Hg^+$ single-ion optical clocks; metrology at the 17th decimal place", *Science*, vol. 319, no. 5871, pp. 1808–1812, 2008.

[14] S. M. Brewer, J. S. Chen, A. M. Hankin, E. R. Clements, C. W. Chou, D. J. Wineland, D. B. Hume, and D. R. Leibrandt, "$^{27}Al^+$ quantum-logic clock with a systematic uncertainty below $10^{-18}$", *Phys. Rev. Lett.*, vol. 123, p. 033201, Jul. 2019.

[15] M. Chwalla, J. Benhelm, K. Kim, G. Kirchmair, T. Monz, M. Riebe, P. Schindler, A. S. Villar, W. Hänsel, C. F. Roos, R. Blatt, M. Abgrall, G. Santarelli, G. D. Rovera, and P. Laurent, "Absolute frequency measurement of the $^{40}Ca^+$ $4s\,^2S_{1/2} - 3d\,^2D_{5/2}$ clock transition", *Phys. Rev. Lett.*, vol. 102, p. 023002, Jan. 2009.

[16] K. Matsubara, H. Hachisu, Y. Li, S. Nagano, C. Locke, A. Nogami, M. Kajita, K. Hayasaka, T. Ido, and M. Hosokawa, "Direct comparison of a $Ca^+$ single-ion clock against a Sr lattice clock to verify the absolute frequency measurement", *Optics Express*, vol. 20, p. 22034, Sept. 2012.

[17] S. A. King, L. J. Spieß, P. Micke, A. Wilzewski, T. Leopold, E. Benkler, R. Lange, N. Huntemann, A. Surzhykov, V. A. Yerokhin, J. R. C. López-Urrutia, and P. O. Schmidt, "An optical atomic clock based on a highly charged ion", *Nature*, vol. 611, pp. 43–47, Nov 2022.

[18] N. Huntemann, C. Sanner, B. Lipphardt, C. Tamm, and E. Peik, "Single-ion atomic clock with $3 \times 10^{-18}$ systematic uncertainty," *Phys. Rev. Lett.*, vol. 116, p. 063001, Feb 2016.

[19] P. Dubé, A. A. Madej, and B. Jian, "$Sr^+$ single-ion clock", *Journal of Physics: Conference Series*, vol. 723, p. 012018, Jun 2016.

[20] A. A. Madej, P. Dubé, Z. Zhou, J. E. Bernard, and M. Gertsvolf, "$^{88}Sr^+$ 445-thz single-ion reference at the $10^{-17}$ level via control and cancellation of systematic uncertainties and its measurement against the si second", *Phys. Rev. Lett.*, vol. 109, p. 203002, Nov 2012.

[21] H. S. Margolis, G. P. Barwood, G. Huang, H. A. Klein, S. N. Lea, K. Szymaniec, and P. Gill, "Hertz-level measurement of the optical clock frequency in a single $^{88}Sr^+$ ion", *Science*, vol. 306, no. 5700, pp. 1355–1358, 2004.

[22] J. von Zanthier, T. Becker, M. Eichenseer, A. Y. Nevsky, C. Schwedes, E. Peik, H. Walther, R. Holzwarth, J. Reichert, T. Udem, T. W. Hänsch, P. V. Pokasov, M. N. Skvortsov, and S. N. Bagayev, "Absolute frequency measurement of the $In^+$ clock transition with a mode-locked laser", *Opt. Lett.*, vol. 25, pp. 1729–1731, Dec 2000.

[23] N. Ohtsubo, Y. Li, K. Matsubara, T. Ido, and K. Hayasaka, "Frequency measurement of the clock transition of an indium ion sympathetically-cooled in a linear trap", *Opt. Express*, vol. 25, pp. 11725–11735, May 2017.

[24] N. Ohtsubo, Y. Li, N. Nemitz, H. Hachisu, K. Matsubara, T. Ido, and K. Hayasaka, "Frequency ratio of an $^{115}in^+$ ion clock and a $^{87}Sr$ optical lattice clock", *Opt. Lett.*, vol. 45, pp. 5950–5953, Nov 2020.

[25] W. H. Oskay, S. A. Diddams, E. A. Donley, T. M. Fortier, T. P. Heavner, L. Hollberg, W. M. Itano,

S. R. Jefferts, M. J. Delaney, K. Kim, F. Levi, T. E. Parker, and J. C. Bergquist, "Single-atom optical clock with high accuracy", *Phys. Rev. Lett.*, vol. 97, p. 020801, Jul 2006.

[26] C. A. Holliman, M. Fan, A. Contractor, S. M. Brewer, and A. M. Jayich, "Radium ion optical clock", *Phys. Rev. Lett.*, vol. 128, p. 033202, Jan. 2022.

[27] I. Ushijima, M. Takamoto, M. Das, T. Ohkubo, and H. Katori, "Cryogenic optical lattice clocks", *Nature Photonics*, vol. 9, 02 2015.

[28] M. Bober, P. Morzyński, A. Cygan, D. Lisak, P. Masłowski, M. Prymaczek, P. Wcisło, P. Ablewski, M. Piwiński, S. Wójtewicz, K. Bielska, D. Bartoszek-Bober, R. S. Trawiński, M. Zawada, R. Ciuryło, J. Zachorowski, M. Piotrowski, W. Gawlik, F. Ozimek, and C. Radzewicz, "Strontium optical lattice clocks for practical realization of the metre and secondary representation of the second", *Measurement Science and Technology*, vol. 26, p. 075201, Jun 2015.

[29] S. Falke, N. Lemke, C. Grebing, B. Lipphardt, S. Weyers, V. Gerginov, N. Huntemann, C. Hagemann, A. Al-Masoudi, S. Häfner, S. Vogt, U. Sterr, and C. Lisdat, "A strontium lattice clock with inaccuracy and its frequency", *New Journal of Physics*, vol. 16, p. 073023, Jul 2014.

[30] N. Hinkley, J. A. Sherman, N. B. Phillips, M. Schioppo, N. D. Lemke, K. Beloy, M. Pizzocaro, C. W. Oates, and A. D. Ludlow, "An atomic clock with $10^{-18}$ instability", *Science*, vol. 341, no. 6151, pp. 1215–1218, 2013.

[31] B. J. Bloom, T. L. Nicholson, J. R. Williams, S. L. Campbell, M. Bishof, X. Zhang, W. Zhang, S. L. Bromley, and J. Ye, "An optical lattice clock with accuracy and stability at the $10^{-18}$ level", *Nature*, vol. 506, pp. 71–75, jan. 2014.

[32] M. Pizzocaro, P. Thoumany, B. Rauf, F. Bregolin, G. Milani, C. Clivati, G. A. Costanzo, F. Levi, and D. Calonico, "Absolute frequency measurement of the $^1$S$_0$ - $^3$P$_0$ transition of 171Yb", *Metrologia*, vol. 54, pp. 102–112, Jan. 2017.

[33] A. Zhang, Z. Xiong, X. Chen, Y. Jiang, J. Wang, C. Tian, Q. Zhu, B. Wang, D. Xiong, L. He, L. Ma, and B. Lyu, "Ytterbium optical lattice clock with instability of order $10^{-18}$", *Metrologia*, vol. 59, p. 065009, Nov 2022.

[34] H. Hachisu, K. Miyagishi, S. G. Porsev, A. Derevianko, V. D. Ovsiannikov, V. G. Pal'chikov, M. Takamoto, and H. Katori, "Trapping of neutral mercury atoms and prospects for optical lattice clocks", *Physical Review Letters*, vol. 100, feb 2008.

[35] L. Yi, S. Mejri, J. J. McFerran, Y. Le Coq, and S. Bize, "Optical lattice trapping of $^{199}$Hg and determination of the magic wavelength for the ultraviolet $^1S_0 \leftrightarrow {}^3P_0$ clock transition", *Phys. Rev. Lett.*, vol. 106, p. 073005, Feb 2011.

[36] R. Tyumenev, M. Favier, S. Bilicki, E. Bookjans, R. L. Targat, J. Lodewyck, D. Nicolodi, Y. L. Coq, M. Abgrall, J. Guéna, L. D. Sarlo, and S. Bize, "Comparing a mercury optical lattice clock with microwave and optical frequency standards", *New Journal of Physics*, vol. 18, p. 113002, Nov 2016.

[37] T. Hänsch and A. Schawlow, "Cooling of gases by laser radiation," *Optics Communications*, vol. 13, no. 1, pp. 68–69, 1975.

[38] S. Chu, L. Hollberg, J. E. Bjorkholm, A. Cable, and A. Ashkin, "Three-dimensional viscous confinement and cooling of atoms by resonance radiation pressure", *Phys. Rev. Lett.*, vol. 55, pp. 48–51, Jul 1985.

[39] D. J. Wineland, R. E. Drullinger, and F. L. Walls, "Radiation-pressure cooling of bound resonant absorbers", *Phys. Rev. Lett.*, vol. 40, pp. 1639–1642, Jun 1978.

[40] H. J. Metcalf and P. van der Straten, "Laser cooling and trapping", 1999.

[41] J. Dalibard and C. Cohen-Tannoudji, "Dressed-atom approach to atomic motion in laser light: the dipole force revisited", *J. Opt. Soc. Am. B*, vol. 2, pp. 1707–1720, Nov 1985.

[42] W. Ketterle and N. J. Van Druten, "Evaporative cooling of trapped atoms", *Advances in Atomic, Molecular, and Optical Physics*, vol. 37, 12 1996.

[43] E. L. Raab, M. Prentiss, A. Cable, S. Chu, and D. E. Pritchard, "Trapping of neutral sodium atoms with radiation pressure", *Phys. Rev. Lett.*, vol. 59, pp. 2631–2634, Dec 1987.

[44] D. W. Rankin, "Crc handbook of chemistry and physics, 89th edition, edited by David R. Lide", *Crystallography Reviews*, vol. 15, no. 3, pp. 223–224, 2009.

[45] D. Steck, "Rubidium 87 D Line Data", 2003.

[46] A. Landé, "Über den anomalen zeemaneffekt (teil i)," *Zeitschrift für Physik*, vol. 5, pp. 231–241, 1921.

[47] C. J. Foot, "Atomic physics", 2005.

[48] H. Batelaan, S. Padua, D. H. Yang, C. Xie, R. Gupta, and H. Metcalf, "Slowing of $^{85}\mathrm{Rb}$ atoms with isotropic light", *Phys. Rev. A*, vol. 49, pp. 2780–2784, Apr 1994.

[49] T. H. Loftus, T. Ido, M. M. Boyd, A. D. Ludlow, and J. Ye, "Narrow line cooling and momentum-space crystals", *Phys. Rev. A*, vol. 70, p. 063413, Dec 2004.

[50] Y. Castin, H. Wallis, and J. Dalibard, "Limit of doppler cooling", *J. Opt. Soc. Am. B*, vol. 6, pp. 2046–2057, Nov 1989.

[51] T. Binnewies, G. Wilpers, U. Sterr, F. Riehle, J. Helmcke, T. E. Mehlstäubler, E. M. Rasel, and W. Ertmer, "Doppler cooling and trapping on forbidden transitions", *Phys. Rev. Lett.*, vol. 87, p. 123002, Aug 2001.

[52] E. A. Curtis, C. W. Oates, and L. Hollberg, "Quenched narrow-line laser cooling of $^{40}\mathrm{Ca}$ to near the photon recoil limit", *Phys. Rev. A*, vol. 64, p. 031403, Aug 2001.

[53] J. E. Sansonetti and G. Nave, "Wavelengths, Transition Probabilities, and Energy Levels for the Spectrum of Neutral Strontium (Sr I)", *Journal of Physical and Chemical Reference Data*, vol. 39, pp. 033103–033103, Sept. 2010.

[54] M. Bober, "Zimne atomy strontu dla zastosowan metrologicznych", PhD thesis, 2012.

[55] A. D. Ludlow, M. M. Boyd, J. Ye, E. Peik, and P. O. Schmidt, "Optical atomic clocks", *Rev. Mod. Phys.*, vol. 87, pp. 637–701, Jun 2015.

[56] X. Xu, T. H. Loftus, J. L. Hall, A. Gallagher, and J. Ye, "Cooling and trapping of atomic strontium", *J. Opt. Soc. Am. B*, vol. 20, pp. 968–976, May 2003.

[57] J. L. Hall, M. Zhu, and P. Buch, "Prospects for using laser-prepared atomic fountains for optical frequency standards applications", *J. Opt. Soc. Am. B*, vol. 6, pp. 2194–2205, Nov 1989.

[58] H. Katori, T. Ido, Y. Isoya, and M. Kuwata-Gonokami, "Magneto-optical trapping and cooling of strontium atoms down to the photon recoil temperature", *Phys. Rev. Lett.*, vol. 82, pp. 1116–1119, Feb 1999.

[59] K. Vogel, T. Dinneen, A. Gallagher, and J. Hall, "Narrow-line doppler cooling of strontium to the recoil limit", *IEEE Transactions on Instrumentation and Measurement*, vol. 48, no. 2, pp. 618–621, 1999.

[60] F. Sorrentino, G. Ferraro, N. Poli, R. Drullinger, and G. M. Tino, "Laser cooling and trapping of atomic strontium for ultracold atoms physics, high-precision spectroscopy and quantum sensors", *Modern Physics Letters B*, vol. 20, p. 1287–1320, Sep 2006.

[61] H. Wallis and W. Ertmer, "Broadband laser cooling on narrow transitions", *J. Opt. Soc. Am. B*, vol. 6, pp. 2211–2219, Nov 1989.

[62] H. Miyake, N. C. Pisenti, P. K. Elgee, A. Sitaram, and G. K. Campbell, "Isotope-shift spectroscopy of the $^1S_0 \rightarrow {}^3P_1$ and $^1S_0 \rightarrow {}^3P_0$ transitions in strontium", *Phys. Rev. Research*, vol. 1, p. 033113, Nov 2019.

[63] T. Mukaiyama, H. Katori, T. Ido, Y. Li, and M. Kuwata-Gonokami, "Recoil-limited laser cooling of $^{87}$Sr atoms near the fermi temperature", *Phys. Rev. Lett.*, vol. 90, p. 113002, Mar 2003.

[64] A. Brusch, R. Le Targat, X. Baillard, M. Fouché, and P. Lemonde, "Hyperpolarizability effects in a Sr optical lattice clock", *Phys. Rev. Lett.*, vol. 96, p. 103003, Mar 2006.

[65] R. Grimm, M. Weidemüller, and Y. B. Ovchinnikov, "Optical dipole traps for neutral atoms", *Advances In Atomic, Molecular, and Optical Physics, Volume 42, 2000, Pages 95-170*, vol. 42, pp. 95–170, 2000.

[66] M. Witkowski, S. Bilicki, M. Bober, D. Kovačić, V. Singh, A. Tonoyan, and M. Zawada, "Photoionization cross sections of ultracold $^{88}$Sr in $^1$P$_1$ and $^3$S$_1$ states at 390 nm and the resulting blue-detuned magic wavelength optical lattice clock constraints", *Opt. Express*, vol. 30, pp. 21423–21438, Jun 2022.

[67] R. H. Dicke, "The effect of collisions upon the doppler width of spectral lines", *Phys. Rev.*, vol. 89, pp. 472–473, Jan. 1953.

[68] A. P. Kulosa, "Lamb-dicke spectroscopy of the $^1S_0 \rightarrow {}^3P_0$ transition in $^{24}$Mg and precise determination of the magic wavelength", PhD thesis, 2015.

[69] J. Mitroy, M. S. Safronova, and C. W. Clark, "Theory and applications of atomic and ionic polarizabilities", *Journal of Physics B: Atomic, Molecular and Optical Physics*, vol. 43, p. 202001, Oct 2010.

[70] N. Manakov, V. Ovsiannikov, and L. Rapoport, "Atoms in a laser field", *Physics Reports*, vol. 141, no. 6, pp. 320–433, 1986.

[71] A. Derevianko and H. Katori, "Colloquium: Physics of optical lattice clocks", *Rev. Mod. Phys.*, vol. 83, pp. 331–347, May 2011.

[72] M. S. Safronova, Z. Zuhrianda, U. I. Safronova, and C. W. Clark, "The magic road to precision", 2015.

[73] S. Porsev and A. Derevianko, "High-accuracy calculations of dipole, quadrupole, and octupole electric dynamic polarizabilities and van der waals coefficients $C_6$, $C_8$, and $C_{10}$ for alkaline-earth dimers", *Journal of Experimental and Theoretical Physics*, vol. 102, pp. 195–205, 02 2006.

[74] S. G. Porsev, A. D. Ludlow, M. M. Boyd, and J. Ye, "Determination of Sr properties for a high-accuracy optical clock", *Phys. Rev. A*, vol. 78, p. 032508, Sep 2008.

[75] V. D. Ovsiannikov, S. I. Marmo, V. G. Palchikov, and H. Katori, "Higher-order effects on the precision of clocks of neutral atoms in optical lattices", *pra*, vol. 93, p. 043420, Apr. 2016.

[76] M. M. Boyd, T. Zelevinsky, A. D. Ludlow, S. Blatt, T. Zanon-Willette, S. M. Foreman, and J. Ye, "Nuclear spin effects in optical lattice clocks", *Phys. Rev. A*, vol. 76, p. 022510, Aug 2007.

[77] M. Takamoto, H. Katori, S. I. Marmo, V. D. Ovsiannikov, and V. G. Pal'chikov, "Prospects for optical clocks with a blue-detuned lattice", *Phys. Rev. Lett.*, vol. 102, p. 063002, Feb 2009.

[78] A. Ludlow, T. Zelevinsky, G. Campbell, S. Blatt, M. Boyd, M. de Miranda, M. Martin, J. Thomsen, S. Foreman, J. Ye, T. Fortier, J. Stalnaker, S. Diddams, Y. Le Coq, Z. Barber, N. Poli, N. Lemke, K. Beck, and C. Oates, "Sr lattice clock at $1 \times 10^{-16}$ fractional uncertainty by remote optical evaluation with a Ca clock", *Science (New York, N.Y.)*, vol. 319, pp. 1805–8, 04 2008.

[79] A. D. Ludlow, M. M. Boyd, T. Zelevinsky, S. M. Foreman, S. Blatt, M. Notcutt, T. Ido, and J. Ye, "Systematic study of the $^{87}$Sr clock transition in an optical lattice", *Phys. Rev. Lett.*, vol. 96, p. 033003, Jan. 2006.

[80] H. Katori, M. Takamoto, V. G. Pal'chikov, and V. D. Ovsiannikov, "Ultrastable optical clock with neutral atoms in an engineered light shift trap", *Phys. Rev. Lett.*, vol. 91, p. 173005, Oct 2003.

[81] T. Middelmann, S. Falke, C. Lisdat, and U. Sterr, "High accuracy correction of blackbody radiation shift in an optical lattice clock", *Physical Review Letters*, vol. 109, Dec 2012.

[82] K. Beloy, "Lattice-induced nonadiabatic frequency shifts in optical lattice clocks", *Physical Review A*, vol. 82, Sep 2010.

[83] A. V. Taichenachev, V. I. Yudin, C. W. Oates, C. W. Hoyt, Z. W. Barber, and L. Hollberg, "Magnetic field-induced spectroscopy of forbidden optical transitions with application to lattice-based optical atomic clocks", *Phys. Rev. Lett.*, vol. 96, p. 083001, Mar 2006.

[84] S. Origlia, “A high-performance bosonic optical lattice clock”, PhD thesis, 2018.

[85] D. G. Matei, T. Legero, S. Häfner, C. Grebing, R. Weyrich, W. Zhang, L. Sonderhouse, J. M. Robinson, J. Ye, F. Riehle, and U. Sterr, “1.5 $\mu$m lasers with sub-10 mhz linewidth”, *Phys. Rev. Lett.*, vol. 118, p. 263202, Jun 2017.

[86] S. Will, “From atom optics to quantum simulation. interacting bosons and fermions in three-dimensional optical lattice potentials”, 2013.

[87] P. Lemonde and P. Wolf, “Optical lattice clock with atoms confined in a shallow trap”, *Phys. Rev. A*, vol. 72, p. 033409, Sep 2005.

[88] M. Glück, “Wannier–Stark resonances in optical and semiconductor superlattices”, *Physics Reports*, vol. 366, p. 103–182, Aug 2002.

[89] F. Gerbier, “Quantum gases in optical lattices", lecture, 2018.

[90] H. Perrin, “Les Houches lectures on optical lattices”, 2019.

[91] G. Tackmann, B. Pelle, A. Hilico, Q. Beaufils, and F. Pereira dos Santos, “Raman-laser spectroscopy of wannier-Stark states”, *Phys. Rev. A*, vol. 84, p. 063422, Dec 2011.

[92] C. Gabbanini, S. Gozzini, and A. Lucchesini, “Photoionization cross section measurement in a Rb vapor cell trap”, *Optics Communications*, vol. 141, no. 1, pp. 25–28, 1997.

[93] G. Ferrari, R. E. Drullinger, N. Poli, F. Sorrentino, and G. M. Tino, “Cooling of Sr to high phase-space density by laser and sympathetic cooling in isotopic mixtures”, *Phys. Rev. A*, vol. 73, p. 023408, Feb 2006.

[94] U. Fano, “Effects of configuration interaction on intensities and phase shifts”, *Phys. Rev.*, vol. 124, pp. 1866–1878, Dec 1961.

[95] W. Mende, K. Bartschat, and M. Kock, “Near-threshold photoionization from the Sr I (5s5p) $^1P^o_1$ state”, *Journal of Physics B Atomic Molecular Physics*, vol. 28, pp. 2385–2393, June 1995.

[96] S. Haq, S. Mahmood, N. Amin, Y. Jamil, and R. Ali, “Measurements of photoionization cross sections from the 5s5p $^1P_1$ and 5s6s $^1S_0$ excited states of strontium”, *Journal of Physics B: Atomic, Molecular and Optical Physics*, vol. 39, p. 1587, 03 2006.

[97] M. Abdel-Hafiz, P. Ablewski, A. Al-Masoudi, H. A. Mart’inez, P. Balling, G. P. Barwood, E. Benkler, M. Bober, M. Borkowski, W. Bowden, R. Ciuryło, H. Cybulski, A. Didier, M. Dolevzal, S. Dorscher, S. Falke, R. M. Godun, R. Hamid, I. R. Hill, R. Hobson, N. Huntemann, Y. L. Coq, R. L. Targat, T. Legero, T. Lindvall, C. Lisdat, J. Lodewyck, H. S. Margolis, T. E. Mehlstaubler, E. Peik, L. Pelzer, M. Pizzocaro, B. Rauf, A. Rolland, N. L. Scharnhorst, M. Schioppo, P. O. Schmidt, R. Schwarz, Caugri Senel, N. Spethmann, U. Sterr, C. Tamm, J. W. Thomsen, A. Vianello, and M. Zawada, “Guidelines for developing optical clocks with $10^{-18}$ fractional frequency uncertainty”, *arXiv: Atomic Physics*, 2019.

[98] G. García and J. Campos, “Transition probabilities for triplet levels of Sr(i)”, *Journal of Quantitative Spectroscopy and Radiative Transfer*, vol. 39, no. 6, pp. 477–483, 1988.

[99] G. Jonsson, C. Levinson, A. Persson, and C. G. Wahlström, "Natural radiative lifetimes in the $^1P_1$ and $^1f_3$ sequences of Sr i", *European Physical Journal A. Hadrons and Nuclei*, vol. 316, no. 3, pp. 255–258, 1984.

[100] P. G. Mickelson, Y. N. M. de Escobar, P. Anzel, B. J. DeSalvo, S. B. Nagel, A. J. Traverso, M. Yan, and T. C. Killian, "Repumping and spectroscopy of laser-cooled Sr atoms using the $(5s5p)^3P_2$–$(5s4d)^3D_2$ transition", *Journal of Physics B: Atomic, Molecular and Optical Physics*, vol. 42, p. 235001, Nov 2009.

[101] S. Zhang, P. Ramchurn, M. Menchetti, Q. Ubaid, J. Jones, K. Bongs, and Y. Singh, "Novel repumping on $^3P_2$-$^3D_2$ for Sr magneto-optical trap and Landé g-factor measurement of $^3D_1$", *Journal of Physics B: Atomic, Molecular and Optical Physics*, vol. 53, p. 235301, Oct 2020.

[102] R. Drever, J. Hall, F. Kowalski, J. Hough, G. Ford, A. Munley, and H. Ward, "Laser phase and frequency stabilization using an optical resonator", *Appl. Phys. B*, vol. 31, pp. 97–105, 06 1983.

[103] M. Bober, J. Zachorowski, and W. Gawlik, "Designing zeeman slower for strontium atoms - towards optical atomic clock", 2010.

[104] T. W. Hänsch, A. L. Schawlow, and G. W. Series, "The spectrum of atomic hydrogen", *Scientific American*, vol. 240, pp. 94–111, 1979.

[105] R. Drever, J. Hall, F. Kowalski, J. Hough, G. Ford, A. Munley, and H. Ward, "Laser phase and frequency stabilization using an optical resonator", *Appl. Phys. B*, vol. 31, pp. 97–105, 06 1983.

[106] E. D. Black, "An introduction to Pound–Drever–Hall laser frequency stabilization", *American Journal of Physics*, vol. 69, pp. 79–87, 2001.

[107] B. Rauf, M. C. V. López, P. Thoumany, M. Pizzocaro, and D. Calonico, "Phase noise cancellation in polarisation-maintaining fibre links", *Review of Scientific Instruments*, vol. 89, p. 033103, Mar 2018.

[108] D. Calonico, E. K. Bertacco, C. E. Calosso, C. Clivati, G. A. Costanzo, M. Frittelli, A. Godone, A. Mura, N. Poli, D. Sutyrin, G. M. Tino, M. Zucco, and F. Levi, "High-accuracy coherent optical frequency transfer over a doubled 642-km fiber link", *Applied Physics B*, vol. 117, pp. 979–986, 2014.

[109] L. S. Ma, P. Jungner, J. Ye, and J. L. Hall, "Delivering the same optical frequency at two places: accurate cancellation of phase noise introduced by an optical fiber or other time-varying path", *Opt. Lett.*, vol. 19, pp. 1777–1779, Nov 1994.

[110] K. Khabarova, A. Galyshev, S. Strelkin, A. Kostin, G. Belotelov, O. Berdasov, A. Gribov, N. Kolachevsky, and S. Slyusarev, "Spectroscopy of intercombination transition $^1S_0 \rightarrow {}^3P_1$ for secondary cooling of strontium atoms", *Quantum Electronics*, vol. 45, pp. 166–170, 02 2015.

[111] J. C. Hill, "Design and construction of apparatus for optically pumping $^{87}$Sr", master thesis, 2017.

[112] T. M. Brzozowski, M. Brzozowska, J. Zachorowski, M. Zawada, and W. Gawlik, "Probe spec-

troscopy in an operating magneto-optical trap: The role of raman transitions between discrete and continuum atomic states", *Phys. Rev. A*, vol. 71, p. 013401, Jan. 2005.

[113] M. Brzozowska, T. M. Brzozowski, J. Zachorowski, and W. Gawlik, "Nondestructive study of nonequilibrium states of cold trapped atoms", *Phys. Rev. A*, vol. 72, p. 061401, Dec 2005.

[114] J. Guo, P. R. Berman, B. Dubetsky, and G. Grynberg, "Recoil-induced resonances in nonlinear spectroscopy", *Phys. Rev. A*, vol. 46, pp. 1426–1437, Aug 1992.

[115] B. Lounis, P. Verkerk, J. Y. Courtois, C. Salomon, and G. Grynberg, "Quantized atomic motion in 1D cesium molasses with magnetic field", *Europhysics Letters (EPL)*, vol. 21, pp. 13–17, Jan. 1993.

[116] D. Grison, B. Lounis, C. Salomon, J. Y. Courtois, and G. Grynberg, "Raman spectroscopy of Cesium atoms in a laser trap", *Europhysics Letters (EPL)*, vol. 15, pp. 149–154, may 1991.

[117] J.-Y. Courtois, G. Grynberg, B. Lounis, and P. Verkerk, "Recoil-induced resonances in cesium: An atomic analog to the free-electron laser", *Phys. Rev. Lett.*, vol. 72, pp. 3017–3020, May 1994.

[118] C. Radzewicz, M. Bober, P. Morzyński, A. Cygan, D. Lisak, D. Bartoszek-Bober, P. Masłowski, P. Ablewski, J. Zachorowski, W. Gawlik, R. Ciuryło, and M. Zawada, "Accuracy budget of the $^{88}$Sr optical atomic clocks at KL FAMO", *Physica Scripta*, vol. 91, p. 084003, Jul 2016.

[119] J. Ye, H. J. Kimble, and H. Katori, "Quantum state engineering and precision metrology using state-insensitive light traps", *Science*, vol. 320, pp. 1734–1738, Jun 2008.

[120] T. Akatsuka, M. Takamoto, and H. Katori, "Three-dimensional optical lattice clock with bosonic $^{88}$Sr atoms", *Phys. Rev. A*, vol. 81, p. 023402, Feb 2010.

[121] K. Gibble, "Scattering of cold-atom coherences by hot atoms: Frequency shifts from background-gas collisions", *Phys. Rev. Lett.*, vol. 110, p. 180802, May 2013.

[122] S. G. Porsev and A. Derevianko, "Multipolar theory of blackbody radiation shift of atomic energy levels and its implications for optical lattice clocks", *Phys. Rev. A*, vol. 74, p. 020502, Aug 2006.

[123] P. Morzyński, M. Bober, D. Bartoszek-Bober, J. Nawrocki, P. Krehlik, u. Śliwczyński, M. Lipinski, P. Masłowski, A. Cygan, P. Dunst, M. Garus, D. Lisak, J. Zachorowski, G. Wojciech, C. Radzewicz, R. Ciuryło, and M. Zawada, "Absolute measurement of the $^1S_0 \rightarrow {}^3P_0$ clock transition in neutral $^{88}$Sr over the 330 km-long stabilized fibre optic link," *Scientific Reports*, vol. 5, p. 17495, 12 2015.

[124] M. S. Safronova, S. G. Porsev, U. I. Safronova, M. G. Kozlov, and C. W. Clark, "Blackbody-radiation shift in the Sr optical atomic clock", *Physical Review A*, vol. 87, jan 2013.

[125] K. Beloy, N. Hinkley, N. B. Phillips, J. A. Sherman, M. Schioppo, J. Lehman, A. Feldman, L. M. Hanssen, C. W. Oates, and A. D. Ludlow, "Atomic clock with $1 \times 10^{-18}$ room-temperature blackbody stark uncertainty", *Phys. Rev. Lett.*, vol. 113, p. 260801, Dec 2014.

[126] M. Takamoto, I. Ushijima, N. Ohmae, T. Yahagi, K. Kokado, H.-a. Shinkai, and H. Katori, "Test

of general relativity by a pair of transportable optical lattice clocks", *Nature Photonics*, vol. 14, pp. 1–5, 07 2020.

[127] P. Delva, J. Lodewyck, S. Bilicki, E. Bookjans, G. Vallet, R. L. Targat, P.-E. Pottie, C. Guerlin, F. Meynadier, C. L. Poncin-Lafitte, O. Lopez, A. Amy-Klein, W.-K. Lee, N. Quintin, C. Lisdat, A. Al-Masoudi, S. Dörscher, C. Grebing, G. Grosche, A. Kuhl, S. Raupach, U. Sterr, I. Hill, R. Hobson, W. Bowden, J. Kronjäger, G. Marra, A. Rolland, F. Baynes, H. Margolis, and P. Gill, "Test of special relativity using a fiber network of optical clocks", *Physical Review Letters*, vol. 118, Jun 2017.

[128] T. Bothwell, C. Kennedy, A. Aeppli, D. Kedar, J. Robinson, E. Oelker, A. Staron, and J. Ye, "Resolving the gravitational redshift across a millimetre-scale atomic sample", *Nature*, vol. 602, p. 420, 2022-01 2022.

[129] J. Grotti, S. Koller, S. Vogt, S. Häfner, U. Sterr, C. Lisdat, H. Denker, C. Voigt, L. Timmen, A. Rolland, F. Baynes, H. Margolis, M. Zampaolo, P. Thoumany, M. Pizzocaro, B. Rauf, F. Bregolin, A. Tampellini, P. Barbieri, and D. Calonico, "Geodesy and metrology with a transportable optical clock", *Nature Physics*, vol. 14, 05 2018.

[130] G. Lion, I. Panet, P. Wolf, C. Guerlin, S. Bize, and P. Delva, "Determination of a high spatial resolution geopotential model using atomic clock comparisons", *Journal of Geodesy*, vol. 91, pp. 597–611, jan 2017.

[131] H. Denker, L. Timmen, C. Voigt, S. Weyers, E. Peik, H. Margolis, P. Delva, P. Wolf, and G. Petit, "Geodetic methods to determine the relativistic redshift at the level of $10^{-18}$ in the context of international timescales: a review and practical results", *Journal of Geodesy*, vol. 92, 12 2017.